In situ and ex situ electron microscopy and X-ray diffraction characterization of the evolution of a catalytic system - from synthesis to deactivation

Gardini, Diego

Publication date:
2015

Document Version
Publisher's PDF, also known as Version of record

In situ and *ex situ* electron microscopy and X-ray diffraction characterization of the evolution of a catalytic system - from synthesis to deactivation

Ph.D. thesis by

Diego Gardini

Center for Electron Nanoscopy
Technical University of Denmark

September 14^{th}, 2015

Abstract

Heterogeneous catalysis represents a research field of undeniable importance for a multitude of technological and industrial processes. Supported catalysts are nowadays at the base of the large-scale production of most chemicals and are used for the removal of air pollutants from automotive engines. In the last years, heterogeneous catalysis has also acquired a major role in the growing field of green chemistry, where minimization of waste products and increased synthesis efficiency are of utmost importance.

The catalytic properties of a material system are strongly connected to its overall structure. Factors such as size, shape, chemical composition and crystal structure, define the final activity, selectivity and stability towards a specific chemical reaction. In this perspective, the rational design of novel catalysts requires a strong material characterization effort, in order to maximize the understanding of the structural properties and mechanisms at the origin of catalytic activity.

This thesis presents the potential and uniqueness of *ex situ* and *in situ* transmission electron microscopy (TEM) and X-ray diffraction (XRD) techniques in the characterization of several supported material systems at different stages of their catalytic life. Starting by synthesis, passing by operation and ending through deactivation, the combined use of the two techniques allowed to investigate the evolution of the catalytic activity of these systems in connection with their morphological, crystallographic and chemical properties.

Three hydrodeoxygenation (HDO) catalysts, Ni/ZrO_2, Mo_2C/ZrO_2 and $Ni\text{-}MoS_2/ZrO_2$ have been investigated in the initial and final stage of their catalytic life: synthesis and deactivation.

The combined use of TEM imaging and spectroscopy allowed to investigate the influence of the synthesis procedure on the activity of Ni/ZrO_2. A relation between the size distribution of supported Ni particles and the catalytic activity profiles could be established using this approach. Furthermore, TEM and XRD allowed to assess the correct formation of the active phases of both Mo_2C/ZrO_2 and $Ni\text{-}MoS_2/ZrO_2$ catalysts.

The stability of Ni/ZrO_2 and $Ni\text{-}MoS_2/ZrO_2$ catalysts upon exposure to different poisoning species was studied by the acquisition of energy dispersive X-ray spectroscopy (EDX) maps. For Ni/ZrO_2, sulfur and potassium were found to cause a permanent deactivation whereas chlorine adsorption on the catalyst active site was found to be reversible. The exposure of $Ni\text{-}MoS_2/ZrO_2$ to different H_2S and H_2O feed concentrations lead to important modifications of the catalyst active phase. Low H_2S concentrations in the feed were found to induce a sulfur depletion of the NiMoS active phase, whereas

presence of water in the feed induced an S-O exchange at the edges of MoS_2 slabs. Both processes were connected to loss of activity during prolonged catalytic tests. Finally, environmental TEM (ETEM) studies allowed to investigate *in situ* the effect of water exposure on Mo_2C/ZrO_2. A combination of high resolution TEM (HRTEM) and electron energy loss spectroscopy (EELS) revealed the degradation of the supported carbide particles probably due to the formation of volatile molybdenum hydroxide species.

The activity of silver nanoparticles as catalyst for soot oxidation was studied in operative conditions. The carbon oxidation reaction was investigated *in situ* in the ETEM and fundamental insights on the mechanisms leading to catalytic activity were obtained. The silver phase exhibited significant mobility during soot oxidation as a result of the presence of attractive forces between Ag nanoparticles and the soot matrix. This mobility was found to be dependent on the silver particle size and it was responsible of lowering the carbon oxidation temperature by a mechanism ensuring the constant presence of a reactive carbon-silver-oxygen interface during reaction. Small silver particles were observed to catalyze carbon oxidation at lower temperature than big ones, due to the lower temperature needed to trigger silver mobility.

Resumé

Heterogen katalyse repræsenterer et forskningsområde, som er utroligt vigtigt for teknologiske og industrielle processer. Supporterede katalysatorer udgør i dag fundamentet for stor-skala produktion af de fleste kemikalier og bruges til at fjerne luftforurening fra forbrændingsmotorer. I de seneste år har heterogen katalyse fået en større rolle inden for den voksende grønne kemi, hvor formindskelse af affaldsprodukter og forøget synteseeffektivitet er af allerstørste vigtighed.

En katalysators effektivitet hænger nøje sammen med dens generelle struktur. Faktorer såsom størrelse, form, kemisk sammensætning og krystalstruktur afgør den samlede aktivitet, selektivitet og stabilitet i forbindelse med en specifik kemisk reaktion. I dette perspektiv kræver rational design af nye katalysatorer en stor indsats inden for materialekarakterisering, for at maksimere forståelsen af strukturelle egenskaber og mekanismer i katalyse.

Denne afhandling beskriver potentialet og det helt unikke ved at benytte ex situ og in situ transmissionselektronmikroskopi (TEM) og Røntgendiffraktion (XRD) til karakterisering af supporterede materialesystemer på deres forskellige stadier. Kombinationen af de to karakteriseringsteknikker gør det muligt at undersøge udviklingen af disse systemers katalytiske aktivitet sammen med deres morfologi, krystallografi og kemiske egenskaber i løbet af katalysatorens syntese, funktion og til sidst deaktivering.

Tre katalysatorer anvendt til de såkaldte hydrodeoxygenering reaktioner (fjernelse af oxygen), Ni/ZrO_2, Mo_2C/ZrO_2 og $Ni\text{-}MoS_2/ZrO_2$ er blevet undersøgt på det indledende og afsluttende stadie: Syntese og deaktivering.

Kombinationen af TEM- billeddannelse og spektroskopi gjorde det muligt at undersøge synteseprocedurens indflydelse på aktiviteten af Ni/ZrO_2. Forholdet mellem størrelsesfordelingen af supporterede Ni-partikler og den katalytiske aktivitetsprofil blev undersøgt. Desuden gjorde TEM og XRD det muligt at vurdere den korrekte dannelse af aktive faser for både Mo_2C/ZrO_2 og $Ni\text{-}MoS_2/ZrO_2$-katalysatorerne.

Ved brug af energidispersiv Røntgen-spektroskopi (EDX) kortlægning var det muligt at studere stabiliteten af Ni/ZrO_2- og $Ni\text{-}MoS_2/ZrO_2$-katalysatorerne, efter at de var blevet udsat for forskellige elementer, der potentielt kan ødelægge katalysatorens aktivitet. Ni/ZrO_2 udviste permanent deaktivering i tilfælde af svovl- og kaliumforurening, mens kloradsorption på de katalytisk aktive 'sites' viste sig at være reversible. $Ni\text{-}MoS_2/ZrO_2$ udsat for forskellige H_2S og H_2O koncentrationer i 'feed-gassen' medførte vigtige modifikationer af den katalytisk aktive fase. Lav H_2S koncentration i feed-gassen medførte en svovludtømning af den aktive NiMoS-fase, mens vands tilstedeværelse i feed-gassen medførte en S-O-udveksling ved de aktive MoS_2-pladers kanter.

Begge processer medførte en lavere aktivitet ved længerevarende katalytiske test. Endelig gjorde environmetal TEM (ETEM) det muligt at studere effekten på nanoskala af Mo_2C/ZrO_2 udsat for vand in situ. En kombination af højopløst TEM (HRTEM) og elektron-energitabs-spektroskopi (EELS) viste en degradering af de supporterede karbidpartikler, hvilket sandsynligvis skyldes dannelsen af flygtige molybdænhydroxidforbindelser.

Sølvnanopartiklers aktivitet som katalysator for sodoxidering blev undersøgt ved operative betingelser. Kuloxideringsreaktionen blev undersøgt in situ i ETEMet, hvilket gav fundamental indsigt i mekanismerne, der medfører katalytisk aktivitet. Som resultat af tiltrækkende kræfter mellem sølvnanopartiklerne og sodmatricen, udviste sølvfasen signifikant mobilitet under sodoxideringen. Denne mobilitet viste sig afhængig af sølvpartiklernes størrelse og var ansvarlig for en nedsættelse af kuloxideringstemperaturen ved en mekanisme, som sikrede en konstant tilstedeværelse af reaktive kul-sølv-ilt-overgang under reaktionen. Det blev observeret, at små sølvpartikler medvirkede til en lavere oxideringstemperatur end store partikler, da det krævede en lavere temperatur at igangsætte sølvmobiliteten.

Acknowledgments

This thesis describes the work carried out during my Ph.D. project at the Center for Electron Nanoscopy of the Technical University of Denmark (DTU Cen) between September 2012 and September 2015, under the supervision of Professor Jakob Birkedal Wagner and Associate Professor Christian Danvad Damsgaard. My first thanks go to them. Thank you for your unconditional support and for fostering my curiosity and enthusiasm. Working with you has been a real pleasure.

This project is the result of a strong collaboration between DTU Cen and the Department of Chemical and Biochemical Engineering (DTU Kemiteknik).
Synthesis and catalytic testing of hydrodeoxygenation catalysts (Chapter 4) have been carried out by Peter Mølgaard Mortensen as a part of his Ph.D. project. Thank you Peter for the time spent together and your precious advices. I really appreciate your method and competence.
Soot oxidation studies (Chapter 5) have been carried out in collaboration with Assistant Professor Jakob Munkholt Christensen. I would like to thank Jakob for his infinite patience and for the enthusiasm he dedicated to our work.
Special thanks also go to Professor Anker Degn Jensen for his support. I appreciated your valuable opinion and feedback on my research throughout these three years.

Many thanks to Professor Jan-Dierk Grunwaldt from Karlsruhe Institute for Technology (KIT) for his advices and support during the meetings we had in Denmark and Germany.

Part of the experiments presented in this thesis have been performed at the Interdisciplinary Center for Electron Microscopy (CIME) at EPFL, Switzerland and in the Electron Microscopy for Materials Science (EMAT) research group at the University of Antwerp, Belgium. The scientific staffs at CIME and EMAT are gratefully acknowledged for their assistance.

None of this would have happened without the support of my colleagues and friends at Cen. Thank you for making me feel welcome from the very first day. Together we shared the most warm and positive environment. I owe a lot of gratitude to Willie, Jens, Zoli and Hossein. Thank you for always being there when I needed it, at work and outside. I will miss our moka club.

In particular, I would like to say thanks to my friend Davide. We shared together office, flat and some of the best moments I had in Denmark (and abroad!). Thanks for being the person you are. Special thanks to Filippo for the countless nights spent in the workshop and his (many) contagious passions and hobbies. Thanks to Manuel for his positive way of life. You made me smile when the mood was down. Thanks to

Hugo for the time spent together discussing about the most diverse arguments. Huge thanks to Zanza and Riccardo for your constant presence and support, no matter how far we are from each other. Thanks to Valeria for being so special to me. You make my life happier. Thanks to Roberto for the wonderful design of the thesis cover. Thanks to all my friends in Denmark and in Italy. You are simply too many to be listed here!

Finally, my most sincere gratitude goes to my family, who watched and supported me from the distance. Thank you for the love, affection and encouragement you gave me. This thesis is dedicated to you.

Contents

CHAPTER 1

Introduction

In 1540 the german botanist, pharmacist and physician Valerius Cordus noticed that the addition of sulfuric acid ("sour oil of vitriol") to ethanol ("triply-distilled wine"), led to the formation of a substance that he named "sweet oil of vitriol". With his procedure, Valerius Cordus was the first to synthesize ether (which would be used three centuries later as an anesthetic), and involuntarily reported the first use of an inorganic catalyst.

The history of catalysis has its roots in the alchemic era, where the knowledge of chemical reactions was mainly empirical and there was no concept of valence or bonds, but rather one of affinity. In this period, the work done on catalyzed reactions consisted mainly of isolated observations that were rarely documented or explained. It was only in 1836 that the Swedish chemist Jöns Jakob Berzelius published a report in which a number of earlier findings on chemical changes in both homogeneous and heterogeneous systems were reviewed, showing that these could be rationally explained by the introduction of a new concept. Berzelius proposed the existence of a new force called the "catalytic force", and he called "catalysis" the decomposition of bodies by this force. In a short paper summarizing his ideas he wrote [1]:

> "It is, then, proved that several simple or compound bodies, soluble and insoluble, have the property of exercising on other bodies an action very different from chemical affinity. By means of this action they produce, in these bodies, decompositions of their elements and different recombinations of these same elements to which they remain indifferent."

further developing the idea of a catalysts as a substance that remain unaltered through the reaction.

Since Berzelius' intuition, a new period characterized by systematic investigations and discovery of new catalytic processes started. During this time, thanks to the development of thermodynamics (and modern chemistry in general), the fundamental theory of catalysis was written and the growing academic knowledge started to translate into tangible industrial applications. It soon became clear that catalysis could be applied in most chemical reactions and that significant financial benefits could be gained by implementing a proper catalyst in an industrial process. The growing need of

bulk chemicals, boosted by both World Wars and, later, the fast expansion of the petrochemical industry, consolidated the economical role of catalysis in modern society.

Table 1.1: Important industrial heterogeneous catalytic processes. Data from [2]

Process	Year	Typical catalyst
SO_2 oxidation to sulfuric acid	1875	V_2O_5-K_2SO_4/SiO_2
Methanol to formaldehyde	1890	Ag
Olefin hydrogenation	1902	Ni, Pt
Hydrogenation of edible fats and oils	1900s	Ni
Ammonia synthesis	1913	Fe supported on Al_2O_3
Ammonia oxidation	1906	Pt-Rh
Fisher-Tropsch synthesis	1938	Fe, Co, Ru

Depending on whether a catalyst exists in the same phase as the reactants, catalytic actions can be classified in two distinct categories. The first case, known as homogeneous catalysis, is typical of acids or organometallic compounds and it includes reactions where the catalyst is in the same physical phase as the reactants. The second case instead will be the subject of the studies presented in this thesis and it is known as heterogeneous catalysis. In heterogeneous catalysis, the reaction occurs at the interface of two (or more) phases, with a typical example being gas-solid interactions, although gas-liquid-solid and gas-solid-solid are not uncommon. The vast majority of practical heterogeneous catalysts are solids, often metals, metal oxides or zeolites. An overview of the most important industrial heterogeneous catalytic processes is shown in Table 1.1.

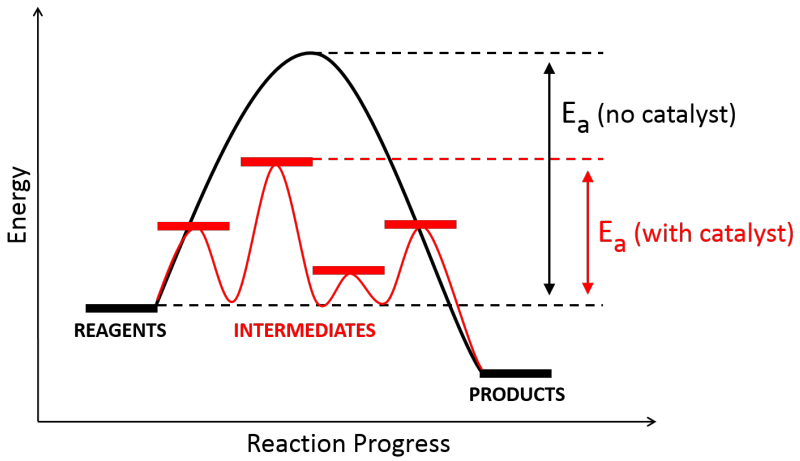

Figure 1.1: Schematic representation of a catalyzed (red) and uncatalyzed (black) generic reaction pathway.

The main function of a catalyst is to increase the rate of a targeted chemical reaction so that to increase the conversion of the reactants into specific products. In order to do so, a catalyst provides an alternative path to the original reaction involving one or multiple transition states of lower activation energy (Figure 1.1).

In heterogeneous catalysis, the activity of a catalyst will largely rely on a mechanism involving the adsorption and desorption of reactants and products over specific portions of the catalyst surface called active sites. These can be, for example, single atoms, defects, or particular crystal facets and the control of their number and availability to the reactants is of crucial interest in catalysis research.

In order to increase the surface area of a catalyst, and hence the number of active sites, a supporting material is often used. This has the role to prevent agglomeration of the catalytically active phase upon synthesis and operation (sintering) and in some cases enhances its activity through physicochemical interactions such as charge transfer or encapsulation [3]. The maximal surface exposure is often reached in a typical heterogeneous catalyst by synthesis of the active phase in the form of nanoparticles supported on a high surface area material, normally a metal oxide such as alumina, silica or activated carbon.

The crystal structure of these nanoparticles can also play a very important role towards the final catalytic activity, as the atomic arrangement will directly influence both the electronic properties and the surface structure of the active phase. TiO_2 nanoparticles, for example, show different reactive oxygen species (ROS) generation activity depending on their crystal structure, with anatase nanoparticles being more active than their rutile counterpart due to the higher aptitude of anatase facets to adsorb oxygen in the form of O_2^- and O^- [4].

Finally, depending on the presence and the concentration of certain chemical modifiers in the reaction environment, the activity of a catalyst can be either promoted or inhibited. The first case is typical of hydrotreating sulfide catalysts, where nickel or cobalt atoms replace specific molybdenum atoms in the MoS_2 structure, weakening the neighbouring Mo-S bonds and increasing the number of sulfur vacancy active sites. On the contrary, some chemical species that might be present as impurities or reaction products can deposit on the surface of the catalyst or strongly adsorb on its active sites, ultimately inhibiting its catalytic action. This is the case for example of coking, a deactivation process consisting in the deposition of carbonaceous materials on the surface of a catalyst during operation [5].

The activity and stability of an heterogeneous catalyst is hence strongly correlated to three main properties that together define its overall structure: morphology, crystallinity and chemistry. The implementation of a characterization procedure able to provide information on each of these material properties is thus of utmost importance for the design and test of an active and stable catalytic system.

The aim of the PhD project presented in this thesis is to explore the potential and uniqueness of the combination of *ex situ* and *is situ* electron microscopy and X-ray diffraction (XRD) techniques in the characterization of an heterogeneous catalytic system. A particular focus will be given on the role of transmission electron microscopy (TEM) as a tool for increasing the understanding of the mechanisms behind the activity of a catalyst at every stage of its life. Starting from synthesis, passing by operation and ending through deactivation, a combination of TEM imaging and spectroscopy techniques will be used to extract invaluable information on the morphological, crystallographic and chemical evolution of several material systems, allowing to draw a direct correlation between their structure and catalytic properties.

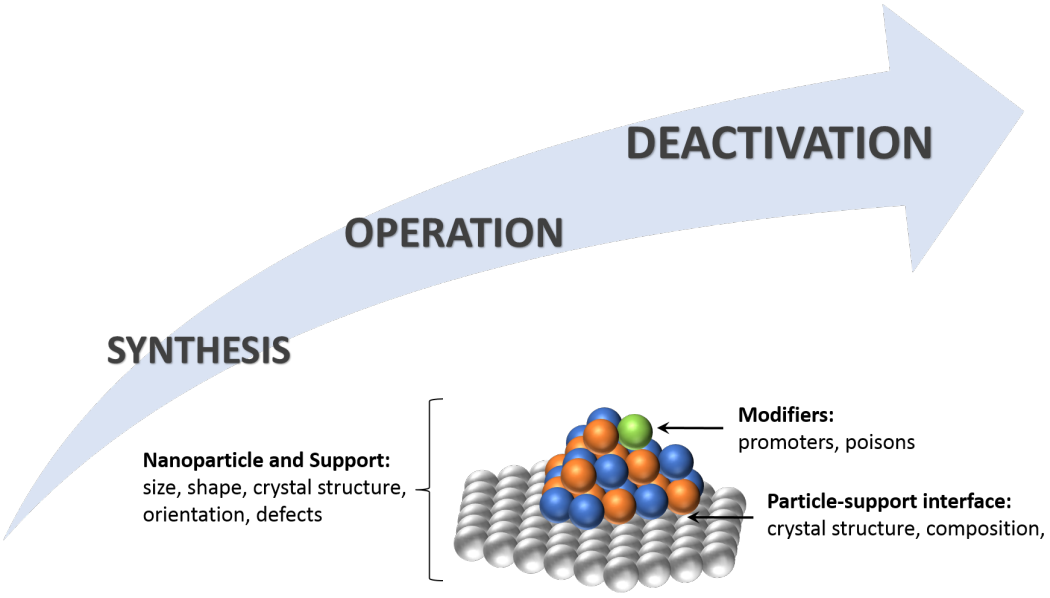

Figure 1.2: Characteristics affecting the activity and selectivity of a supported nanoparticle catalytic system during all stages of its life.

In a collaborative approach with the Department of Chemical and Biochemical Engineering of the Technical University of Denmark (DTU Kemiteknik), three bio-oil hydrodeoxygenation catalysts (Ni/ZrO_2, Mo_2C/ZrO_2, $Ni\text{-}MoS_2/ZrO_2$) and one soot oxidation catalyst (silver nanoparticles) have been investigated. The characterization study carried out on Ni/ZrO_2, Mo_2C/ZrO_2 and $Ni\text{-}MoS_2/ZrO_2$ has its focus on I) the influence of the synthesis procedure on the catalytic activity of these material systems and II) the mechanisms leading to activity loss, thus covering the initial and final stages of the catalysts life. Furthermore, the mechanisms behind the catalytic activity of silver nanoparticles during soot oxidation have been studied by an *in situ* ETEM based approach, allowing the direct characterization of this catalyst in operative conditions.

CHAPTER 2

Instrumentation and techniques

In this chapter, a brief description of the transmission electron microscope and the related techniques used in this thesis is given. Both *in situ* and *ex situ* aspects of electron microscopy are addressed, with a particular focus on the description of the environmental TEM and sample holders used for the *in situ* experiments presented in Chapter 4 and 5. The basic principles of X-ray diffraction and the description of the in situ XRD setup used in Chapter 4 are presented as well.

2.1 The transmission electron microscope

In an optical microscope, the Rayleigh criterion defines the smallest distance that can be resolved between two points as:

$$\Delta d = \frac{0.61\lambda}{\mu sin(\beta)} \tag{2.1}$$

where λ is the wavelength of the radiation involved, μ is the refractive index of the medium and β is the semiangle of collection of the magnifying lenses. As the resolution is proportional to the wavelength of the source, many derivations of conventional light microscopes have been built using UV or X-Ray sources in order to increase the instrumental resolving power.

In a TEM an electron-transparent sample is illuminated with high energy electrons generated by an electron gun and accelerated by an applied voltage. The electrons transmitted through the specimen are used to create an image and extract spectroscopic information. As it will be shown in the following sections, the interaction between the electron beam and the sample generates a number of different signals that can be analyzed by the use of appropriate detector placed inside the microscope column.

Electrons are quantum particles and possess a De Broglie wavelength λ related to their momentum p:

$$\lambda = \frac{h}{p} \tag{2.2}$$

where h is the Plank's constant. When electrons are accelerated by a voltage V, they acquire a kinetic energy that must be equal to the potential energy

$$eV = \frac{1}{2}m_0v^2 \tag{2.3}$$

Considering the definition of particle momentum $p = m_0v$, λ can be rewritten as:

$$\lambda = \frac{h}{\sqrt{2m_0eV}} \tag{2.4}$$

Equation 2.4 is then corrected for relativistic effects taking place at common TEM accelerating voltages (80-400 kV), becoming:

$$\lambda = \frac{h}{\sqrt{2m_0eV\left(1 + \frac{eV}{2m_0c^2}\right)}} \tag{2.5}$$

Typical electron wavelengths are 3.35 pm for 120 kV, 2.51 pm for 200 kV and 1.97 for 300 kV accelerating voltages.

As in light microscopy, the radiation generated from the source needs to be deviated and focused. Electrons are charged particles and their trajectories can be modified by the Lorentz force. In the TEM column multiple coils of conductive material are used to form rotationally symmetric electromagnetic lenses, able to deviate electron trajectories and focus them in a spiral motion.

Different set of lenses exist, each one having a dedicated function. A set of condenser lenses is responsible for the control of the beam intensity and convergence at the specimen. Transmitted electrons are collected by the objective lens, projecting the image of the specimen and its diffraction pattern respectively in the image and back focal plane of the lens. An objective aperture can be used to select which portion of the diffraction pattern should contribute in the formation of the image. If the aperture is centered on the direct beam, a bright field image will be formed. Alternatively, the objective aperture can be displaced in order to select and transmit electrons scattered at particular angles, and a dark field image will be generated (Figure 2.1). Finally, a group of intermediate and projection lenses allows to switch between image and diffraction mode and are responsible for the magnification of the projected image (or diffraction pattern).

As the generated magnetic field is generally not uniform, electromagnetic lenses will focus electrons entering the lens at different distances from the optical axis in different focal planes. This phenomenon is known as spherical aberration and it represents one of the major effects limiting the resolution in a TEM. Nowadays, modern TEMs can be equipped with supplementary lens systems able to compensate spherical aberration and achieve higher resolutions.

Depending on the nature of the specimen, illumination and detection conditions, different contrast mechanisms are possible in the TEM. Mass-thickness contrast arises from incoherent elastic scattering of electrons (Rutherford scattering). The cross section of this scattering phenomenon is a function of the atomic number Z and the

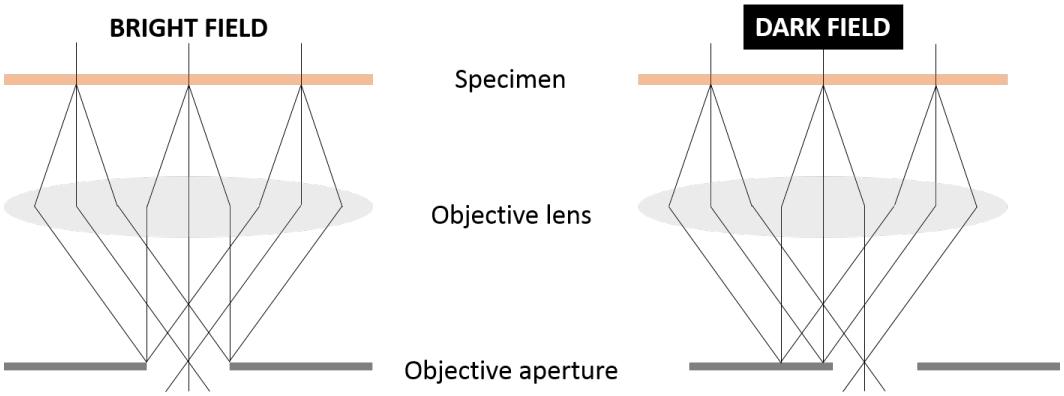

Figure 2.1: Schematic representation of the formation of **(left)** bright field and **(right)** dark field image.

thickness of the specimen. Different samples (or different areas of the same sample) having higher mass/thickness will scatter more primary electrons than lighter and thinner ones. Therefore, in a bright field image, areas of high mass/thickness will appear darker, as less electrons from these regions will be collected by the objective aperture (Figure 2.2).

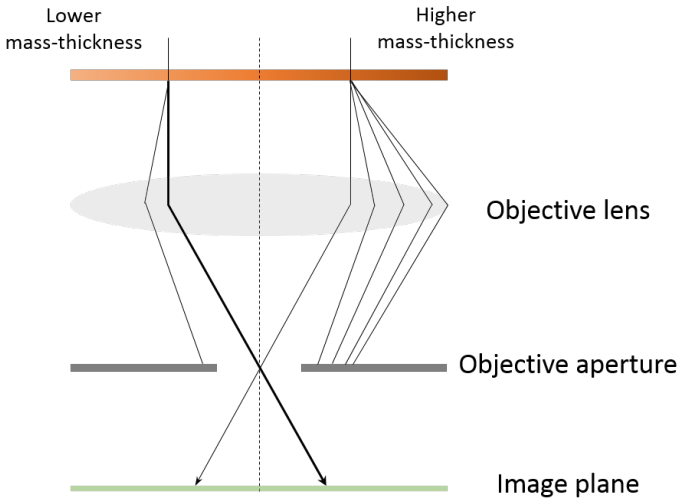

Figure 2.2: Schematic representation of mass-thickness contrast formation. In low mass-thickness areas of the specimen few electrons are scattered and many are undeflected, contributing to bright areas in the image plane. In high mass-thickness areas many electrons are scattered and hence blocked by the objective aperture. The portion of undeflected electrons is smaller, giving rise to darker areas in the image plane.

Diffraction contrast is generated by coherent elastic scattering of electrons by lattice planes of a crystalline sample oriented at a specific Bragg θ_B angle relative to the incident beam. If the diffraction $2\theta_B$ angle exceeds the objective aperture semi-angle α, the related crystalline area will appear darker in the image.

Finally, in addition to amplitude, the phase of the electron wave can be at the origin of contrast formation. The atomic potential of the sample can modulate the

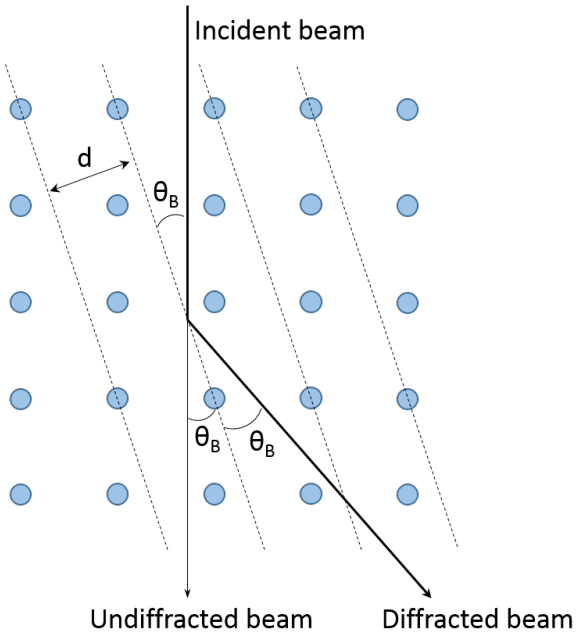

Figure 2.3: Schematic representation of electron diffraction from atomic planes. θ_B represents the Bragg's angle and d the interplanar distance.

incoming electron wave, so that its phase results shifted compared to the phase of a wave traveling in vacuum. This mechanism is called phase contrast and the product of this interference carries (among other contributions) the information on the lattice periodicity of the crystal. For this reason phase contrast is the main responsible for the formation of high resolution TEM images.

2.2 Scanning transmission electron microscopy

Unlike conventional TEM, where a parallel electron beam illuminates the sample, in scanning transmission electron microscopy (STEM) a convergent electron probe is used. The image is formed by rastering the probe on the region of interest and collecting the trasmitted intensity as a function of probe position. In STEM, annular detectors are used and depending on the collected angular range, different contrast mechanisms contribute to the image formation. Figure 2.4 shows a schematic representation of the different detectors and related collected angular range for STEM imaging.

Similar to TEM, bright field STEM (BF-STEM) images are formed collecting the direct beam and electrons scattered at small angles ($<$ 10 mrad). In conventional TEM, this would correspond to the use of a narrow objective aperture centered on the direct beam. Electrons scattered at higher angles (between 10 and 50 mrad) are collected by an annular dark field (ADF) detector, forming a dark field image. Both BF and ADF-STEM relies on mass-thickness contrast, however the ADF image is heavily influenced by Bragg diffraction effects and can be efficiently used to distinguish between an amorphous and a crystalline region. Finally, a high-angle annular dark field (HAADF) detector is used to collect electrons scattered at angles larger than 50

mrad. As this angular region is dominated by elastic incoherent scattering events, the contrast in the resulting HAADF image will depends solely on the atomic number Z (with a $\approx Z^{1.7}$ dependency) and thickness of the sample.

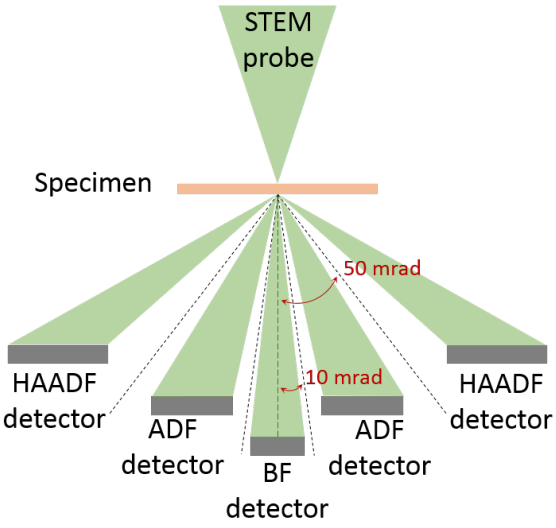

Figure 2.4: Schematic representation of the collection geometry of STEM signals.

2.3 Spectroscopy techniques

Electron energy-loss spectroscopy

Electron Energy-Loss Spectroscopy (EELS) is a general term grouping together different techniques that analyses the energy distribution of the electrons transmitted through the specimen.

In TEM, the interaction between the incident electron beam and the specimen can lead to different scattering phenomena. As already introduced, when the primary beam interacts with the electrostatic field of the specimen nuclei, elastic Rutherford scattering occurs and the electrons are deflected to large angles with no appreciable loss of energy (Figure 2.5a). If the interaction is instead with the specimen electrons, inelastic scattering events occur and the corresponding energy transfer can cause the excitation of atomic electrons to higher energy states.

Different scenarios are therefore possible. Inner shell electrons receiving an amount of energy exceeding their binding energy can undergo a transition from their ground state to an unoccupied state above the Fermi level (Figure 2.5b). The vacancy left in the inner shell can then be filled by an electron from the outer shell and the corresponding electronic jump is associated by liberation of energy in the form of an X-ray photon or as kinetic energy of another atomic electron (Auger emission). In the same way, outer shell electrons can undergo excitation by the incident electrons to higher energy levels (Figure 2.5c). If the transition state is above the vacuum level, electrons can be emitted as secondary electrons. Moreover, electrons in the outermost atomic orbital are often delocalized and can undergo collective, resonant oscillations called plasmon excitations.

Other outer shell electron transition phenomena are possible, such as interband and intraband transitions.

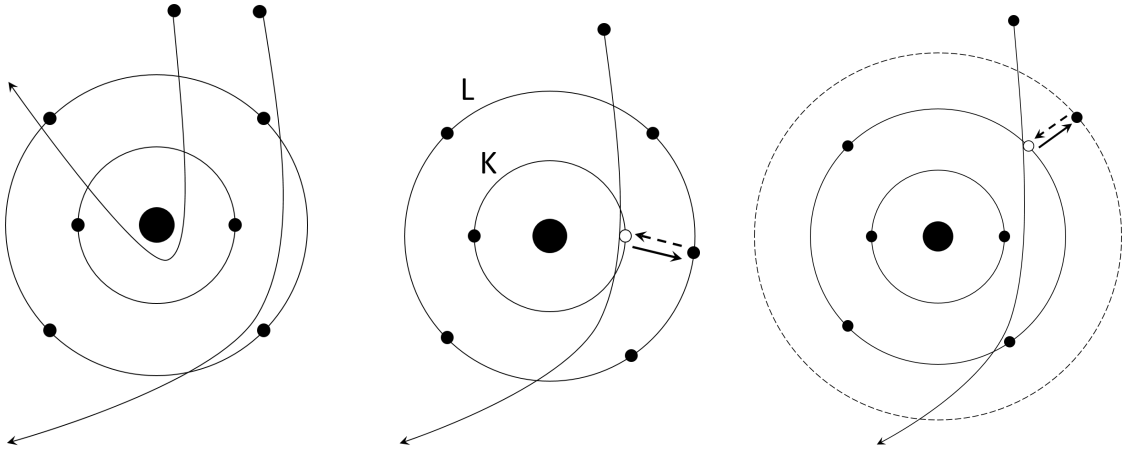

(a) Elastic **(b)** Inner shell inelastic **(c)** Outer shell inelastic

Figure 2.5: Electron scattering by a single carbon atom. **(a)** Elastic scattering caused by Coulomb attraction by the nucleus. At the same time, Coulomb repulsion can excite **(b)** inner or **(c)** outer shell electrons to higher energy states originating inelastic scattering. Broken arrows represent de-excitation of electrons.

In the electron microscope an electron spectrometer is used to separate the transmitted beam in its kinetic energy components and generate an energy distribution spectrum. The EELS spectrum hence shows the number of electrons as a function of their energy loss suffered during the interaction with the specimen. The spectrum can be divided in two sections, a low-loss region and a core-loss region.

The low-loss region extends from 0 to about 50 eV and includes elastically scattered electrons constituting the zero loss peak and small energy losses due to excitation of outer-shell electrons. Included in the zero loss peak are also all energy transfers under the detection limit of the instrument, such as electron-phonon scattering events.

Energy losses from about 50 to several thousands of eV are part of the so called core-loss region. In this range the main energy loss mechanism is the excitation of inner shell electrons. In the spectrum, these transitions usually take the form of steps or edges superimposed on a decreasing background. The energy loss associated to such edges is characteristic for each chemical element, giving a qualitative interpretation of the composition of the sample.

Energy dispersive X-ray spectroscopy

Energy dispersive X-ray spectroscopy (EDX, XEDS or EDS), studies the energy distribution of the X-rays emitted from the specimen.

As described in the previous section, X-ray photons can be emitted as a product of inner shell excitation and relaxation transitions. Additionally, X-ray can be generated by a mechanism involving the deceleration of primary electrons by the electrostatic field of the specimen nuclei. This phenomenon is called Bremsstrahlung and gives rise to a continuous energy distribution.

The EDX spectrum is thus generally composed by a continuous background generated by Bremsstrahlung radiation underlying characteristic peaks representative of electronic transition from outer to inner shell of specific atoms. As these transition are characteristic of the atomic electronic structure, EDX provides a straightforward way to identify the elements present in the specimen.

Due to the geometry of emission and collection of X-rays (Figure 2.6), the detection efficiency of EDX detectors remain nowadays low (1-3%), especially when compared with the EELS technique ($\approx 50\%$). X-rays are generated isotropically and in the TEM they are collected and analyzed by an EDX detector facing the specimen area. However, as regions far from the specimen (such as the objective lens pole pieces) can be hit by primary electrons elastically scattered by the specimen, the EDX detector must be shielded from the X-ray signal coming from these undesired areas. A collimator is thus used to decrease the acceptance solid angle of detection and block most of the undesired X-rays. In EELS instead, the spectroscopic information is contained in the transmitted electrons, which can be easily deflected and transferred to the electron spectrometer. However, the compact design of new EDX Si-drift detectors has allowed new microscope-detector geometries in which multiple detectors can be placed symmetrically around the specimen area and thus collect a bigger portions of the generated X-ray radiation. A system of this kind has been used for the collection of the EDX maps shown in this thesis.

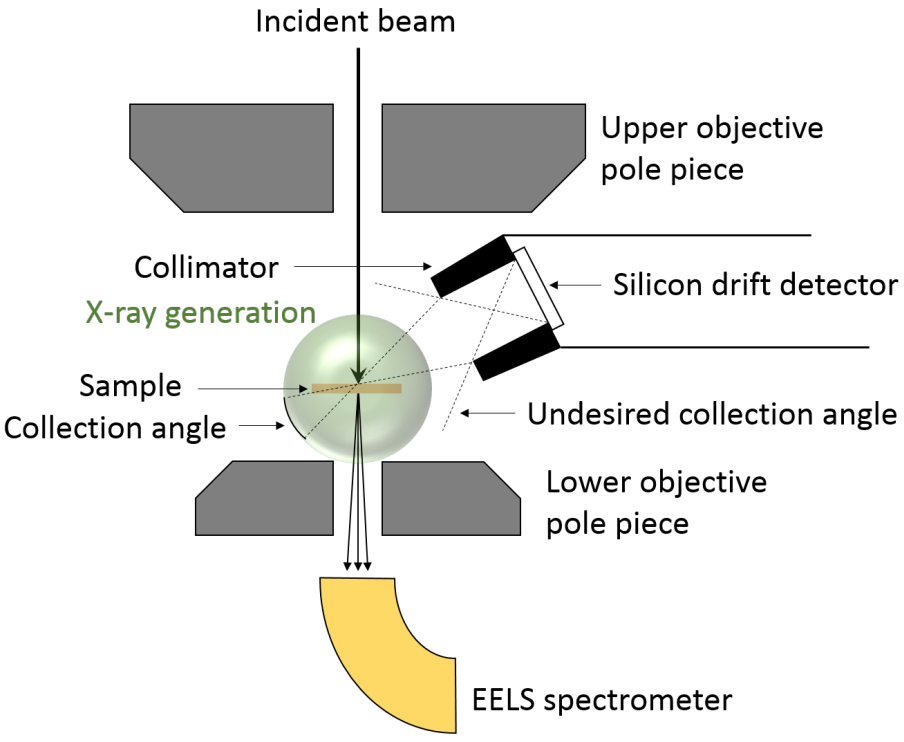

Figure 2.6: Schematic representation of the typical EDX collection geometry in the TEM column.

2.4 Environmental transmission electron microscopy

The environmental TEM

TEM experiments in presence of gases can normally be performed using two different approaches: dedicated closed cell TEM holders or differentially pumped TEM columns.

In the first case the specimen is loaded in a holder where it is enclosed between two electron transparent windows (e.g. C or SiN) containing the gas atmosphere. In some designs the atmosphere is static, in others an external pumping systems allows to establish a gas flow. This approach allows the exposure of the sample to pressures up to 1.5 bar [6, 7] and has the main advantages of being compatible with different microscopes, without requiring any further modification of the TEM column. The main drawbacks of this approach are related to the presence of the two membranes. These, together with the gas atmosphere, limit the image resolution due to scattering with the primary and transmitted electrons and are also responsible for blocking a big portion of the generated X-rays.

As opposed to the closed-cell approach, the differential pumped TEM or environmental TEM (ETEM) allows the exposure of the sample to a gas atmosphere introduced directly in the TEM column. As electrons scatter both elastically and inelastically with gas molecules leading to degradation of the image quality, the high pressure pathway needs to be reduced as much as possible. For this reason, pressure limiting apertures are placed in the bore of the pole-pieces and additional pumping (turbo molecular, ion getter pumps) is used. The gas flow is hence confined in the pole piece gap, far from delicate and critical regions such as the electron gun. Typical ETEM pressures are in the order of 10^2 Pa and in general smaller than 3000 Pa. Although limited in pressure range, if compared to closed-cells, this approach allows the exposure of a sample to a gas environment using all commercially available TEM holders. The absence of strong scattering elements such as windows allows furthermore to achieve high spatial resolutions and take full advantage of EDX and EELS spectroscopy techniques.

All *in situ* experiments presented in this thesis have been carried out using a FEI Titan 80-300 ETEM. A schematic diagram of the microscope is given in Figure 2.7.

TEM heating holders

In the TEM, specimen heating is provided using commercially available or custom heating holders generally relying on two different designs.

In furnace type heating holders (Figure 2.8a) a common 3 mm TEM grid supporting the sample is mounted in contact with a furnace element having a low thermal expansion coefficient. A bulk heating element, such as a tungsten wire, is then placed in close proximity of the furnace. When a current is sent through the wire, heat is generated by Joule effect and the furnace (and consequently the sample) is heated. A thermocouple is usually present close to the sample area in order to monitor the temperature of the specimen. A low thermal expansion coefficient for the material composing the furnace is required in order to minimize the sample drift during the heating and cooling stages of the *in situ* TEM experiment. The main advantage of using a furnace type heating holder is given by the possibility of using common TEM

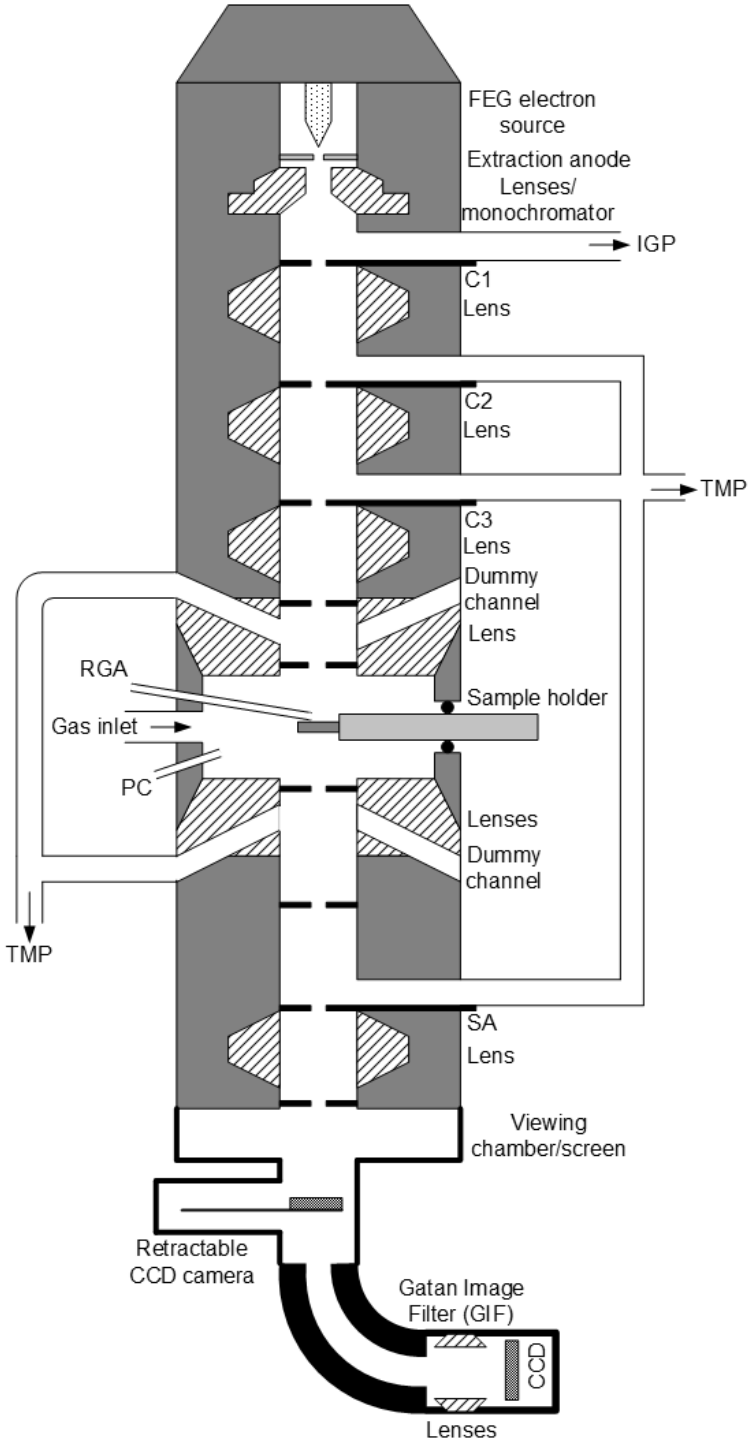

Figure 2.7: Schematic diagram of a differentially pumped TEM column. FEG: field emission gun; IGP: ion getter pump; TMP: turbo molecular pump; RGA: residual gas analyzer; PC: plasma cleaner; C1: first condenser aperture; SA: selected area aperture.

grids for supporting the sample. The holder geometry usually allows to accommodate also more special samples such as TEM lamellas. However, due to the presence of a bulk heating system, a large portion of the tip of the holder is normally heated. The result of this process is a severe specimen drift caused by the thermal expansion of all mechanical components present in the proximity of the sample. This sample drift is the main factor limiting the use of this kind of holders for *in situ* dynamic studies.

A more recent design involves instead the use of micro electromechanical systems (MEMS) in order to provide a more localized heating (Figure 2.8b). The sample is loaded on a millimeter-sized MEMS chip where a small membrane has the double function of mechanical support and heating. The chip is then mounted on the tip of a specific TEM holder and inserted in the microscope. On the membrane, a set of holes is present in order to ensure the transmission of electrons. Additional electron transparent thin films (C, Si_3N_4) can provide further mechanical support to the sample suspended on the membrane holes. Heating is provided through Joule effect by a micron-sized heating coil embedded in the membrane [8]. Alternative designs exist, for example a current can be sent through the whole membrane, which then acts as the effective heating element [9]. The sample temperature is determined by monitoring the resistance of the heating element (coil or membrane itself) by two- or four-terminal sensing. Contrary to furnace type, MEMS heating holders provide a considerably more localized heating profile and consequently a reduced sample drift. Furthermore, the micron-sized heating elements present a drastically lower thermal inertia than bulk heaters and are able to reach heating rates of the order of 10^2 °C/ms. The high mechanical stability upon heating and cooling cycles makes MEMS heaters the optimal choice when carrying out dynamic studies.

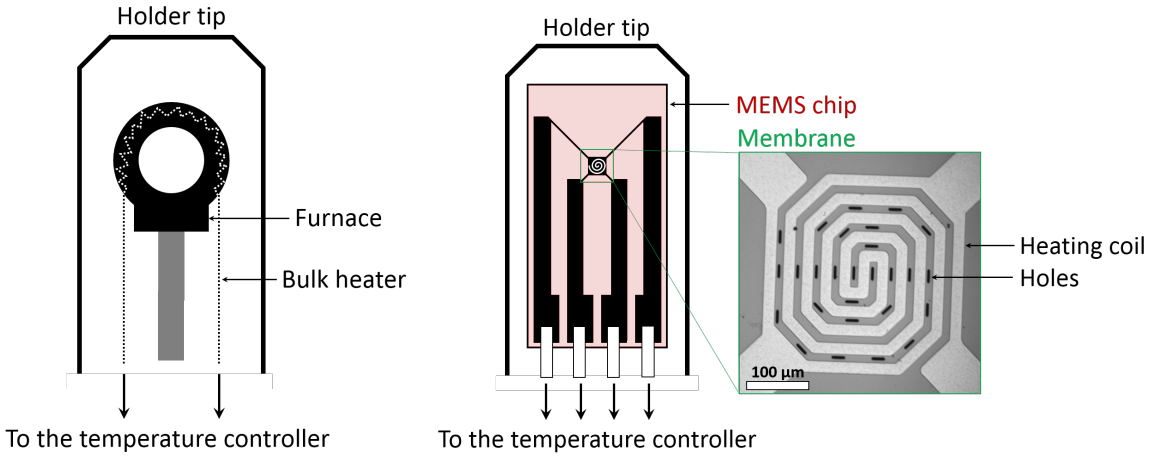

(a) Furnace type **(b)** MEMS type

Figure 2.8: Schematic representation of the tip of a **(a)** furnace type and **(b)** MEMS TEM heating holders [8].

2.5 X-ray diffraction

X-rays interact with the atomic electron cloud following two main processes: Rayleigh scattering and Compton scattering. Rayleigh scattering is an elastic process where every single electron of the specimen atomic cloud oscillates as a result of the interaction with the electric field associated with the incoming radiation. This motion is periodic and accelerated, leading to the emission of radiation having the same wavelength as the incoming one. Compton scattering is instead an inelastic process and can be described under the particle picture: a X-ray photon colliding with an electron is deflected and loses part of its energy. This energy transfer is dependent on angle of scattering and not on the nature of the scattering medium.

A sample exposed to X-rays experiences both phenomena at the same time, however with different intensities. Rayleigh scattering intensity is given by:

$$I_{coh} \propto (\boldsymbol{F_1} + \boldsymbol{F_2} + \boldsymbol{F_3} + ...)^2 \tag{2.6}$$

where $\boldsymbol{F_1}$ is the vectorial scattered amplitude by atom 1, whereas Compton intensity is proportional to the simple vectorial sum of the same quantities.

When scatterers are arranged in an ordered configuration (like atoms in a crystal lattice), coherent scattering is predominant and will give rise to diffraction effects. Incoherent scattering will be responsible for noise contributions. Diffraction is a complex interference phenomenon having a discrete nature. The scattered amplitude $F(s)$ from a non ordered set of atoms is normally non-zero for every scattering vector $\boldsymbol{s}$, whereas for a crystal lattice $F(s)$ is generally 0 except for specific values of $\boldsymbol{s}$, defined by the lattice parameters.

A first interpretation of scattering conditions was given in 1913 by W. L. Bragg, who considered a crystal as a superposition of parallel semireflective lattice planes spaced by a distance d (Fig. 2.9).

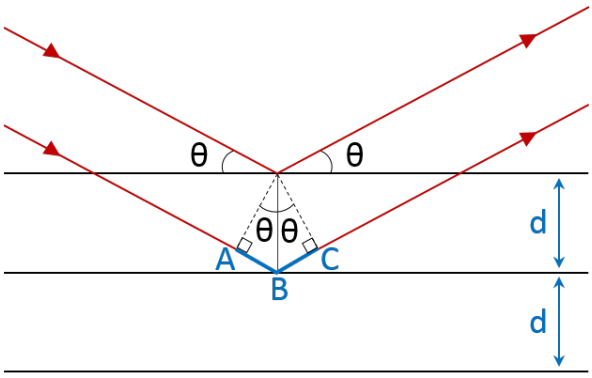

Figure 2.9: Schematic representation of Bragg's reflection.

The difference in optical path between two reflected parallel x-rays from two adjacent planes is:

$$AB + BC = 2dsin(\theta) \tag{2.7}$$

The condition for having constructive interference is fulfilled when:

$$n\lambda = 2dsin(\theta) \tag{2.8}$$

where λ is the wavelength of the incoming radiation and n is a natural number. The angle θ that verifies this condition is called Bragg's angle. Eq. 2.8 is called Bragg's Law.

In 1914 Laue proposed a more accurate description of the phenomenon abandoning the semi-reflecting planes approach introduced by Bragg and considering punctual scatterers. A monochromatic radiation hitting with an angle Φ a one dimensional lattice having a periodicity a, will undergo constructive interference if the relation:

$$a[cos(\Phi) + sin(\Psi)] = h\lambda \tag{2.9}$$

is satisfied. Ψ is the scattering angle and h is an integer. The solution of Eq. 2.9 is a family of coaxial cones, corresponding to different values of h. Expanding to a three dimensional lattice requires the solution of the system of equations:

$$\begin{cases} a[cos(\Phi_1) + sin(\Psi_1)] = h\lambda \\ b[cos(\Phi_2) + sin(\Psi_2)] = k\lambda \\ c[cos(\Phi_3) + sin(\Psi_3)] = l\lambda \end{cases} \tag{2.10}$$

and the lattice will scatter only in the directions defined by the intersections of the three cone families (Figure 2.10).

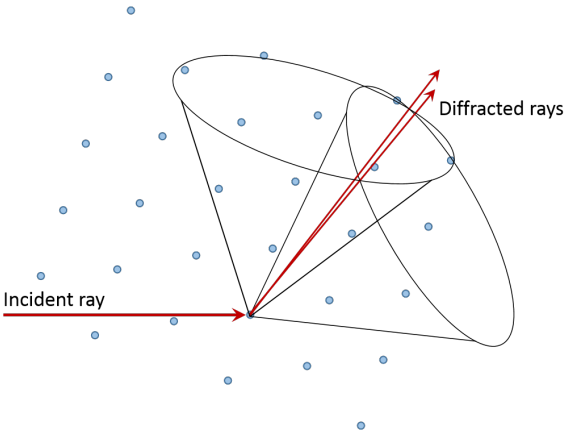

Figure 2.10: Laue cones for a two dimensional lattice.

Laue equations tell that X-rays interacting with a single crystal will give rise to a series of diffraction spots (single crystal diffraction pattern). These can be recorded using a CCD and the analysis of the distances, positions and intensities of the diffraction spots allows to extract crystallographic information on the specimen such as Bravais lattice and crystallographic system.

A crystalline powder sample is composed by a multitude of crystals oriented in random directions. For any possible (hkl) plane there will always be some crystallites at the correct Bragg's angle. Therefore, because of the rotational symmetry around the incident beam, diffracted rays will form a cone of half-apex angle 2θ. When these cones are projected on a 2D support as a screen or a photographic plate, they will form circles. A punctual detector intercept every circle and allows the visualization of a a

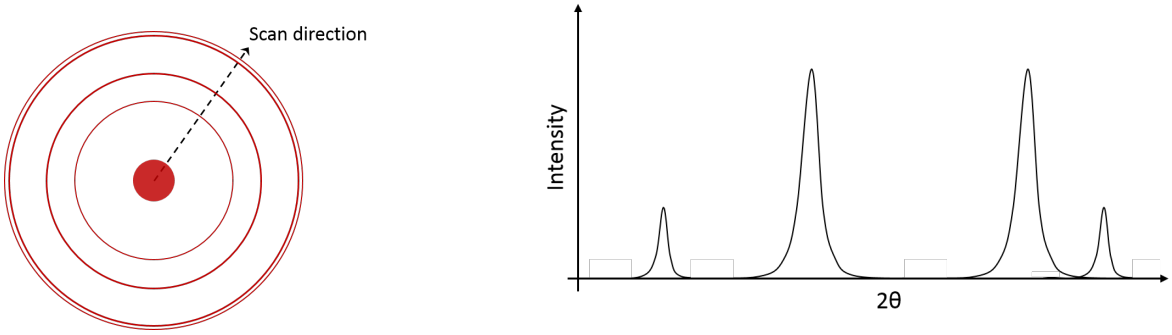

(a) 2D diffraction pattern **(b)** 1D diffraction pattern

Figure 2.11: Schematic representation of **(a)** a 2D and **(b)** a 1D X-ray diffraction pattern.

graph representing the intensity of every solution as a function of the angle (Fig.2.11a and 2.11b).

Peak positions are depending on specimen's Bravais lattice whereas intensities are related to the symmetry and crystalline structure. Peak's shape and width depends strongly on experimental conditions and can reveal intrinsic properties of the sample such as crystallites average size and strain effects.

In situ XRD

In situ XRD allows to study the changes in sample crystallinity upon exposure to a heat and gas treatment.

Generally, the gas environment is confined in an *in situ* cell where the sample is loaded. The cell is connected to an external gas systems and it features X-ray transparent windows (typically thin Be metal sheets) allowing the transmission of the incident and diffracted X-rays. Alternative designs consist in the use of thin capillaries (usually made of glass or sapphire) and are generally employed for synchrotron studies. Heating is provided by the use of a resistive element embedded in the cell or placed in proximity of the capillary. Figure 2.12 shows a schematic diagram of the Anton Paar XRK 900 *in situ* cell used for the experiments presented in this thesis.

Approximately 230 mm^3 of the sample is loaded on a ceramic stage equipped with a thermocouple. After loading, the sample stage is inserted in the cell where it is surrounded by the heating elements. A water cooling system allows to control the cooling rate of the gas environment. Heating and cooling rates for this setup are between 1 and 40 °C/min and the maximum temperature that can be reached is 900 °C.

As an example, Figure 2.13 shows the reduction of CuO to Cu in 95% He / 5 % H_2 followed by *in situ* XRD [10]. This techniques allowed to determine the presence of an intermediary Cu_2O phase before the achievement of the total copper reduction.

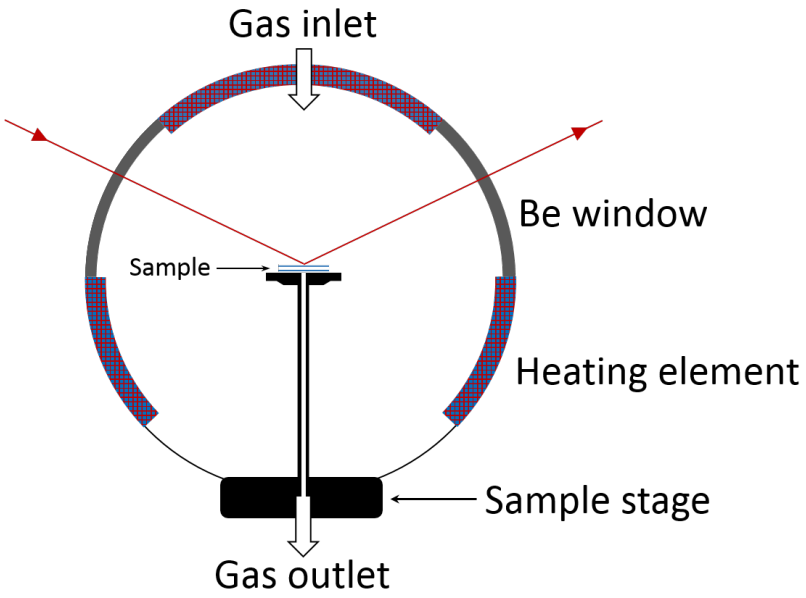

Figure 2.12: Schematic diagram of the Anton Paar XRK 900 *in situ* XRD cell.

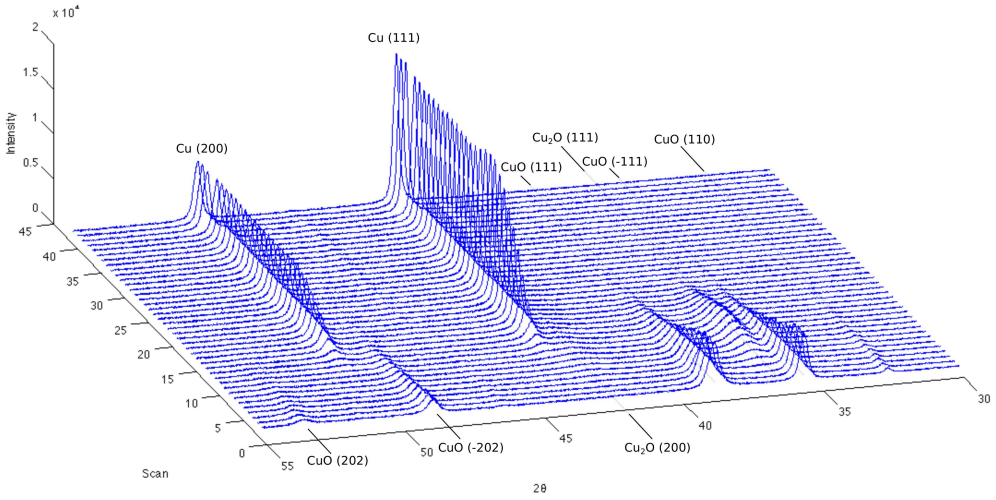

Figure 2.13: Reduction of CuO to Cu followed by *in situ* XRD. Gas composition: 95% He / 5 % H_2. P = 200 mBar, T = 250 °C, flow rate = 40 mL/min. Each scan has a duration of 3 min and 38 s. Figure from [10].

CHAPTER 3

Electron microscopy as the necessary characterization tool in heterogeneous catalysis

The characterization of an heterogeneous catalytic system often requires the use of multiple analytical techniques, each of which provides specific information and requires particular sample preparation or experimental conditions. Among these, electron microscopy is the only one that can provide physicochemical information of individual nanoscale structures. Other techniques are generally designed to either probe a large number of (supported) nanoparticles, e.g. XRD, X-ray photoelectron spectroscopy, X-ray absorption spectroscopy (XAS), Raman spectroscopy, ultraviolet-visible spectroscopy, etc. or require strict conditions on the sample geometry and examining conditions, e.g. scanning tunnel microscopy, atomic-force microscopy.

A brief overview of the analytical capability of transmission electron microscopy towards the characterization of heterogeneous catalysts will be given in this chapter, with the aim of covering both advantages and limitations of this technique.

3.1 Single particle characterization

Spatial and size distribution of particles

As already introduced in Chapter 1, the performance of a supported catalyst is directly related to the number and availability of active sites. As these often correspond to specific features present on the nanoparticles surface, the activity of a single nanoparticle will be strongly correlated (among other factors) to its surface area, and ultimately to its size. Determining the size distribution of the supported phase can thus give valuable insights on the catalytic properties of the system in analysis. For nanoparticles larger than 2-3 nm, XRD may be a suitable choice for extracting this information, however this technique provides averaged results (average particle size) and reflects only the size of the crystalline domains, which may not correspond to the size of the

nanoparticle (e.g. polycrystalline or amorphous nanoparticles). Electron microscopy, on the other hand, can provide a direct visualization of the supported phase, including small amorphous particles, clusters or even single atoms, allowing to extract realistic size distributions describing the sample in analysis.

Particle shape and crystallographic structure

The shapes of the nanoparticles play an important role in determining the reactivity and selectivity of supported heterogeneous catalysts. Catalytic reactions might only take place on certain nanoparticle facets, whereas other facets might be either not active or host reactions producing undesired side products. A notable example is ammonia synthesis, where (111) and (211) facets of iron crystals were reported to be 5-6 times more active than (100) and (210) facets, due to the higher presence of Fe atoms with seven nearest neighbors [11].

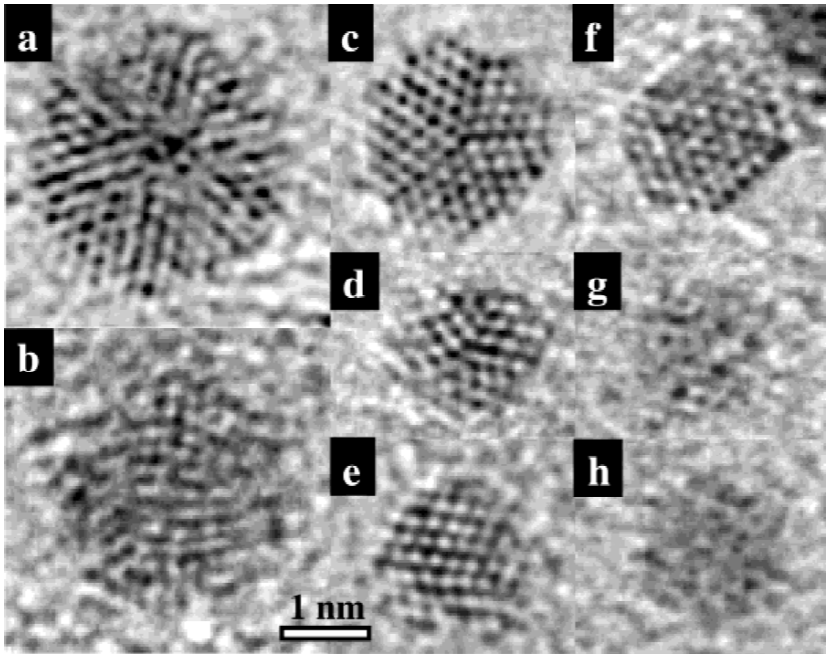

Figure 3.1: HREM images of Au nanoparticles with various shapes: **(a)** icosahedral particle, threefold axis; **(b)** icosahedral particle, twofold axis; **(c)** decahedral particle, fivefold axis; **(d)** multiply twined particle; **(e)** single-twined particle with defects and steps; **(f)** truncated octahedral; and **(g)** and **(h)** "glassylike" nanoparticles. Figure from [12].

Overall, the analysis of the shape of a nanoparticle by electron microscopy can give information on the relative ratio of specific edge, corner and surface atoms present on its surface. For example, metal particles belonging to the face-centered cubic crystallographic system can be found in cubic shape, exposing only (100) facets, or decahedral and icosahedral shapes, exposing only (111) facets. In the case of truncated octahedral nanoparticles, both (111) and (100) facets are exposed.

The possibility of exploring simultaneously shape and the crystallographic structure offered by HRTEM (Figure 3.1) is thus of great importance in the shape-controlled synthesis of supported nanoparticle catalysts and for other non-catalytic systems where

the shape is an important factor, such as quantum dots or plasmonic systems.

Moreover, the supporting phase might not behave as an inert "spectator" of the catalytic process, but rather have an active role, constituting together with the supported nanoparticle a unique complex system responsible for the catalytic properties. In this perspective, the use of electron microscopy becomes not only beneficial, but rather necessary in order to get insights on the physicochemical mechanisms leading to activity. HRTEM allows to extract invaluable information both on the crystallographic and amorphous nature of the nanoparticle-support interface, and the use of spectroscopic techniques in combination of STEM can provide a chemical and electronic characterization of these important regions. Figure 3.2 shows an example of the application of HRTEM in the study of particle-support interaction in supported rhodium nanoparticles. When the Rh metal precursor is impregnated on CeO_2 and $Ce_{0.8}Tb_{0.2}O_{2-x}$ and subsequently reduced at 1173 K, only the latter support was reported to decorate the formed Rh particle [13].

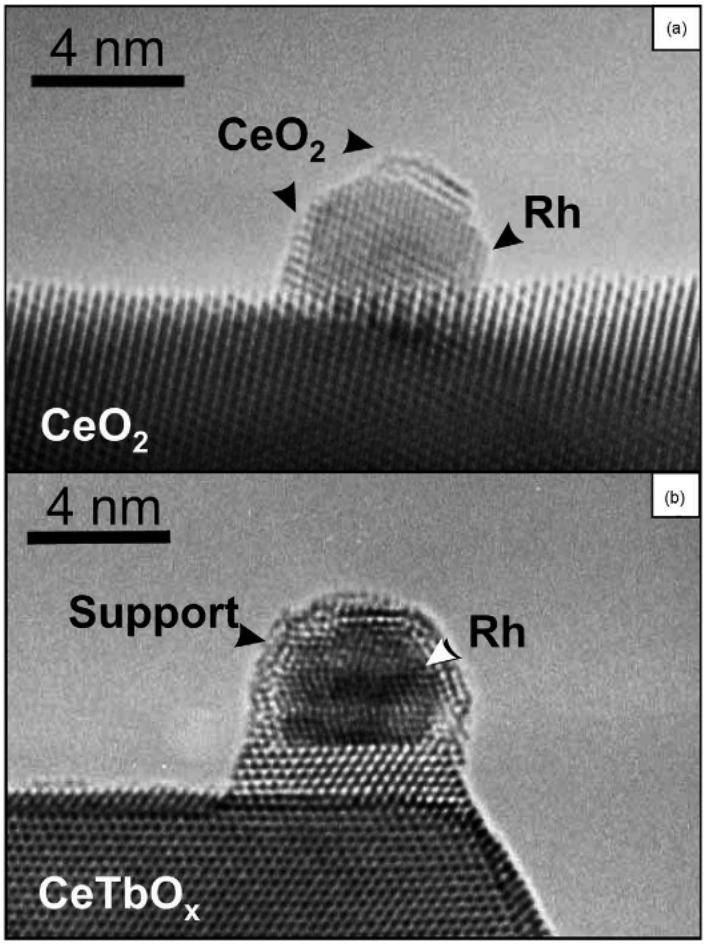

Figure 3.2: HRTEM micrographs of **(a)** 2.5% Rh/CeO_2 catalyst reduced at 1173K and **(b)** 0.5% $Rh/Ce_{0.8}Tb_{0.2}O_{2-x}$ catalyst reduced at 1173 K. Figure from [13].

Z-contrast imaging

The HAADF-STEM technique introduced in the previous chapter is ideal in the characterization of supported catalyst, in particular the one consisting of high atomic number nanoparticles dispersed on low atomic number supports. As the efficiency of high-angle elastic scattering is proportional to Z, the use of HAADF-STEM might overcome the limitations arising from mass-thickness contrast in bright field imaging. As an example, Figure 3.3 shows a comparison between HRTEM and HAADF-STEM micrograph of a carbon nanotube supporting ruthenium nanoparticles. In HRTEM, smaller Ru nanoparticles do not generate enough contrast to be distinguished from the carbon support. In HAADF-STEM instead, due to the higher sensitivity to Z variations (Z_{Ru}= 44 vs. Z_C = 6), smaller Ru nanoparticles become visible. However, in less optimum cases that the example presented, the difference between the atomic numbers of the supported and supporting phase might not be high enough to generate a contrast sufficient for the analysis, especially in the case of highly porous supports. This will be the case for the Ni/ZrO_2 and Mo_2C/ZrO_2 catalysts presented in the following chapter.

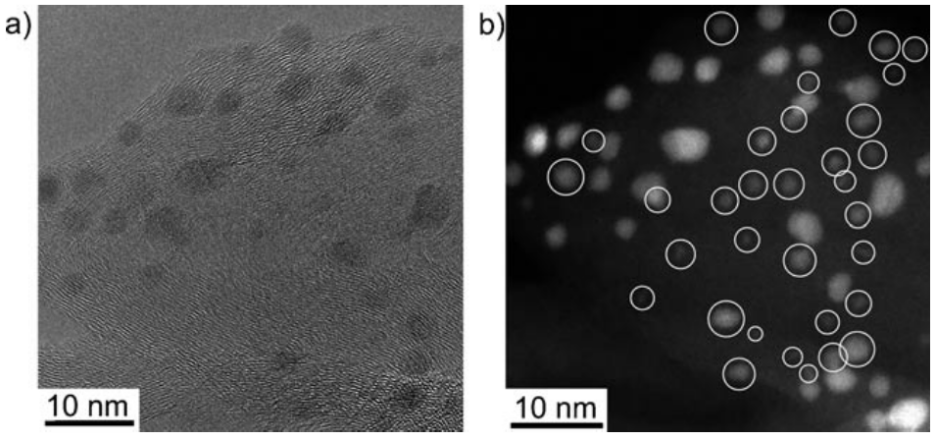

Figure 3.3: **(a)** HRTEM and **(b)** HAADF-STEM micrograph of Ru nanoparticles supported on carbon nanotubes. The images were taken from the same area. The smaller particles circled in (b) are not visible in the HRTEM micrograph. Figure from [14].

3.2 Spectroscopy techniques

As already introduced, electron beam specimen interactions cause inner and outer shell excitations, which in turn give rise to the generation of a number of signals.

The use of a small electron probe (as in STEM) to excite the sample, allows thus to extract direct information on the elemental composition at the nanoscale. This is particularly interesting for example in the design and characterization of nanostructured bi- or multimetallic alloy catalysts, where the catalytic properties are directly related to the sample composition and crystal structure, or in the study of deactivated catalysts, in order to reveal the presence and distribution of poisoning species. STEM-EDX and STEM-EELS techniques can be used to probe specific portions of the specimen, such as nanoparticle-support interfaces, or extract elemental concentration profiles and build

compositional maps providing invaluable information on the two-dimensional elemental distribution in whole sample areas (Figure 3.4).

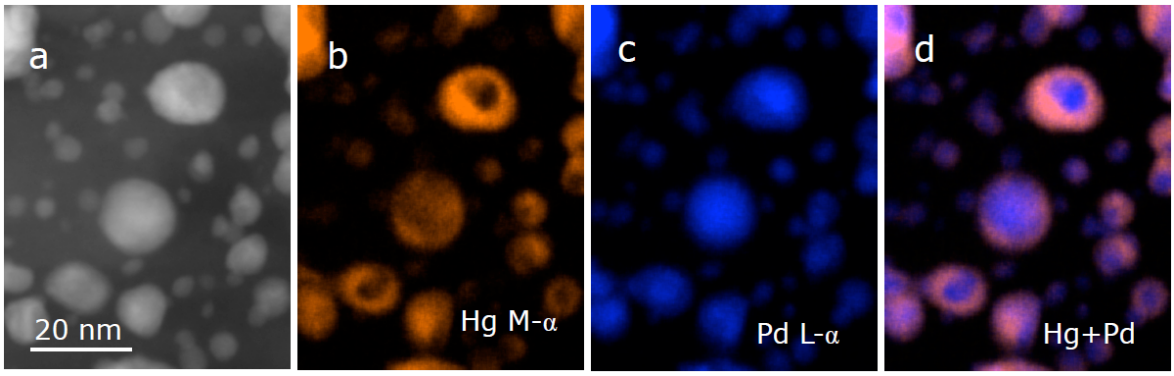

Figure 3.4: STEM-EDX mapping of Pd-Hg alloy nanoparticles supported on glassy carbon. **(a)** HAADF-STEM image of the analysed region. **(b-d)**: Hg M_α, Pd L_α and combined Pd + Hg chemical maps. Figure from [15].

Furthermore, the use of STEM-EELS can provide information about the oxidation state and electronic structure at the nanoscale level, crucial for the understanding of the fundamental properties of a heterogeneous catalyst. Compared to techniques giving the same information, such as X-ray absorption, STEM-EELS measurements do not require the use of synchrotron radiation sources and allow to probe single nanoparticles or interfaces.

3.3 Environmental TEM

Transmission electron microscopy has the potential to unravel the structure, composition and chemical state of complex heterogeneous catalytic systems to the nanoscale level, thus providing vital information in the interpretation of catalytic activity. However, as traditional *ex situ* TEM studies are carried out at room temperature and under high vacuum, their results might not reflect the active state of an heterogeneous catalyst, usually operating at elevated temperatures and high pressures. In this perspective, combining TEM with environmental capabilities allows to study catalytic systems *in situ*, providing insights on the structural modification of a catalytic system in a reactive environment resembling the operating conditions of the catalyst.

Depending on the surrounding atmosphere, the outermost layers of a nanoparticle may restructure due to surface energy variations induced by adsorption of gas molecules. It is hence important to investigate these dynamic structural variations in order to get insights on the "real" catalyst active phase. The use of an aberration-corrected ETEM allowed, for example, the study of Au/CeO_2 catalysts under CO/air atmosphere, revealing and expansion of the outermost Au layer from 0.20 nm (in vacuum) to 0.25 nm [16] (Figure 3.5). The combination of ETEM observation and *ab initio* calculations furthermore revealed that this restructuring is responsible for the accommodation of a higher number of CO molecules on the nanoparticle surface due to

a change from cubic to hexagonal in the bonding arrangement of the topmost surface Au atoms.

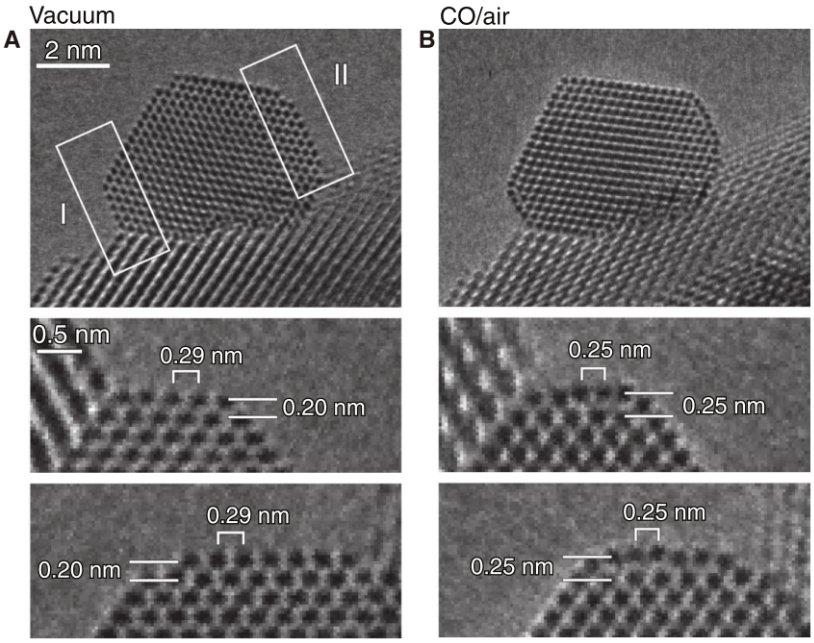

Figure 3.5: Au {100} reconstructed surface under catalytic conditions. The CeO_2 supported gold nanoparticle in **(a)** vacuum and **(b)** a reaction environment (1 vol % CO in air/gas mixture at 45 Pa at room temperature). Regions I and II in the topmost figures are enlarged and rotated in the second and third figures respectively. Figure from [16].

Moreover, the use of electron-based spectroscopy characterization tools such as STEM-EDX or STEM-EELS in a controlled atmosphere allows to link the local chemical information to the structural evolution of the catalyst during gas treatment inside the microscope. Using quantitative STEM-EELS, Sharma [17] showed that the oxidation state of single ceria nanoparticles as a function of temperature in a reducing atmosphere could be monitored by considering the relative intensity of Ce $M_{4,5}$ white-lines in the EELS spectrum (Figure 3.6).

Not only is environmental TEM a powerful tool for the understanding of the catalytic active phase, but also it has a major role in the determination of the mechanisms leading to deactivation of supported nanoparticle systems. As it has been mentioned in Section 3.1, the dispersion of the supported phase might have a large influence on the final catalytic activity, due to its direct correlation with the number of active sites available for the reaction. Sintering is a deactivation mechanism that leads to the increase in particle size through two specific mechanisms involving either the migration of small entities/atomic species from one particle to another (Ostwald ripening), or migration of entire particles until coalescence between two or more particle takes place (particle migration and coalescence). As both mechanisms might take place depending on reaction conditions, the study of supported nanoparticle systems under different gas and temperature environments becomes crucial in the determination of the deactivation steps during a catalytic process [18].

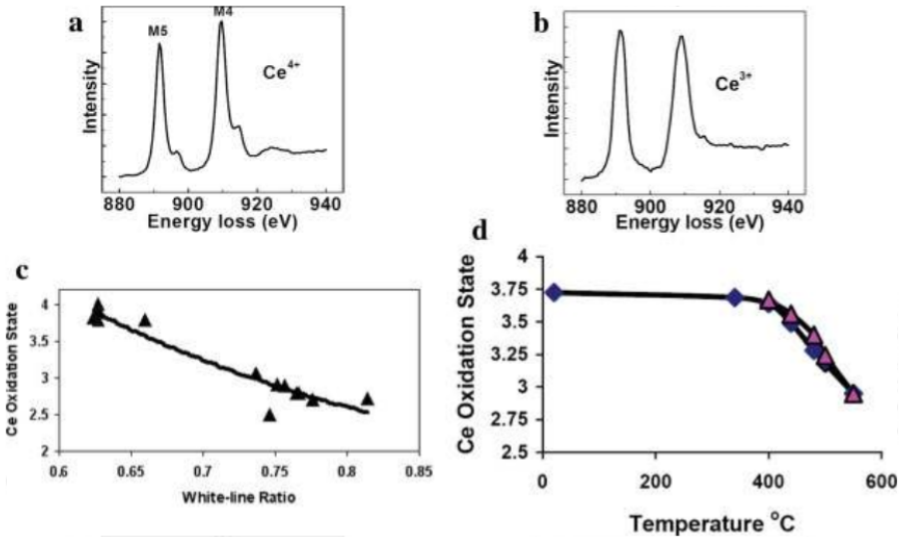

Figure 3.6: Background-subtracted electron energy-loss spectra showing Ce $M_{4,5}$ white-lines at **(a)** room temperature and **(b)** at 685 °C. **(c)** Relationship between Ce oxidation state and white-line ratio. **(d)** Change in Ce oxidation state upon heating (squares) and cooling (triangles). Figure from [17].

3.4 Limitations

Locality

The possibility of investigating the morphology, chemistry and crystallographic nature of specific areas of a sample is one of the unparalleled advantages of the use of electron microscopy in catalyst characterization. However, the extremely local nature of electron microscopy represents as well one of its major limitations.

Extracting information at the nanoscale requires the analysis of very small portions of the sample, therefore electron microscopy data have intrinsically poor statistics. In order to extract representative information, measurements need thus to be repeated in different part of the specimen. Moreover, it is frequent that electron microscopists miss out the analysis of very large particles. Although these usually do not have a direct role in the performance of the catalyst, they represent a waste of a large portion of active phase, indirectly affecting the final catalytic activity. For example, a 1 μm spherical particle equals the same surface area as that of 1,000,000 1 nm small nanoparticles, and hence the agglomeration of active phase may rapidly lead to the loss of many active sites.

Another important limitation connected to the extreme locality of TEM analysis is the sample mechanical stability. As a consequence of the high magnifications used, any mechanical instability connected to vibrations or thermal expansion might results in a severe sample drift. This effect is usually reduced by isolating the microscope column in a soundproof and thermally stable dedicated room.

Particle visibility

The visibility of supported nanoparticles when imaged with a transmission electron microscope can often be an issue, especially in the case of high surface area supports, typical of heterogeneous catalysts.

In bright field imaging, the visibility of supported nanoparticles depends mostly on the mass/thickness ratio between nanoparticle and support. For example, if supported on thin carbon films, clusters of platinum atoms or even single Pt atoms can be directly imaged. On the contrary, when the thickness of the support starts to increase or variates irregularly (as in the case of porous supports), the visibility of supported nanoparticles drastically decreases. The shape and the structure of the nanoparticles are overshadowed by the contrast of the support and smaller nanoparticles become invisible. Acquiring out-of-focus micrographs can enhance the visibility of supported nanoparticles. However, as Figure 3.7 shows, in this condition it is not possible to measure accurately the size of the supported phase anymore. As already shown in Section 3.2, the use of HAADF-STEM in the case of samples showing an high Z difference between nanoparticles and support, might allow to solve the visibility issue.

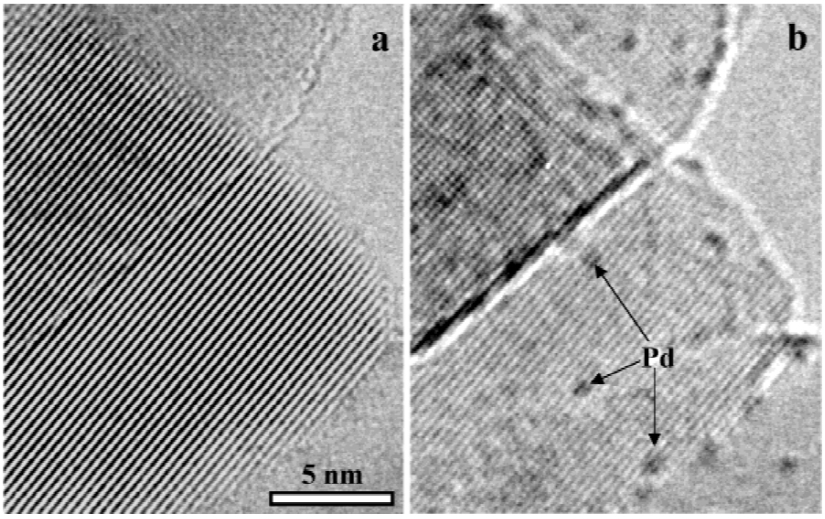

Figure 3.7: HRTEM micrographs of a titania-supported Pd catalyst illustrating the variations of particle visibility with the defocus of the electron beam. Image adapted from [12].

Hence, in order to simplify the study of catalysts, various forms of less porous model catalysts are currently used. Among these, thin metal oxide films supported on TEM metal grids and metal oxide spheres are the most common. The use of low porosity supports such as SiO_2 nanospheres (Figure 3.8) allows to observe the supported phase in profile-view, with the nanoparticle hanging into vacuum. This allows a direct analysis of the sole particle, excluding the support from any probe spectroscopy measurement [19]. However, as the morphology of the model support can largely differ from the case of the original catalyst, particular care should be given in the interpretation of model catalyst data such as particle size distribution and dispersion.

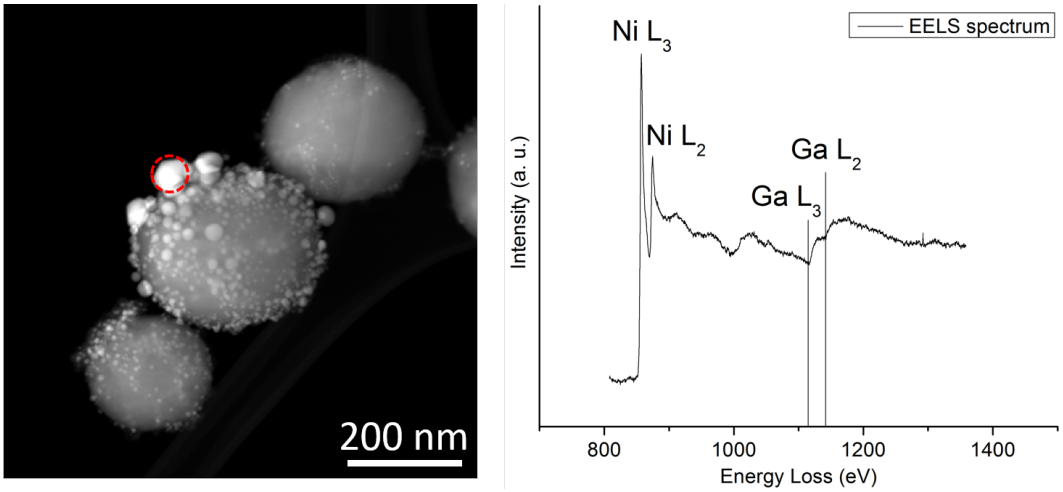

Figure 3.8: NiGa nanoparticles supported on a group of SiO_2 spheres. **(Left)** STEM-HAADF micrograph, **(right)** background-subtracted STEM-EELS spectrum of the NiGa nanoparticle highlighted in red.

Beam effect

Although source of useful information, the electron beam can cause temporary or permanent modifications of the surface and bulk structure of a specimen. Depending on the nature of the interaction between the primary electrons and the specimen, different phenomena might take place.

Electrons undergoing elastic scattering with the nuclei of the specimen can, in some circumstances, transfer enough energy to cause bulk atomic displacement or electron-beam sputtering of atoms from the surface of the sample. Usually, this effect can be minimized by lowering the energy of the electron beam [20]. In the case of atomic displacement shown in Figure 3.9, a STEM probe was used for carrying out the EDX mapping of a KCl crystal, resulting in a regular series of drilled holes on the specimen.

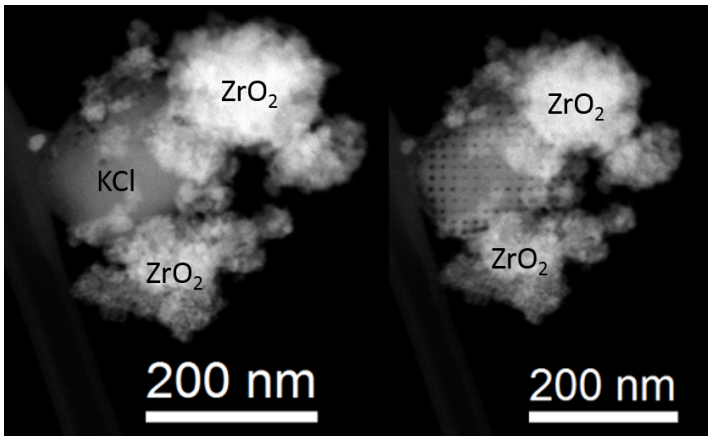

Figure 3.9: A KCl crystal surrounded by ZrO_2 before **(left)** and after **(right)** STEM-EDX mapping. Holes are visible after mapping as a result of beam induced atomic displacement.

When inelastic scattering events between the primary electrons and the electrons of the specimen occur, a considerable amount of energy can be transferred, most of which is converted into heat. Beam heating is known to cause melting of small metal clusters [21] and is generally considered a major problem when imaging organic materials. Another beam effect linked to inelastic scattering events and causing specimen degradation is radiolysis. Depending on the material, several mechanisms have been proposed to explain the conversion of the energy acquired by atomic electrons to kinetic energy and momentum of atomic nuclei [20]. In particular, during *in situ* TEM experiments, radiolysis is responsible for the ionization of gas molecules exposed to the electron beam. Ionized gas species present an increased reactivity when compared to the relatively inert parent molecules, and their presence might affect the observed in situ experiment in a non-predictable way. Hence, the beam current density is an important parameter to take into consideration when performing *in situ* studies.

Pressure gap

Finally, it is important to remember that the high-pressure and high-temperature working conditions of a typical catalytic reaction are usually not compatible with the experimental conditions of an *in situ* TEM analysis. Although temperatures up to 1000 °C can be reached by the use of MEMS heating holders, industrial catalytic applications can require gas pressures of hundreds of Bar: a condition unreachable in a TEM. Typical in situ TEM gas pressures are in the mbar to bar regime and therefore a considerable pressure gap exists between in situ observations and real catalytic applications. Even in laboratory-scale catalytic tests, where the typical pressures are in the range of few bar, the relevance of ETEM studies can be questioned.

3.5 Conclusion

In this chapter a concise review of the advantages and limitations of the use of transmission electron microscopy for the characterization of heterogeneous catalysts has been given.

Among many characterization techniques, electron microscopy possesses the unique capability of providing morphological, crystallographic and chemical information at the nanoscale and atomic level. By the use of BFTEM, HRTEM and STEM techniques, the size, shape and structure of single supported nanoparticles can be studied, allowing to build particle size distributions and to study the dependence of catalytic activity to specific nanoparticles surfaces. The extreme local nature of TEM analysis allows furthermore to investigate particle-support interaction phenomena such as encapsulation or decoration, or to identify amorphous species which are invisible in traditional catalyst routine analyses involving, for example, XRD. Moreover, by the use of EDX and EELS techniques, especially in combination with STEM, a chemical characterization of the sample at the nanoscale becomes possible. STEM-EDX and STEM-EELS techniques are used to build chemical maps of specific portions of the specimen, and EELS can be used to obtain information on the electronic structure of the catalyst in analysis. However, although locality represents one of the main advantages of electron

microscopy, it is also one of its main limitations. TEM information has intrinsically poor statistical value, as it is derived from the analysis of a very small portion of the sample and thus might not be representative of the real overall condition of the specimen.

In situ TEM techniques allows the characterization of a catalyst under a reaction environment that mimics the conditions of a real catalytic setup. In this way, fundamental insights on the structural modifications of a catalyst in a reactive environment can be obtained. Furthermore, *in situ* electron microscopy allows to study the mechanisms leading to the deactivation of a catalyst, such as changes in morphology (e.g. sintering) or structural modifications. However, a substantial gap exists between the pressure values used in typical industrial catalytic tests and ETEM experiments, hence the relevance of these experiments can often be questioned.

Moreover, beam-induced modifications of the specimen, such as atomic displacement, sputtering and radiolysis might further complicate the execution and interpretation of TEM experiments. These phenomena, naturally present in high vacuum measurements, acquire further importance during *in situ* studies, where inert gas molecules can be ionized to more reactive species.

Electron microscopy is hence a fundamental technique in the development and optimization of modern heterogeneous catalysts. However, although able to provide unique insights on the mechanisms behind catalyst activity, electron microscopy reaches its full potential when used in combination of complementary techniques such as XRD, XAS, XPS, etc. These techniques are able to provide a more ensemble-average sample characterization and do not suffer from electron beam effects. Moreover, techniques such as *in situ* XRD can operate at pressures of several bar, helping in bridging the pressure gap typical of *in situ* TEM experiments.

CHAPTER 4

Synthesis and deactivation of hydrodeoxygenation catalysts

The aim of this chapter is to explore the potential and uniqueness of electron microscopy as a tool for the understanding of the mechanisms behind catalytic activity, with an emphasis on the characterization of the initial and final stages of the catalyst life: synthesis and deactivation. For this purpose, Ni/ZrO_2, Mo_2C/ZrO_2 and $Ni\text{-}MoS_2/ZrO_2$, three catalytic systems for bio-oil hydrodeoxygenation, have been studied in collaboration with DTU Kemiteknik. Sample synthesis and catalytic testing have been carried out by Peter Mølgaard Mortensen as a part of his Ph.D. and will be briefly described in this thesis. For a more extensive description of the setup used and procedures please refer to the appended papers [Paper1] and [Paper2].

4.1 Introduction

The increasing demand in energy sources, coupled with the depletion of crude oil reserves directs nowadays research in the direction of alternative fuels, the ideal candidate being similar to conventional fuels in terms of compatibility with present infrastructures, but at the same time CO_2 sustainable. In this perspective, biomass derived fuels (bio-oils) may play a key role in future applications as these can be produced within a relatively short cycle and are considered more CO_2 neutral than conventional fossil fuels [22].

More than 300 different compounds have been identified in bio-oil, the main ones being water and oxygen-containing species (alcohols, ketones, aldehydes, furans, carboxylic acids, etc.). The presence of these oxygenated compounds degrades the properties of the bio-oil (low heating value, polarity) and limits its storage durability (acidic nature, repolimerization) [22].

The removal of these oxygenated compounds (bio-oil upgrade) can be carried out through hydrodeoxygenation (HDO). HDO is a hydrogenolysis reaction in which hydrogen is used to cleave a carbon-oxygen single bond and form H_2O as a byproduct. The overall reaction, considering the elemental composition of typical bio-oil and nor-

malizing by the carbon content, can be generally written as [22]:

$$CH_{1.4}O_{0.4} + 0.7H_2 \rightarrow 1"CH_2" + 0.4H_2O \tag{4.1}$$

Where "CH_2" represents an unspecified hydrocarbon product.

Uncatalyzed HDO of phenol to benzene reaches complete conversion at temperatures up to at least 600 °C in atmospheric pressure and stoichiometric conditions [22]. In order to reduce the operating temperature and increase the reaction rate the use of a catalyst is thus required. Catalyzed HDO is normally carried out at temperatures between 250 and 450 °C and a high pressure in the range of 75-300 bar has been described as providing a higher solubility of hydrogen in the oil and hence a higher availability of hydrogen in the vicinity of the catalyst [22]. As bio-oil is derived from biomass, it will also contain traces of several inorganic compounds like transition metals, alkali metals, chlorine, sulfur and phosphorous. These represent a significant concern for catalyzed HDO, as they can act either as catalyst inhibitors, leading to a non permanent deactivation, or as poisons that might irreversibly compromise the catalytic activity [23].

As of now, a variety of different catalysts has been tested in literature for the HDO process [22, 24]. This chapter will present the characterization work carried out on two reduced metal type catalysts (Ni/ZrO_2, Mo_2C/ZrO_2) and one sulphide catalyst ($Ni\text{-}MoS_2/ZrO_2$), three systems that showed high activity in HDO of phenol, a bio-oil model molecule [24]. The distinction in two categories arises from the different proposed reaction mechanisms leading to hydrodeoxygenation and will be discussed in each relevant section. For these catalytic systems, the effectiveness of the synthesis procedure in connection to the catalyst's structure, performance and stability has been investigated by means of electron microscopy and X-ray diffraction. In addition, this characterization procedure followed long term stability experiments carried out at DTU Kemiteknik aiming at evaluating the resistance of the catalyst to several relevant poisoning species. The information extracted from the characterization were hence used to describe the possible mechanisms leading to deactivation.

4.2 Ni/ZrO_2

HDO reaction mechanism

Hydrodeoxygenation over reduced metal type catalysts is believed to be a three steps process involving (Figure 4.1) [24]:

1. Adsorption of the oxy compound on the catalyst surface. Depending on which type of active metal is used, this step can take place either on the support or directly on the metal. This last case is peculiar of noble metals, whereas adsorption on the support is thought to occur mainly in the case of reduced non-noble metal catalysts through oxygen vacancy sites of the support metal oxide.

2. Activation of H_2 on the surface of the active metal and donation of hydrogen to the oxy compound.

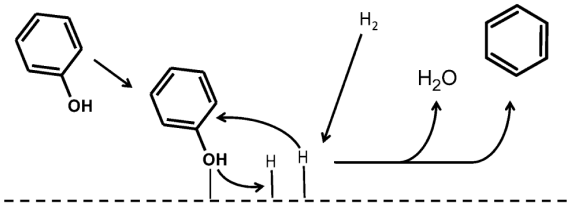

Figure 4.1: Proposed mechanism for phenol HDO reaction over reduced metal type catalysts. Figure from [24].

3. Desorption of the final product.

Two different types of active sites are hence present on these kind of catalysts: vacancy sites on the oxide support where adsorption of phenolic compounds takes place and low coordinated, exposed metal sites facilitating the deoxygenation reaction. Besides the ability to adsorb oxy compounds, the support is also required to have a low acidity in order to avoid saturation of phenolic species on its surface that could turn into potential carbon precursors and finally lead to coking of the catalyst. ZrO_2 proved to meet both requirements and was hence chosen as the catalyst support material, also considering its broad availability on the market as an high surface support (mainly in its tetragonal crystallographic form).

The influence of the preparation method on catalyst stability

The influence of the preparation method on the overall HDO activity of Ni/ZrO_2 was investigated by testing two batches of catalysts prepared following different synthesis procedures. Both samples were synthesized using the incipient wetness method and the content of nickel fixed to 5 wt%. In one case, the catalyst was directly reduced in H_2 at 500 °C after drying (referred as Ni-DR) and in the second case, in order to obtain a different nickel particle size [25], it was calcined for 2 hours at 400 °C and then reduced (referred as Ni-CR). Both catalyst batches were tested in a high pressure gas and liquid continuous flow setup using guaiacol as a bio-oil model molecule (see [Paper1] for a detailed explanation of the testing procedure). As Figure 4.2 shows, Ni-DR presented higher maximal degree of deoxygenation and better overall stability when compared to Ni-CR.

In order to elucidate the role of the preparation method on the Ni/ZrO_2 catalytic performance, a set of characterization techniques have been used. As a first approach, XRD was used to get information on the average crystallographic composition of the sample. However, as it will be shown along the following sections, this technique soon demonstrated its limitations, justifying a more TEM-oriented approach.

XRD analysis of the spent samples

Powder X-ray diffraction analysis of both samples after 80-110 h catalytic test was carried out in order to identify the present crystallographic phases and give an estimate

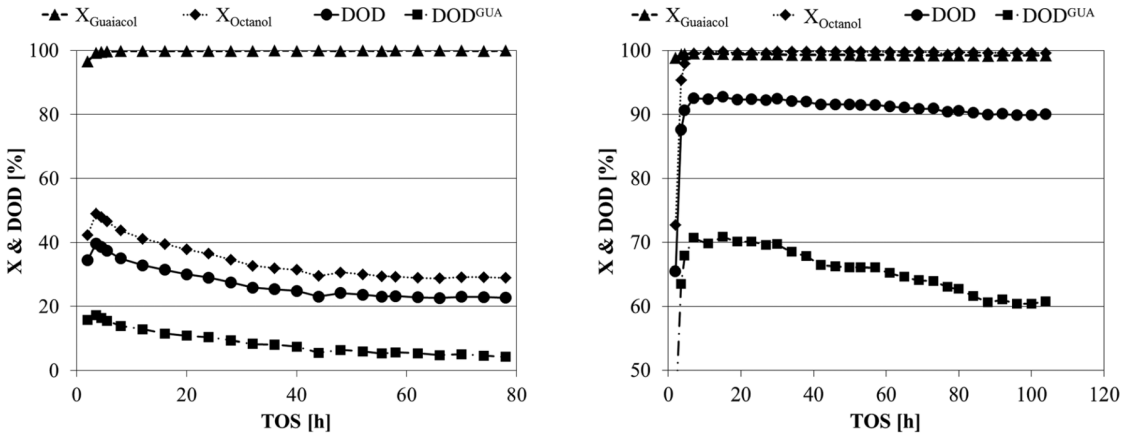

(a) Stability of Ni-CR **(b)** Stability of Ni-DR

Figure 4.2: Conversion of guaiacol and 1-octanol and degree of deoxygenation (DOD) for **(a)** Ni-CR and **(b)** Ni-DR as a function of time on stream. DOD^{GUA} is the degree of deoxygenation of the guaiacol feed. T = 250 °C, P = 100 bar. Figures from [26].

of nickel crystallite sizes. Patterns were acquired using a PANalytical X'Pert PRO diffractometer in a Bragg-Brentano Theta-Theta geometry at a $25° < 2\theta < 100°$ range using a monochromatic Cu-Kα radiation (λ=1.5418 Å) and automatic anti-scatter and divergence slits. Background subtraction and peak identification was carried out using the PANalytical HighScore Plus 3.0.5 software.

As Figure 4.3 shows, both Ni-CR and Ni-DR background subtracted diffraction patterns confirm the presence of a tetragonal zirconia phase corresponding to the support and present a weak reflection at approximately $2\theta = 44.5°$ identified as cubic Ni 111. The sole presence of the statistically strongest Ni 111 reflection in the diffraction patterns is not unexpected, as the nickel loading on these catalysts is rather low (5 wt%). Furthermore, the remaining four Ni-$Fm\bar{3}m$ reflections have a theoretical statistical intensity which is less than half than the only visible Ni 111 peak. Their experimental intensity most likely vanishes in the instrumental noise level.

However, a qualitative comparison of the Ni crystallite size between the two catalysts could be given applying the Scherrer formula on the Ni 111 reflection:

$$\tau = \frac{K\lambda}{\beta cos\theta} \tag{4.2}$$

where τ is the average crystallite size, K is a dimensionless shape factor, λ is the X-ray wavelength, β is the peak broadening measured at half the maximum intensity (FWHM) after subtracting the instrumental peak broadening and θ is the Bragg angle. The crystallite size estimation was carried out neglecting lattice strain effects. In an effort of providing a reliable measure of β, FWHM of Ni 111 reflections were extracted by fitting the experimental peaks using Voigt functions in Origin Pro (Figure 4.4), leading to 0.62° for Ni-CR and 0.70° for Ni-DR. The instrumental peak broadening was measured using a standard LaB_6 sample. In conclusion, Scherrer analysis of the samples led to an average Ni crystallite size of 20 nm for Ni-CR and 17.5 nm for Ni-DR, considering an instrumental peak broadening of 0.062° at $2\theta = 44.5°$ and $K = 0.9$ (generally accepted assuming isotropic spherical crystals).

It is important to mention that the use of the Scherrer equation should be limited to follow trends in analogously treated specimens (and hence not in a quantitative way), as XRD peak broadening in a polycrystalline powder is influenced by a great number of parameters (size-strain effects, shape factors), whose contribution can be difficultly separated [27].

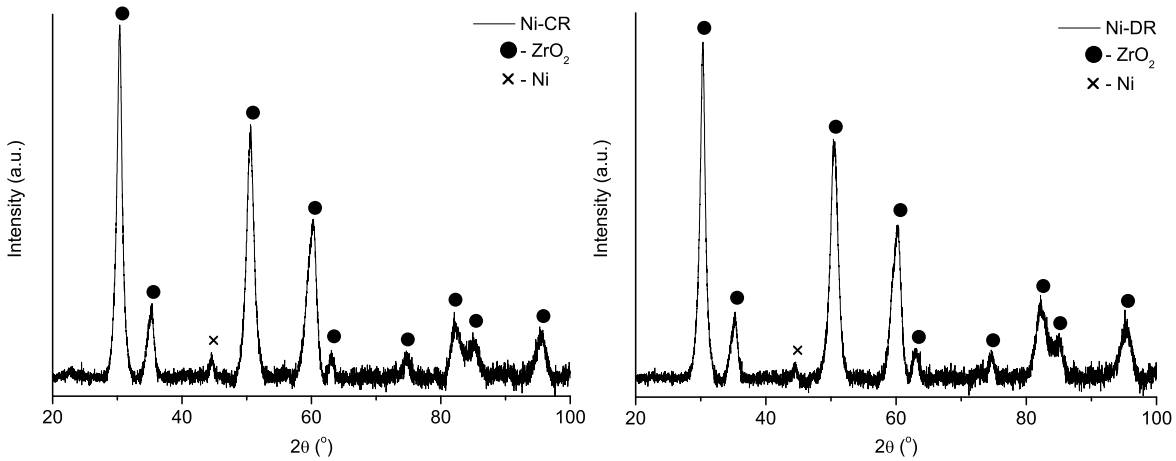

(a) XRD of Ni-CR **(b)** XRD of Ni-DR

Figure 4.3: X-ray diffraction patterns of **(a)** Ni-CR and **(b)** Ni-DR catalysts. Reference phases: ZrO_2-P42/nmcz [28], Ni-Fm$\bar{3}$m [29].

In order to further investigate the supported nickel phase overcoming the signal to noise limitations due to the low loading and including a more reliable analysis of the size and distribution of both crystalline and amorphous species, transmission electron microscopy was used.

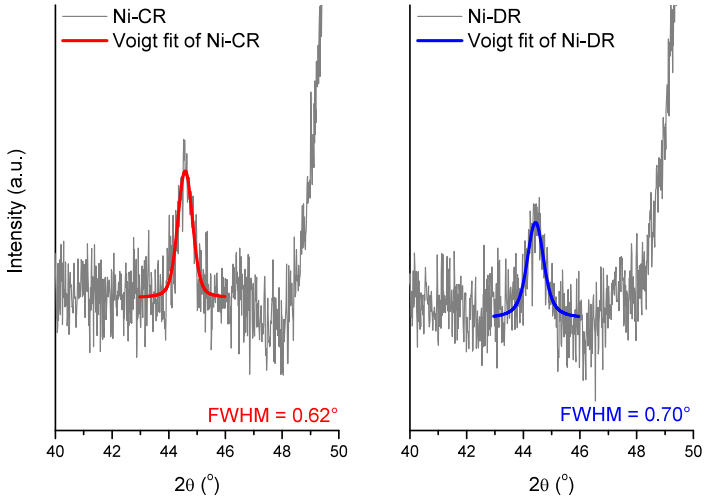

Figure 4.4: XRD patterns of **(left)** Ni-CR and **(right)** Ni-DR in the 2θ range 40-50°. In color is represented the Voigt fit of Ni (111) peak used for nickel crystallite size estimation.

TEM analysis

TEM analysis of Ni/ZrO_2 was carried out using a probe-corrected FEI Titan 80-300 transmission electron microscope operated at 300 keV. Catalyst powders were crushed in an agate mortar and dry dispersed on lacey carbon supported copper grids.

As previously mentioned in Chapter 2, in bright field TEM the thickness and the mass of the phases composing the sample have a major contribution on the image contrast. In Ni/ZrO_2, thickness variations due to the highly porous support (average crystallite size approximately 10 nm), coupled with the similar mass of nickel (atomic number $Z_{Ni} = 28$) and zirconia (average atomic number $\bar{Z}_{ZrO_2} \approx 18.7$) will hence generate contrast variations that do not allow to univocally identify the supported nickel nanoparticles (Figures 4.5a and 4.5b). Even in HAADF-STEM imaging, where the contrast is mostly given by Rutherford scattering and is proportional to approximately $Z^{1.7}$, sample thickness still plays a major role. The contrast due to the mass difference between zirconia and nickel is not enough to overcome the contribution given by the high porosity of the support, which ends up masking the location of the nickel particles (Figure 4.5c).

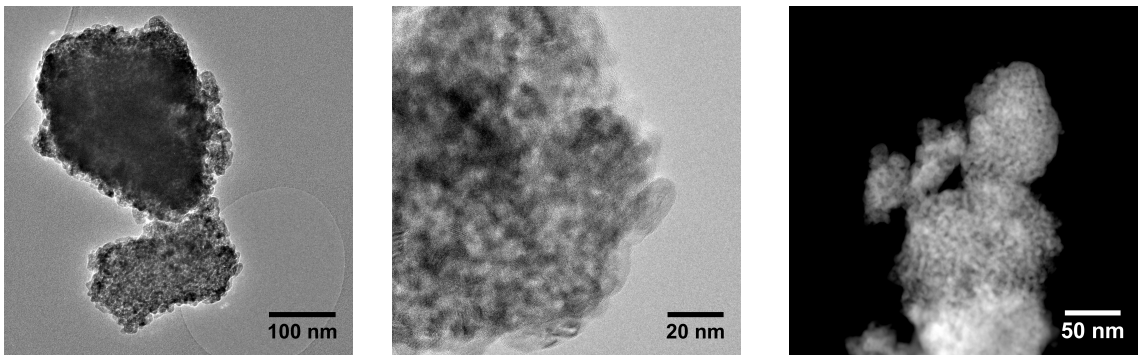

(a) BFTEM Overview **(b)** BFTEM **(c)** HAADF-STEM

Figure 4.5: TEM analysis of Ni-DR showing **(a)** a BFTEM micrograph of an overview of the sample and **(b)** BFTEM and **(c)** STEM-HAADF micrographs of different areas of the sample.

In order to overcome the limitations arising from the similar size and mass of nickel particles and zirconia support, a spectroscopic approach involving STEM-EDX elemental mapping was used to characterize the supported nickel phase. As already introduced in Chapter 3 this technique allows the parallel acquisition of the HAADF and X-ray signal for each scanning point and hence the generation of STEM chemical maps. STEM-EDX analysis was carried out using a FEI Tecnai Osiris operated at 200 keV at the Interdisciplinary Centre for Electron Microscopy (CIME), École Polytechnique Fédérale de Lausanne (EPFL), Switzerland. Maps were smoothed using a 7x7 pixels kernel smoothing algorithm implemented in the Bruker Esprit software used for acquisition.

Representative STEM-EDX elemental maps for both Ni-CR and Ni-DR are shown in Figure 4.6a and 4.6b, respectively, and reveal the presence and the distribution of Ni particles in both catalysts. From these and other acquired maps it was possible to estimate the Ni particle size being on average 9 nm for Ni-DR and 18 nm for Ni-CR

based on size measurements of more than 80 particles for each catalyst. Size distributions for both calcined and directly reduced samples are shown in Figure 4.7. Although the number of analyzed particles cannot be considered fully statistical representative, the size distribution for Ni-DR was noticed to be more homogeneous than Ni-CR. In particular, for the calcined sample a tail toward larger particles sizes was observed (see insets in Figure 4.7), together with the presence of very big outliers ($>$ 100 nm) indicating that calcination could lead to agglomeration of some nickel during the preparation procedure. It is important here to mention that using the nickel X-ray signal to estimate the Ni average particle size does not take into account any spontaneous oxidation effect that could occur by exposure of the sample to air. However, XRD measurement did not reveal any bulk oxidation of the nickel phase, and although surface oxidation might occur (and remain undetected by XRD), it is not expected to influence the nickel particle size by a great extent.

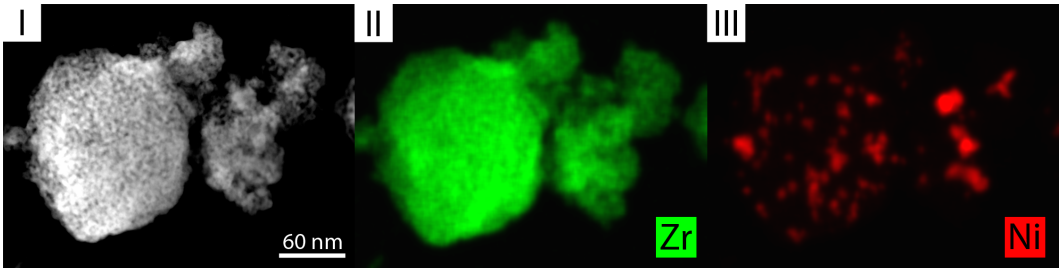

(a) Ni-CR

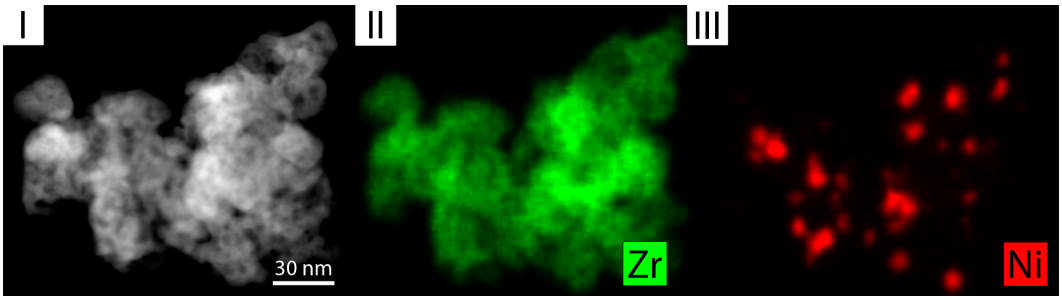

(b) Ni-DR

Figure 4.6: STEM-EDX elemental mapping of **(a)** Ni-CR and **(b)** Ni-DR. Sub-image (I): STEM-HAADF micrograph. Sub-image (II): zirconium EDX elemental distributions. Sub-image (III): nickel EDX elemental distributions.

The difference in the Ni particle size distribution for Ni-CR and Ni-DR was ascribed to the different synthesis procedure, although the effect of catalytic testing itself cannot be completely excluded *a priori*. However, Figure 4.3 and further BFTEM analysis showed that the catalytic testing of both catalysts did not lead to any evident growth of the dimension of the zirconia particles support; a condition that would have favored the sintering of the supported Ni phase. Instead, calcination of $Ni(NO)_3$ catalysts has been previously reported to cause growth of Ni crystallite sizes when compared to direct reduction [30].

The difference in nickel particle size could hence be at the basis of the different catalytic behavior of the two catalysts. Smaller nickel particles possess a higher sur-

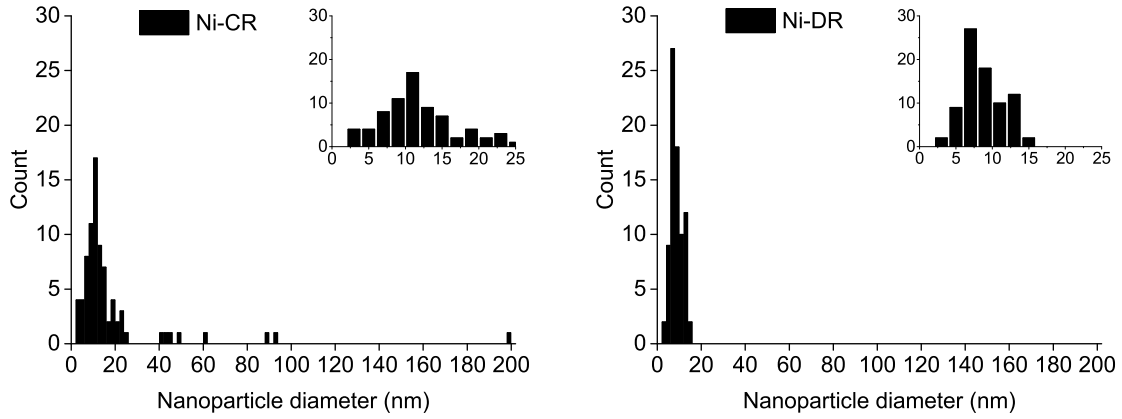

(a) Ni-CR (b) Ni-DR

Figure 4.7: STEM-EDX nickel size distributions of **(a)** Ni-CR and **(b)** Ni-DR catalysts.

face and a bigger fraction of step/corner sites, more active for the C-O bond breaking reaction and hence responsible for the deoxygenation activity of the catalyst [31]. In this perspective, the calcined sample possess an inhomogeneous Ni particle distribution with the presence of >40 nm particles with low step/corner site ratio, which could explain its overall lower catalytic activity. Concerning the deactivation behavior of the two catalysts, carbon deposition has been described as one of the main mechanisms leading to the loss of activity during prolonged HDO operation, causing the block of both catalyst's pore structure and active sites [23]. Carbon layers have been described to grow by nucleation on the step sites of the nickel crystals and increase their thermodynamical stability with increasing growing size [32]. Thus, a HDO catalyst with large nickel particles able to support the growth of extended carbon layers is considered more prone to coking, and would deactivate faster, as confirmed by the catalytic behavior of Ni-CR shown in Figure 4.2a.

Deactivation by poisoning

As already introduced, inorganic compounds naturally present in bio-masses, such as alkali metals, chlorine and potassium could lead to catalyst deactivation by poisoning. A poison is a substance which adsorbs on active catalysts sites, with the result of either competing with the reactants or changing the nature of the active site, incapacitating the desired reaction any further. The understanding of the mechanisms leading to deactivation by poisoning is thus of fundamental importance for the design of better, more stable catalysts or in order to plan strategies aiming at reducing the exposure of the catalyst to the most severe poisoning species.

In this work, the long term stability of Ni-DR in presence of sulfur, chlorine and potassium has been tested and the deactivated, spent catalyst analyzed by means of electron microscopy and X-ray diffraction in order to increase the understanding on the deactivation mechanisms involved. The persistence and nature of the poisoning species on the spent catalysts were investigated through scanning electron microscopy EDX (SEM-EDX) and XRD in order to provide a characterization able to cover both amorphous and crystallographic phases. The choice of SEM over TEM arises from

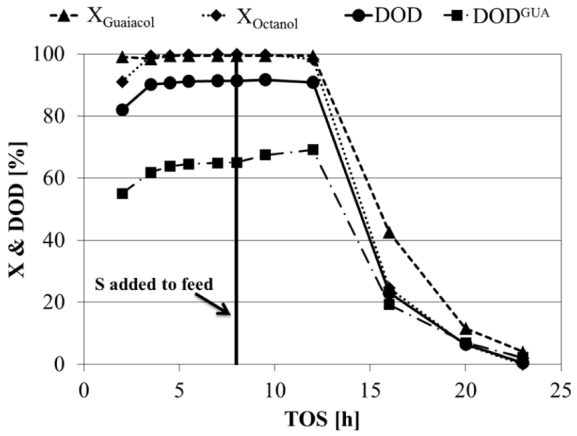

(a) Deactivation with octanethiol

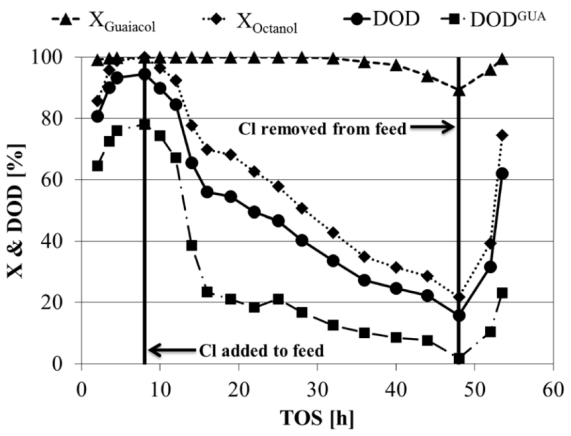

(b) Deactivation with chlorooctane

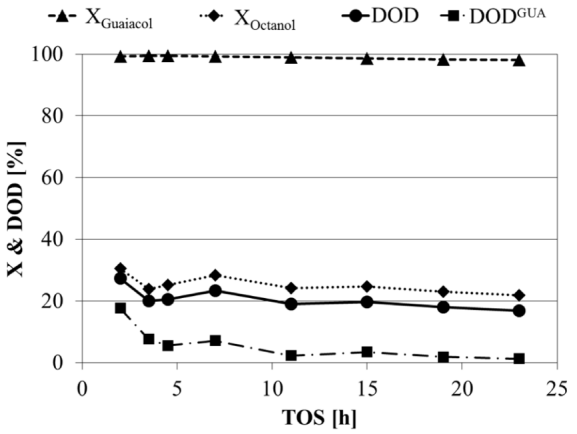

(c) Deactivation by impregnation with KCl

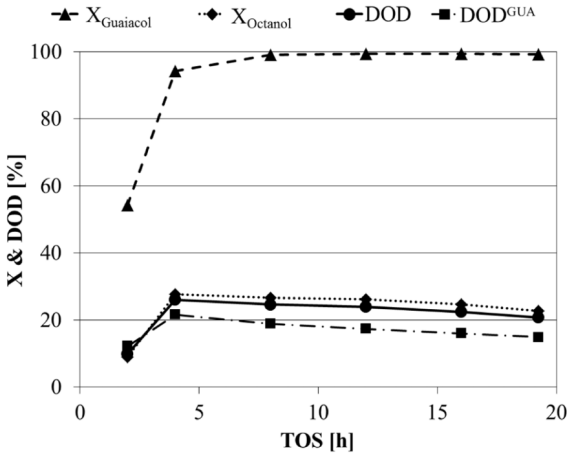

(d) Deactivation by impregnation with KNO_3

Figure 4.8: Conversion of guaiacol and 1-octanol and DOD over Ni-DR catalysts as a function of time when deactivated by **(a)** octanethiol, **(b)** chlorooctane, **(c)** KCl and **(d)** KNO_3. Octanethiol and chlorooctane were added to the feed after 8 h of time on stream as indicated on the respective figures. Chlorooctane was removed from the feed again after 48 h. T = 250 °C, P = 100 bar. Figures from [26].

the need to probe a bigger volume of the catalyst, compensating the intrinsically low X-ray emission signal typical of thin samples and addressing the locality issue of TEM information. SEM-EDX spectra were acquired using an FEI Quanta 200 ESEM FEG operated at 10 keV and equipped with an Oxford Instruments 80 mm^2 silicon drift detector. A few particles of 300-600 μm sieved fractions of the catalyst were fixed to standard SEM aluminum stubs with Vishay Micro-Measurements M-Bond epoxy resin and mechanically polished in order to reach a flat geometry configuration. Moreover, the spatial distribution of poisoning species was investigated by STEM-EDX in a similar manner as for the identification of Ni particles shown in the previous section.

Sulfur poisoning

Sulfur has been described to be present in bio-oils with concentrations up to 0.8 wt% and is therefore of significant concern for catalyzed hydrodeoxygenation [26]. The stability of Ni-DR upon sulfur poisoning has been tested introducing 0.3 vol% 1-octanethiol (corresponding to 0.05 wt% S) in the feed during an activity experiment similar to the one described in Section 4.2. As Figure 4.8a shows, introduction of octanethiol led to total deactivation of the catalyst after approximately 12 h, with complete loss of deoxygenation activity and reactants conversion.

The presence of sulfur in the spent catalyst was initially assessed by SEM-EDX analysis, revealing the tendency of this poisoning species to persistently bind to the Ni-DR catalyst during HDO operation (Figure 4.9a). Further investigations carried out by means of STEM-EDX (Figure 4.9c) confirmed the persistence of sulfur and revealed a very similar spatial distribution of nickel and sulfur signals, suggesting the preferential adsorption of sulfur on the nickel particles. By extending the analysis to the crystallographic phases present in the deactivated catalyst, XRD measurements (Figure 4.9b) confirmed the presence of the zirconia support and revealed a weak reflection at $2\theta = 45.2\ ^\circ$ that could be identified as hexagonal NiS. No reflections ascribed to metallic nickel were observed, however a weak NiO reflection was detected, probably due a partial nickel oxidation during sample storage. XRD analysis for this sample was carried out on the same specimen used for complementary XAS measurements, and therefore showed the presence of cellulose as a result of the XAS sample preparation procedure.

STEM-EDX and XRD analysis hence suggest that introducing 1-octanethiol in the feed leads to the deactivation of Ni-DR by the conversion of Ni to an inactive NiS phase. This result was furthermore confirmed by complementary XAS measurements [26], where X-ray absorption near edge structure (XANES) analysis showed that the Ni-K-edge of sulfur deactivated Ni-DR catalysts could be refined to a NiS phase.

Chlorine poisoning

Deactivation experiments of Ni-DR by chlorine were carried out by introducing 0.3 vol% 1-chlorooctane in the feed, corresponding to 0.05 wt% Cl, the average quantity of organic bound chlorine that can be found in real bio-oil [36]. As Figure 4.8b shows, exposure to chlorine for 40h led to an overall drop in deoxygenation activity, whereas the guaiacol conversion rate was only slightly affected. After 48h of TOS a chlorine-free

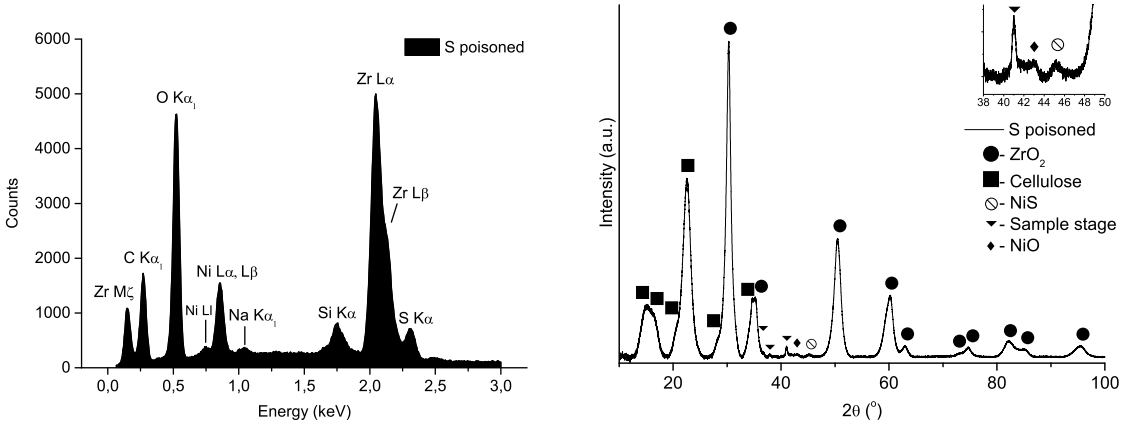

(a) SEM-EDX (b) XRD

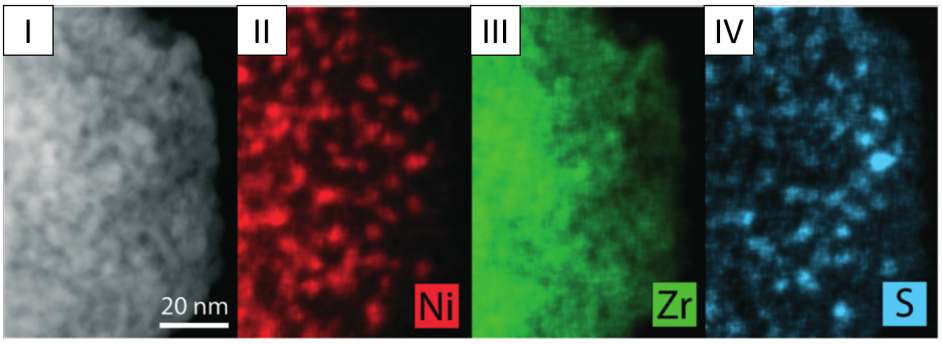

(c) STEM-EDX

Figure 4.9: Characterization of the sulfur poisoned Ni-DR catalyst showing **(a)** SEM-EDX spectrum, **(b)** XRD pattern and (c) STEM-EDX elemental maps. Sub-image (I): STEM-HAADF micrograph. Sub-image (II): Ni EDX elemental distributions. Sub-image (III): zirconium EDX elemental distributions. Sub-image (IV): sulfur EDX elemental distributions. Reference phases for XRD indexing: NiS-P63/mmc [33], Cellulose [34], NiO-Fm$\bar{3}$m [35]. Additional reflections were ascribed to the sample stage used for measurements. Presence of Na in the SEM-EDX spectrum could be ascribed to contamination during sample preparation. Si is present in the ZrO_2 support as SiO_2 impurity.

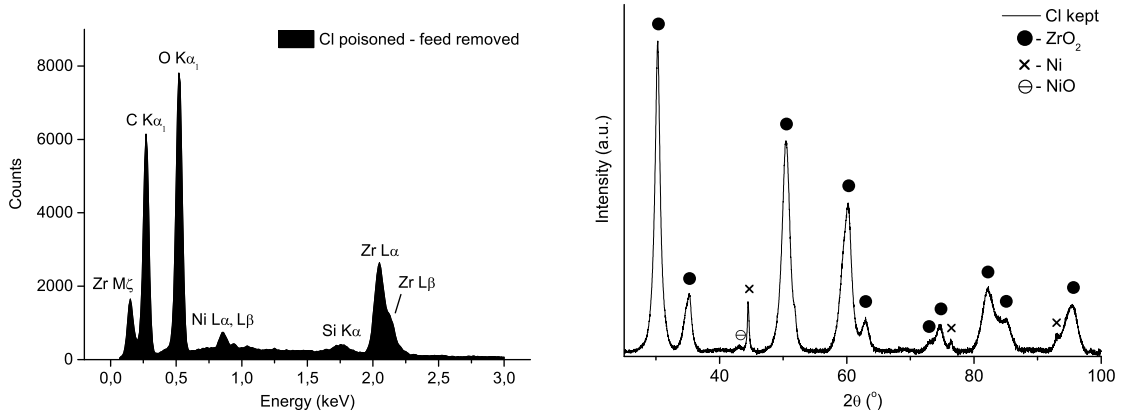

(a) SEM-EDX (b) XRD

Figure 4.10: Characterization of the chlorine poisoned Ni-DR catalyst showing **(a)** SEM-EDX spectrum and **(b)** XRD pattern.

feed was restored and the catalyst activity was observed to increase towards the initial activity level before the end of the experiment.

SEM-EDX measurements carried out on the spent catalyst after the test did not reveal the presence of chlorine (Figure 4.10a). In order to verify whether the absence of this poisoning species in the spent sample was due to restoring of a chlorine-free feed prior to the end of the activity measurement, an additional catalytic test was performed maintaining 1-chlorooctane in the feed until the end of the test. SEM-EDX investigations of the spent Ni-DR from this last experiment further confirmed the absence of chlorine, supporting the non-persistent nature of this poisoning species.

XRD analysis of the spent sample (Figure 4.10b) identified the presence of zirconia and nickel phases. The nickel fcc phase was observed to have higher intensity when compared with measurements of the spent Ni-DR reference catalyst (Figure 4.3b), with Ni 220 and 311 reflections now being clearly visible. Voigt fitting of Ni 111 peak at $2\theta = 44.5°$ allowed to measure a FWHM of approximately 0.32°, less than half of the reference Ni-DR (0.70°), suggesting an increase in the size of the nickel crystalline domains. Using the Scherrer equation this was estimated to be 39 nm. Unfortunately, no STEM-EDX analysis could be carried out on this sample due to the lack of instrument time during the external research stay at CIME.

Activity measurements and SEM-EDX analysis point out that deactivation by chlorine appears to be partly reversible, indicating that Cl species blocking the HDO active sites can rapidly desorb when the chlorooctane feed is interrupted. Reversible adsorption of chlorine on nickel catalysts has already been reported in literature [37] and has been associated to the formation of a Cl equilibrium surface layer on the nickel particles. This is in accordance with the present study, where chlorine poisoning proved to hinder mostly the deoxygenation activity of Ni/ZrO_2, taking place on low coordinated nickel sites. Furthermore, XRD analysis of the spent catalyst revealed a growth in the Ni crystalline domains when compared to the reference Ni-DR. As reported by Ohtsuka [38] this behavior could be explained by the formation of mobile Ni-Cl species upon reaction of HCl with surface oxides. It is important here to notice that the activity level regained by the catalyst upon interruption of the Cl containing feed exceeds

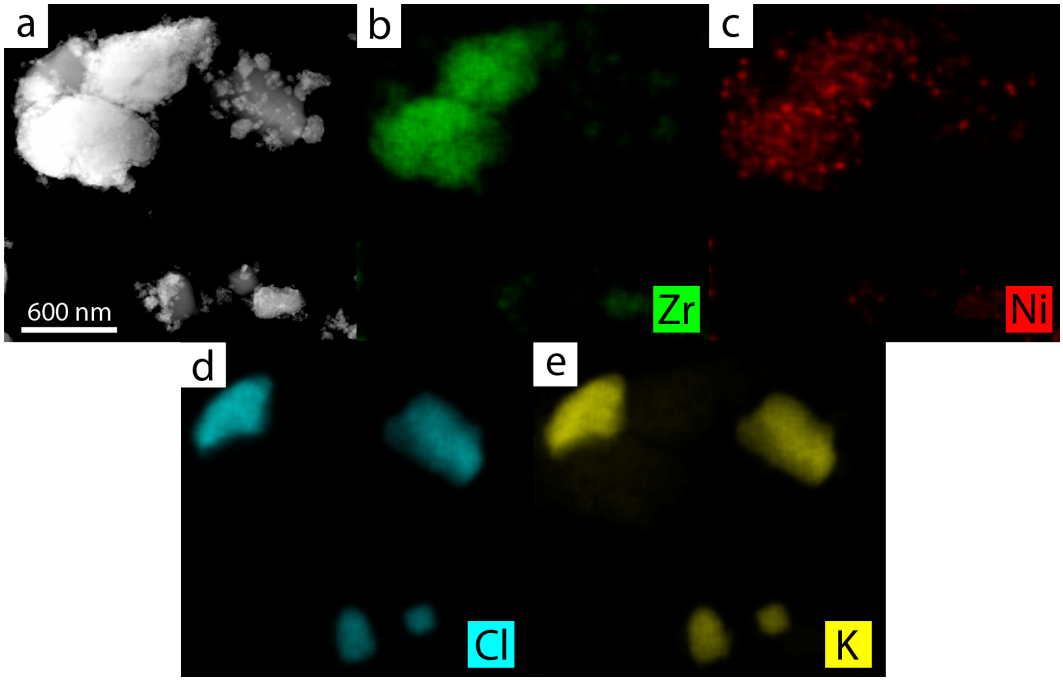

Figure 4.11: **(a)** STEM-HAADF micrograph of the spent KCl co-impregnated catalyst with **(b)** zirconium, **(c)** nickel, **(d)** chlorine and **(e)** potassium EDX elemental distributions.

the Ni-CR case, even if the average Ni crystallite size in Ni-CR was estimated to be the approximately half (20 nm) of the Cl poisoned catalyst. This apparently controversial result could be explained when considering the presence of the aforementioned >40 nm outliers in the size distribution of Ni-CR. These could be representative for the presence of large portions of inactive Ni phase and consequently justifying the poor catalytic activity. In the case of Cl poisoned Ni-DR instead, Ni particle growth could have been a more homogeneous process, leading to a shift of the whole particle size distribution to bigger values and hence a comparatively smaller reduction of the catalytic activity when compared to Ni-CR. Further STEM-EDX analysis are however required to confirm this assumption.

In conclusion, although chlorine adsorption proved to be a reversible process, it was shown to induce a permanent sintering of the nickel particles, which in turn could be responsible for a loss of catalytic activity (as shown in Section 4.2).

Potassium poisoning

Potassium represents one of the main alkali impurity present in bio-oil, with concentrations reaching up to 0.3 wt% [36]. The effect of this species on the HDO catalytic activity of Ni/ZrO_2 was tested by co-impregnating KCl on Ni-DR in stoichiometric amount relative to Ni prior to catalytic test in the flow reactor. As shown by Figure 4.8c, KCl had the effect of deactivating mainly the deoxygenation reactions and left the hydrogenation of guaiacol almost unaltered, as reported for chlorine deactivation. However, contrary to chlorine, KCl deactivation seemed to be irreversible, with no restoration of activity throughout 23h time on stream.

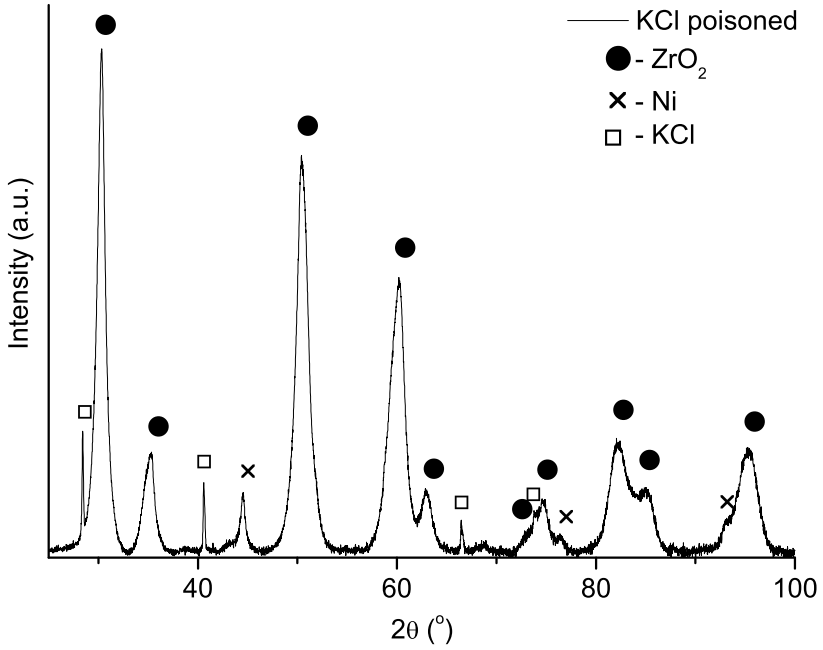

Figure 4.12: XRD pattern of the spent KCl co-impregnated catalyst. KCl reference phase from [39].

STEM-EDX (Figure 4.11) and XRD analysis (Figure 4.12) of the spent sample revealed that co-impregnation by KCl led to the formation of large (>100 nm) KCl crystals in contact with the catalyst. Similarly to the case of chlorine deactivated samples, XRD measurements showed stronger Ni reflections when compared to the reference Ni-DR catalyst, with Ni (111) peak having a FWHM of 0.54°. Sintering of nickel particles was confirmed by means of STEM-EDX mapping and the average nickel particle size was estimated to be 24 nm.

In order to exclude the contribution of chlorine species and study the effect and mechanisms of potassium poisoning, a new batch of Ni-DR was impregnated with KNO_3 in stoichiometric amount relative to Ni. Similarly to the KCl case, activity measurements (Figure 4.8d) revealed once more the total hydrogenation of guaiacol and an overall deactivation of the deoxygenation reactions. However KNO_3 poisoned Ni-DR was observed to be 2-3 times more active in the deoxygenation of guaiacol when compared to the KCl impregnated catalyst.

SEM-EDX investigations revealed the persistence of potassium on the deactivated sample (Figure 4.13a). However, XRD measurements (Figure 4.13b) did not show any potassium containing crystalline phase, indicating a more homogeneous dispersion of this species compared to that in the KCl co-impregnated catalyst. Nickel was identified in both metallic Ni and NiO, most likely as a result of exposure of the sample to air. The average size of nickel particles was estimated by STEM-EDX mapping to be 9 nm. This indicates that sintering did not take place, contrary to the case of KCl co-impregnated catalyst, where part of the chlorine might have be converted to HCl and contributed to the Ni particle growth mechanism as exposed in the chlorine poisoning section. The larger nickel average particle size could hence be responsible for the lower guaiacol deoxygenation activity of KCl co-impregnated Ni-DR when compared

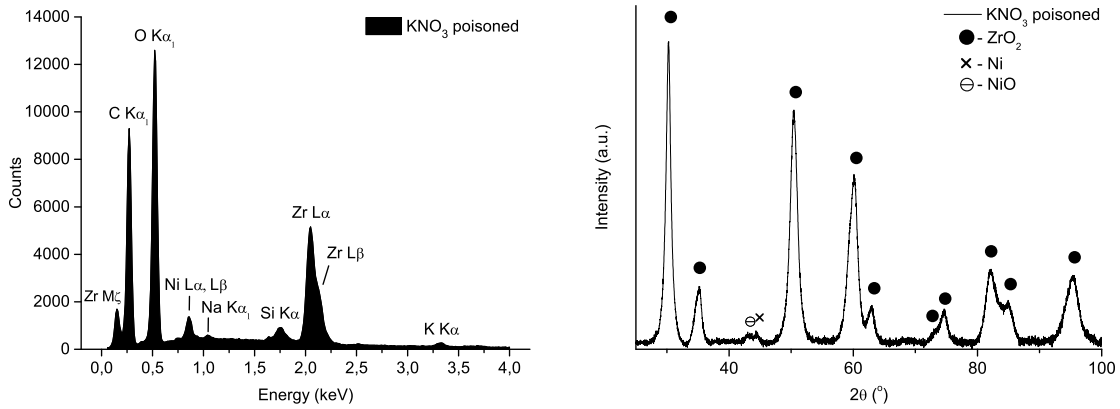

(a) SEM-EDX **(b)** XRD

Figure 4.13: Characterization of the spent KNO_3 co-impregnated Ni-DR catalyst showing **(a)** SEM-EDX spectrum and **(b)** XRD pattern.

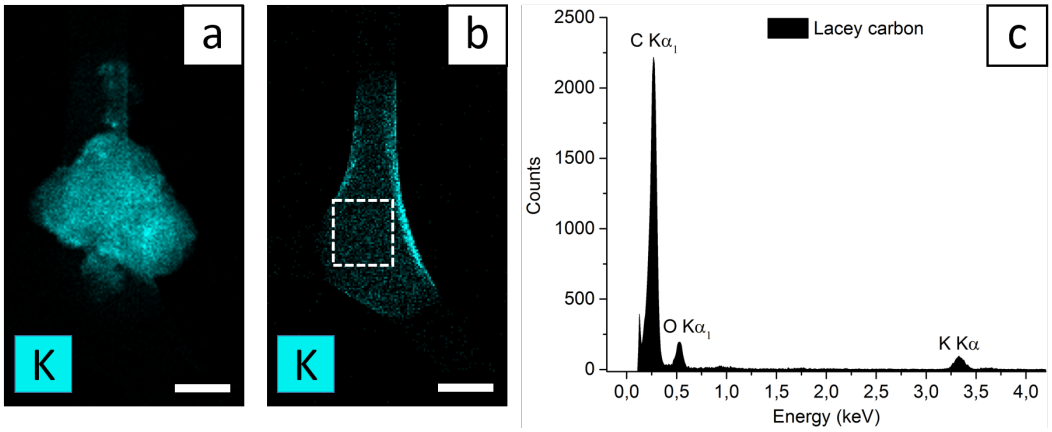

Figure 4.14: Redistribution of potassium during STEM-EDX analysis of KNO_3 co-impregnated Ni-DR. **(a)** The potassium EDX elemental map was acquired until a portion of the catalyst felt off the **(b)** supporting lacey carbon. **(c)** EDX analysis of the highlighted area in (b) confirming the presence of potassium on the carbon film. Scalebar is 30 nm.

to KNO_3 co-impregnation.

In an attempt to study the spatial distribution of potassium in the deactivated sample, STEM-EDX mapping resulted in the redistribution of this element all over the scanned area (Figure 4.14). This could be ascribed to the high mobility of potassium ions under the effect of the electron beam, as reported by other studies in literature [40, 41].

In conclusion, from both co-impregnation experiments with KCl and KNO_3, potassium was observed to be deposited persistently in the catalyst structure and hinder the deoxygenation activity of Ni-DR permanently. Hence, potassium could be responsible for blocking the low coordinated Ni sites active for the deoxygenation reaction. This is in accordance with Bengaard *et al.* [32] who showed deactivation of steam reforming nickel catalysts by adsorption of alkali metals on the step sites of nickel crystallites.

Summary

Long term activity and resistance of the Ni/ZrO_2 transition metal type catalyst for the HDO of guaiacol were tested in a high pressure flow reactor. The analysis of the spent catalyst by means of SEM, TEM and XRD, coupled with the information from XAS complementary techniques, allowed to increase the understanding on the mechanisms behind catalyst activity and deactivation. Only by the combination of these techniques, a deeper interpretation of the catalytic test data could be provided, resulting in:

1. Activity and log term stability of the catalyst was found to be connected to the size of the supported nickel particles. Smaller particles (9 nm) gave higher activity than larger ones (18 nm) as a result of the increased number of step/corner sites active for C-O bond breaking reaction. The difference in stability was ascribed to the increased thermodynamical stability of the deposited carbon on larger particles during coking.

2. Addition of sulfur in the feed resulted in a fast deactivation of the catalyst over 12h of TOS due to the conversion of Ni into an inactive NiS phase.

3. Deactivation by chlorine was found to be partially reversible when the chlorine feed was interrupted. This species is believed to bind reversibly to the low coordinated nickel surface sites forming an equilibrium surface layer. Moreover, chlorine was reported to induce sintering of the Ni particles, most likely by the formation of mobile Ni-Cl species.

4. Potassium poisoning was found to be persistent and affected mostly the deoxygenation activity of the catalyst, probably due to permanent absorption on Ni low coordinated sites.

4.3 Mo_2C/ZrO_2

Although HDO on reduced transition metal catalysts has been proved to be promising [24, 42], the previous section represents a good example of the tendency of these catalysts to deactivate in presence of a number of impurities.

A less investigated group of catalyst which has received recent increasing attention [43, 44] is transition metal carbides. Their properties have been reported to be similar to noble metal catalysts for certain reactions [45–47], exhibiting even higher reactivity in reactions involving oxygen and hydrogen [47]. A notable example of this category is Mo_2C, which has been used as hydrodesulfurization (HDS) catalyst due to its reported tolerance to sulfur [48]. Due to the similarities in electronic properties and structure between noble metals and transition metal carbides, the HDO reaction on Mo_2C catalysts is believed to follow the same mechanism as presented in Section 4.2 with reduced metal catalysts.

Activity and deactivation by water

In a similar procedure to what has been presented in the previous section, the activity and stability of Mo_2C/ZrO_2 catalyst was tested in a high pressure flow reactor.

Catalysts were synthesized by wetness impregnation of an adequate quantity of $(NH_4)_6Mo_7O_{24}{\cdot}4H_2O$ precursor on the zirconia support in order to reach a 15 wt% MoO_3 loading. The supported precursor was dried in air at 70 °C for 12h and the carbide was produced directly in the flow reactor setup by heating to 200 °C in N_2 at atmospheric pressure, and then ramping to 550 °C at 0.5 °C/min in 50 Nml/min 20% CH_4 in H_2. The sample was finally held at this temperature for 4h prior to test. The carburization procedure was chosen to be carried out in situ due to the tendency of the carbide phase to oxidize upon exposure to air.

The activity and stability of the catalyst were evaluated by testing the HDO of phenol in 1-octanol as model compound mixture of bio-oil. As Figure 4.15a shows, after 76h of TOS the conversion of phenol decreased by approximately 50%, demonstrating a more severe loss of activity when compared to the tests carried out on Ni/ZrO_2 catalysts with similar model compounds (Section 4.2 and [26]). Moreover, in a similar experiment, 33% vol. water was co-fed to the phenol/octanol solution, resulting in an even more severe deactivation, with complete loss of activity after 48h of TOS (Figure 4.15b).

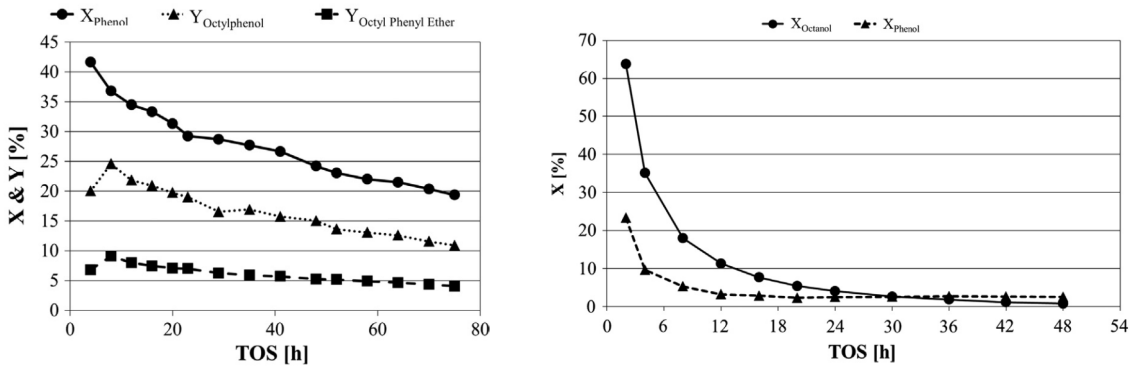

(a) **(b)**

Figure 4.15: Stability of Mo_2C/ZrO_2 during HDO of phenol and 1-octanol, **(a)** shows the conversion and yields of phenol-related compounds and **(b)** shows the conversion of phenol and octanol when 33 vol% water is co-fed. T=300 °C, P=100 bar. Figures from [49]

Hence, from catalytic tests, water was found to be a severe deactivation specie of the Mo_2C/ZrO_2 catalytic system during HDO of phenol. Furthermore, as water is normally formed as by-product from the deoxygenation reaction, it could also be responsible for the loss of activity observed in the experiment with the sole phenol and 1-octanol in the feed (Figure 4.15a), thus justifying the need for a clear understanding of the mechanism behind this important deactivation process.

In an *in situ* synchrotron XRD experiment carried out by collaborators [49], Mo_2C/ZrO_2 catalyst was exposed to 5 vol% H_2 in He saturated with water for 2h at 1 bar and T=300 °C, leading to the formation of a crystalline MoO_2 phase (Figure 4.16). Molybdenum (IV) oxide has been reported to be inactive for HDO [50] and hence oxidation of supported Mo_2C could be at the base of the water-induced activity loss observed in the catalytic tests.

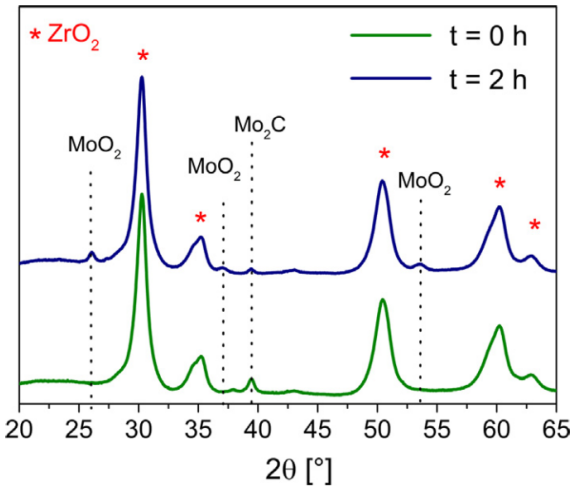

Figure 4.16: *In situ* synchrotron XRD patterns recorded during aging of Mo_2C/ZrO_2. Feed gas: 5 vol% H_2 in He saturated with water. The sample was exposed to water for 2 h at 300 °C. t=0 h is the pattern prior to water exposure and t =2 h is after exposure. Figure from [49].

In order to provide a more deep understanding of the effect of water on the structure of Mo_2C/ZrO_2, a combination of *in situ* XRD and environmental transmission electron microscopy has been used. The *in situ* XRD setup was employed to synthesize a Mo_2C/ZrO_2 sample meeting the requirements for TEM analysis and exposure to water was carried out in the ETEM in order to provide a chemical and atomic-level characterization of the sample able to include both crystalline and amorphous phases.

In situ XRD synthesis of Mo_2C/ZrO_2

As described in the case of Ni/ZrO_2, TEM characterization of Mo_2C/ZrO_2 samples as synthesized for the tests in the flow reactor was found to be difficult due to the lack of contrast. Mo_2C has an average atomic number of $\bar{Z}_{Mo_2C} = 30$, almost identical to Ni ($Z_{Ni} = 28$), which makes identification of small carbide nanoparticles challenging when supported on high surface zirconia. An unambiguous identification of the Mo_2C phase in the TEM is necessary for a reliable high resolution and STEM microanalysis characterization. In particular, the presence of carbide particles reaching from the supporting ZrO_2 into vacuum is crucial during STEM-EELS analysis in order to avoid the detection of oxygen present in the support.

Hence, in order to increase the visibility of the supported carbide phase and increase the probability of free-hanging Mo_2C particles, a less porous, monoclinic ZrO_2 support was preferred. The overall larger particle size of the chosen monoclinic ZrO_2 support in comparison to the tetragonal ZrO_2 used for flow reactor experiments was confirmed by BFTEM analysis (Figure 4.17). As no strong metal-support interactions such as encapsulation by sub-stoichiometric oxides or reductive formation of intermetallic phases have been reported in ZrO_2-supported metal nanoparticles systems [51], the change in crystallographic structure from tetragonal to monoclinic was not expected to have an influence on the water resistance of the carbide phase.

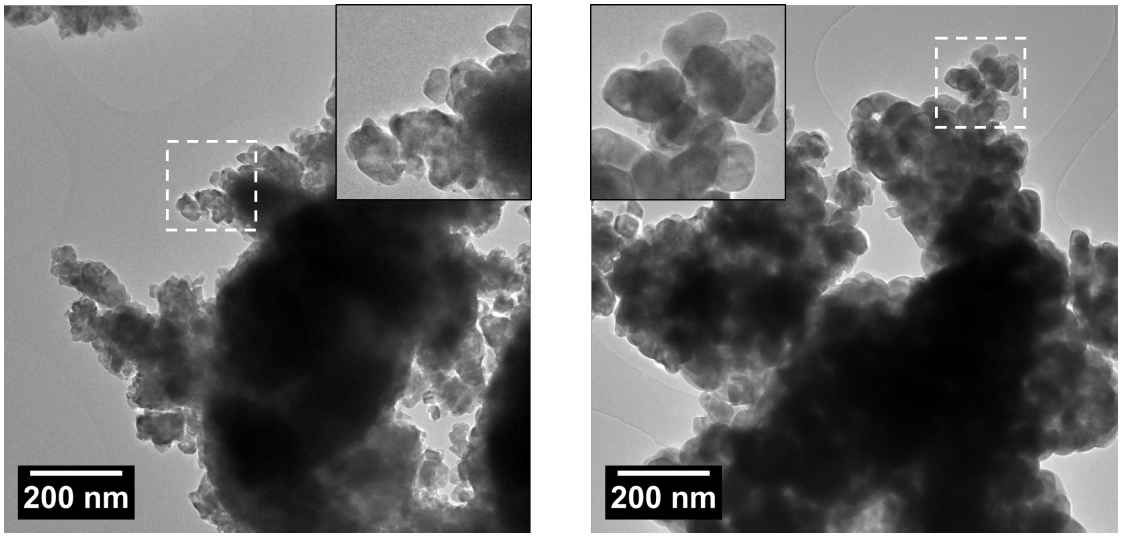

(a) Tetragonal ZrO_2 **(b)** Monoclinic ZrO_2

Figure 4.17: BFTEM micrograph of **(a)** the tetragonal ZrO_2 support used for the synthesis of Mo_2C/ZrO_2 catalyst tested in the flow reactor and **(b)** lower surface area monoclinic ZrO_2 chosen for *in situ* XRD synthesis. Areas highlighted by white dashed squares are magnified in the insets.

Description of the synthesis procedure

Monoclinic ZrO_2 supported Mo_2C catalysts (Mo_2C/m-ZrO_2) were synthesized by a incipient wetness impregnation method using ammonium heptamolybdate tetrahydrate $(NH_4)_6Mo_7O_{24}{\cdot}4H_2O$ as precursor. The amount of water needed for the dissolution of the precursor salts was calculated measuring the total water uptake of the support (0.55 mL/g), choosing the final desired mass of catalyst to be synthesized and taking into account the water already contained in the hydrated precursor. Considering the limited water uptake of the low surface support, the solubility of the precursor was found to be the limiting parameter for the maximum molybdenum loading of the synthesized catalyst, corresponding to approximately 16 wt% MoO_3/m-ZrO_2. The maximum loading was preferred in order to maximize the amount of carbide phase and hence increasing the chances to find Mo_2C nanoparticles suitable for the TEM analysis.

An *in situ* XRD setup composed by a PANalytical X'Pert PRO diffractometer in a Bragg-Brentano Theta-Theta geometry and an Anton Paar XRK 900 reactor chamber was used for the treatment of the precursor-loaded zirconia. This setup allows the simultaneous control of the gas composition and temperature of the reactive environment, leading to a direct monitor of the evolution of the sample crystallinity during treatment.

The carbide was produced directly in the *in situ* setup by a two step process involving first the decomposition of the supported precursor into a molybdenum oxide phase and then the carburization of the oxide to the final Mo_2C. Decomposition was carried out in a $2.0 \cdot 10^4$ Pa He atmosphere by heating the sample at 40 °C/min to 400 °C and dwelling at this temperature for 4h. Thereafter, the sample was cooled down to 70 °C and the gas environment was changed to a CH_4:H_2=1:4 carburizing mixture in Ar.

In an effort of enhancing the comparability between this synthesis procedure and the *in situ* carburization synchrotron studies carried out by collaborators [49], the partial pressure of the carburizing mixture was set to P_{carb}=5.0 · 10^3 Pa. In the carburizing environment, the sample is heated at 1 °C/min to 600 °C and held at this temperature for 12h.

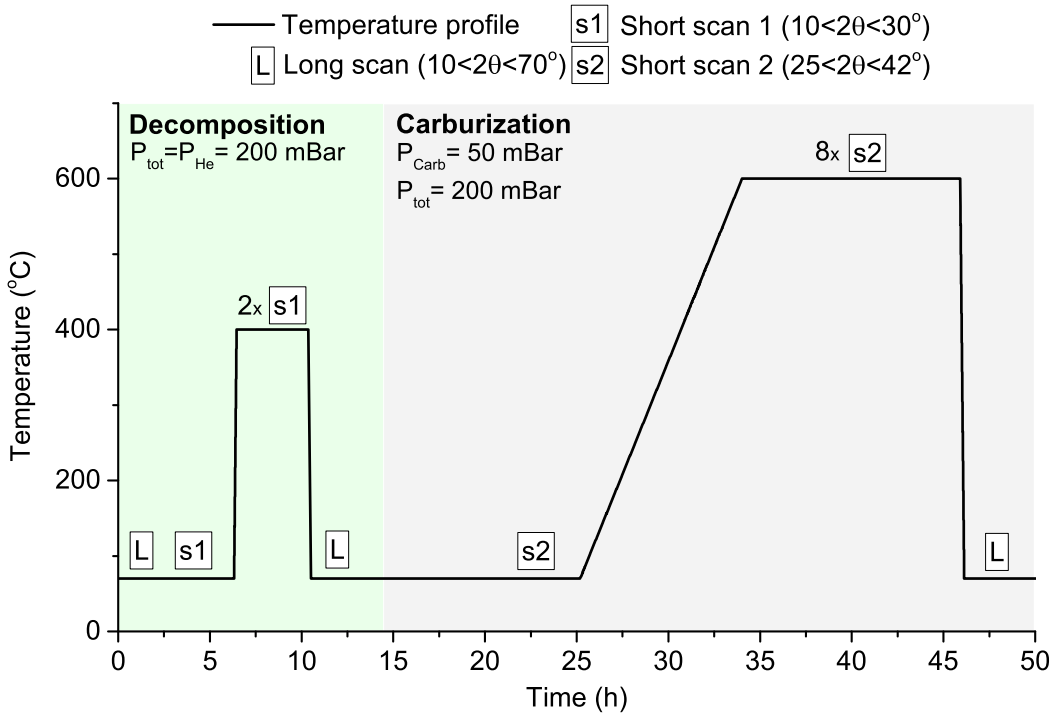

Figure 4.18: Temperature and gas environment evolution during synthesis of the Mo_2C/m-ZrO_2 catalyst.

The correct formation of all intermediary phases leading to the molybdenum carbide, was monitored by periodic XRD measurements carried out during both decomposition and carburization. XRD patterns were acquired with a Cu-Kα source operated at 45 kV and 40 mA and with a Ni-filter, automatic anti-scatter and divergence slits and a monochromator on the diffracted beam. Three different series of scans were acquired. Long scans in an angular range $10<2\theta<70°$ with the duration of 4h (indicated as "L" in Figure 4.18) were recorded at the beginning and at the end of the decomposition and carburization step. Short scans of the duration of 2h ("Short scan 1" in Figure 4.18) and 1.5h ("Short scan 2" in Figure 4.18) were instead acquired at reaction temperatures in restricted angular ranges where relevant changes of the crystalline phases in analysis were expected to take place. This allows to increase the time resolution of the analysis, in an effort of avoiding crystallographic changes within the same acquired pattern, which could lead to a difficult data interpretation.

Furthermore, the composition of the effluent gases were analyzed using a quadrupole mass spectrometer in order to identify the reaction products.

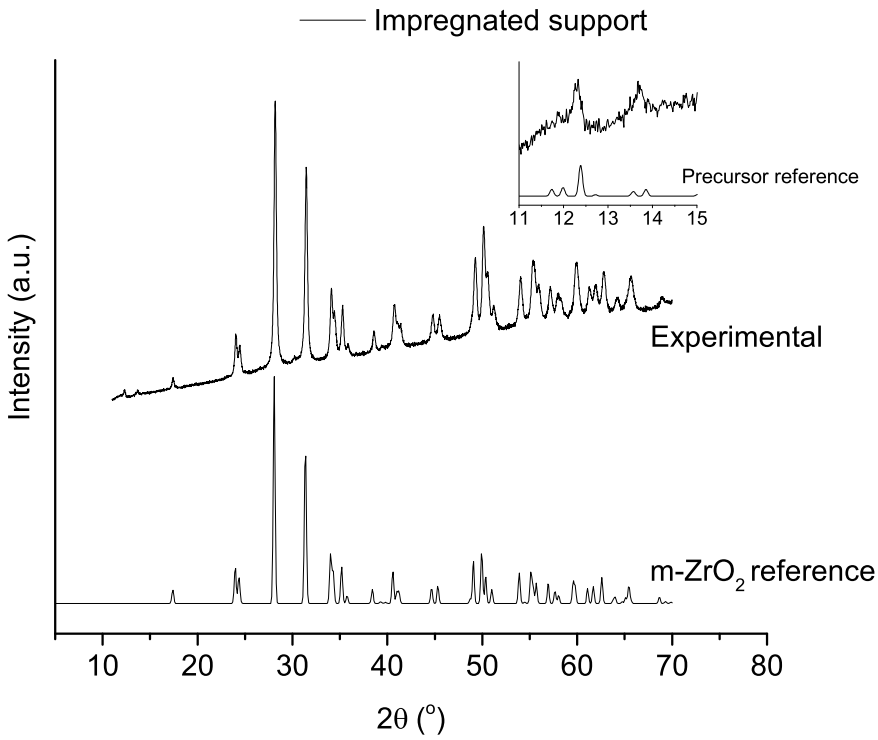

Figure 4.19: XRD pattern of the ammonium heptamolybdate precursor loaded on m-ZrO_2 prior to the decomposition step. In the inset, a close up on the $11<2\theta<15°$ region, where the strongest reflections of the precursor phase are located. Reference phases: ZrO_2-P121/c [52], Precursor [53].

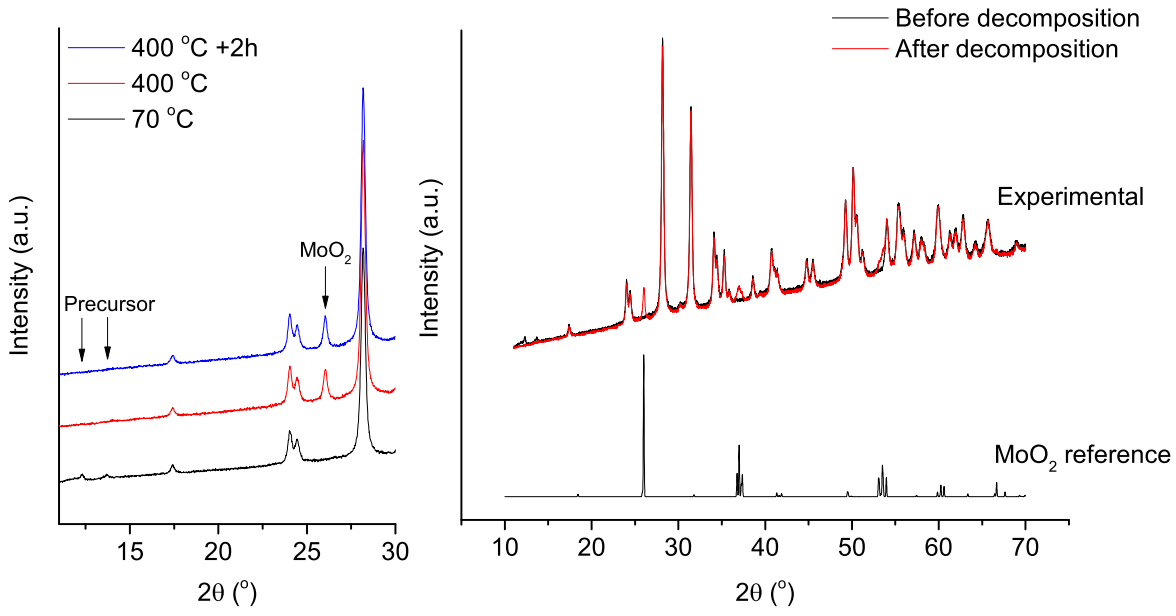

(a) During decomposition **(b)** After decomposition

Figure 4.20: Decomposition step of the synthesis of Mo_2C/m-ZrO_2. **(a)** In situ XRD pattern recorded during decomposition and **(b)** XRD pattern comparison of the sample before and after the decomposition process. MoO_2-P121/c reference phase from [54].

Results and characterization

XRD analysis of the impregnated support confirmed the presence of both monoclinic ZrO_2 and ammonium heptamolybdate (Figure 4.19). During the decomposition step, reflections belonging to the molybdate phase disappeared upon reaching T=400 °C and a new reflection at $2\theta \approx 26.0°$, identified as monoclinic MoO_2 011, became evident (Figure 4.20a). Holding the sample for 2h more at this temperature did not show any substantial change of the as-formed phase. Direct comparison of XRD patterns acquired in the full 2θ angular range before and after decomposition confirmed the formation of a molybdenum (IV) oxide phase (Figure 4.20b).

It is important to mention that the formation of a crystalline MoO_2 phase during thermal decomposition of ammonium heptamolybdate is peculiar, since the predicted products of the reaction do not include this oxide:

$$(NH_4)_6Mo_7O_{24} \cdot 4H_2O \rightarrow 7MoO_3 + 7H_2O + 6NH_3 \tag{4.3}$$

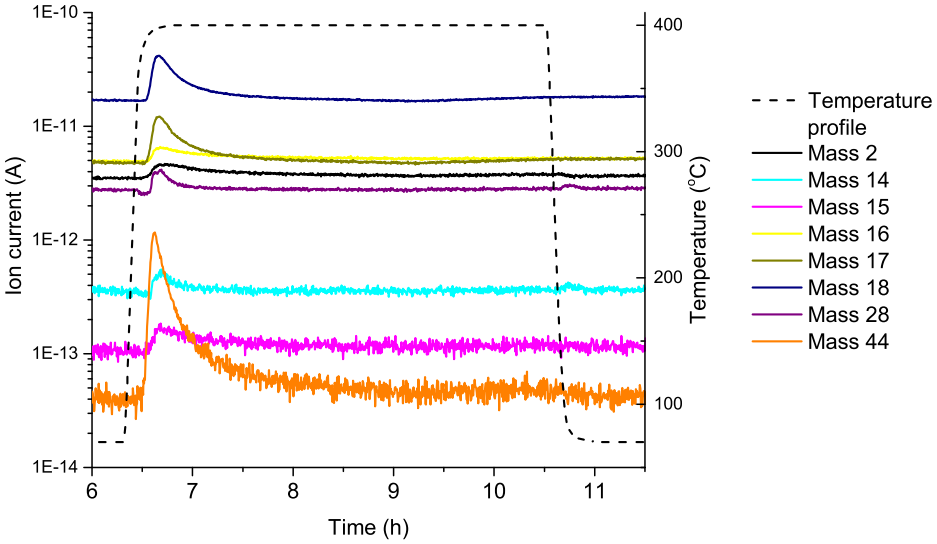

Figure 4.21: Ion current of the fragments ion detected by the quadrupole mass spectrometer in the gas atmosphere during decomposition.

A possible explanation for the formation of MoO_2 could be given taking into consideration the influence of the zirconia support. In their extensive study of the thermal decomposition of ammonium molybdate in an inert gas atmosphere, Thomazeau *et al.* [55] showed that the acidity of the support plays an important role on the final oxidation state of the supported molybdenum oxide phase. Their studies on ZrO_2 revealed a partial reduction of Mo(VI) to Mo(V) species, and on strong acidic supports such as C, SiO_2 and Nb_2O_5 they reported the formation of MoO_2, proposing an autoreduction mechanism of ammonium salts following the reaction:

$$3(NH_4)_6Mo_7O_{24} \rightarrow 21MoO_2 + 30H_2O + 7N_2 + 4NH_3 \tag{4.4}$$

However, from quadrupole mass spectrometry analysis shown in Figure 4.21, decomposition of ammonium molybdate on monoclinic ZrO_2 led to a considerable increase

of mass 44, normally associated to the production of CO_2 or N_2O. Due to the absence of carbon sources in the reaction, this ion current increase was then assigned to the formation of the latter. The presence of N_2O indicates that oxidation of the ammonia produced during decomposition (Reaction 4.3) could have taken place. This oxidation might be a process facilitated by the acidity of the ZrO_2, especially in its monoclinic form [56], responsible for fixating NH_3 molecule on its surface and leading to the reduction of the supported MoO_3 according to the reaction:

$$4MoO_3 + 2NH_3 \rightleftharpoons 4MoO_2 + N_2O + 3H_2O \tag{4.5}$$

The production of water during decomposition was confirmed by peaks in ion current for masses 16 (related also to N_2O), 17 and 18. Masses 14, 16 and 28 could be ascribed to N_2O and the peak in mass 2 indicates the production of H_2. Further investigations are needed to account for the presence of this last gas in the reaction environment.

Carburization of the MoO_2/m-ZrO_2 sample was observed to proceed slowly with the gradual decrease of the intensities related to the MoO_2 reflections. Simultaneously a reflection at $2\theta \approx 39.4°$ close to both 121 and 102 orthorombic Mo_2C reflections (2θ = 39.41 and 39.52°, respectively) or to the 101 hexagonal Mo_2C reflection (2θ = 39.51°) was observed to appear (Figure 4.22). Comparing the XRD pattern acquired in the complete angular range before and after the carburization process, the reflection at $2\theta \approx 39.4°$ was the only evident change that could be ascribed to the formation of a new phase (Figure 4.23). Taking into account that the possible matching Mo_2C reflections listed above have the strongest (and second strongest in the case of the orthorombic), theoretical intensity within each phase, the unambiguous determination of the true crystallographic system of the supported carbide was not possible through XRD analysis.

In situ oxidation in the ETEM

In situ oxidation by water was investigated in a FEI Titan 80-300 TEM equipped with a differentially pumped environmental cell (described in Section 2). The Mo_2C/m-ZrO_2 sample was dry dispersed on a gold TEM grid and mounted on a Gatan inconel bulk heating holder. Upon sample loading and prior to the exposure to oxidative conditions, the sample was characterized by means of HRTEM and EELS analysis, in order to identify the formed carbide phase. EELS spectra were acquired in STEM mode (incident semi-angle α=13 mrad, collection semi-angle β=25.5 mrad) using a dispersion of 0.2 eV/channel in the energy range $180<\Delta E<589$ eV in order to include the molybdenum $M_{4,5}$, M_3, M_2 edges and the carbon and oxygen K edges.

As Figure 4.24a shows, exposed carbide nanoparticles could be observed in the Mo_2C/m-ZrO_2 catalyst synthesized in the *in situ* XRD setup. These appeared to have an overall more irregular morphology when compared to the larger and rounder supporting zirconia nanoparticles, a feature that allowed a straightforward identification of the carbide phase during TEM analysis. All Mo_2C nanoparticles analyzed by TEM in this work were observed to have a polycrystalline nature and, when possible, HRTEM

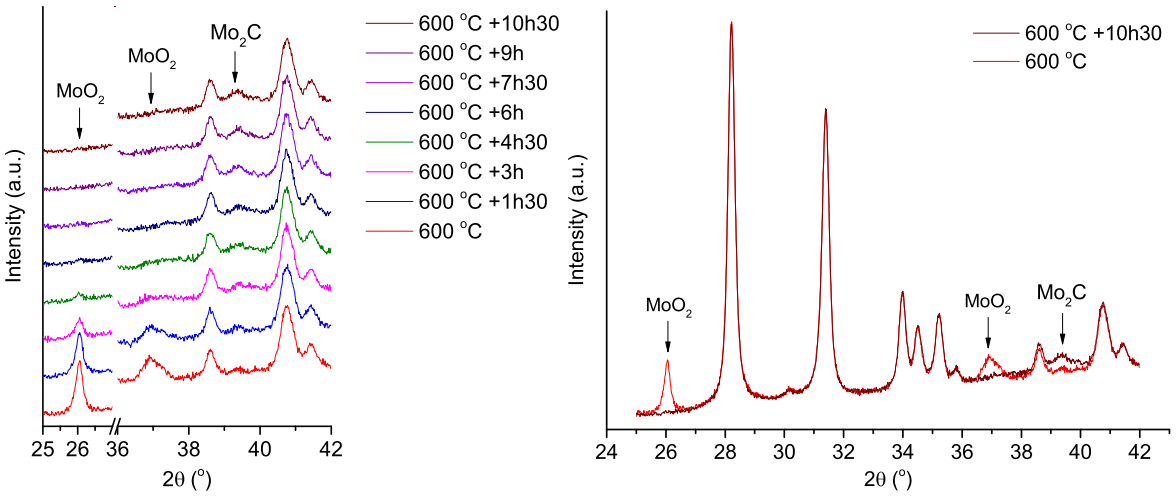

(a) During carburization **(b)** After carburization

Figure 4.22: Carburization step of the synthesis of Mo_2C/m-ZrO_2. **(a)** In situ XRD pattern recorded during carburization and **(b)** XRD pattern comparison of the sample at the first and last step of the carburization process.

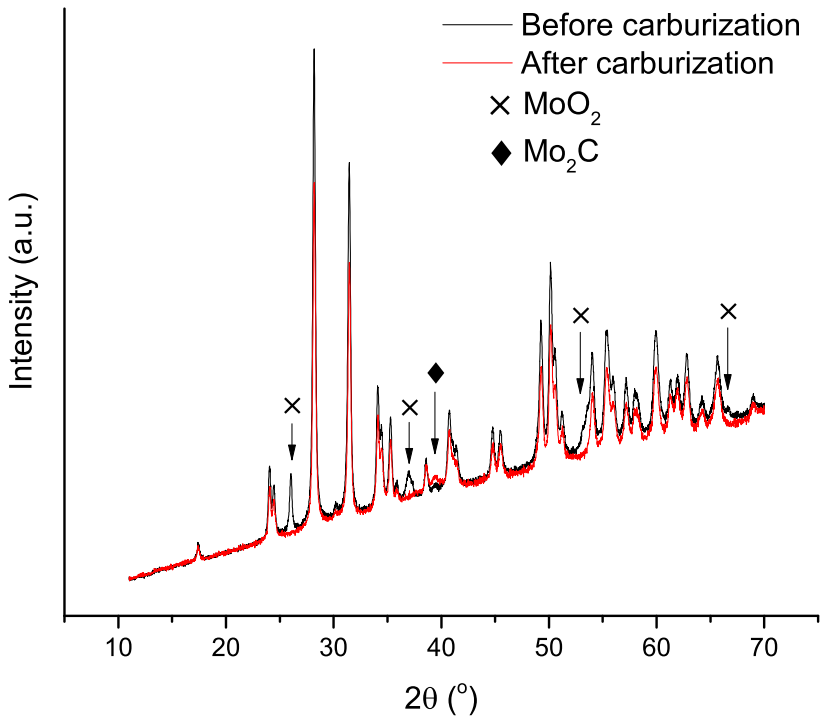

Figure 4.23: Comparison of the XRD patterns of the sample before and after carburization.

analysis was carried out to identify the phase of each crystallite. All nanoparticles analyzed could be matched to the hexagonal Mo_2C phase (see Figure 4.24b as an example). Moreover, STEM-EELS analysis carried out probing the same area used for HRTEM investigations revealed the presence of Mo and C elements, and showed similar edge shapes to what reported by Kuimalee *et al.* in their study of hexagonal Mo_2C [57] (Figure 4.24c).

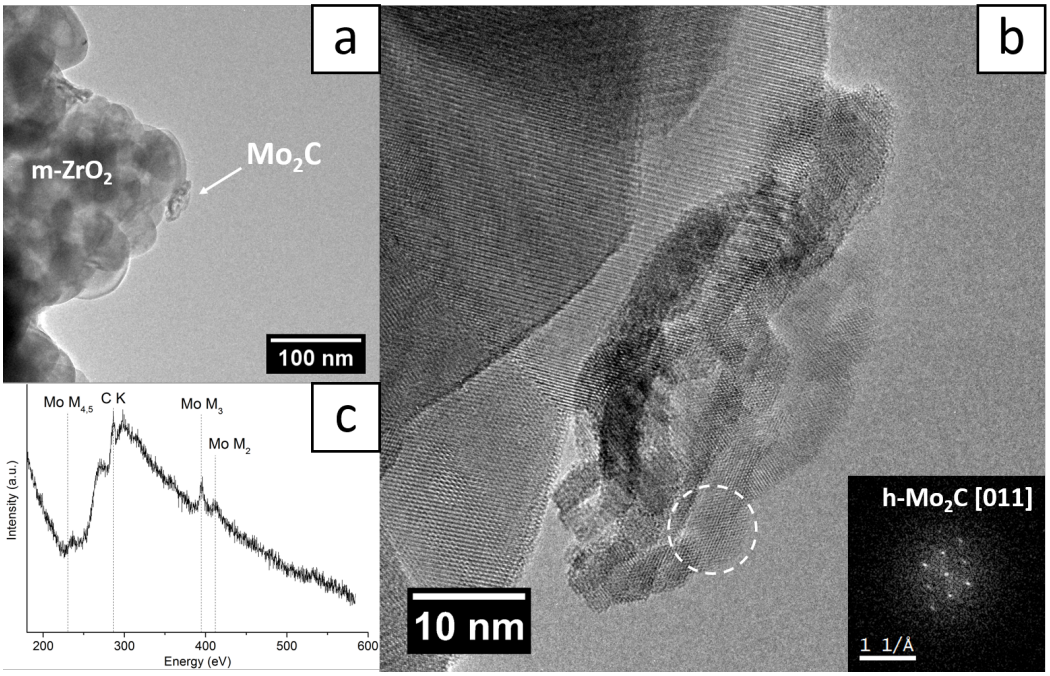

Figure 4.24: Transmission electron microscopy characterization of the Mo_2C/m-ZrO_2 catalyst. **(a)** Low magnification BFTEM micrograph of a region of the sample. **(b)** HRTEM micrograph of the carbide nanoparticle highlighted in (a). In the inset is shown the digital diffractogram of the dashed circle area. **(c)** Core-loss EELS spectrum of the dashed circle area highlighted in (b).

After the initial characterization, the electron beam was blanked and water vapor was introduced in the microscope through a leak valve. Upon reaching a stable pressure of p_{H_2O}=280 Pa, the temperature was raised to T=400 °C and the Mo_2C/m-ZrO_2 catalyst was held in the oxidative environment for 16h. These specific experimental conditions were chosen after a series of preliminary experiments revealing no substantial structural modifications of the carbide phase after up to 17h of exposure at T=300 °C to a similar water pressure. Furthermore, following experiments confirmed the stability of the supported Mo_2C after exposure to p_{H_2O}=280 Pa, T=400 °C for 1h, justifying the choice of longer reaction times at this specific temperature.

After 16h of water exposure, the heating was interrupted and the sample was let to cool down to room temperature in the water vapor environment. Post-treatment HRTEM analysis was carried out at p_{H_2O}=280 Pa in order to evaluate morphological and crystallographic changes from the initial state. The sample was cooled prior to the analysis in order to avoid induced structural modifications arising by the combined effect of the electron beam, high temperature and water environment. No post-treatment

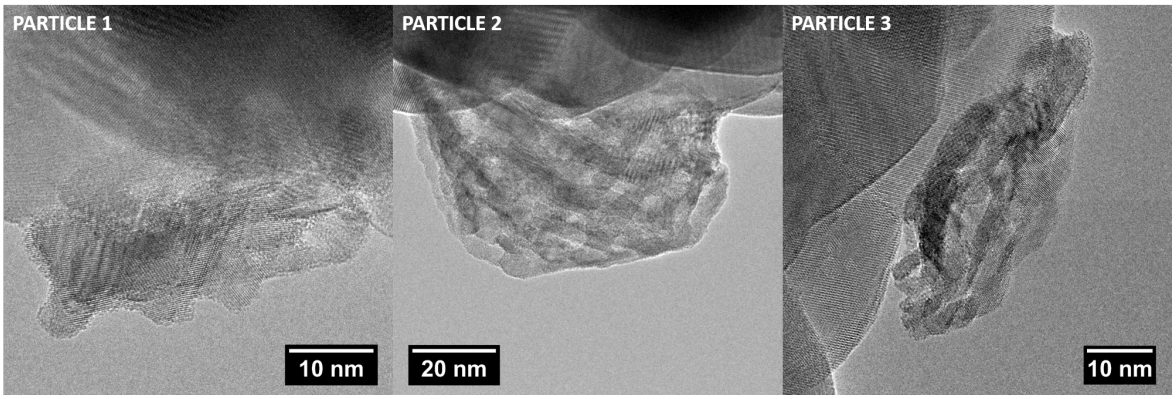

(a) Before water exposure

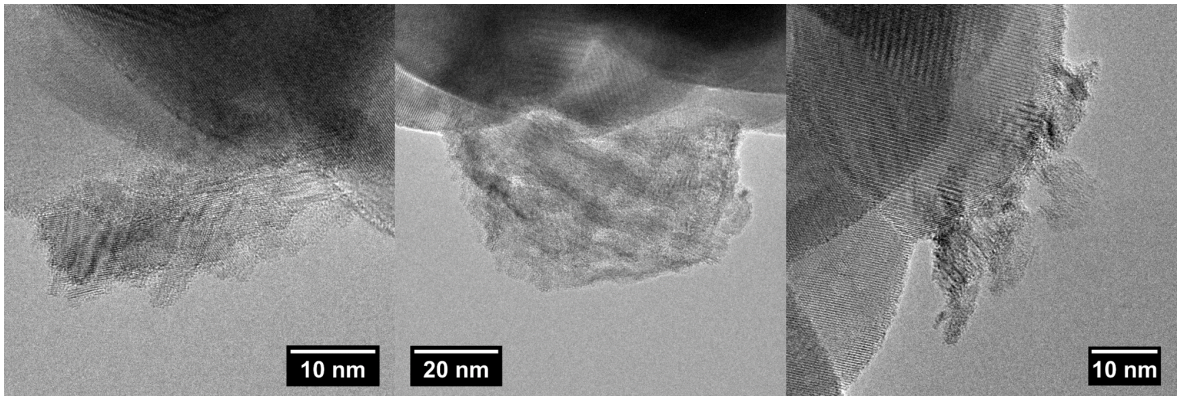

(b) After water exposure

Figure 4.25: BFTEM micrographs of three supported carbide particles of the Mo_2C/m-ZrO_2 catalyst **(a)** before and **(b)** after exposure to p_{H_2O}=280 Pa, T=400 °C for 16h. Micrographs were acquired at room temperature, in (a) vacuum and (b) at p_{H_2O}=280 Pa.

EELS analysis was carried out, as the oxygen signal detected would have been highly influenced by the presence of H_2O molecules in the sample environment.

As Figure 4.25 shows, treating the catalyst for 16h at T=400 °C in water vapor led to an overall morphology change of the supported carbide phase. After water exposure, all Mo_2C nanoparticles presented missing parts and generally more irregular contours. Mass loss was observed to be more severe for smaller/thinner nanoparticles (Particle 1 and 3 in Figure 4.25b). Post-treatment HRTEM analysis of the supported carbide phase revealed a partial loss of crystallinity, with amorphous regions coexisting with original Mo_2C structures (Figure 4.26).

As Mo_2C is expected to be stable in absence of oxidizing agents up to temperatures of 1200-1400 °C [58,59], the disappearance of portions of the carbide phase at T=400 °C observed by TEM analysis might be related to the formation of volatile $MoO_3 \cdot H_2O$ species. The tendency of metallic molybdenum and MoO_3 to sublimate at lower temperatures when exposed to a water-rich environment as compared to vacuum is a well known phenomenon [60–62], and in particular the volatility of MoO_3 powders at 600 °C was reported to increase by 17 times when adding 66 vol% of H_2O to the air environment [60]. Hence, the loss of the carbide phase might be ascribed to a two-step process

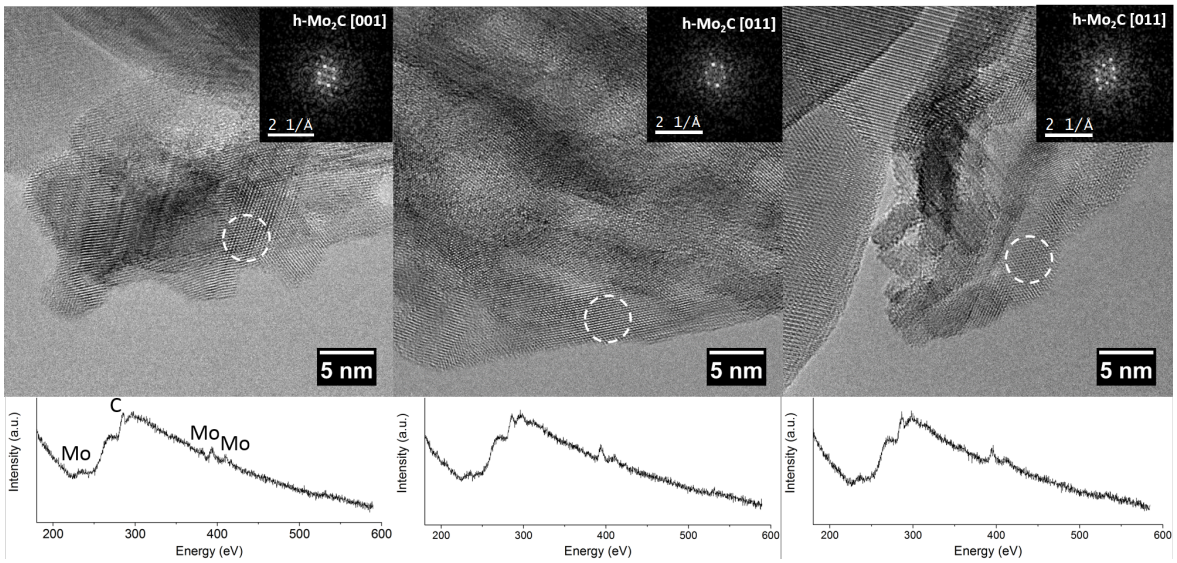

(a) Before water exposure

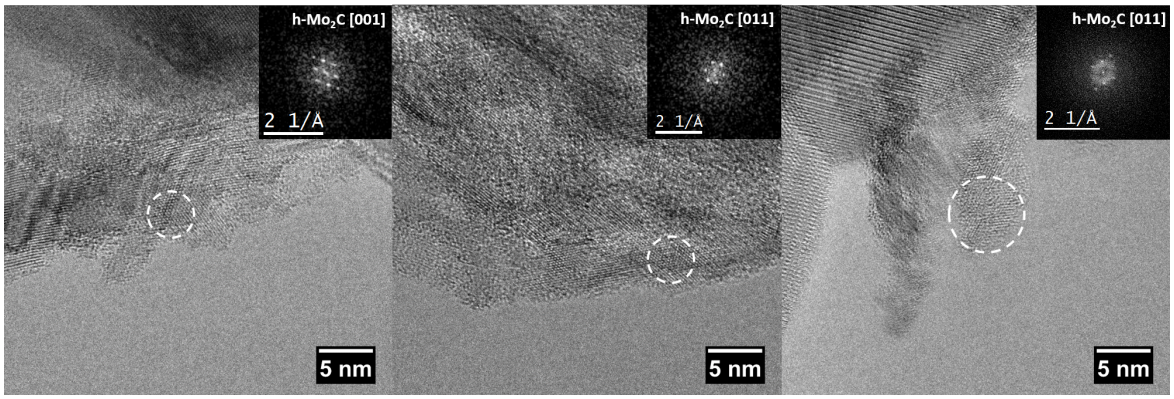

(b) After water exposure

Figure 4.26: HRTEM micrographs of three supported carbide particles of the Mo_2C/m-ZrO_2 catalyst **(a)** before and **(b)** after exposure to p_{H_2O}=280 Pa, T=400 °C for 16h. For each nanoparticle, the STEM-EELS spectrum and the digital diffractogram of the dashed circle region is given. Micrographs were acquired at room temperature, in (a) vacuum and (b) at p_{H_2O}=280 Pa. This figure is reproduced in an enlarged and more detailed version as Figure A.1 in Appendix A.

involving an initial oxidation of Mo_2C to a MoO_3 phase, and subsequent formation of the volatile oxyhydrate $MoO_3 \cdot H_2O$.

In the *in situ* synchrotron XRD aging of Mo_2C/ZrO_2 carried out by collaborators and briefly presented in Section 4.3, MoO_2 was reported as the product of the exposure of the carbide phase to a water-saturated feed of 5 vol% H_2 in He. However, in the ETEM experiment presented in this section, the formation of MoO_3 could not be considered unreasonable, as the lack of an H_2 feed would exclude the reduction of MoO_3 to MoO_2.

However, it is important to consider that although the sample was cooled down to room temperature after water exposure, the presented post-treatment TEM analysis

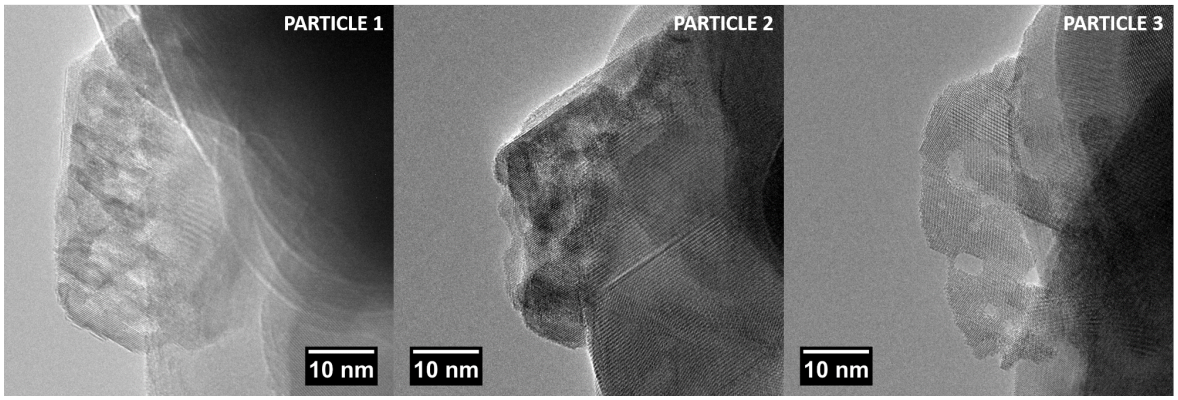

(a) Before water exposure

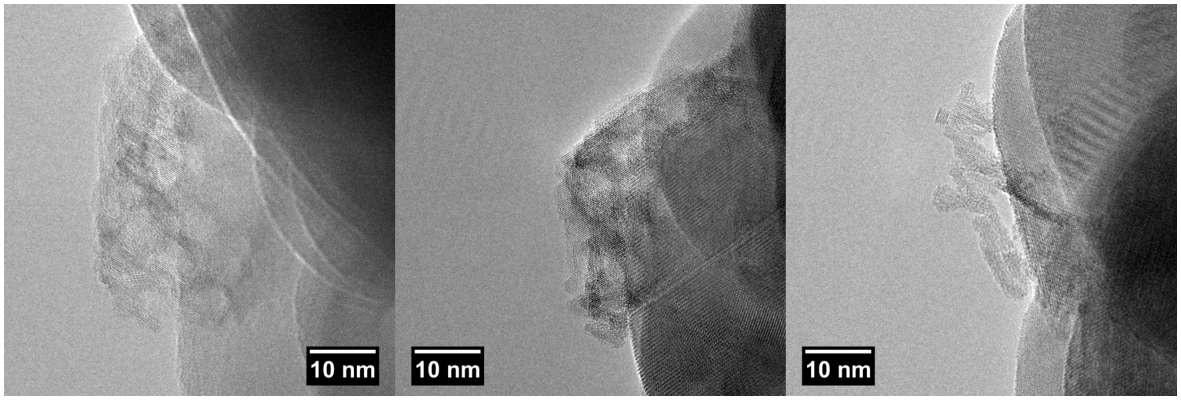

(b) After water exposure

Figure 4.27: BFTEM micrographs of three supported carbide particles of the Mo_2C/m-ZrO_2 catalyst **(a)** before and **(b)** after exposure to p_{H_2O}=280 Pa, T=400 °C for 16h. Micrographs were acquired in vacuum at room temperature.

was carried out keeping the sample in the water vapor environment, hence any structural modification arising from the exposure of the catalyst to the incident electron beam in presence of H_2O (such as electron beam-induced oxidation [63]) could not be excluded *a priori*. For this reason, the *in situ* oxidation experiment was repeated, and prior to post-treatment analysis the sample area was cooled down and pumped to a pressure p=$3.6 \cdot 10^{-4}$ Pa. In addition, this allowed to include STEM-EELS measurements of the water exposed sample, in order to provide a chemical analysis able to assess the presence of oxygen.

As Figure 4.27 shows, post-treatment analysis in vacuum revealed once more the disappearance of portions of the supported carbide phase, in agreement with observations made in water vapor. However, overall less amorphous regions were observed during HRTEM analysis, with larger carbide particles showing clear crystalline edges (Particle 1 and 2 in Figure 4.28). This could indicate that the presence of amorphous regions as observed in the previous experiment might have been the result of a beam effect, possibly a beam induced oxidation of the carbide phase to an amorphous molybdenum oxide.

Moreover, during acquisition of STEM-EELS spectra of the water exposed samples, the carbon K edge was observed to grow in intensity. This could be ascribed to the

formation of a growing carbon layer, typical of electron beam-induced carbon deposition processes [64]. This phenomenon was observed to occur exclusively when probing Mo_2C particles, and not the m-ZrO_2 support. HRTEM imaging after post-treatment STEM-EELS analysis confirmed the presence of an irregular amorphous layer covering the carbide particles (Figure 4.28c).

Considering that no beam induced carbon deposition was observed during pre-treatment STEM-EELS characterization, pristine Mo_2C can not be considered as the carbon source responsible for this effect. Carbon deposition might hence have occurred as the result of the interaction between the e-beam and a well dispersed carbon-containing phase coexisting with the crystalline Mo_2C. Possible candidates could be molybdenum oxycarbide or oxycarbohydride phases, as a weak oxygen signal was detected in the post-treatment STEM-EELS spectra (Particle 1 and 2 in Figure 4.28b). These phases have been reported as products of the partial carburization of MoO_3 based catalyst [50], and in the study presented in this thesis they might be formed as the result of a partial oxidation of the supported carbide phase.

Summary

The effect of water on the atomic structure and chemical composition of a Mo_2C/ZrO_2 catalysts at relevant temperatures for HDO and at 280 Pa was studied by a combination of *in situ* XRD and environmental TEM techniques. A low surface area sample, suitable for a reliable TEM analysis, was synthesized by decomposition and carburization of a supported precursor. The evolution of the crystalline phases during synthesis was followed in an *in situ* XRD setup. Exposure to water of the synthesized carbide samples in the ETEM resulted in the following observations:

1. After 16h at T=400 °C and p_{H_2O}=280 Pa portions of the supported carbide phase were observed to have disappeared, probably due to a mechanism involving oxidation of Mo_2C to MoO_3 and subsequent formation of volatile $MoO_3{\cdot}H_2O$ species.

2. The presence of a weak oxygen signal, together with the tendency for carbon growth were observed during STEM-EELS analysis of the post-treated carbide particles. This was ascribed to the interaction between the electron beam and a dispersed carbon-rich phase, most likely molybdenum oxycarbide or oxycarbohydride.

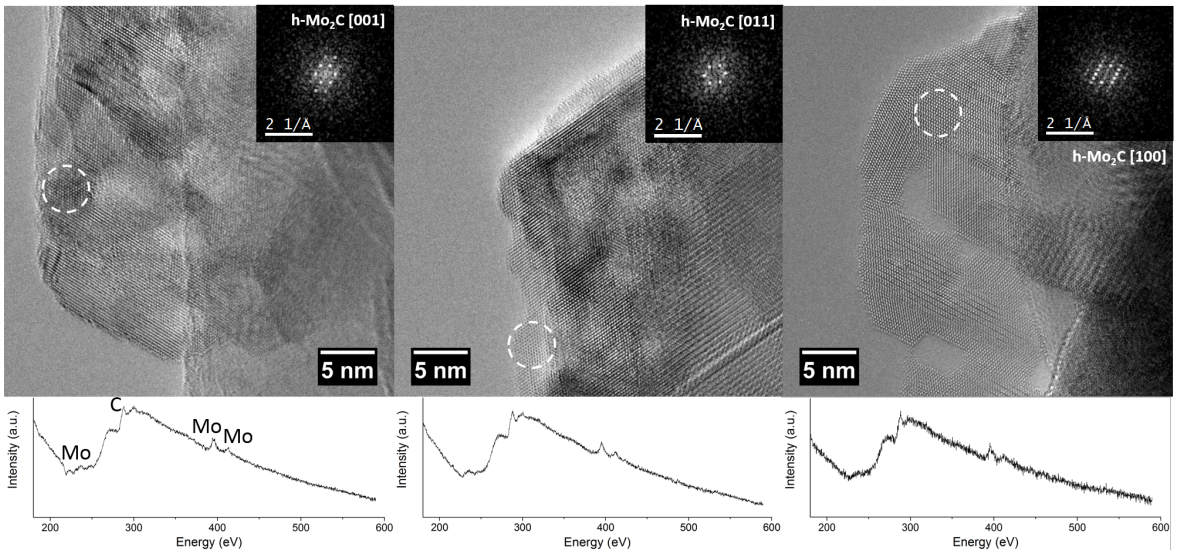

(a) Before water exposure

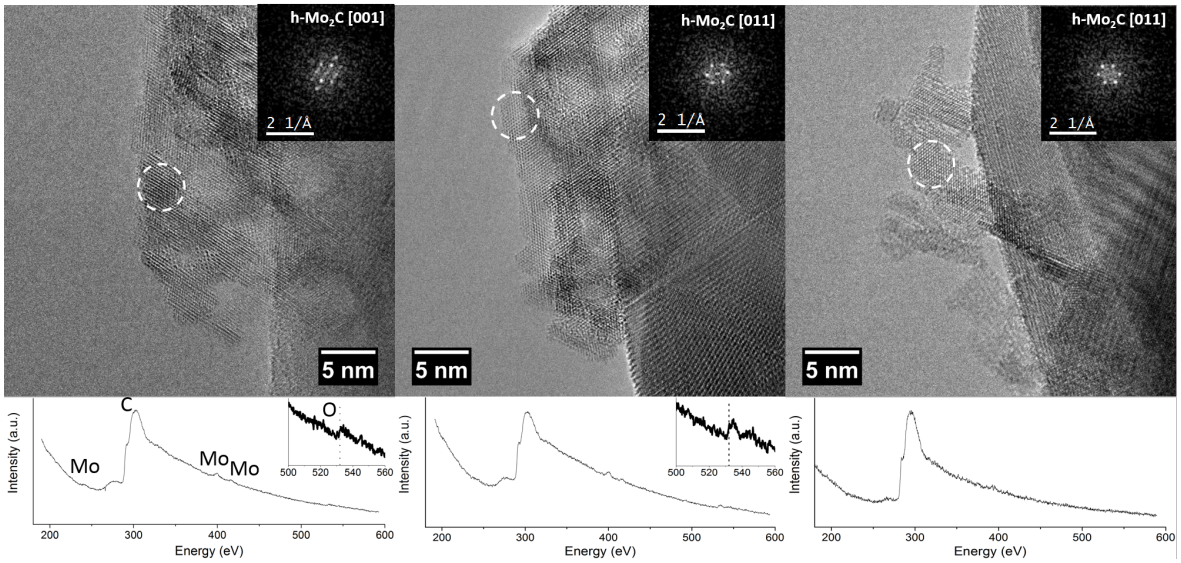

(b) After water exposure

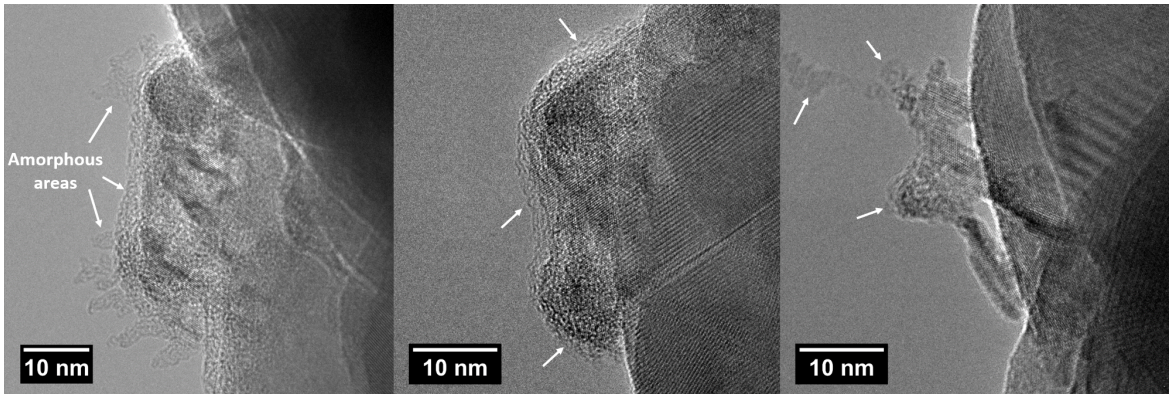

(c) After water exposure and STEM-EELS analysis

Figure 4.28: HRTEM micrographs of three supported carbide particles of the Mo_2C/m-ZrO_2 catalyst **(a)** before, **(b)** after exposure to p_{H_2O}=280 Pa, T=400 °C for 16h and **(c)** after post-treatment STEM-EELS analysis. For each nanoparticle, the STEM-EELS spectrum and the digital diffractogram of the dashed circle region is given. Micrographs were acquired in vacuum at room temperature. This figure is reproduced in an enlarged and more detailed version as Figure A.2 in Appendix A.

4.4 Ni-MoS_2/ZrO_2

HDO reaction mechanism

Co-MoS_2 and Ni-MoS_2 are known traditional hydrotreating catalyst and have been frequently tested for the HDO reaction [22]. In these catalysts, cobalt or nickel act as promoters of the MoS_2 structure, donating electrons to the molybdenum atoms in order to weaken the Mo-S bond and generate a sulphur vacancy site. These sites are active for HDO and other hydrotreating reactions such as hydrodesulfurization (HDS).

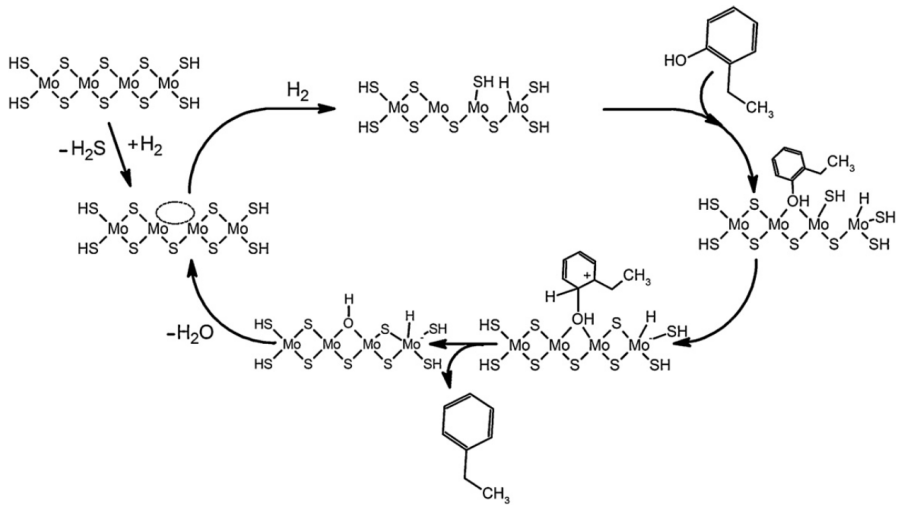

Figure 4.29: Proposed mechanism of HDO of 2-ethylphenol over a promoted sulfide catalysts. The dashed circle indicates the catalytically active vacancy site. Figure from [24].

Figure 4.29 depicts the fundamental steps of the mechanism describing the HDO of 2-ethylphenol over a promoted sulfide catalyst [65]. These can be summarized as:

1. The oxygen of the molecule is adsorbed on a edge vacancy site of a MoS_2 lamellar structure, activating the compound.

2. S-H species, generated by feeding H_2, enable proton donation from the sulfur to the attached molecule, forming a carbocation.

3. This can undergo direct C-O bond cleavage, forming the deoxygenated compound and leaving an -OH group on the surface of the catalyst.

4. The -OH group is finally removed in the formation of water.

Promotion by nickel has been indicated to be slightly superior to cobalt promotion [65] and in this work ZrO_2 was chosen once more as a support material in order to increase the dispersion of the Ni-MoS_2 active phase.

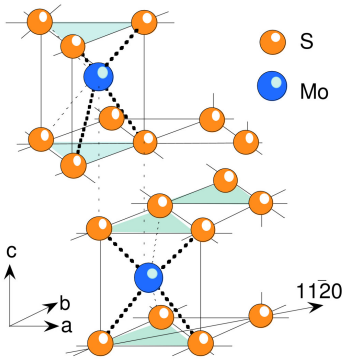

Figure 4.30: Structure of hexagonal MoS_2. Figure from [70].

Characterization of the as-synthesized catalyst

Catalyst synthesis is described in detail in [Paper2] and consists in a sequential impregnation of a molybdenum and nickel precursor separated by a drying step. The two metals are impregnated in order to reach a final loading of 15 wt% for Mo and 3 wt% for Ni. After impregnation, the catalyst is first calcined and then sulfided in dimethyl disulfide, in order to allow the formation of Ni-promoted MoS_2 structures.

From the description of the HDO mechanism given in the above section, it is clear that the synthesis of a MoS_2 phase rich in sulfur vacancies is of fundamental importance for achieving high deoxygenation activities. In order to assess the correct synthesis of the Ni-MoS_2 active phase and study its distribution on the zirconia support, a characterization approach based on electron microscopy and X-ray diffraction was used.

Structure of Ni-MoS_2 active phase

Due to their application in the hydrotreating of conventional fossil fuels, sulphide catalysts have been characterized by mean of a very broad range of techniques. Most of the articles found on literature [66–69] aim at explaining the influence of promoting species on the activity of supported and unsupported MoS_2 catalysts.

MoS_2 is a layered transition metal sulfide (LTMS) having a lamellar structure composed of S-Mo-S bonds ordered in a hexagonal array, forming layers stacked in the c direction. These are kept together by van der Waals forces and are characterized by a Mo layer distance of 0.62 nm (Figure 4.30). MoS_2 by itself is only moderately active [66] and, as already mentioned, the addition of cobalt or nickel promoters is necessary to achieve high catalytic conversions. The nature of the promotion effect has been the subject of many studies in the past and only after the early 1980s, EXAFS, Mössbauer and infrared techniques showed that Co (or Ni) atoms could replace part of the Mo atoms on the edge of MoS_2 layers, generating the so called Co-Mo-S (or Ni-Mo-S) phase [71–73]. More recent STM studies allowed the visualization of single-layer MoS_2 nanoclusters at the atomic scale [74] and consequently the identification of the exact position of promoter atoms in Co-Mo-S and Ni-Mo-S phases [75, 76].

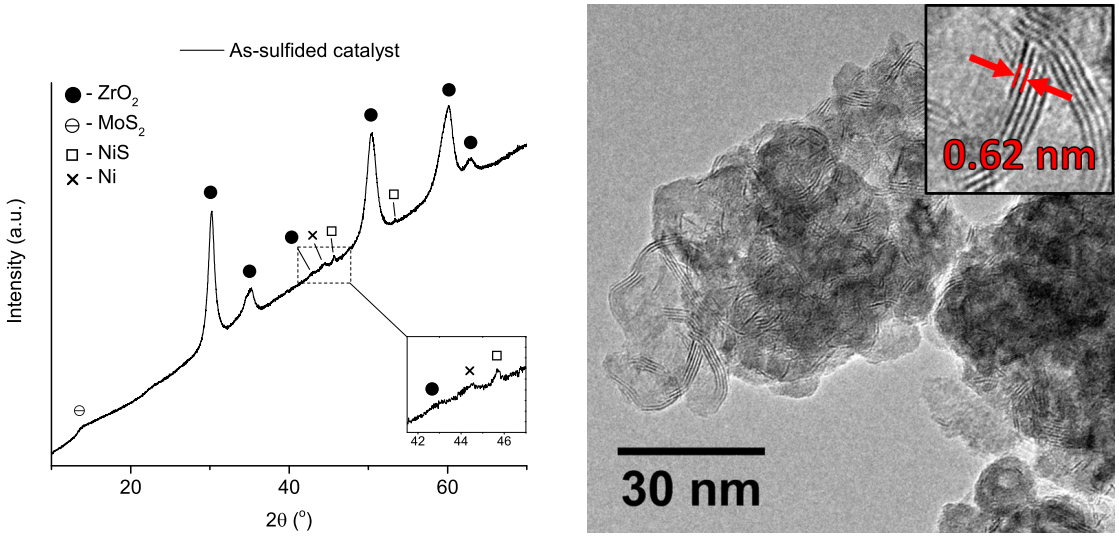

(a) XRD **(b)** BFTEM

Figure 4.31: Characterization of the as-synthesized Ni-MoS_2/ZrO_2 catalyst by **(a)** X-ray diffraction and **(b)** BFTEM imaging. Inset in (b) shows MoS_2 structures with characteristic interlayer distance of 0.62 nm. MoS_2 reference phase from [77].

Identification of the Ni-MoS_2 active phase

XRD measurements on the as-sulfided catalyst confirmed the presence of the tetragonal zirconia support and revealed minor reflections that could be indexed as hexagonal MoS_2, hexagonal NiS and cubic Ni phases (Figure 4.31a). The presence of crystalline Ni species is not surprising as they might represent leftovers from the synthesis procedure that have not been incorporated in the MoS_2 phase. The sulfidation of Mo oxide precursor species was confirmed by the identification of lamellar structures in BFTEM imaging, which are presenting an interlayer distance of 0.62 nm and matching the MoS_2 c stacking distance (Figure 4.31b).

Due to its peculiar layered arrangement, identification of MoS_2 structures oriented perpendicular to the stacking direction by BFTEM is straightforward on thin, peripheral areas of the Ni-MoS_2/ZrO_2 sample. On the contrary, when investigating thicker areas, mass-thickness contrast was found to be insufficient, similarly to the case of Ni/ZrO_2 catalysts (Section 4.2).

The elongated and curved morphology of MoS_2 structures as observed by BFTEM could be at the base of the overall poor XRD signal associated to the sulfide phase. Indeed, the exclusive presence of the 0002 reflection associated to the c stacking direction could be explained when considering that crystallographic periodicity at the origin of diffraction signal could be better maintained in the direction perpendicular rather than tangential to the bending of the lamellar structures (Figure 4.32). Furthermore the broadening of this reflection could be ascribed to the variation of the interlamellar distance in presence of tight curvatures.

In order to univocally identify the active phase of the catalyst and overcome the BFTEM imaging limitations, STEM-EDX elemental maps of the as-sulfided sample

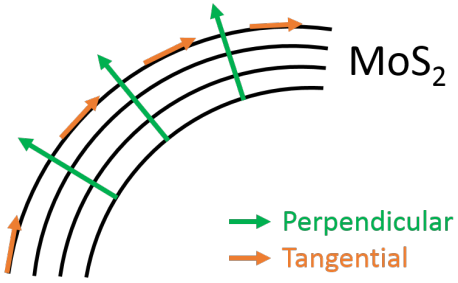

Figure 4.32: Representation of the projected MoS_2 layered structure with (green) perpendicular and (orange) tangential generic periodicity directions.

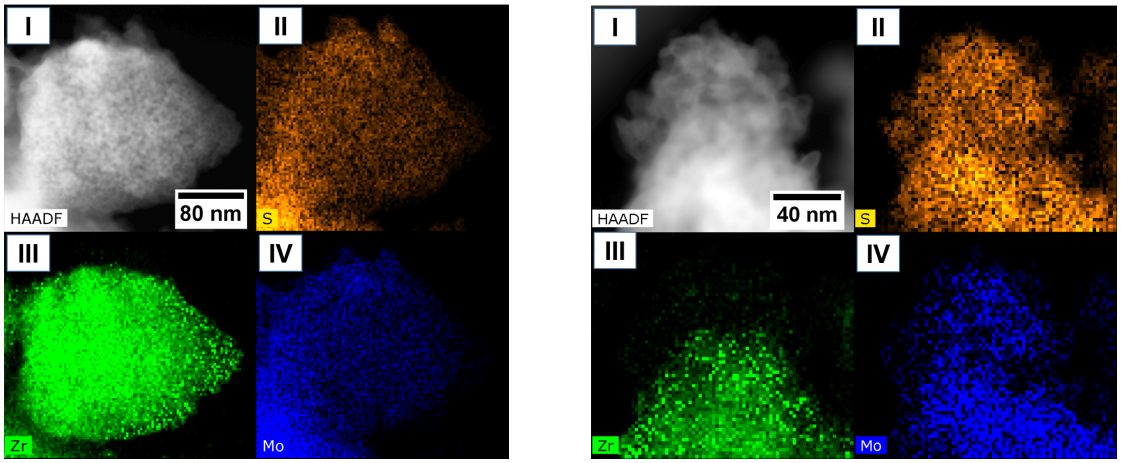

(a) General sulfide coverage **(b)** Areas richer in sulfide phase

Figure 4.33: HAADF-STEM imaging and EDX mapping of Ni-MoS_2/ZrO_2 as-sulfided catalysts presenting **(a)** general MoS_2 coverage and **(b)** areas richer in sulfide phase. Sub-image (I): STEM-HAADF overview of the site in analysis. Sub-images (II) sulfur, (III) zirconium and (IV) molybdenum EDX elemental distributions.

were acquired, as in the case of Ni/ZrO_2. Two characteristic areas of the catalyst are shown in Figure 4.33. In both cases elemental maps II, III and IV can be compared in order to evaluate the spatial distribution of S, Zr and Mo elements, respectively. Overall, MoS_2 structures were found covering the zirconia support homogeneously (Figure 4.33a), forming in some cases enriched areas of higher density (Figure 4.33b).

Further STEM-EDX investigations were carried out in order to study the distribution of nickel species in the as-sulfided catalyst. As Figure 4.34 shows, EDX analysis of a portion of the sample containing MoS_2 structure confirmed the presence of nickel (Figure 4.34a,c), thus suggesting the effective incorporation of this promoter species in the layered sulfide and the formation of the desired Ni-MoS_2 active phase. Furthermore, Ni-containing nanoparticles were identified (Figure 4.34b), in accordance with the results of XRD analysis (Figure 4.31a).

In conclusion, TEM and XRD characterization of the as-sulfided sample allowed the identification of Ni-MoS_2 structures dispersed on the ZrO_2 support, confirming the successful synthesis of the intended catalyst phase.

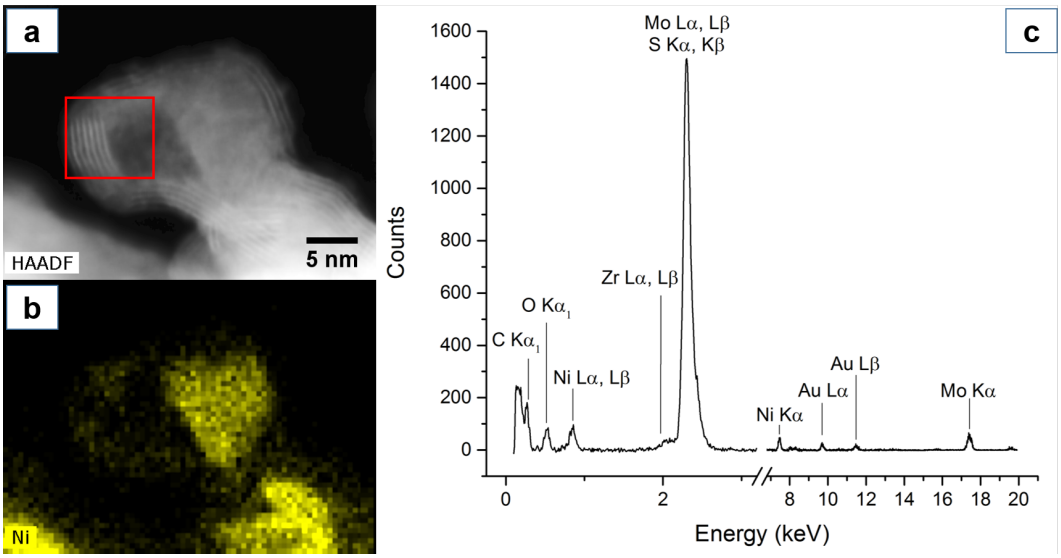

Figure 4.34: Nickel distribution in the as-sulfided catalyst. **(a)** HAADF-STEM micrograph of the portion of the sample analyzed. In red, an area containing MoS_2 structures is highlighted. **(b)** Nickel EDX elemental distribution. **(c)** EDX spectrum of the area highlighted in (a).

Effect of H_2S and water in the feed

As already discussed in the previous sections, deactivation of reduced metal type HDO catalysts can occur following different mechanisms such as coking, poisoning, sintering and competitive adsorption. In the case of Ni/ZrO_2, sulfur in particular has been proven to be a severe poison, capable of converting the active metallic nickel into an inactive NiS phase.

The effect of sulfur on HDO over sulfide catalysts is, however, far from clear. Though proved to inhibit the overall HDO activity [78], small quantities of H_2S are believed to be necessary during HDO to maintain the sulfidation level of the catalyst. Water or high quantities of oxygenated compounds (characteristic of bio-oil), may indeed lead during operation to a partial reoxidation of the sulfide phase, compromising the activity of the catalyst [79]. Contrary to HDS, where H_2S is formed as direct product of the desulfurization of the S-rich feed, bio-oil may not contain enough sulfur compounds capable of acting as resulfiding agents for the catalyst, thus requiring an H_2S co-feed.

Figures 4.35 shows the stability of the catalyst during HDO of phenol and 1-octanol when co-feeding 0.3 vol% 1-octanethiol or 2 vol% DMDS. The first case is representative of the type and concentration of sulfur typical of real bio-oil [36] and the second corresponds to an H_2S concentration almost 30 times higher. As Figure 4.35b shows, the addition of 2 vol% DMDS resulted in a significant increase in the stability of the catalyst when compared to the 1-octanethiol case (Figure 4.35a). In a further experiment (Figure 4.36), 33 vol% H_2O was added to the 2 vol% DMDS co-feed, resulting in a loss of the catalyst's deoxygenation activity and stability when compared to the test with the sole sulfur co-feed (Figure 4.35b).

Hence, activity tests showed that an insufficient sulfur co-feed and the addition of

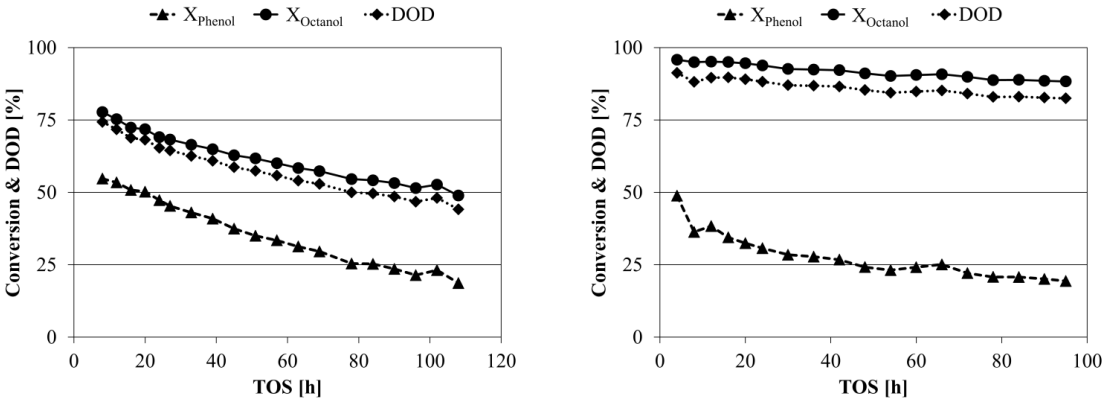

(a) 0.3% 1-octanethiol in the feed **(b)** 2% DMDS in the feed

Figure 4.35: Stability of Ni-MoS_2/ZrO_2. (a) shows conversions of 1-octanol and phenol in a case with 0.3 vol% 1-octanethiol in the feed and (b) in a case with 2 vol% DMDS in the feed. T = 280°C, P = 100 bar. Figures from [Paper2]

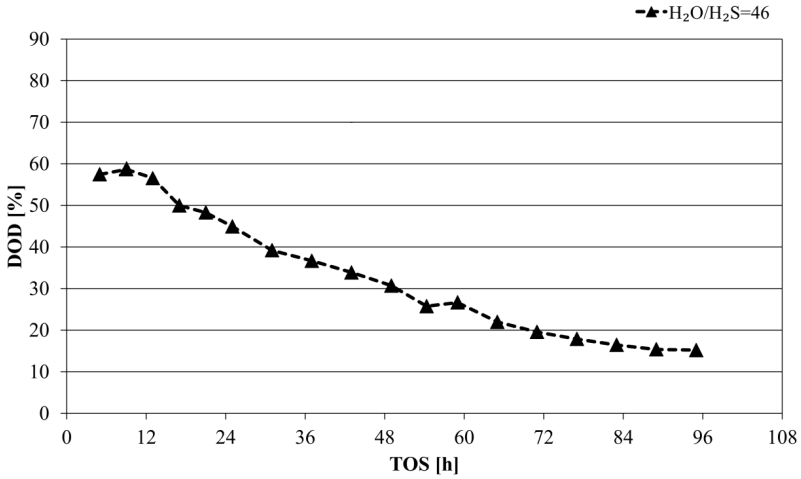

Figure 4.36: DOD of a phenol/1-octanol feed when co-feeding 33 vol% H_2O and 2 vol% DMDS, corresponding to a H_2O/H_2S ratio of 46. T = 280°C, P = 100 bar. Figure adapted from [Paper2]

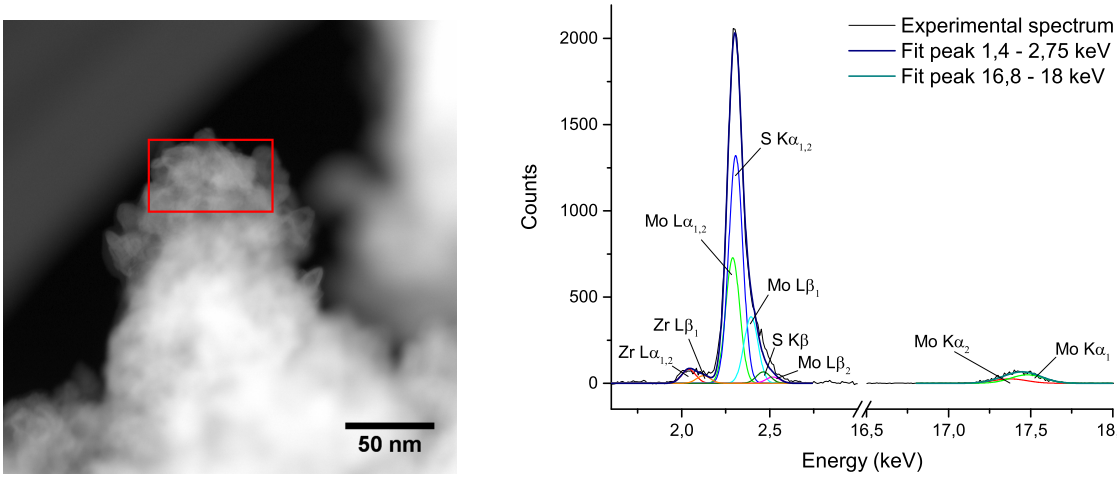

(a) Selected area **(b)** EDX spectrum and peak deconvolution

Figure 4.37: Mo K$\alpha_{1,2}$ and S K$\alpha_{1,2}$ X-ray signal measurement. **(a)** HAADF-STEM micrograph of a typical Ni-MoS_2 area. In red the portion used for analysis. **(b)** EDX spectrum from the area highlighted in (a) and Gaussian peak deconvolution. Sections of the spectrum not containing relevant peak for the analysis have been omitted.

water are responsible for the long term deactivation of Ni-MoS_2/ZrO_2 catalyst. In order to increase the understanding on the mechanisms leading to this activity and stability loss, a STEM-EDX based approach has been used to analyze the modifications of the spent catalyst active phase.

For each sample analyzed, the ratio between Mo K$\alpha_{1,2}$ and S K$\alpha_{1,2}$ X-ray emission peaks from Ni-MoS_2 areas was calculated by multiple Gaussian fit of portions of the EDX spectrum. This ratio is representative of the relative Mo/S concentration and can therefore indicate whether loss of sulfur from the active phase took place during HDO activity. It is important to stress that this analysis gives only qualitative results, and the calculated Mo/S X-ray emission ratio does not represent a proper relative concentration value (wt% or at%) of the two elements. A quantitative analysis has been attempted using the Bruker Esprit software, resulting however in final Mo/S wt% ratios with an unreasonably large associated experimental error. The source of this error remain at present unknown, due to the impossibility of investigating the quantification procedure carried out by the commercial software in detail. For this reason, a manual data treatment allowing a realistic estimate of experimental error bars was preferred, although giving qualitative results.

For each analyzed catalyst, EDX spectra of Ni-MoS_2 rich areas were collected. Due to the partial overlap of Mo, S and Zr experimental peaks in the energy range 1.9 – 2.7 keV, regions with free hanging active phase were preferred, in order to minimize the Zr contribution in the spectrum. An example of an area selected for the analysis and the resulting (partial) EDX spectrum is given in Figure 4.37.

After background removal by bremsstrahlung fit, Mo K$\alpha_{1,2}$ and S K $\alpha_{1,2}$ peak areas were extracted by Gaussian fit of Zr L$\alpha_{1,2}$, Zr Lβ_1, Mo L$\alpha_{1,2}$, S K$\alpha_{1,2}$, Mo Lβ_1, S Kβ, Mo Lβ_2 peaks in the energy range 1.4 – 2.75 keV and Mo Kα_2, Mo Kα_1 in the range

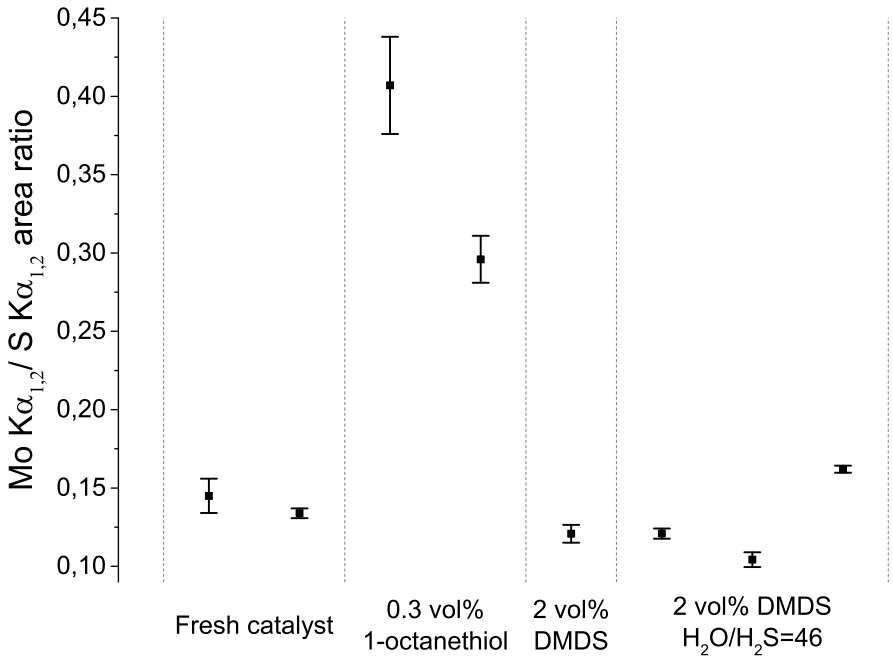

Figure 4.38: Mo K$\alpha_{1,2}$/S K$\alpha_{1,2}$ X-ray emission peaks ratios for freshly sulfided Ni-MoS_2/ZrO_2 catalysts and catalyst tested with different sources of sulfur in the feed and varying H_2O/H_2S feed ratios. Multiple data points per catalyst represent measurements carried out in different areas of the same sample.

16,8 – 18 keV. A detailed explanation of the procedure used for the Gaussian fit and the error estimation is given in Appendix B.

As Figure 4.38 shows, active phase regions of the catalyst co-fed with 0.3 vol% 1-octanethiol presented the highest Mo/S X-ray emission ratio, indicating a more severe loss of sulfur during catalytic testing. On the other hand, co-feeding 2 vol% DMDS resulted in a ratio similar to the fresh as-sulfided catalyst, meaning that consistently less sulfur is lost from the sample when co-feeding higher quantities of H_2S. Mo/S X-ray emission ratios for the water exposed sample were found to be similar to the fresh catalyst, indicating that the deactivation in this case might occur following a different mechanism than depletion of the sulfide phase.

Inductively coupled plasma optical emission spectroscopy (ICP-OES) measurements carried out by collaborators (see [Paper2]) are in agreement with STEM-EDX analysis, showing a loss of sulfur for the 0.3 vol% 1-octanethiol exposed catalyst and similar sulfur levels for both fresh, and water exposed samples. Additionally, ICP-OES revealed that the tendency for carbon formation was low for all tested sulfide catalyst (< 4 wt%), supporting the assumption that the different deactivation behavior observed were not related to different carbon deposition rates, as seen for example for Ni/ZrO_2.

The stability of bulk MoS_2 phase towards oxidation by water is furthermore supported by thermodynamic calculations, indicating a positive ΔG for all relevant reactions at the experimental conditions of the activity tests (see [Paper2]). However, although bulk oxidation of the sulfide phase should not readily take place in presence of water, DFT calculations by Badawi *et al.* [79] showed that sulfur-oxygen exchanges

are possible in the outer layer of MoS_2 structures when $H_2O/H_2S > 40$ and T = 350 °C. This exchange would be responsible for the modification of the electronic properties of the sulfide edge sites, consequently compromising the activity and stability of the catalyst.

Summary

Ni-MoS_2/ZrO_2 sulfide catalysts were synthesized and tested for the HDO of phenol in a high pressure flow reactor. A combination of XRD and TEM techniques was used to assess the goodness of the synthesis procedure and the formation of the desired Ni-promoted active phase, crucial for reaching high deoxygenation activity. Moreover, the effect of H_2S and water in the feed was studied by a combination of STEM-EDX, catalytic data and complementary ICP-OES measurements, resulting in:

1. Addition of an extra H_2S co-feed (2 vol% DMDS) allowed to maintain the initial level of sulfur in the catalyst active phase during operation. This led to an overall higher catalyst activity and stability when compared to the case of co-feeding lower amounts of H_2S (0.3 vol% 1-octanethiol), corresponding to the amount of sulfur naturally present in bio-oil.

2. Addition of water in the feed resulted in the deactivation of the catalyst. A mechanism involving the depletion of sulfur from the active phase could be excluded. DFT calculations suggests that S-O exchanges might occur at the edges of MoS_2 slabs, modifying the electronic properties of the catalyst's active sites.

4.5 Conclusion

The characterization work carried out on Ni/ZrO_2, Mo_2C/ZrO_2 and Ni-MoS_2/ZrO_2 presented in this chapter provides a clear example of the potential and uniqueness of electron microscopy as a tool for studying the synthesis and deactivation of a catalytic system.

Synthesis is an important step in the design of a catalyst and the knowledge of the structural and chemical properties of the active phase is crucial for the interpretation of activity and stability data. In this perspective, the electron microscopy based approach presented in this study allowed the direct visualization of Ni-MoS_2/ZrO_2 active phase and confirmed the incorporation of nickel in the MoS_2 structures of the catalyst, confirming the essential Ni promotion. In the case of Mo_2C/ZrO_2 investigations, an *in situ* XRD technique was used to synthesize a catalyst suitable for ETEM investigation and the use of a combination of HRTEM and STEM-EELS techniques allowed to univocally identify the crystallographic and chemical nature of the supported carbide phase. Furthermore, as shown for the case of Ni/ZrO_2, variations of the synthesis procedure could lead to great modification of activity and stability of the studied catalyst. Once more, electron microscopy allowed to overcome the limitations of complementary techniques such as XRD, enabling the direct analysis of the supported nickel particles and giving invaluable insights in determining the correlation between Ni particle size and activity tests.

Concerning deactivation, this study showed how an HDO catalyst can loose activity following different mechanisms such as coking, sintering or poisoning. Contrary to other characterization techniques providing results on the average structure and composition of a sample, electron microscopy allowed both a "semi-average" (SEM-EDX) and more local (BFTEM, HRTEM, STEM-EELS and STEM-EDX) analysis of the deactivated catalyst, increasing the understanding on the mechanisms behind the deactivation of the active phase during operation. This allowed, for example, to assess the persistence of different poisoning species in Ni/ZrO_2 catalysts and determine their effect on the active supported Ni particles. Sulfur and potassium were found to permanently deactivate the catalyst by respectively forming an inactive NiS phase and absorbing on uncoordinated nickel sites. Chlorine poisoning was found instead to be partially reversible, however it caused sintering of the supported nickel particles. In the case of Mo_2C/ZrO_2 catalysts, a combination of HRTEM and STEM-EELS techniques was used to investigate the effect of water exposure to individual supported carbide particles, revealing the disappearance of part of the Mo_2C phase probably due to the formation of volatile molybdenum hydroxide species. Furthermore, as showed for the case of Ni-MoS_2/ZrO_2, STEM-EDX mapping allowed to investigate the depletion of sulfur locally in the sulfide structures of the catalyst upon exposure to different H_2S concentrations and water in the feed. This once more provided fundamental insights in the deactivation mechanisms of this catalytic system, suggesting that a bulk sulfur depletion could take place when co-feeding insufficient amounts of H_2S and a S-O exchange, limited to the edges of MoS_2 slabs, could occur upon exposure to H_2O.

Electron microscopy hence proved to be an essential tool for studying the synthesis and deactivation of a catalytic system. In the next chapter, the focus will be shifted to the understanding of the mechanisms at the base of the activity of a catalyst during operation, with an emphasis on the role of environmental electron microscopy.

CHAPTER 5

Activity of silver during the catalyzed oxidation of soot

As it has been shown previously, electron microscopy proved to be an invaluable resource for increasing the understanding of the mechanisms behind the synthesis and deactivation processes of a catalytic system.

In this chapter, the emphasis will be moved to the potential and uniqueness of this technique in the characterization of the central stage of the catalyst's life: operation. For this purpose, a combination of *ex situ* and *in situ* electron microscopy has been used to investigate the peculiar behavior of silver nanoparticles as a catalyst for soot oxidation. Sample preparation and catalytic activity experiments have been carried out by Assistant Professor Jakob Munkholt Christensen (DTU Kemiteknik), and will be briefly described. For a more extensive description of the setup used and procedures please refer to the appended [Paper3].

5.1 Introduction

Soot particles emitted from the exhaust of diesel vehicles are likely to cause lung cancer and to affect the local climate and air quality [80, 81]. For that reason these particles are typically filtrated with the aid of a ceramic filter installed in the vehicles exhaust system [82, 83]. However, the filter needs periodic regenerations in which its temperature is increased and the soot is burned away. The growing back pressure due to the soot deposit and the temperature rise required for the regeneration procedure lead to an increase of fuel consumption [84]. In order to limit this increase, it is desirable to develop soot oxidation catalysts that can lower the regeneration temperature, ideally to the temperature of the exhaust gases during normal vehicle operation.

The heterogeneously catalyzed soot oxidation is a gas/solid/solid interaction in which the contact between soot and catalyst plays a very important role in the catalytic activity [85]. Two contact conditions are generally defined: loose contact and tight contact. In tests where soot and catalyst are crushed together (so-called tight contact), carbon oxidation has been reported to occur at a significantly lower temperature, than

when soot and catalyst are stirred together with a spatula (so-called loose contact) [85]. Several experiments in real diesel soot filters have indicated the presence of both contact types [86–88], confirming the need of a more deep understanding of the two contact conditions and their implications on the mechanisms behind the catalyzed soot oxidation reaction.

In terms of what generally constitutes a good soot oxidation catalyst, both the surface area [89, 90] and the strength of the oxygen-catalyst bond are fundamental for the final catalytic activity [91]. Metallic silver has been reported to activate oxygen by dissociative adsorption already at low temperature [92, 93], and silver-based catalysts are well known to exhibit high activity for catalytic soot oxidation [94–96]. In particular, it is interesting that soot oxidation at relatively low temperatures has been achieved in loose contact with silver [95, 96].

It is therefore relevant to investigate the behavior of silver nanoparticles at the conditions of catalytic soot oxidation. In this chapter, a combination of *ex situ* and *in situ* transmission electron microscopy techniques will be used to characterize soot:silver mixtures in different contact conditions before, during and after the oxidation reaction. Environmental TEM observations of the oxidation reaction will be coupled with flow reactor tests carried out by collaborators at DTU Kemiteknik in order to gain fundamental understandings on the mechanism at the base of the catalyst activity.

5.2 Soot/catalyst contact

As already introduced, both loose and tight contact conditions have been reported to take place in real diesel soot filters, justifying the need for a description of the relative distribution of silver and soot in the two cases. In order to emulate the different contact conditions, approximately 2 mg of certified soot (NIST: "SRM 2975 Diesel Particulate Matter") and commercial silver nanoparticles in a ratio of 1:5 (wt:wt) were stirred together with a spatula (loose contact) or crushed together in an agate mortar (tight contact). Mixtures were dry dispersed on lacey carbon supported copper grids and analyzed by means of BFTEM and STEM techniques. Contrary to the case of HDO catalysts presented in the previous chapter, silver and soot were found to differ enough in mass and morphology to describe their distribution relying on mass-thickness and Z contrast. Figure 5.1 illustrates the contact between the solids in the two contact conditions. In loose contact silver was observed to form big agglomerates sharing a limited number of contact points with the soot mass. In tight contact silver particles were instead observed to be more dispersed, and most of the surface of the catalyst appears to have an interface to the soot.

STEM analysis of the two samples revealed the presence of small nanoparticles of approximately 2-5 nm diameter in both contact modes (Figure 5.2). These were mostly observed in the near vicinity of big silver clusters and were found as well intermixed with portions of the soot distant from the main Ag agglomerates. STEM-EDX point analysis measurements carried out on a single particle (Figure 5.3a) and on areas containing a group of few particles (Figure 5.3b) revealed in both cases the presence of the elements silver, carbon and sulfur. Considering carbon and sulfur as the main components of the

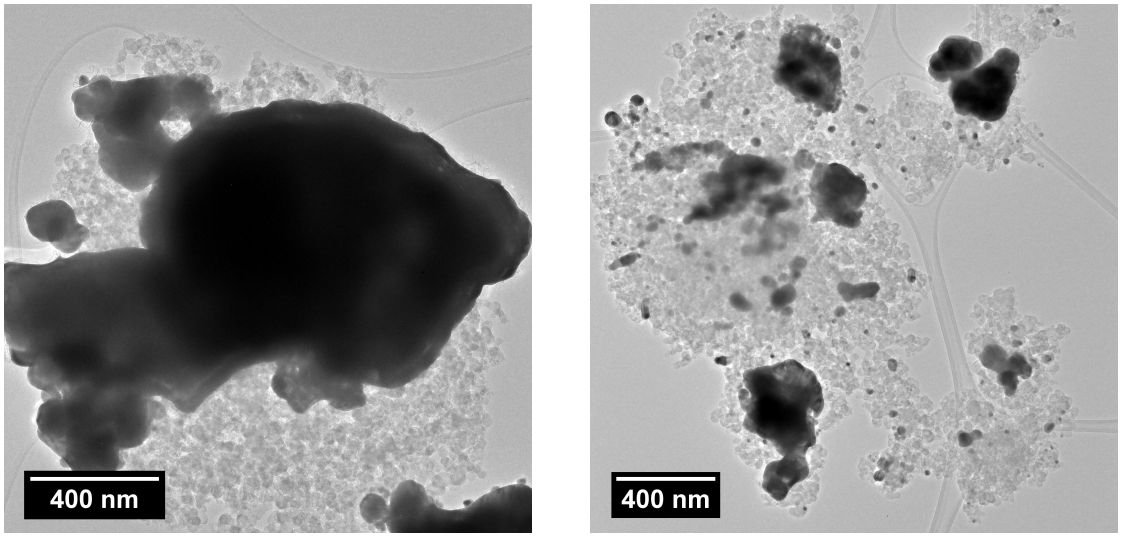

(a) Loose contact **(b)** Tight contact

Figure 5.1: Bright Field TEM micrograph of a soot:silver (1:5 wt:wt) mixture in **(a)** loose contact and **(b)** tight contact condition. Darker agglomerates represent the silver fraction of the specimen while the lighter porous structure is the soot. In both micrographs the lacey carbon support holding the specimen is visible.

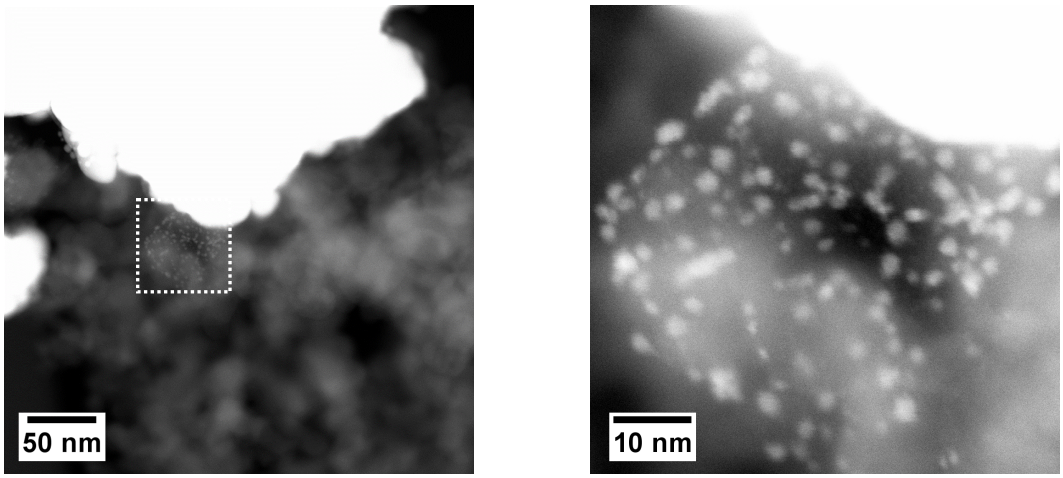

(a) Overview **(b)** Detail

Figure 5.2: **(a)** STEM micrograph of a soot:silver (1:5 wt:wt) mixture in loose contact mode. A group of small nanoparticles (white dashed box) close to a silver agglomerate is highlighted. **(b)** Close-up on the particle area. Contrast has been enhanced in order to better visualize the soot underlying the catalyst.

soot fraction [97], the small nanoparticles identified by STEM might represent a finely divided fraction of the silver catalyst. The copper signal in the spectrum originated from the TEM grid and the observed sodium might be a part of the ash in the soot.

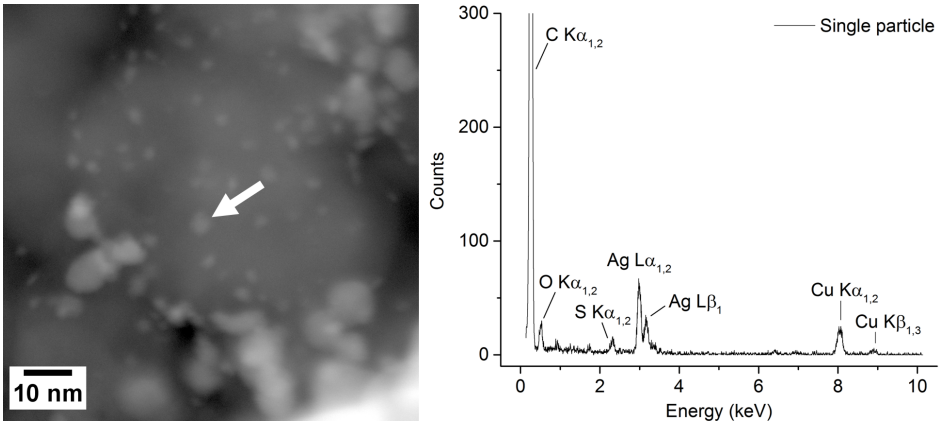

(a) Single particle analysis

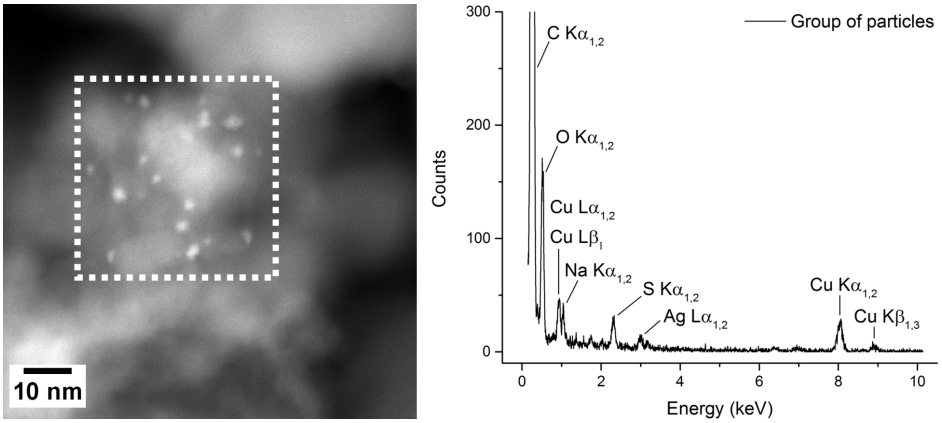

(b) Group particles analysis

Figure 5.3: STEM micrograph (left) and STEM-EDX spectrum (right) of **(a)** a silver single particle and **(b)** a group of silver particles. Graphical elements in white indicate the origin of the EDX signal on the sample.

5.3 Activity in catalytic oxidation

The catalytic activity of Ag for soot oxidation was measured carrying out a temperature programmed oxidation (TPO) in a flow reactor setup, where the CO and CO_2 concentrations in the effluent gas products were analyzed using a calibrated IR analyzer. The reactor was fed with 1 NL/min flow of 10.2 vol% O_2 in N_2 and the temperature was ramped from 25 to 750 °C at a rate of 11 °C/min.

Figure 5.4 shows the carbon oxidation rate as a function of temperature for pure soot, and for soot mixed with Ag in tight or loose contact. The silver catalyst exhibited high activity for soot oxidation, with tight contact mixtures showing a maximumin in the oxidation rate roughly 75 °C earlier than loose contact mixtures. The sharp peak in the oxidation rate at a temperature of 325 °C was not due to soot oxidation, but occurred because the commercial silver sample contained minor amounts of polyvinylpyrrolidone (PVP) added as a stabilizer/dispersant. Further experiments confirmed that oxidation of this polymer in absence of soot occurs in a sharp peak just above 300 °C (see Supplementary Information of [Paper3], appended to this thesis). In a rerun experiment, where the spent silver sample was mixed again with soot in

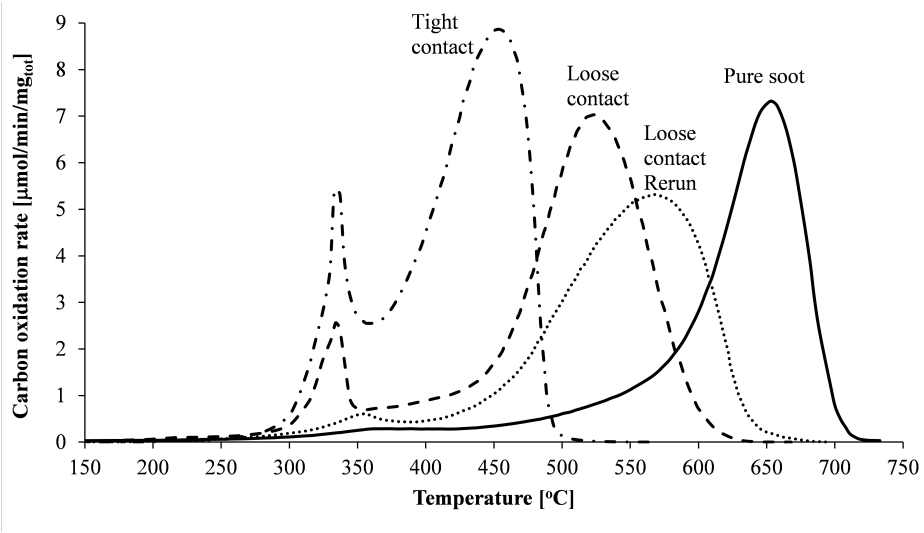

Figure 5.4: The rate of carbon oxidation (normalized by the total, initial mass of carbon) as a function of temperature in tight or loose contact with soot. Experimental conditions: soot:silver = 1:5 wt:wt, ramp = 11 °C/min, 1 NL/min, 10.2 vol% O_2 in N_2. Figure from [Paper3].

loose contact, the activity was observed to decrease, with the maximal oxidation rate now appearing approximately 50 °C later than in the original loose contact condition. However, the spent silver catalyst was observed to retain significant activity, being able to oxidize most of the soot 100 °C earlier than in the non-catalyzed experiment ("Loose contact rerun" in Figure 5.4).

Hence, the contact condition between soot and silver was found to have a great influence on the temperature of maximal carbon oxidation rate. In order to improve the understanding of the catalytic behavior of metallic silver, *in situ* TPO of soot:silver mixture was carried out in an environmental TEM, allowing a direct visualization of the oxidation reaction.

5.4 *In situ* ETEM studies of catalytic oxidation

The soot:silver mixtures were dry dispersed on the surface of MEMS thermal EMheater-chips (DENSsolutions) with no carbon support film and then mounted in an SH30 heating holder (DENSsolutions). The use of MEMS thermal chips minimizes the thermomechanical sample drift occurring during temperature ramping (Section 2.4) and consequently enabling the record of oxidation time lapses. The samples were exposed to 300 Pa O_2 and heated in the temperature range 150 – 854 °C at the same rate of flow reactor TPO experiments (11 °C/min). Micrographs of the oxidation reaction are acquired every 25 seconds and finally combined together to form playable time-lapses of 8 frames per second ([Movie1] and [Movie2] in the Supporting Information of this thesis).

Loose contact

Figure 5.5 shows four key frames representing soot oxidation in the ETEM in the loose contact condition. As [Movie1] shows, between 25 and 280 °C no evident changes in soot or Ag morphology were observed (Figure 5.5a). As the temperature increased from 280 to 472 °C, silver particles began to coalesce, forming larger round-shaped agglomerates (Figure 5.5b). At 500 °C coalesced silver agglomerates were observed to be mobile, moving on the soot agglomerate ("soot cake") and actively oxidizing the soot particles. Soot oxidation at the Ag/C interface could be visually confirmed by the disappearance of soot particles in contact with silver. The mobility was estimated visually to be maximal around 700 °C (Figure 5.5c) and oxidation was reported to end at about 760 °C, when all the soot was consumed and the silver had coalesced to a single particle (Figure 5.5d).

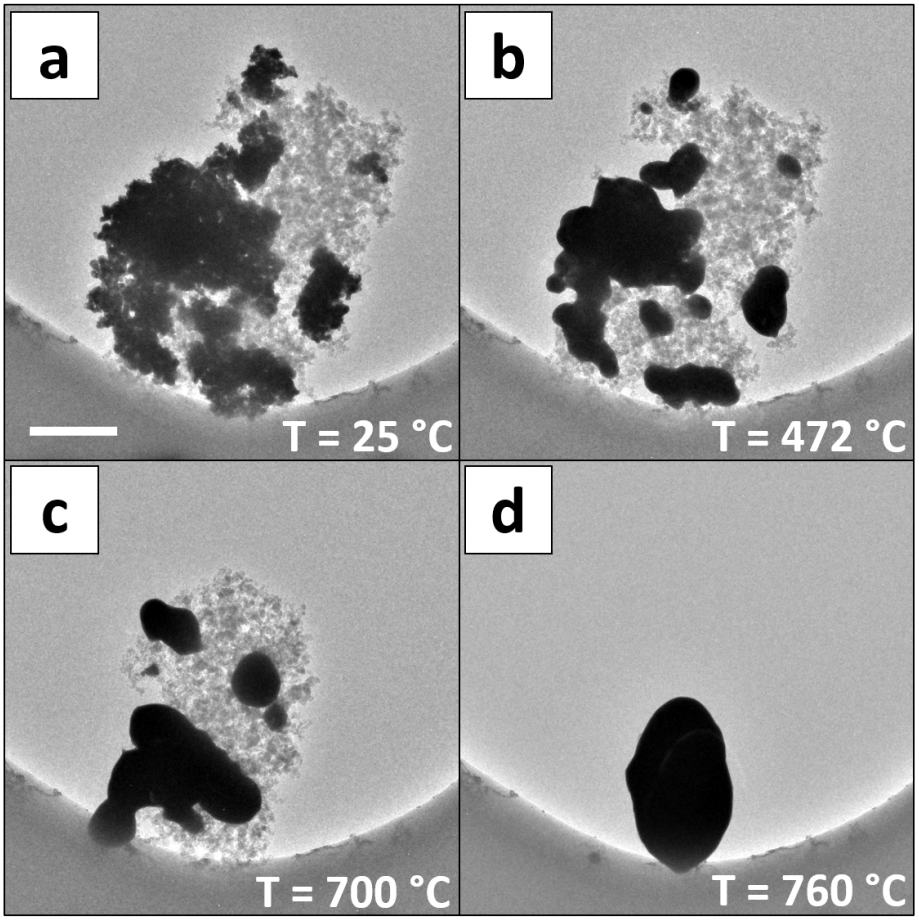

Figure 5.5: BFTEM micrographs of *in situ* soot oxidation in the ETEM in loose contact condition showing **(a)** initial distribution and morphology of silver and soot, **(b)** coalescence of silver particles, **(c)** mobility of coalesced silver agglomerates over the soot cake and **(d)** final silver agglomeration. Scalebar is 500 nm.

Tight contact

Similarly to what has been presented in the previous paragraph for loose contact, the four steps of *in situ* soot oxidation in the tight contact condition are summarized in Figure 5.6. As [Movie2] shows, in the temperature range 25-250 °C no obvious changes in soot or Ag morphology were observed, except for the collapse of part of the soot structure on the right hand side of the specimen area (Figure 5.6a). Between 250 and 338 °C silver particles coalesced forming round agglomerates. Silver coalescence was observed to occur approximately 30 °C earlier compared to the loose contact condition due to the presence in the sample of smaller particles - naturally requiring lower temperatures for initiating the coalescence process. Starting from T=342 °C the small silver particle groups exhibited high mobility over the soot cake (Figure 5.6b). Oxidation activity by silver particles could be again identified by disappearance of soot. Silver mobility was estimated to be maximal around 526 °C (Figure 5.6c). Around 700 °C soot oxidation was observed to be complete (Figure 5.6d).

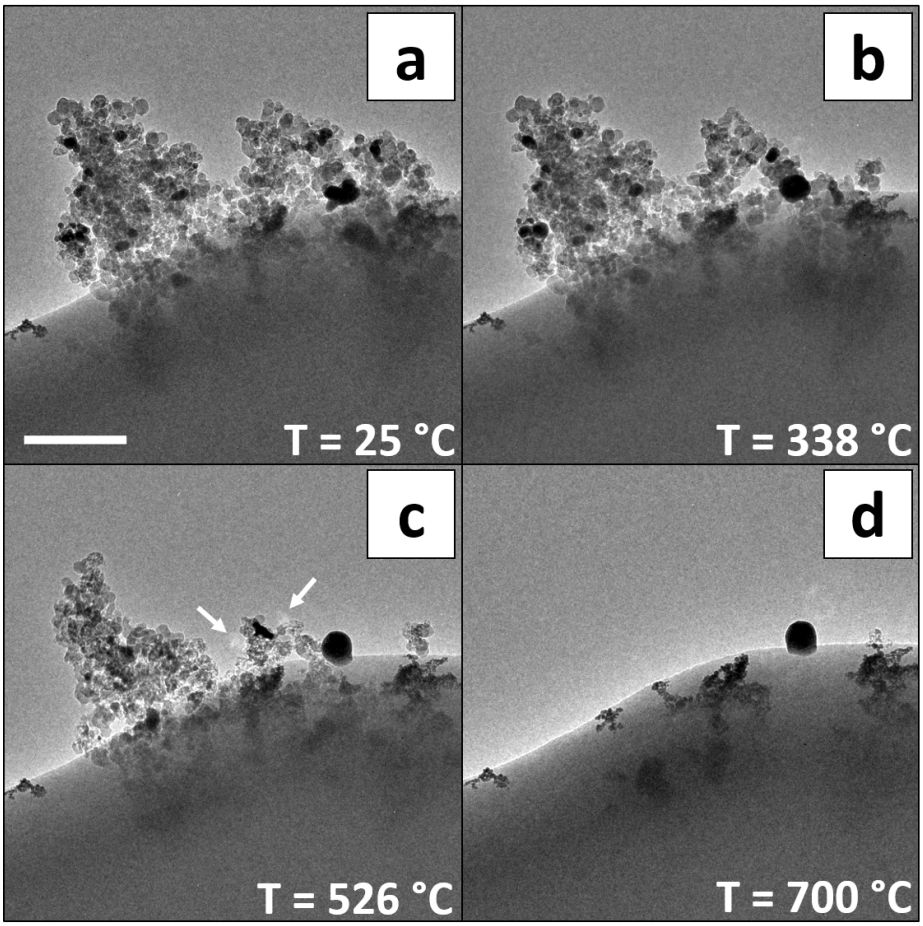

Figure 5.6: BFTEM micrographs of in situ soot oxidation in the ETEM in tight contact condition showing **(a)** initial distribution and morphology of silver and soot, **(b)** coalescence of silver particles, **(c)** mobility of coalesced silver agglomerates over the soot cake and **(d)** final silver agglomeration. White arrows indicate reflections typical of crystalline materials in BFTEM imaging. Scalebar is 300 nm.

Origin of silver mobility and its implications on catalytic activity

Previous reports in literature proved that the oxidation of graphite single crystals can be effectively catalyzed by a two-step mechanism involving the mobility of metallic nanoparticles [98, 99]. At 500 °C in a 670 Pa O_2 atmosphere, platinum nanoparticles were found to initially penetrate the graphite basal plane to produce pits. Upon temperature increase to 735 °C the particles were reported to move parallel to the graphite surface, digging relatively straight channels with sudden change of direction by 60 and 120° [98]. In a similar experiment, between 327 – 577 °C and in an atmosphere of 4.5 – 13 Pa O_2, silver nanoparticles deposited on graphene were reported to catalytically remove carbon atoms, producing channels aligned parallel to the <100> graphene directions [100]. This channeling effect could be explained by taking the adhesion energy between the metal particle and the carbon edge atoms in contact with it into consideration. This adhesion has been ascribed to van der Waal forces at the metal/carbon interface [99], although chemical bonding cannot be completely excluded. In DFT calculations Pizzocchero *et al.* [101] did observe a bonding between the edge of graphene and silver. During oxidation, the temperature is high enough to enhance the mobility of silver atoms and cause wetting of the graphite surface. As carbon atoms are removed by catalytic oxidation, these attractive forces at the interface pull the silver particle along with the reaction front causing the particle to move. The straightness and preferential orientation of the channels would then arise from the anisotropic reactivity of the oxidation reaction along different lattice directions, as seen in both graphite and graphene oxidation, where channels were found to be oriented parallel to the <100> directions.

Silver particle motion on an amorphous and 3-dimensional structure like soot is not expected to follow any preferential direction, but rather to reflect the local variations of the Ag-C interface due to soot morphology. As shown in Section 5.4 and summarized in Table 5.1 the onset of silver mobility and the mobility peak temperatures remain very dependent on the initial contact, although silver was found to start coalescing at approximately the same temperature for both loose and tight contact.

Table 5.1: Temperature (in °C) onsets and ranges for silver sintering, mobility peak and end of soot oxidation as observed from ETEM experiments.

	Loose contact	**Tight contact**
Coalescence	280-472	250-338
Mobility onset	500	342
Maximal mobility	700	526
Complete soot oxidation	760	700

As shown by *in situ* oxidation experiments, mobility of silver in the tight contact condition was found to occur at consistently lower temperature than in the loose contact condition. In loose contact, silver particles in larger clusters are kept together by the Ag-Ag cohesive energy from large agglomerates in contact with the soot cake (Figure 5.7a). Upon temperature increase, silver particles start to coalesce forming round

agglomerates (Figure 5.7b). Silver was observed to maintain a partially crystalline state after coalescence phase and throughout the rest of the *in situ* oxidation experiment for both contact modes. This was confirmed by the report of typical BFTEM diffraction reflections from moving silver particles (Figure 5.6) and the acquisition of time lapsed electron diffraction patterns during additional in situ oxidation experiments (Appendix C). As the temperature rises, silver layers situated at the edge of the coalesced agglomerates have sufficient energy to overcome the internal Ag-Ag cohesive energy and start wetting the soot surface, causing a local deformation of the agglomerate (Figure 5.7c). When the temperature is high enough, catalytic carbon oxidation occurs and the attractive forces between silver and soot will maintain the contact between silver and the progressing oxidation front, causing a net movement of the Ag agglomerate (Figure 5.7d).

The local geometry of the silver/soot interface can greatly influence the magnitude of the attractive forces. In extreme cases, wetting can cause portions of silver agglomerates to deform to the point where separation occurs and smaller silver particles released from the main Ag agglomerate start to move on the soot cake (Figure 5.8).

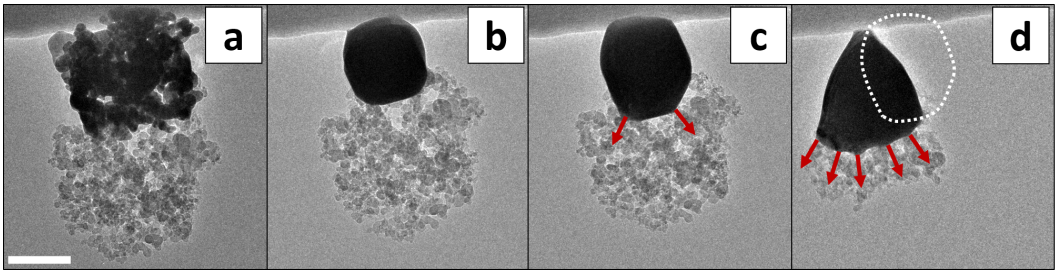

Figure 5.7: Wetting and movement of a silver agglomerate during *in situ* oxidation of soot:silver mixture in loose contact condition. BFTEM micrographs shows **(a)** initial agglomeration and morphology of silver and soot, **(b)** coalescence of silver particles, **(c)** initial deformation of coalesced silver agglomerate due to capillary forces and **(d)** movement of silver agglomerate. Arrows in red indicate the direction of deformation of the silver agglomerate. The previous position of the silver agglomerate as observed in (c) is highlighted in subfigure (d) with a dashed white line. Scalebar is 200 nm.

In the case of tight contact, where the oxidation occurs at a lower temperature, the silver is present as smaller agglomerates (or isolated silver particles), and not only is the carbon/silver interface greater than in the loose contact case, but the mobility of an isolated silver particle is also not restricted by the same Ag-Ag cohesive energy as a silver particle within a larger cluster. It is hence natural that the tight contact mixture exhibits mobility at lower temperatures compared to loose contact in complete consistency with the lower oxidation temperature.

Ag mobility thus plays a key role in the catalyzed oxidation of soot by constantly ensuring the presence of a silver-carbon-oxygen reactive interface. This reciprocal relationship between oxidation and mobility was verified in an *in situ* control experiment, wherein a soot:silver mixture in tight contact mode did not show any mobility effect when heated in absence of oxygen (in vacuum), thus confirming that soot oxidation is necessary for mobility to take place (Figure 5.9).

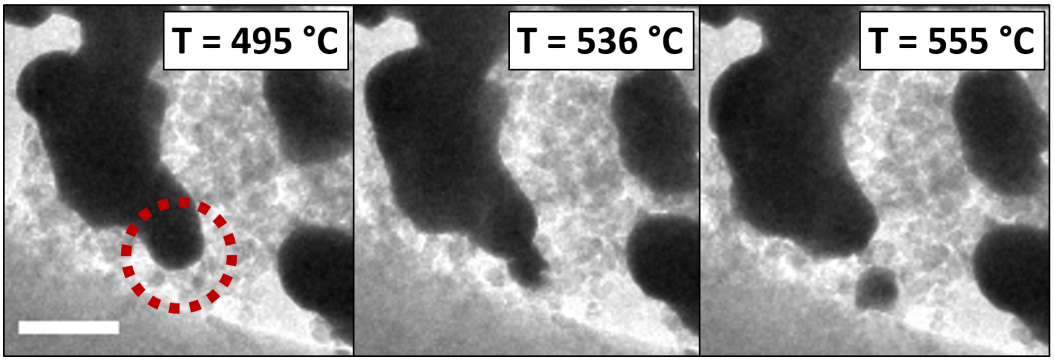

Figure 5.8: BFTEM micrographs showing the detachment of a small portion of silver from a bigger agglomerate during *in situ* oxidation of soot:silver mixture in loose contact condition. Scalebar is 200 nm.

The oxidation temperature differences observed in the flow reactor experiments for soot:silver mixtures in loose and tight contact conditions (Section 5.3, Table 5.2), could then be ascribed to the different temperatures required to trigger the mobility of silver for the two different contact conditions. In tight contact, small silver particles requires lower temperatures to start moving and actively oxidize the soot cake while being moved by van der Waal forces. Vice-versa, in loose contact, higher temperatures are needed in order for van der Waal forces to overcome the silver agglomerates internal Ag-Ag cohesive energy and initiate oxidative mobility.

Table 5.2: Peak and ending temperatures (in °C) of soot oxidation as observed from activity measurements (Section 5.3).

	Loose contact	**Tight contact**
Carbon oxidation rate peak	520	450
Complete soot oxidation	625	500

5.5 Pressure gap and relevance of the ETEM *in situ* studies

In this study, ETEM experiments at a comparatively low oxygen pressure were used to explain catalytic activity results in the flow reactor tests with a partial pressure representative for real diesel vehicle exhaust. However, a pressure gap of two orders of magnitude divides the two experimental setups, and its effect should be investigated in order to assess the relevance of the ETEM studies presented.

For this purpose, a flow reactor TPO of a soot:silver mixture in tight contact has been carried out until the temperature reached 450 °C, approximately 10 °C after the maximal carbon oxidation rate, and rapidly interrupted by stopping the oxygen feed and cooling down the system. The sample was extracted from the setup and a portion of it was dry dispersed on a conventional TEM copper grid with lacey carbon support and imaged in the TEM (Figure 5.10).

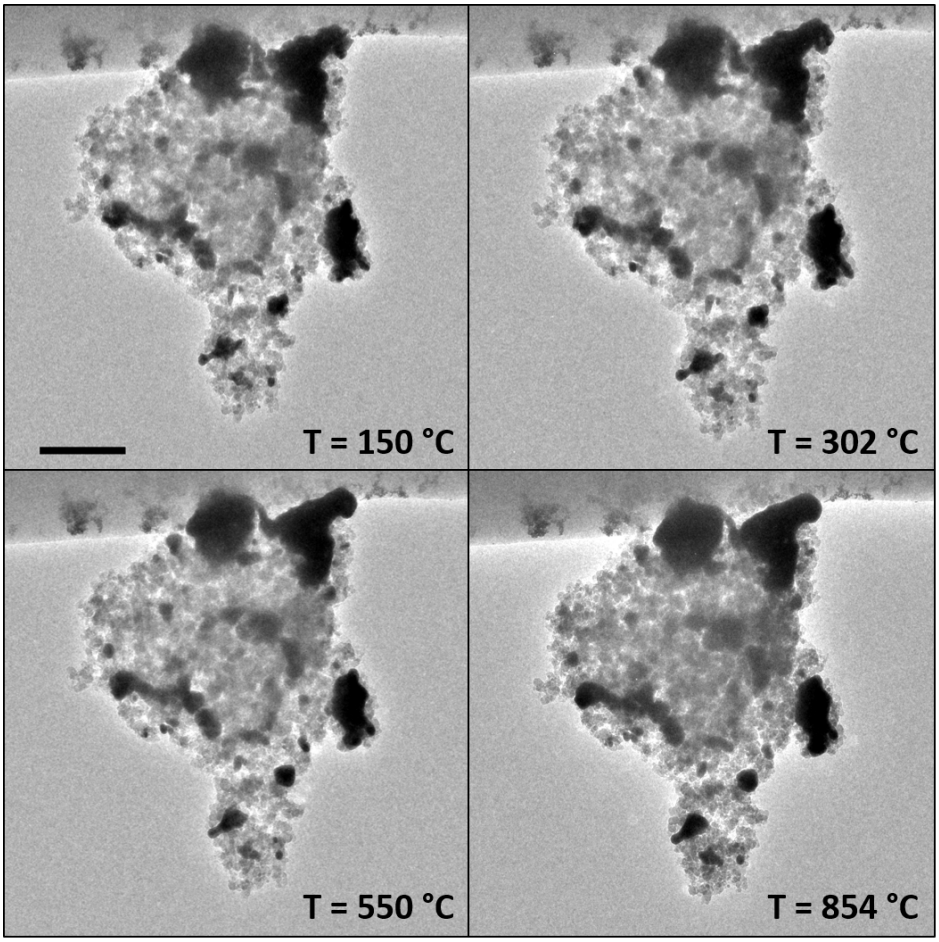

Figure 5.9: BFTEM micrographs of *in situ* vacuum heating of a silver:soot mixture in tight contact condition showing no silver mobility. Scale bar is 400 nm.

BFTEM analysis revealed the presence of partially consumed soot structures and local deformations of the larger silver agglomerates (white dashed circles in Figure 5.10). These deformations could be ascribed to the wetting of the soot structures as observed in the ETEM (Figure 5.7c), and hence could confirm the mobile nature of silver during soot oxidation in the flow reactor setup. It is important to notice that large silver agglomerates are representative of the portions of the sample in loose contact with the soot and therefore are not expected to show high mobility at the temperature of maximal carbon oxidation rate of tight contact mixtures (T=526 °C, in the electron microscope). However, from the *in situ* studies presented in Section 5.5, this temperature was found to be high enough to trigger wetting and initial mobility of large silver agglomerates, which would lead to the deformations observed in Figure 5.10.

However, although evidences of silver mobility could be identified during soot oxidation in the flow reactor setup, an absolute temperature discrepancy remains between observations of oxidative mobility in the ETEM and carbon oxidation in the flow reactor experiments. In order to verify the influence of the pressure gap on this temperature offset, TPO of a soot:silver mixture in loose contact was carried out in the flow reac-

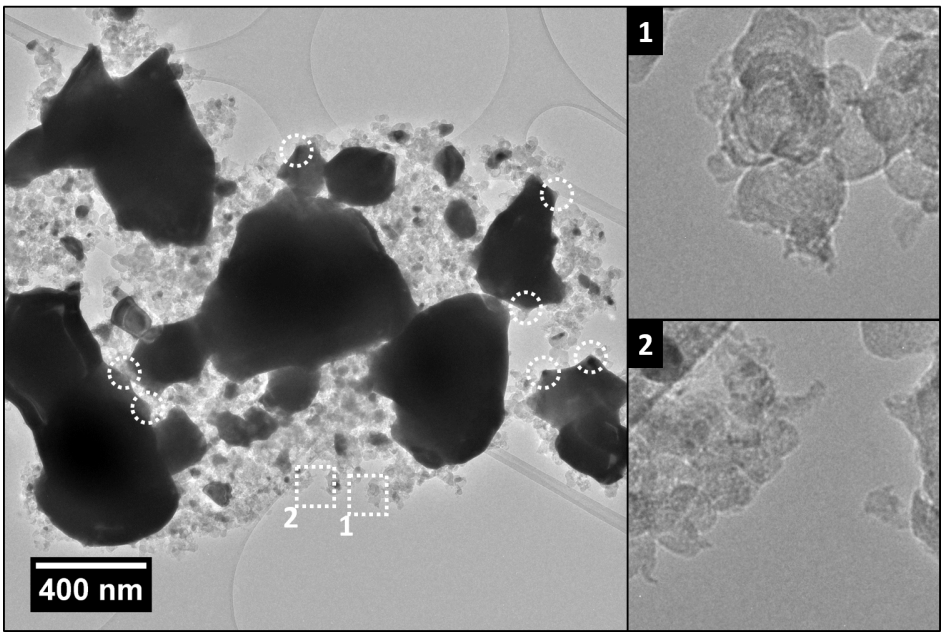

Figure 5.10: BFTEM micrographs of soot:silver mixture in tight contact condition subjected to a TPO experiment in the flow reactor setup interrupted at T=450 °C. The areas in the dashed rectangle show consumption of soot structures and are presented magnified on the right hand side of the figure. Dashed circles indicate areas of local deformation of the silver agglomerates.

tor at an oxygen partial pressure of pO_2=296 Pa, very similar to the one used during ETEM experiments. As Figure 5.11 shows, reducing the oxygen partial pressure to ETEM conditions had the effect to shift the carbon oxidation rate peak to approximately T=675 °C, reasonably close to the estimated temperature of maximal silver mobility observed in loose contact (T=700 °C). Furthermore, the carbon oxidation rate was observed to increase approximately starting from T=500 °C, the same temperature at which silver exhibited initial mobility in the ETEM.

Finally, under the assumption that soot oxidation is first order in the oxygen pressure, a rate expression for the oxidation reaction was derived by fitting of kinetic parameters (see [Paper3]). Figure 5.11 shows that the same rate expression could be used to provide a reasonable description of the oxidation behavior at both original and ETEM oxygen pressures, further confirming the relevance of ETEM observations for the interpretation of flow reactor catalytic data despite of the pressure gap between the two methods. Moreover, due to the large agreement between ETEM observations and TPO flow reactor experiments carried out at ETEM pressures, the effect of the electron beam was not considered to have a large influence on silver mobility in the experimental conditions used for this study. However, further experiments at different beam doses are needed to validate this hypothesis.

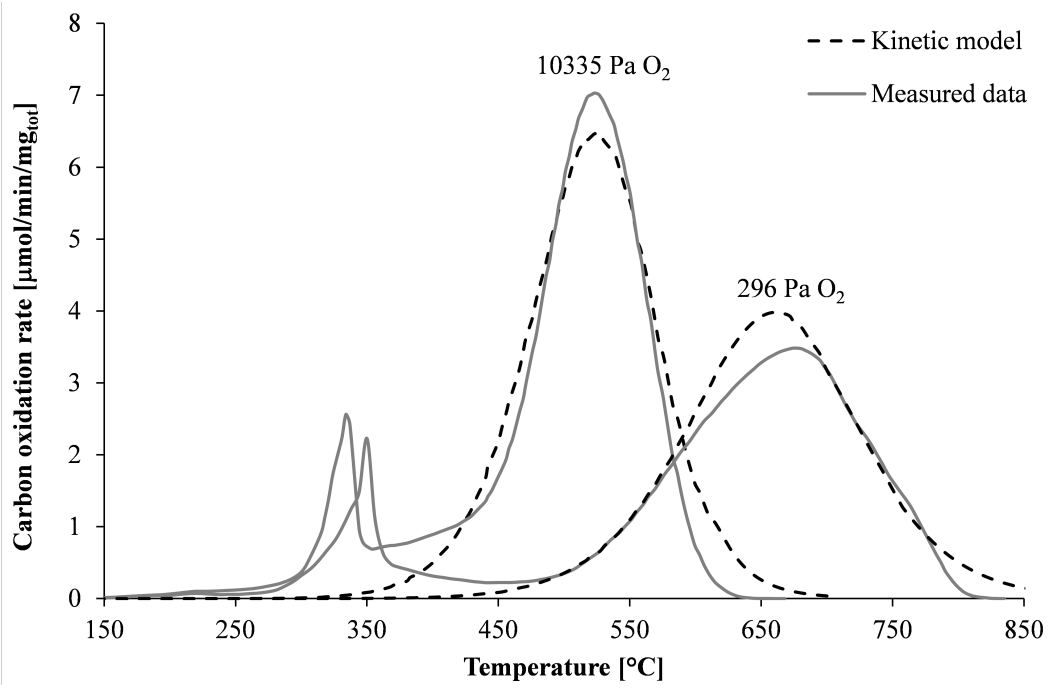

Figure 5.11: The rate of carbon oxidation (normalized by the total, initial mass of carbon) in loose contact with silver as a function of temperature with two different oxygen partial pressures. Solid lines represent the experimental data and dashed lines the theoretical profiles calculated according to the kinetic model presented. Experimental conditions: Soot:silver = 1:5 wt:wt, T ramp = 11 °C/min, 10335 Pa O_2 = 1 NL/min, 10.2 vol% O_2 in N_2, 296 Pa O_2 = 1 NL/min 3000 ppmv O_2 in N_2. Figure from [Paper3].

5.6 Conclusion

In this chapter a combination of *ex situ* and *in situ* transmission electron microscopy techniques was used to obtain unique information on the peculiar activity of silver nanoparticles as catalyst for soot oxidation.

In TPO experiments carried out in a flow reactor, soot:silver mixtures in a ratio 1:5 wt:wt showed different catalytic activity depending on the contact condition between soot and catalysts. In tight contact condition, obtained by crushing silver and soot together, the temperature of maximal carbon oxidation rate was observed to be lower than in the case of loose contact condition, obtained by simply stirring the two powders with a spatula.

In order to increase the understanding on the mechanisms behind this difference in activity, an initial *ex situ* TEM approach was used to investigate the distribution of soot and silver in the two contact conditions. BFTEM analysis revealed the presence of a finer dispersion of silver particles for tight contact mixtures when compared to loose contact mixtures, characterized by the presence of large silver agglomerates. Furthermore, the use of environmental TEM allowed the direct visualization of the oxidation reaction, revealing a correlation between the TPO activity difference and the significant mobility of silver in oxidative conditions. In the tight contact mixture the initial dispersion of the silver particles is greater, and the onset of mobility was

found to occur at a lower temperature, as a result of the balance between the attractive forces connecting silver agglomerates to the porous soot matrix and the size of the silver agglomerates themselves. This mobility behavior, responsible for ensuring the constant presence of a reactive carbon-silver-oxygen interface during the reaction, was hence found to be at the base of the difference in catalytic activity during TPO for the two soot:silver mixtures.

Electron microscopy hence proved to be a powerful tool for obtaining fundamental understanding of the mechanisms behind the activity of a catalytic system in operative conditions. In particular, the use of environmental TEM, allowed the direct visualization of the catalyst in action, a contribution of unparalleled value for the interpretation of average catalytic activity data.

CHAPTER 6

Conclusion and outlook

In this project, the catalytic activity of different supported material systems has been investigated by means of *ex situ* and *in situ* electron microscopy, in combination with XRD studies. The characterization of these systems has been carried out at different stages of their catalytic life in order to study the correlation between their activity and the evolution of their morphological, crystallographic and chemical properties.

The synthesis and deactivation of three HDO catalysts, Ni/ZrO_2, Mo_2C/ZrO_2 and $Ni\text{-}MoS_2/ZrO_2$ have been investigated, and the results have been presented in Chapter 4.

As the first stage of the catalyst life, synthesis defines the initial structure and properties of the catalyst active phase. Electron microscopy proved, in the first place, to be an invaluable resource for the visualization of the catalyst active phase, from the single nanoparticle to the atomic scale level. As opposed to complementary techniques such as XRD, electron microscopy enabled the identification and characterization of single nanoparticles for the three material systems in analysis. In the case of Ni/ZrO_2, this allowed to establish a relation between the size distribution of Ni particles and the catalytic activity/deactivation profiles. For $Ni\text{-}MoS_2/ZrO_2$, a STEM-EDX based approach proved the incorporation of nickel in the MoS_2 structures of the catalyst, thus confirming the essential Ni promotion. Finally, when the study of the Mo_2C/ZrO_2 system required the synthesis of a new batch of catalyst supported on larger ZrO_2 particles, a combination of HRTEM and STEM-EELS techniques allowed to assess the formation of the correct supported phase.

Deactivation involves the loss of activity and represents the last stage of the life of a catalyst. Several deactivation mechanisms exist, each one involving modifications of the catalyst active phase or its environment. Once again, the unique capability of electron microscopy to provide morphological, crystallographic and chemical information at the single-nanoparticle level, allowed to shed light on the mechanisms leading to this activity loss. In the study of the resistance of Ni/ZrO_2 upon exposure to several poisoning agents, a combination of SEM-EDX, STEM-EDX and XRD techniques was used. Sulfur was found to induce a permanent structural modification, by a formation of an inactive NiS phase. Potassium and chlorine deactivated the catalyst instead by

adsorption on uncoordinated nickel sites. In the case of Mo_2C/ZrO_2 catalysts, the use of environmental TEM allowed to investigate the effect of water exposure on individual supported carbide particles. A combination of HRTEM and STEM-EELS analyses revealed the partial degradation of the supported phase, probably due to the formation of volatile molybdenum hydroxide species. Finally, the exposure of Ni-MoS_2/ZrO_2 to various H_2S and H_2O feed concentrations was investigated by a qualitative STEM-EDX approach. Low H_2S concentrations in the feed were found to induce a sulfur depletion of the NiMoS active phase, whereas presence of water in the feed was found to induce an S-O exchange at the edges of MoS_2 slabs.

Chapter 5 focused on the study of a catalytic system in operative conditions. The mechanisms behind the activity of silver nanoparticles as catalyst for soot oxidation were investigated by carrying out an *in situ* TPO in the ETEM. Imaging catalytic reactions at the nanoscale shed light on the difference in carbon oxidation temperature between soot:silver mixtures characterized by a different silver dispersion. ETEM observations revealed that the silver phase exhibit significant mobility during soot oxidation as a result of the presence of attractive forces between Ag nanoparticles and the soot matrix. This mobility was found to be dependent on the silver particle size and it was shown to lower the carbon oxidation temperature by ensuring the constant presence of a reactive carbon-silver-oxygen interface during oxidation. Soot:silver mixtures characterized by a finer dispersion of the Ag phase exhibited thus a lower carbon oxidation temperature than mixtures presenting larger Ag agglomerates due to the lower temperature needed to trigger silver mobility.

Electron microscopy hence proved to be an irreplaceable tool for the characterization of a supported material system at all stages of its catalytic life. The possibility of investigating the structural modifications of individual, supported nanoparticles proved to be crucial in the determination of the mechanisms leading to catalytic activity, representing an invaluable resource in the materials scientist toolbox.

6.1 Outlook and future work

Besides many advantages, several limitations need to be tackled in order for electron microscopy to reach its full potential. Problems such as the extreme locality of TEM information and beam damage can in principle be solved by the analysis of more sample areas and by reducing the beam current. Others, such as the pressure gap between ETEM experiments and real catalytic applications, require the development of new dedicated equipment, such as the closed-cell holder presented in Section 2.4 able to confine a gas environment at ambient pressure.

However, real advances in the overall quality, validity and interpretation of TEM studies will be obtained only by embracing strategies aiming at combining microscope observations with complementary characterization techniques. In particular, new sample observation systems compatible with both TEM and a second setup have been developed in the last years. These shared platforms allow new exciting horizons to be seen in both *in situ* and *ex situ* high pressure material characterization.

For example, further developing the idea of sample transfer in vacuum, Damsgaard *et al.* demonstrated the use of a novel TEM holder concept allowing specimen transfer between different setups without variations of the reactive environment [102]. The use of MEMS heating and the presence of a sealing compartment allows to isolate the sample in a controlled gas composition and at elevated temperature. In this way, experiments demanding high pressure reactive environments can be performed in a dedicated high pressure setup able to host the TEM holder. At the end of (or during) the experiment, the sample can be sealed and transferred under the same high pressure (and eventually, temperature) conditions to an ETEM in order study the structural variations induced by the treatment.

Similarly, Li *et al.* reported the development of a new portable microreactor compatible with both *in situ* STEM and XAS measurements [103]. By modifying a commercially available liquid cell TEM sample holder, the group obtained a hybrid setup allowing specimen observation in a custom gas composition up to ambient pressures.

For what concerns the work presented in this thesis, new experiments could be designed taking into account the use of different complementary techniques and equipments allowing *in situ* high pressure studies.

As an example, TPO experiments of soot:silver mixtures could be carried out at 1 bar in the TEM using a closed-cell heating holder. This would enhance the comparability of TEM results with flow reactor experiments, closing the pressure gap and approaching the environmental conditions of real diesel engines. A second example is the deactivation of the Mo_2C/ZrO_2 catalyst in presence of water. Exposure to water could be repeated at higher pressures, in order to limit the volatility of the molybdenum hydroxide phase formed. Another option would be to use a TEM transfer holder to carry out the water deactivation in an *is situ* XRD setup and further analyze the sample in the ETEM. This approach would further have the advantage of producing results directly compatible with *in situ* synchrotron XRD studies found in literature. Finally, for the case of Ni-MoS_2/ZrO_2, further XAS experiment are required in order to confirm the role of water during catalyst deactivation.

Bibliography

[1] J. J. Berzelius, "Quelques idées sur une nouvelle force agissant dans les combinaisons des corps organiques," *Annales de Chimie et de Physique*, vol. 61, no. 146, 1836.

[2] Z. Ma and F. Zaera, "Heterogeneous catalysis by metals," in *Encyclopedia of Inorganic and Bioinorganic Chemistry*, pp. 1–16, Chichester, UK: John Wiley & Sons, Ltd, Mar. 2014.

[3] C. M. Y. Yeung, K. M. K. Yu, Q. J. Fu, D. Thompsett, M. I. Petch, and S. C. Tsang, "Engineering Pt in ceria for a maximum metal-support interaction in catalysis," *Journal of the American Chemical Society*, vol. 127, no. 51, pp. 18010–18011, 2005.

[4] J. Jiang, G. Oberdörster, A. Elder, R. Gelein, P. Mercer, and P. Biswas, "Does nanoparticle activity depend upon size and crystal phase?," *Nanotoxicology*, vol. 2, pp. 33–42, Jan. 2008.

[5] D. L. Trimm, "Catalysts for the control of coking during steam reforming," *Catalysis Today*, vol. 49, no. 1-3, pp. 3–10, 1999.

[6] J. F. Creemer, S. Helveg, G. H. Hoveling, S. Ullmann, A. M. Molenbroek, P. M. Sarro, and H. W. Zandbergen, "Atomic-scale electron microscopy at ambient pressure," *Ultramicroscopy*, vol. 108, no. 9, pp. 993–998, 2008.

[7] "Hummingbird Scientific gas flow TEM holder." http://hummingbirdscientific.com/products/gas-flow/.

[8] "DENSsolutions TEM heating holder." http://denssolutions.com/products/heating/.

[9] "Protochips Aduro TEM heating holder." http://www.protochips.com/products/aduro.html.

[10] D. Gardini, "Reduction of Copper Oxide," tech. rep., Department of Physics, Technical University of Denmark, 2011.

[11] D. R. Strongin, J. Carrazza, S. R. Bare, and G. A. Somorjai, "The Importance of C_7 Sites and Surface Roughness in the Ammonia Synthesis Reaction over Iron," *Journal of Catalysis*, vol. 103, pp. 213–215, Jan. 1987.

[12] J. Liu, "Advanced electron microscopy characterization of nanostructured heterogeneous catalysts," *Microscopy and Microanalysis*, vol. 10, pp. 55–76, Feb. 2004.

[13] S. Bernal, J. J. Calvino, M. A. Cauqui, J. M. Gatica, C. López Cartes, J. A. Pérez Omil, and J. M. Pintado, "Some contributions of electron microscopy to the characterisation of the strong metal–support interaction effect," *Catalysis Today*, vol. 77, pp. 385–406, Jan. 2003.

[14] B. Zhang, W. Zhang, and D. S. Su, "Towards a more accurate particle size distribution of supported catalyst by using HAADF-STEM," *ChemCatChem*, vol. 3, pp. 965–968, June 2011.

[15] D. Deiana, *Atomic-level Electron Microscopy of Metal and Alloy Electrocatalysts*. PhD thesis, Technical University of Danmark, 2014.

[16] H. Yoshida, Y. Kuwauchi, J. R. Jinschek, K. Sun, S. Tanaka, M. Kohyama, S. Shimada, M. Haruta, and S. Takeda, "Visualizing gas molecules interacting with supported nanoparticulate catalysts at reaction conditions," *Science*, vol. 335, pp. 317–319, Jan. 2012.

[17] R. Sharma, "Kinetic measurements from in situ TEM observations," *Microscopy Research and Technique*, vol. 72, pp. 144–152, Mar. 2009.

[18] T. W. Hansen, A. T. Delariva, S. R. Challa, and A. K. Datye, "Sintering of catalytic nanoparticles: Particle migration or ostwald ripening?," *Accounts of Chemical Research*, vol. 46, no. 8, pp. 1720–1730, 2013.

[19] I. Sharafutdinov, C. F. Elkjær, H. W. P. de Carvalho, D. Gardini, G. L. Chiarello, C. D. Damsgaard, J. B. Wagner, J.-D. Grunwaldt, S. Dahl, and I. Chorkendorff, "Intermetallic compounds of Ni and Ga as catalysts for the synthesis of methanol," *Journal of Catalysis*, vol. 320, pp. 77–88, Dec. 2014.

[20] R. F. Egerton, P. Li, and M. Malac, "Radiation damage in the TEM and SEM," *Micron*, vol. 35, no. 6, pp. 399–409, 2004.

[21] P. Williams, "Motion of small gold clusters in the electron microscope," *Applied Physics Letters*, vol. 50, no. 24, p. 1760, 1987.

[22] P. M. Mortensen, J.-D. Grunwaldt, P. A. Jensen, K. G. Knudsen, and A. D. Jensen, "A review of catalytic upgrading of bio-oil to engine fuels," *Applied Catalysis A: General*, vol. 407, pp. 1–19, Nov. 2011.

[23] E. Furimsky, "Deactivation of hydroprocessing catalysts," 1999.

[24] P. M. Mortensen, J.-D. Grunwaldt, P. A. Jensen, and A. D. Jensen, "Screening of catalysts for hydrodeoxygenation of phenol as a model compound for bio-oil," *ACS Catalysis*, vol. 3, no. 8, pp. 1774–1785, 2013.

[25] C. Louis, Z. Cheng, and M. Che, "Characterization of nickel/silica catalysts during impregnation and further thermal activation treatment leading to metal particles," *The Journal of Physical Chemistry*, vol. 97, pp. 5703–5712, 1993.

[26] P. M. Mortensen, D. Gardini, H. W. P. de Carvalho, C. D. Damsgaard, J.-D. Grunwaldt, P. A. Jensen, J. B. Wagner, and A. D. Jensen, "Stability and resistance of nickel catalysts for hydrodeoxygenation: carbon deposition and effects of sulfur, potassium, and chlorine in the feed," *Catalysis Science & Technology*, vol. 4, pp. 3672–3686, June 2014.

[27] P. Scardi, M. Leoni, and R. Delhez, "Line broadening analysis using integral breadth methods: A critical review," *Journal of Applied Crystallography*, vol. 37, no. 3, pp. 381–390, 2004.

[28] B. Bondars, G. Heidemane, J. Grabis, K. Laschke, H. Boysen, J. Schneider, and F. Frey, "Powder diffraction investigations of plasma sprayed zirconia," *Journal of Materials Science*, vol. 30, no. 6, pp. 1621–1625, 1995.

[29] E. R. Jette and F. Foote, "Precision determination of lattice constants," *The Journal of Chemical Physics*, vol. 3, no. 10, p. 605, 1935.

[30] R. van Hardeveld and F. Hartog, "Influence of metal particle size in nickel-on-aerosil catalysts on surface site distribution, catalytic activity, and selectivity," in *Advances in Catalysis*, vol. 22, pp. 75–113, 1972.

[31] P. M. Mortensen, *Catalytic Conversion of Bio-Oil to Fuel for Transportation*. Phd thesis, Technical University of Denmark, 2013.

[32] H. Bengaard, "Steam reforming and graphite formation on Ni catalysts," *Journal of Catalysis*, vol. 209, no. 2, pp. 365–384, 2002.

[33] S. N. Black, D. A. Jefferson, and P. Henderson, "An electron-optical study of nickel monosulfide," 1984.

[34] S. Park, J. O. Baker, M. E. Himmel, P. A. Parilla, and D. K. Johnson, "Cellulose crystallinity index: measurement techniques and their impact on interpreting cellulase performance," *Biotechnology for biofuels*, vol. 3, p. 10, Jan. 2010.

[35] G. A. Slack, "Crystallography and domain walls in antiferromagnetic NiO crystals," *Journal of Applied Physics*, vol. 31, no. 9, pp. 1571–1582, 1960.

[36] T. N. Trinh, P. A. Jensen, D. J. Kim, N. O. Knudsen, H. R. Sørensen, and S. Hvilsted, "Comparison of lignin, macroalgae, wood, and straw fast pyrolysis," *Energy and Fuels*, vol. 27, no. 3, pp. 1399–1409, 2013.

[37] J. D. Ortego, J. T. Richardson, and M. V. Twigg, "Catalytic steam reforming of chlorocarbons: Methyl chloride," *Applied Catalysis B: Environmental*, vol. 12, no. 4, pp. 339–355, 1997.

[38] Y. Ohtsuka, "Influence of hydrogen chloride treatment on the dispersion of nickel particles supported on carbon," Sept. 1989.

[39] V. L. Cherginets, V. N. Baumer, S. S. Galkin, L. V. Glushkova, T. P. Rebrova, and Z. V. Shtitelman, "Solubility of Al_2O_3 in some chloride-fluoride melts," *Inorganic Chemistry*, vol. 45, no. 18, pp. 7367–7371, 2006.

[40] S. Hodson and J. Marshall, "Migration of potassium out of electron-microscope specimens," *Journal of microscopy*, vol. 93, pp. 49–53, Feb. 1971.

[41] K. Jurek and O. Gedeon, "Volume and composition surface changes in alkali silicate glass irradiated with electrons," *Microchimica Acta*, vol. 161, no. 3-4, pp. 377–380, 2008.

[42] V. A. Yakovlev, S. A. Khromova, O. V. Sherstyuk, V. O. Dundich, D. Y. Ermakov, V. M. Novopashina, M. Y. Lebedev, O. Bulavchenko, and V. N. Parmon, "Development of new catalytic systems for upgraded bio-fuels production from bio-crude-oil and biodiesel," *Catalysis Today*, vol. 144, no. 3-4, pp. 362–366, 2009.

[43] Z. He and X. Wang, "Hydrodeoxygenation of model compounds and catalytic systems for pyrolysis bio-oils upgrading," *Catalysis for Sustainable Energy*, vol. 1, pp. 28–52, 2012.

[44] E. Furimsky, "Hydroprocessing challenges in biofuels production," *Catalysis Today*, vol. 217, pp. 13–56, 2013.

[45] R. B. Levy and M. Boudart, "Platinum-like behavior of tungsten carbide in surface catalysis," *Science (New York, N.Y.)*, vol. 181, no. 4099, pp. 547–549, 1973.

[46] L. Leclercq, K. Imura, S. Yoshida, T. Barbee, and M. Boudart, *Synthesis of new catalytic materials: Metal carbides of the group VI B elements*, vol. 3. Elsevier Scientific Publishing Company, 1979.

[47] A. J. Medford, A. Vojvodic, F. Studt, F. Abild-Pedersen, and J. K. Nørskov, "Elementary steps of syngas reactions on $Mo_2C(001)$: Adsorption thermochemistry and bond dissociation," *Journal of Catalysis*, vol. 290, pp. 108–117, 2012.

[48] E. Furimsky, "Metal carbides and nitrides as potential catalysts for hydroprocessing," *Applied Catalysis A: General*, vol. 240, no. 1-2, pp. 1–28, 2003.

[49] P. M. Mortensen, H. W. P. de Carvalho, J.-D. Grunwaldt, P. A. Jensen, and A. D. Jensen, "Activity and stability of Mo_2C/ZrO_2 as catalyst for hydrodeoxygenation of mixtures of phenol and 1-octanol," *Journal of Catalysis*, vol. 328, pp. 208–215, Aug. 2015.

[50] T. Prasomsri, M. Shetty, K. Murugappan, and Y. Román-Leshkov, "Insights into the catalytic activity and surface modification of MoO_3 during the hydrodeoxygenation of lignin-derived model compounds into aromatic hydrocarbons under low hydrogen pressures," *Energy & Environmental Science*, vol. 7, no. 8, p. 2660, 2014.

[51] R. Thalinger, M. Stöger-Pollach, W. Hetaba, M. Feuerbacher, B. Klötzer, and S. Penner, "Electron microscopy investigations of metal-support interaction effects in M/Y_2O_3 and M/ZrO_2 thin films (M=Cu,Ni)," *Materials Chemistry and Physics*, vol. 143, no. 1, pp. 167–177, 2013.

[52] D. K. Smith and W. Newkirk, "The crystal structure of baddeleyite (monoclinic ZrO_2) and its relation to the polymorphism of ZrO_2," *Acta Crystallographica*, vol. 18, no. 6, pp. 983–991, 1965.

[53] E. Shimao, "The Structure of $Mo_7O_{24}^{6-}$ Ion in the Crystal of Ammonium Heptamolybdate Tetrahydrate," *Bulletin of the Chemical Society of Japan*, vol. 40, no. 7, pp. 1609–1613, 1967.

[54] T. Leisegang, A. A. Levin, J. Walter, and D. C. Meyer, "In situ X-ray analysis of MoO_3 reduction," *Crystal Research and Technology*, vol. 40, no. 1-2, pp. 95–105, 2005.

[55] C. Thomazeau, V. Martin, and P. Afanasiev, "Effect of support on the thermal decomposition of $(NH_4)_6Mo_7O_{24}{\cdot}4H_2O$ in the inert gas atmosphere," *Applied Catalysis A: General*, vol. 199, no. 1, pp. 61–72, 2000.

[56] Y. Zhao, W. Li, M. Zhang, and K. Tao, "A comparison of surface acidic features between tetragonal and monoclinic nanostructured zirconia," *Catalysis Communications*, vol. 3, no. 6, pp. 239–245, 2002.

[57] S. Kuimalee, T. Chairuangsri, J. T. H. Pearce, D. V. Edmonds, A. P. Brown, and R. M. D. Brydson, "Quantitative analysis of a complex metal carbide formed during furnace cooling of cast duplex stainless steel using EELS and EDS in the TEM.," *Micron*, vol. 41, pp. 423–9, July 2010.

[58] M. Qian and L. C. Lim, "Phase stability of microfine Mo_2C phases in high vacuums," *Journal of Materials Science Letters*, vol. 18, no. 15, pp. 1253–1254, 1999.

[59] R. G. Wilson and W. E. McKee, "Vacuum thermionic work functions and thermal stability of TaB_2, ZrC, Mo_2C, $MoSi_2$, $TaSi_2$, and WSi_2," *Journal of Applied Physics*, vol. 38, no. 4, pp. 1716–1718, 1967.

[60] T. Millner and J. Neugebauer, "Volatility of the oxides of tungsten and molybdenum in the presence of water vapour," *Nature*, vol. 163, pp. 601–602, Apr. 1949.

[61] G. Wirtz, L. B. Sis, and J. S. Wheeler, "Sublimation of MoO_3 from WO_3-MoO_3 catalysts during the oxidation of toluene," *Journal of Catalysis*, vol. 38, pp. 196–205, June 1975.

[62] G. R. Belton and A. S. Jordan, "The volatilization of molybdenum in the presence of water vapor," *Journal of Physical Chemistry*, vol. 69, no. 6, pp. 2065–2071, 1965.

[63] P. S. Spinney, D. G. Howitt, S. D. Collins, and R. L. Smith, "Electron beam stimulated oxidation of carbon," *Nanotechnology*, vol. 20, p. 465301, Nov. 2009.

[64] A. J. V. Griffiths and T. Walther, "Quantification of carbon contamination under electron beam irradiation in a scanning transmission electron microscope and its suppression by plasma cleaning," *Journal of Physics: Conference Series*, vol. 241, July 2010.

[65] Y. Romero, F. Richard, and S. Brunet, "Hydrodeoxygenation of 2-ethylphenol as a model compound of bio-crude over sulfided Mo-based catalysts: Promoting effect and reaction mechanism," *Applied Catalysis B: Environmental*, vol. 98, pp. 213–223, Aug. 2010.

[66] M. Ramos, G. Berhault, D. A. Ferrer, B. Torres, and R. R. Chianelli, "HRTEM and molecular modeling of the MoS_2–Co_9S_8 interface: understanding the promotion effect in bulk HDS catalysts," *Catalysis Science & Technology*, vol. 2, no. 1, p. 164, 2012.

[67] F. L. Deepak, R. Esparza, B. Borges, X. Lopez-Lozano, and M. Jose-Yacaman, "Direct imaging and identification of individual dopant atoms in MoS_2 and WS_2 catalysts by aberration corrected scanning transmission electron microscopy," *ACS Catalysis*, vol. 1, no. 5, pp. 537–543, 2011.

[68] M. Ramos, D. Ferrer, E. Martinez-Soto, H. Lopez-Lippmann, B. Torres, G. Berhault, and R. R. Chianelli, "In-situ HRTEM study of the reactive carbide phase of Co/MoS_2 catalyst," *Ultramicroscopy*, vol. 127, pp. 64–69, Apr. 2013.

[69] F. Besenbacher, M. Brorson, B. S. Clausen, S. Helveg, B. Hinnemann, J. Kibsgaard, J. V. Lauritsen, P. G. Moses, J. K. Nørskov, and H. Topsøe, "Recent STM, DFT and HAADF-STEM studies of sulfide-based hydrotreating catalysts: Insight into mechanistic, structural and particle size effects," *Catalysis Today*, vol. 130, pp. 86–96, Jan. 2008.

[70] C. V. Ramana, U. Becker, V. Shutthanandan, and C. M. Julien, "Oxidation and metal-insertion in molybdenite surfaces: evaluation of charge-transfer mechanisms and dynamics," *Geochemical transactions*, vol. 9, p. 8, 2008.

[71] H. Topsøe, B. S. Clausen, R. Candia, C. Wivel, and S. Mørup, "In situ Mössbauer emission spectroscopy studies of unsupported and supported sulfided Co-Mo hydrodesulfurization catalysts: Evidence for and nature of a Co-Mo-S phase," *Journal of Catalysis*, vol. 68, pp. 433–452, Apr. 1981.

[72] B. S. Clausen, H. Topsøe, R. Candia, J. Villadsen, B. Lengeler, J. Als-Nielsen, and F. Christensen, "Extended X-ray absorption fine structure study of the cobalt-molybdenum hydrodesulfurization catalysts.," *Journal of Physical Chemistry*, vol. 85, no. 25, pp. 3868–3872, 1981.

[73] N. Y. Topsøe and H. Topsøe, "Characterization of the structures and active sites in sulfided Co-Mo/Al_2O_3 and Ni-Mo/Al_2O_3 catalysts by NO chemisorption," *Journal of Catalysis*, vol. 84, pp. 386–401, 1983.

[74] S. Helveg, J. Lauritsen, E. Lægsgaard, I. Stensgaard, J. Nørskov, B. Clausen, H. Topsøe, and F. Besenbacher, "Atomic-scale structure of single-layer MoS_2 nanoclusters," *Physical Review Letters*, vol. 84, no. 5, pp. 951–954, 2000.

[75] J. Lauritsen, "Atomic-scale structure of Co–Mo–S nanoclusters in hydrotreating catalysts," *Journal of Catalysis*, vol. 197, pp. 1–5, Jan. 2001.

[76] J. V. Lauritsen, J. Kibsgaard, G. H. Olesen, P. G. Moses, B. Hinnemann, S. Helveg, J. K. Nørskov, B. S. Clausen, H. Topsøe, E. Lægsgaard, and F. Besenbacher, "Location and coordination of promoter atoms in Co- and Ni-promoted MoS_2-based hydrotreating catalysts," *Journal of Catalysis*, vol. 249, pp. 220–233, July 2007.

[77] R. G. Dickinson and L. Pauling, "The crystal structure of molybdenite," *Journal of the American Chemical Society*, vol. 45, no. 6, pp. 1466–1471, 1923.

[78] T. R. Viljava, R. S. Komulainen, and A. O. I. Krause, "Effect of H_2S on the stability of CoMo/Al_2O_3 catalysts during hydrodeoxygenation," *Catalysis Today*, vol. 60, no. 1, pp. 83–92, 2000.

[79] M. Badawi, J. F. Paul, S. Cristol, E. Payen, Y. Romero, F. Richard, S. Brunet, D. Lambert, X. Portier, A. Popov, E. Kondratieva, J. M. Goupil, J. El Fallah, J. P. Gilson, L. Mariey, A. Travert, and F. Maugé, "Effect of water on the stability of Mo and CoMo hydrodeoxygenation catalysts: A combined experimental and DFT study," *Journal of Catalysis*, vol. 282, pp. 155–164, Aug. 2011.

[80] C. Ris, "U.S. EPA health assessment for diesel engine exhaust: a review.," *Inhalation toxicology*, vol. 19 Suppl 1, pp. 229–239, 2007.

[81] W. L. Chameides and M. Bergin, "Climate change. Soot takes center stage.," *Science*, vol. 297, no. 5590, pp. 2214–2215, 2002.

[82] B. A. A. L. van Setten, M. Makkee, and J. A. Moulijn, "Science and technology of catalytic diesel particulate filters," *Catalysis Reviews*, vol. 43, pp. 489–564, Nov. 2001.

[83] J. Adler, "Ceramic diesel particulate filters," *International Journal of Applied Ceramic Technology*, vol. 439, no. 2005, pp. 429–439, 2008.

[84] A. M. Stamatelos, "A review of the effect of particulate traps on the efficiency of vehicle diesel engines," *Energy Conversion and Management*, vol. 38, no. 1, pp. 83–99, 1997.

[85] J. P. A. Neeft, M. Makkee, and J. A. Moulijn, "Metal oxides as catalysts for the oxidation of soot," *The Chemical Engineering Journal and the Biochemical Engineering Journal*, vol. 64, pp. 295–302, Nov. 1996.

[86] A. G. Konstandopoulos and E. Papaioannou, "Update on the science and technology of diesel particulate filters," *KONA Powder and Particle Journal*, vol. 26, no. 26, pp. 36–65, 2008.

[87] A. G. Konstandopoulos, E. Papaioannou, D. Zarvalis, S. Skopa, P. Baltzopoulou, E. Kladopoulou, M. Kostoglou, and S. Lorentzou, "Catalytic filter systems with direct and indirect soot oxidation activity," *SAE Papers*, Apr. 2005.

[88] P. A. Kumar, M. D. Tanwar, S. Bensaid, N. Russo, and D. Fino, "Soot combustion improvement in diesel particulate filters catalyzed with ceria nanofibers," *Chemical Engineering Journal*, vol. 207-208, pp. 258–266, 2012.

[89] Q. Liang, X. Wu, X. Wu, and D. Weng, "Role of surface area in oxygen storage capacity of ceria-zirconia as soot combustion catalyst," *Catalysis Letters*, vol. 119, no. 3-4, pp. 265–270, 2007.

[90] J. M. Christensen, D. Deiana, J.-D. Grunwaldt, and A. D. Jensen, "Ceria prepared by flame spray pyrolysis as an efficient catalyst for oxidation of diesel soot," *Catalysis Letters*, vol. 144, pp. 1661–1666, Oct. 2014.

[91] J. M. Christensen, J.-D. Grunwaldt, and A. D. Jensen, "Submitted,"

[92] S. Böcklein, S. Günther, and J. Wintterlin, "High-pressure scanning tunneling microscopy of a silver surface during catalytic formation of ethylene oxide," *Angewandte Chemie - International Edition*, vol. 52, no. 21, pp. 5518–5521, 2013.

[93] C. T. Campbell, "Atomic and molecular oxygen adsorption on Ag(111)," *Surface Science*, vol. 157, no. 1, pp. 43–60, 1985.

[94] T. Kayama, K. Yamazaki, and H. Shinjoh, "Nanostructured ceria-silver synthesized in a one-pot redox reaction catalyzes carbon oxidation," *Journal of the American Chemical Society*, vol. 132, no. 38, pp. 13154–13155, 2010.

[95] K. Yamazaki, T. Kayama, F. Dong, and H. Shinjoh, "A mechanistic study on soot oxidation over CeO_2–Ag catalyst with 'rice-ball' morphology," *Journal of Catalysis*, vol. 282, pp. 289–298, Sept. 2011.

[96] M. Haneda and A. Towata, "Catalytic performance of supported Ag nanoparticles prepared by liquid phase chemical reduction for soot oxidation," *Catalysis Today*, vol. 242, pp. 351–356, 2015.

[97] F. Liang, M. Lu, M. E. Birch, T. C. Keener, and Z. Liu, "Determination of polycyclic aromatic sulfur heterocycles in diesel particulate matter and diesel fuel by gas chromatography with atomic emission detection," *Journal of Chromatography A*, vol. 1114, no. 1, pp. 145–153, 2006.

[98] R. T. K. Baker, J. A. France, L. Rouse, and R. J. Waite, "Catalytic oxidation of graphite by platinum and palladium," *Journal of Catalysis*, vol. 29, pp. 22–29, 1976.

[99] G. R. Hennig, "Catalytic oxidation of graphite," *Journal of Inorganic and Nuclear Chemistry*, vol. 24, 1962.

[100] T. J. Booth, F. Pizzocchero, H. Andersen, T. W. Hansen, J. B. Wagner, J. R. Jinschek, R. E. Dunin-Borkowski, O. Hansen, and P. Bøggild, "Discrete dynamics of nanoparticle channelling in suspended graphene," *Nano Letters*, vol. 11, no. 7, pp. 2689–2692, 2011.

[101] F. Pizzocchero, M. Vanin, J. Kling, T. W. Hansen, K. W. Jacobsen, P. Bøggild, and T. J. Booth, "Graphene edges dictate the morphology of nanoparticles during catalytic channeling," *Journal of Physical Chemistry C*, vol. 118, no. 8, pp. 4296–4302, 2014.

[102] C. D. Damsgaard, H. Zandbergen, T. W. Hansen, I. Chorkendorff, and J. B. Wagner, "Controlled environment specimen transfer," *Microscopy and microanalysis*, pp. 1–8, 2014.

[103] Y. Li, D. Zakharov, S. Zhao, R. Tappero, U. Jung, A. Elsen, P. Baumann, R. G. Nuzzo, E. A. Stach, and A. I. Frenkel, "Complex structural dynamics of nanocatalysts revealed in Operando conditions by correlated imaging and spectroscopy probes," *Nature Communications*, vol. 6, no. May, p. 7583, 2015.

[104] A. Thompson, D. Attwood, E. Gullikson, H. Malcolm, K.-J. Kim, J. Kirz, and J. Kortright, *X-Ray Data Booklet*. Lawrence Berkeley National Laboratory, 2009.

[105] D. B. Williams and C. B. Carter, *Transmission Electron Microscopy*. Boston, MA: Springer US, 2009.

Appendices

APPENDIX A

Detailed figures from Section 4.3

In the following pages an enlarged and more detailed version of Figures 4.26 and 4.28 is given in order to help the reader of the printed version of this manuscript.

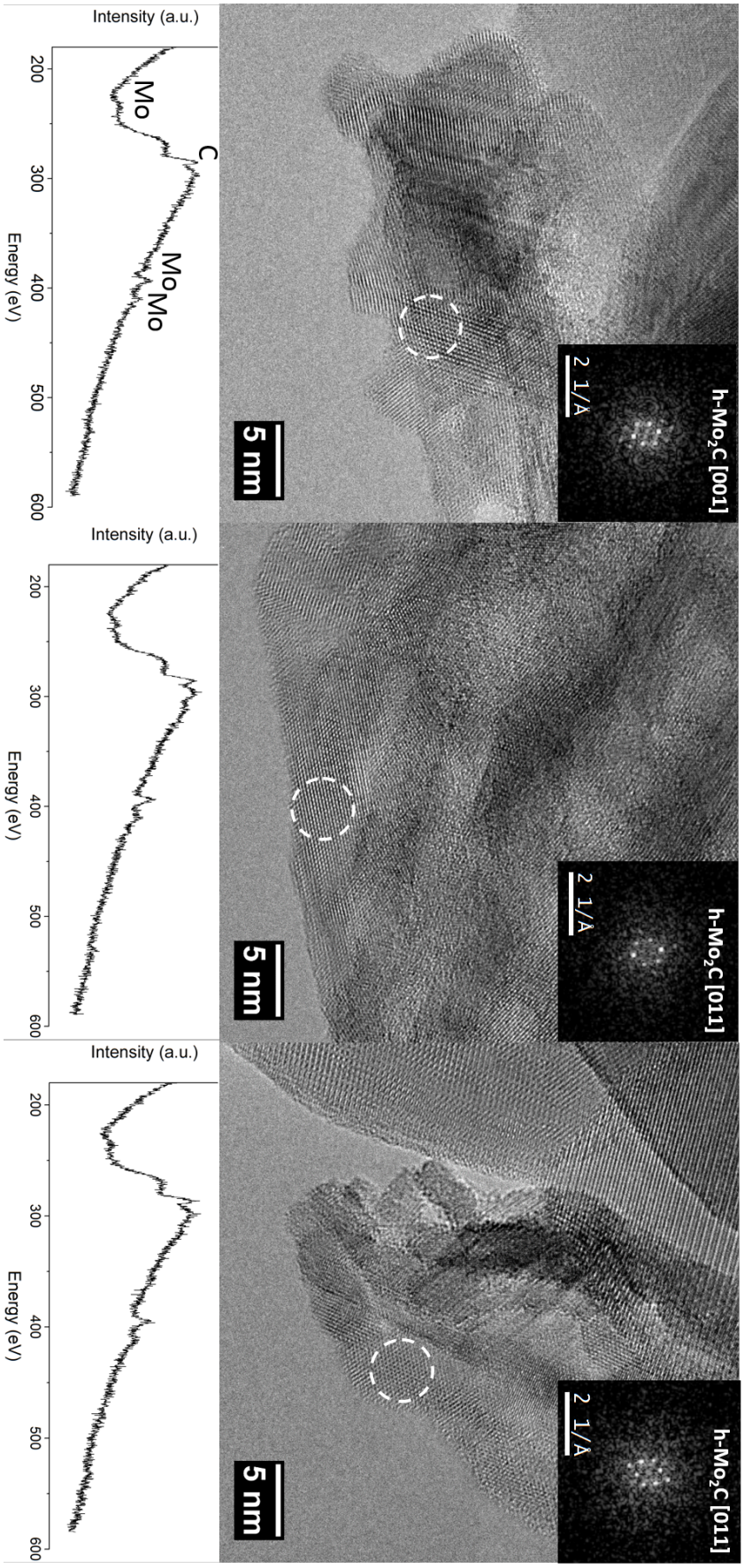

(a) Before water exposure

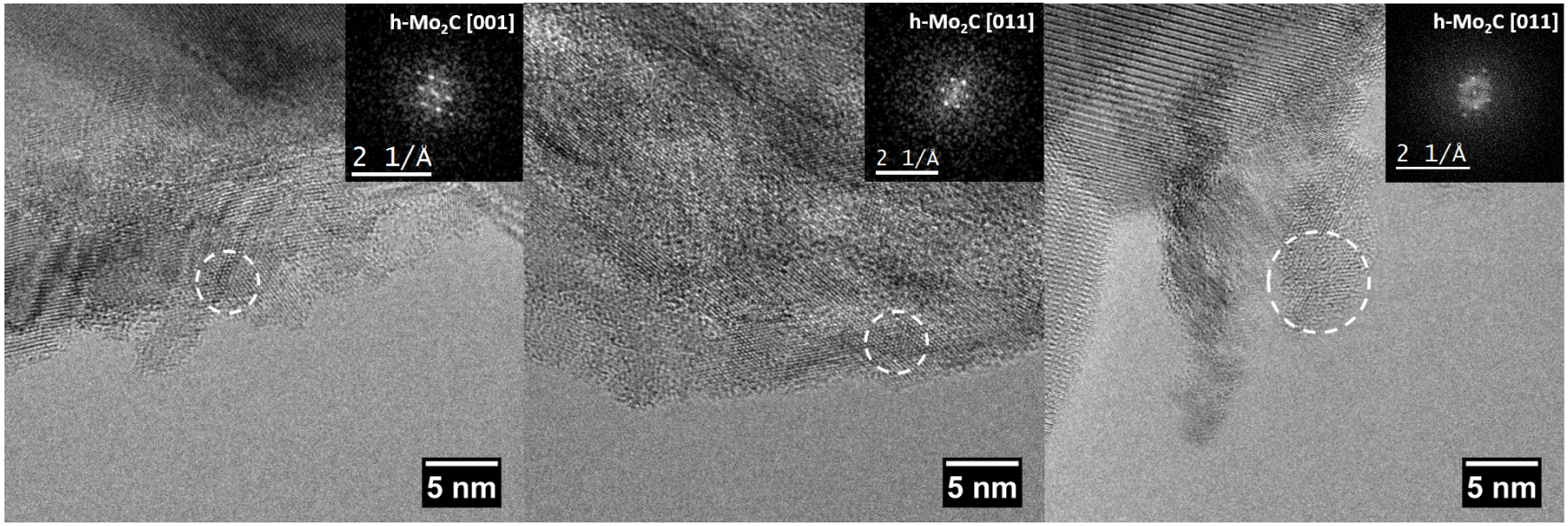

(b) After water exposure

Figure A.1: HRTEM micrographs of three supported carbide particles of the Mo_2C/m-ZrO_2 catalyst **(a)** before and **(b)** after exposure to p_{H_2O}=280 Pa, T=400 °C for 16h. For each nanoparticle, the STEM-EELS spectrum and the digital diffractogram of the dashed circle region is given. Micrographs were acquired at room temperature, in (a) vacuum and (b) at p_{H_2O}=280 Pa.

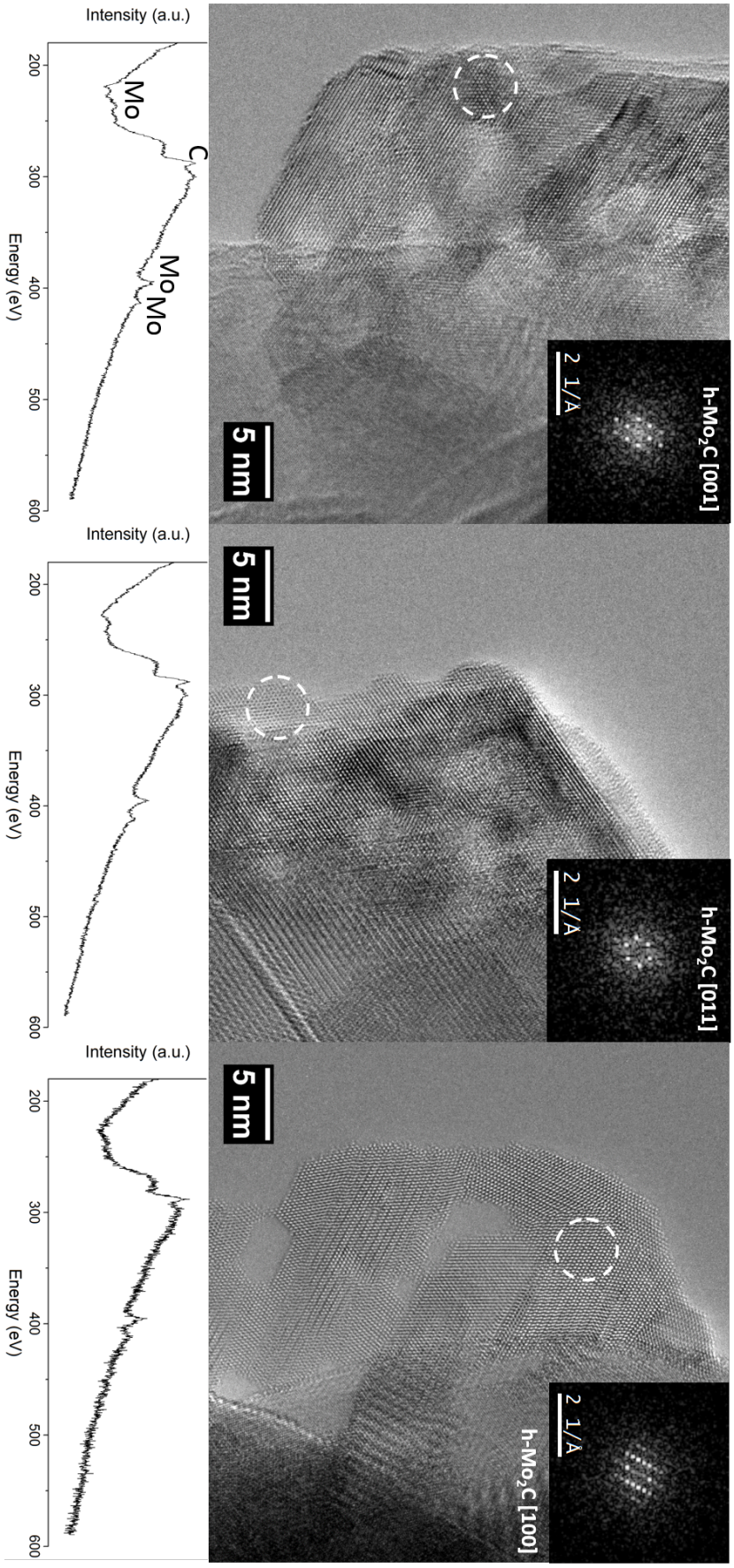

(a) Before water exposure

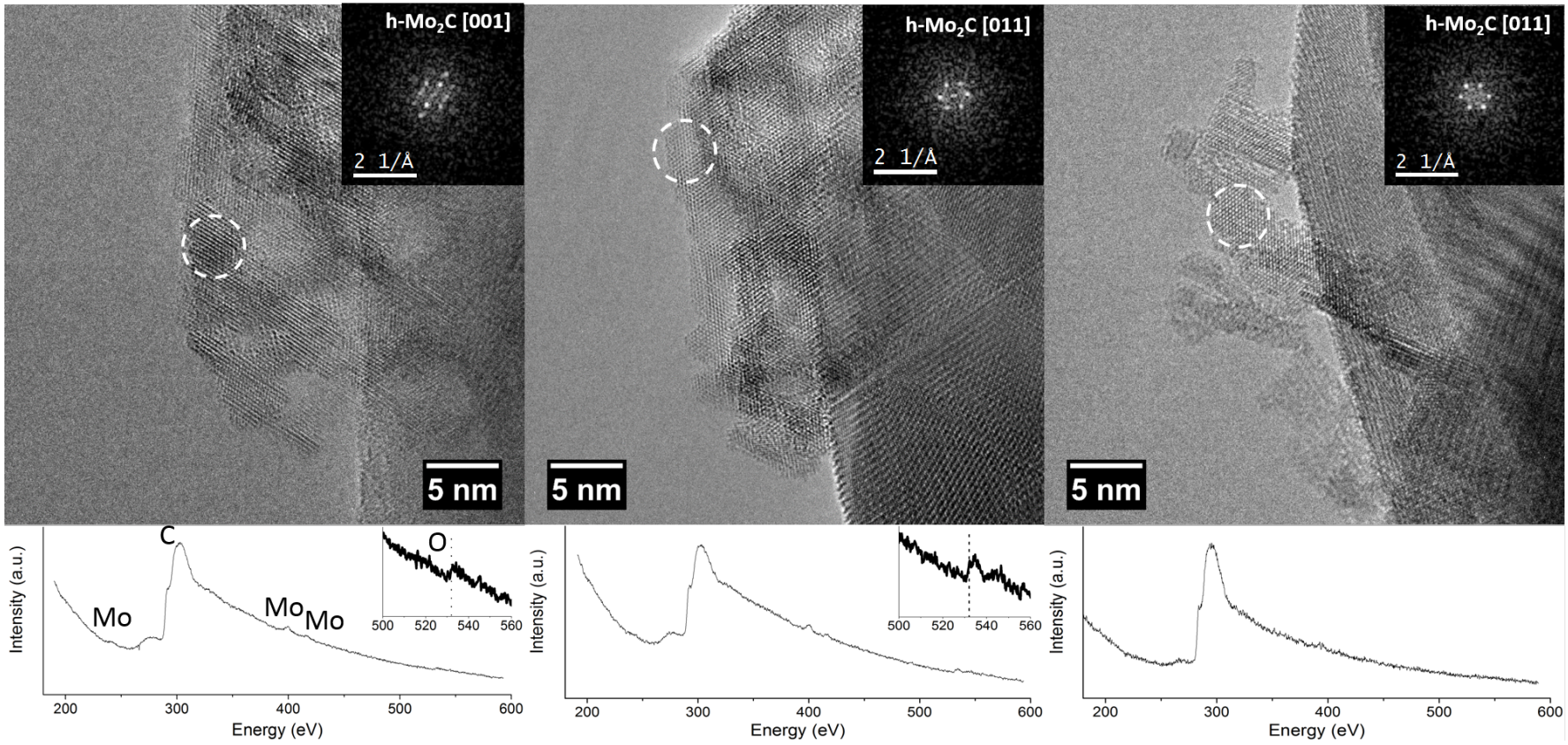

(b) After water exposure

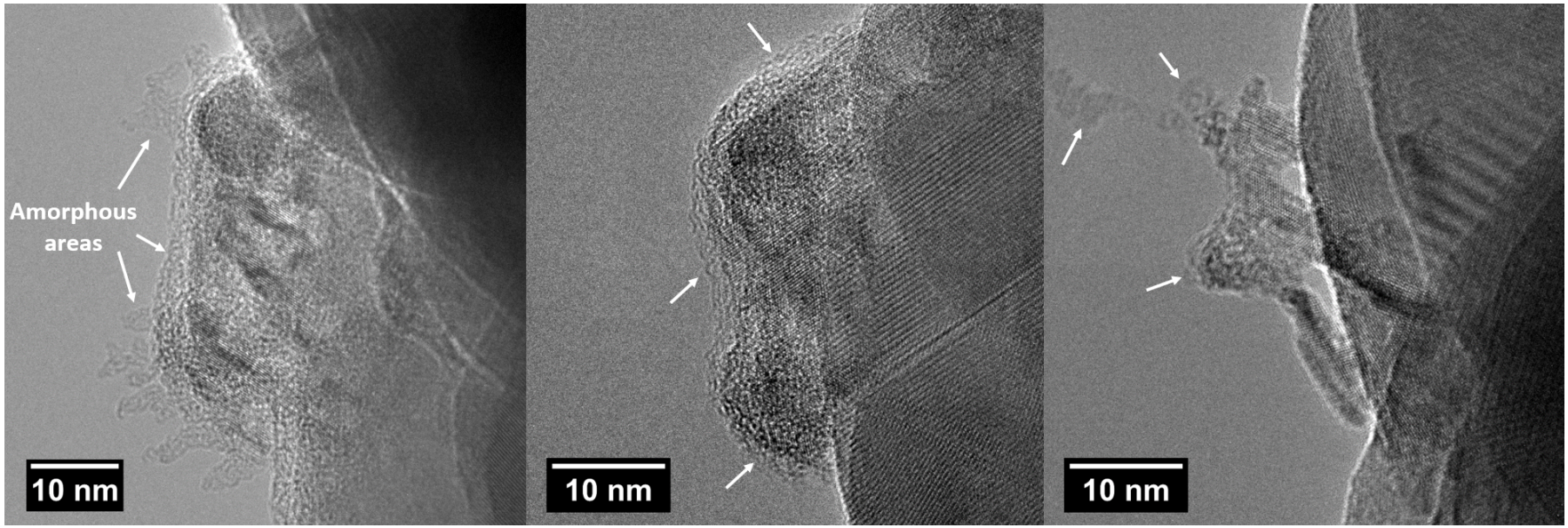

(c) After water exposure and STEM-EELS analysis

Figure A.2: HRTEM micrographs of three supported carbide particles of the Mo_2C/m-ZrO_2 catalyst **(a)** before, **(b)** after exposure to p_{H_2O}=280 Pa, T=400 °C for 16h and **(c)** after post-treatment STEM-EELS analysis. For each nanoparticle, the STEM-EELS spectrum and the digital diffractogram of the dashed circle region is given. Micrographs were acquired in vacuum at room temperature.

APPENDIX B

Determination of Mo K$\alpha_{1,2}$ / S K$\alpha_{1,2}$ X-ray emission peaks ratios

This Appendix presents a detailed explanation of the procedure leading to the determination of Mo/S X-ray emission peaks ratios used in Section 4.4 to study the depletion of the sulphide phase of Ni-MoS_2/ZrO_2 catalysts.

After acquisition, raw EDX spectra were background subtracted manually fitting the bremsstrahlung signal using the Bruker Esprit software. Two distinct regions of the spectra were then selected:

1. **1.4 - 2.75 keV** containing Zr L$\alpha_{1,2}$, Zr Lβ_1, Mo L$\alpha_{1,2}$, S K$\alpha_{1,2}$, Mo Lβ_1, S Kβ, Mo Lβ_2 X-ray experimental peaks

2. **16.8 - 18 keV** containing Mo Kα_2 and Mo Kα_1 X-ray experimental peaks

For each energy region, the net counts associated to each experimental peak was extracted deconvolving the spectrum profile in a number of Gaussian equal to the number of experimental peaks. In order to obtain a reliable fit that could reflect the physics behind X-ray generation and detection, a set of conditions were applied:

1. The center of each Gaussian was fixed to the theoretical position of the associated X-ray line, according to [104].

2. Gaussians within a single energy region were set to share the same FWHM. This was justified by the fact that the major contribution to the FWHM of an experimental X-ray peak is given by the energy resolution of the EDX detector, which is a function of energy [105].

3. The relative amplitude of Gaussians associated to X-ray lines of the same element was fixed according to the intensity ratios between K- and L-shell lines presented in [104].

X-ray counts in the spectrum obey Gaussian statistic [105], hence the absolute error on the peak area was estimated to be $3\sqrt{N}$, where N is the number of net counts for each peak and corresponding to three standard deviations.

Mo Kα$_{1,2}$ peak area was obtained summing Mo Kα$_2$ and Mo Kα$_1$ areas and the associated error was estimated propagating the error of the sum using the formula:

$$\Delta_{A+B} = \sqrt{\Delta_A^2 + \Delta_B^2} \tag{B.1}$$

Where Δ_X represents the absolute error on the generic measure X. The final Mo/S ration is thus obtained dividing the net counts associated to Mo Kα$_{1,2}$ and S Kα$_{1,2}$. The error associated to the ratio was estimated propagating the error of the ratio as follows:

$$\Delta_{A/B} = \frac{A}{B}\sqrt{\left(\frac{\Delta_A}{A}\right)^2 + \left(\frac{\Delta_B}{B}\right)^2} \tag{B.2}$$

The following table presents the result of the analysis and includes the adjusted R^2 values as a measure of the goodness of the Gaussian fit in each energy region.

	Fit peak 1.4 – 2.75 keV			Fit peak 16.8 – 18 keV				
	Adj. R^2	Area S Kα$_{1,2}$	3σ error	Adj. R^2	Area Mo Kα$_{1,2}$	3σ error	Mo/S area ratio	Propagated error
Fresh catalyst	0.997	13115	344	0.945	1896	131	0.1446	0.011
	0.998	139226	1119	0.970	18638	410	0.1339	0.0031
0.3 vol% 1-octanethiol	0.979	5272	218	0.925	2144	139	0.407	0.031
	0.993	14477	361	0.973	4291	197	0.296	0.015
2% DMDS	0.997	37292	579	0.974	4504	201	0.1208	0.0057
2% DMDS H_2O/H_2S=46	0.997	119018	1035	0.978	14394	360	0.1209	0.0032
	0.997	46866	649	0.956	4888	210	0.1043	0.0047
	0.997	332760	1731	0.976	53905	697	0.1620	0.0023

APPENDIX C

In situ ETEM oxidation of soot:silver mixtures acquired in diffraction mode

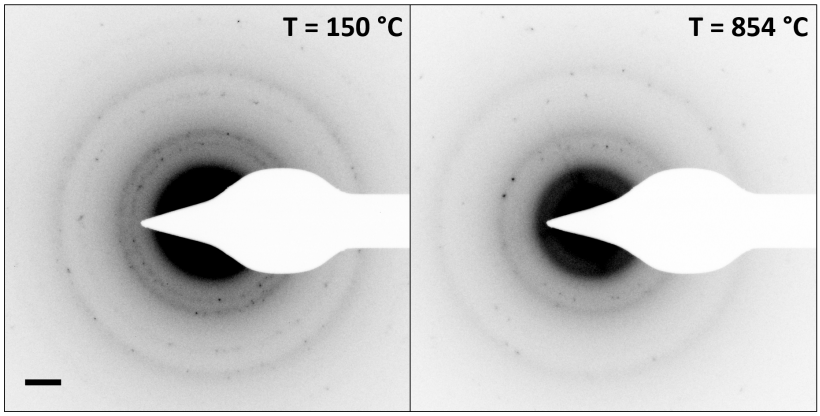

(a) Loose contact condition

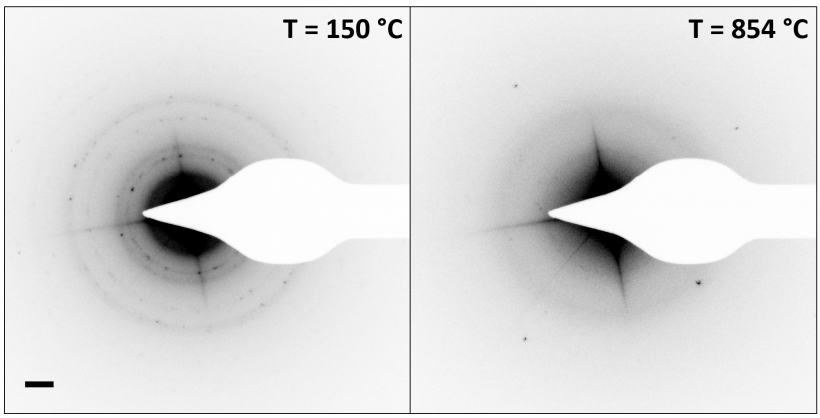

(b) Tight contact condition

Figure C.1: Electron diffraction patterns acquired at the beginning and at the end of in situ oxidation of a silver:soot mixture in **(a)** loose and **(b)** tight contact conditions. Scalebar is 2 nm^{-1}.

Included papers

Paper 1

Stability and resistance of nickel catalysts for hydrodeoxygenation: carbon deposition and effects of sulfur, potassium, and chlorine in the feed

Peter Mølgaard Mortensen, Diego Gardini, Hudson Wallace Pereira de Carvalho, Christian Danvad Damsgaard, Jan-Dierk Grunwaldt, Peter Arendt Jensen, Jakob Birkedal Wagner, Anker Degn Jensen. *Catalysis Science & Technology*, 10(4):3672-3686, 2014.

Paper 2

Inhibition and Deactivation of Ni-MoS_2 by Bio-oil Impurities during Hydrodeoxygenation of Phenol and Octanol

Peter Mølgaard Mortensen, Diego Gardini, Christian Danvad Damsgaard, Jan-Dierk Grunwaldt, Peter Arendt Jensen, Jakob Birkedal Wagner, Anker Degn Jensen. *Under revision.*

Paper 3

Visualizing the Mobility of Silver During Catalytic Soot Oxidation

Diego Gardini, Jakob Munkholt Christensen, Christian Danvad Damsgaard, Anker Degn Jensen, Jakob Birkedal Wagner. *Applied Catalysis B: Environmental*, Accepted.

Catalysis Science & Technology

PAPER

View Article Online
View Journal

Cite this: DOI: 10.1039/c4cy00522h

Stability and resistance of nickel catalysts for hydrodeoxygenation: carbon deposition and effects of sulfur, potassium, and chlorine in the feed†

Peter M. Mortensen,‡[a] Diego Gardini,[b] Hudson W. P. de Carvalho,[c] Christian D. Damsgaard,[bd] Jan-Dierk Grunwaldt,[c] Peter A. Jensen,[a] Jakob B. Wagner[b] and Anker D. Jensen*[a]

Received 22nd April 2014,
Accepted 13th June 2014

DOI: 10.1039/c4cy00522h

www.rsc.org/catalysis

The long term stability and resistance toward carbon deposition, sulfur, chlorine, and potassium of Ni/ZrO_2 as a catalyst for the hydrodeoxygenation (HDO) of guaiacol in 1-octanol (as a model compound system for bio-oil) has been investigated at 250 °C and 100 bar in a trickle bed reactor setup. Without impurities in the feed good stability of the Ni/ZrO_2 catalyst could be achieved over more than 100 h of operation, particularly for a sample prepared with small Ni particles, which minimized carbon deposition. Exposing the catalyst to 0.05 wt% sulfur in the feed resulted in rapid deactivation with complete loss of activity due to the formation of nickel sulfide. Exposing Ni/ZrO_2 to chlorine-containing compounds (at a concentration of 0.05 wt% Cl) on-stream led to a steady decrease in activity over 40 h of exposure. Removal of the chlorine species from the feed led to the regaining of activity. Analysis of the spent catalyst revealed that the adsorption of chlorine on the catalyst was completely reversible, but chlorine had caused sintering of nickel particles. In two experiments, potassium, as either KCl or KNO_3, was impregnated on the catalyst prior to testing. In both cases deactivation was persistent over more than 20 h of testing and severely decreased the deoxygenation activity while the hydrogenation of guaiacol was unaffected. Overall, sulfur was found to be the worst poison, followed by potassium and then chlorine. Thus, removal/limitation of these species from bio-oil is a requirement before long term operation can be achieved with this catalyst.

1. Introduction

Conversion of biomass with flash pyrolysis followed by hydrodeoxygenation has been identified as a prospective path to engine fuels usable in the current infrastructure.[1] In pyrolysis, the biomass is rapidly heated to form char, gas, and a liquid product, the so-called pyrolysis oil or bio-oil. This oil has a low heating value, contains water, is acidic, and has a low shelf storage time, among others, and is therefore not directly suitable as an engine fuel but represents a good energy carrier for bio-energy.[2–4] The unfavorable characteristics of bio-oil are all associated with relatively high oxygen and water content, up to 40 wt% oxygen and 30 wt% water.[1,5]

In hydrodeoxygenation, bio-oil is upgraded with high pressure hydrogen (up to 200 bar) in the presence of a catalyst at temperatures around 300 °C. Hereby the oxygen functionality can be removed, making an oil product more similar to conventional crude oil, which can be used for the production of engine fuels.[1] A challenge in this concept is to find suitable catalysts for HDO which possess good activity and long term stability. Particularly, long term stability is challenging due to the formation of carbon species on the catalysts or due to impurities in the feed.[1,6–10]

Previous work has primarily focused on the traditional hydrotreating catalysts such as Ni–MoS_2 and Co–MoS_2,[1,11,12] noble metal catalysts based on Pd or Ru,[13–16] or nickel based catalysts[17–21] for HDO. However, little work on these catalytic systems has been devoted to evaluate long term stability or resistance toward impurities during HDO.[1,8,9] Elliott *et al.*[13] tested the stability of HDO of real bio-oil in a continuous flow reactor at 340 °C and 75–130 bar over a Pd/C catalyst and found catalyst lifetimes of up to *ca.* 100 h. They reported carbon build-up and thereby plugging as one of the major problems. Other studies have reported lifetimes of

[a] *Department of Chemical and Biochemical Engineering, Technical University of Denmark, Søltofts Plads, Building 229, DK-2800 Lyngby, Denmark. E-mail: aj@kt.dtu.dk; Fax: +45 4588 2258; Tel: +45 4525 2841*
[b] *Center for Electron Nanoscopy, Technical University of Denmark, Fysikvej, Building 307, DK-2800 Lyngby, Denmark*
[c] *Institute for Chemical Technology and Polymer Chemistry, Karlsruhe Institute of Technology (KIT), Engesserstrasse 20, D-79131 Karlsruhe, Germany*
[d] *CINF, Department of Physics, Technical University of Denmark, Fysikvej, Building 307, DK-2800 Lyngby, Denmark*
† Electronic supplementary information (ESI) available: Reduction temperature, transport evaluation, detailed product composition, and XAFS measurements. See DOI: 10.1039/c4cy00522h
‡ Present address: Haldor Topsøe A/S, Nymøllevej 55, DK-2800 Lyngby, Denmark.

up to 200 h for a Co–MoS_2/Al_2O_3 catalyst.[22] However, from an industrial perspective 100–200 h is a short time.

Carbon on the catalyst is formed because many of the oxy compounds present in bio-oil can undergo polymerization and polycondensation reactions on the catalyst surface, forming polyaromatic species which can lead to the blocking of both the pore structure and the active sites of the catalyst.[23]

As bio-oil is derived from biomass, it will contain traces of a range of inorganic compounds like alkali metals, transition metals, chlorine, sulfur, and phosphorus.[24] Especially, potassium, chlorine, and sulfur can be found in relatively high amounts in bio-oil with concentrations of up to 0.3 wt%, 0.6 wt%, and 0.8 wt%, respectively.[25] These are therefore of significant concern.

In the current work, the long term stability of a Ni/ZrO_2 catalyst has been investigated in a continuous flow setup, using a bio-oil model compound system consisting of guaiacol in 1-octanol. The stability of Ni based catalysts is interesting since much research currently is investigating nickel based catalysts intended for use in HDO of bio-oil[17–20] or lignin and lignosulfonate upgrading.[26,27] It is very well known that nickel based catalysts are particularly prone to sulphur deactivation.[28,29] However, recent results from Song *et al.*[26,27] have, surprisingly, indicated that the high partial pressure of hydrogen used in these reactions might help prevent the deactivation of nickel catalysts due to sulphur. Additionally, Ni/ZrO_2 has been specifically found attractive in a screening study for HDO of phenol.[21] Guaiacol was chosen as the bio-oil model compound to make the interpretation of stability comprehensible, with this molecule representing the phenolic fraction. These are present in significant quantities in bio-oil,[30,31] are among the most persistent molecules of bio-oil,[9,32] and are partly responsible for carbon formation.[9,33] 1-Octanol was chosen as the solvent for guaiacol due to its ideal phase characteristics under the given experimental conditions and furthermore to serve as a simple alcohol model compound.

2. Experimental

2.1 Catalyst synthesis

5 wt% Ni/ZrO_2 was prepared by the incipient wetness method with $Ni(NO_3)_2{\cdot}6H_2O$ (Sigma-Aldrich, ≥97.0%) as the precursor. Zirconia was supplied by Saint-Gobain NorPro and of type SZ 6*152 with an impurity of 3.3% SiO_2, a specific surface area of 140 $m^2\ g^{-1}$, and a pore volume of 0.32 ml g^{-1}. This was initially ground to a particle size of 300–600 μm. In the synthesis, the precursor was dissolved in water equivalent to the pore volume of the support and subsequently mixed with the support. After impregnation, the sample was dried at 70 °C for 12 h. A batch of the catalyst was additionally calcined at 400 °C with a heating rate of 10 °C min^{-1} and a holding time of 4 h.

2.2 Catalytic tests

The experiments were performed in a high pressure gas and liquid continuous flow setup, which is schematically shown in Fig. 1. High pressure liquid is fed from a recirculation loop where a liquid pump and a back pressure valve are used to adjust the feed pressure. From this loop, liquid is fed to the reactor through mass flow controllers and mixed with high pressure gas before reaching the catalyst loaded in the reactor. Liquid samples are withdrawn from a high pressure separator regulated on the basis of the liquid height at 25 °C. The liquid product is collected in a sample manifold placed in a small fume hood, where 8 different samples can be collected as a function of time. Gas from the separator flows through a regulator valve controlling the system pressure, passes a flow meter, and ends at a GC-TCD (GC-2014, Shimadzu). Online sampling on the GC-TCD allows analysis in 20 min intervals.

The reactor tube is made of 316 SS steel and has an inner diameter of 8 mm. This is placed inside a 2 cm inner diameter pressure shell which is placed in a three-zone furnace. The feed gas is introduced in the bottom of the pressure shell and heated in up-flow in the pressure shell before being mixed with the liquid feed in the top flange of the pressure shell and then goes into the reactor tube.

For loading of the reactor tube, 2.5 g of the corresponding catalyst in a sieve fraction of 300–600 μm was mixed with 7.5 g of glass beads in a sieve fraction of 212–245 μm to dilute the catalyst bed and thereby obtain better control of the exothermic reactions. The glass bead–catalyst mixture was suspended on a quartz wool plug in the reactor, which was supported on a crossbar in the reactor. The loading profile of the reactor from the crossbar up was 1 cm of quartz wool, 12 cm of catalyst/glass beads, 1 cm of quartz wool, and 25 cm of glass beads (1 mm in diameter).

All catalysts were initially reduced in the reactor tube by heating at a rate of 10 °C min^{-1} to 500 °C in flow rates of 250 Nml min^{-1} H_2 and 250 Nml min^{-1} N_2 at atmospheric pressure and kept under these conditions for 2 h. 500 °C was sufficient for the complete reduction of Ni/ZrO_2 as found by *in situ* X-ray absorption spectroscopy (XAS) (further information is found in the ESI†). The experimental conditions were set directly after reduction.

Evaluation of transport limitations by Mears criterion[34] for the given sieve fraction of catalyst particles revealed that

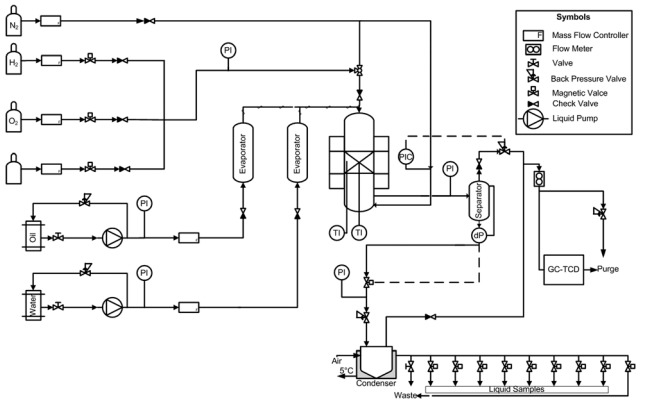

Fig. 1 Flow sheet of the high pressure gas and liquid continuous flow setup used for studying the stability of Ni/ZrO_2 during HDO.

the system was not limited by boundary layer diffusion. However, some internal diffusion resistance was present, at least for the most active catalysts where the effectiveness factor was calculated to be in the range of 0.89–0.97 for the applied particle size distribution. However, as the present work deals with catalyst stability it was concluded that this limitation did not influence the interpretation of the results and may even make the experiments closer to industrial conditions. Additional information on the evaluation of transport limitations can be found in the ESI.†

A feed mixture of 10 vol% guaiacol (Sigma-Aldrich, ≥99%) in 1-octanol (Sigma-Aldrich, ≥99%) was used as the bio-oil model compound system and fed at a flow rate of 0.2 ml min^{-1}. 1-Octanol was chosen as solvent (despite not being considered a bio-oil component) due to its relatively high boiling point (195 °C at ambient pressure[35]) and ability to mix with guaiacol in a homogenous phase. Hydrogen (AGA, 99.9%) and nitrogen (AGA, 99.9%) were fed to the reactor at a flow rate of 300 Nml min^{-1} and 100 Nml ml^{-1}, respectively, corresponding to 6 times the required hydrogen for complete hydrogenation and deoxygenation of the feed. During the reactions the reactor was maintained at a constant pressure of 100 bar and the set point of the reactor oven was 250 °C for all experiments. The actual temperature in the catalyst bed varied between 245 °C in the bottom of the bed and 251 °C in the top part. The slightly higher temperature in the top part of the bed was due to the exothermic reactions taking place.

In the deactivation experiments either 1-octanethiol (Sigma-Aldrich, ≥98.5%) or 1-chlorooctane (Sigma-Aldrich, 99%) was added to the liquid feed corresponding to a concentration of 0.05 wt% S or Cl, respectively. Assuming 100% decomposition to H_2S or HCl, this would correspond to concentrations of 177 ppm_v and 162 ppm_v in the feed gas, respectively.

KCl or KNO_3 was impregnated to separate batches of the catalyst by incipient wetness impregnation. A portion of the uncalcined Ni/ZrO_2 catalyst was weighed and a solution (corresponding to the pore volume of the given fraction of the catalyst) with KCl or KNO_3 in H_2O was prepared. KCl and KNO_3 were impregnated in amounts corresponding to the molar content of nickel. After mixing the solution and the catalyst, it was dried for 12 h at 70 °C.

A blank experiment without the catalyst was performed under the same conditions as the experiments. This led to a conversion of 2% for guaiacol and hardly any conversion of 1-octanol, showing that the reactor was not catalytically active for the reaction.

2.3 Product analysis

Analysis of the liquid product was done with a Shimadzu GC-MS/FID-QP2010 Ultra EI gas chromatograph fitted with a Supelco Equity-5 column. Identification of the products was done using a mass spectrometer (MS) where their concentration was quantified using a flame ionization detector (FID). External standards were prepared for guaiacol, cyclohexanol, cyclohexane, methanol, 1-octanol, and heptane. The concentrations of the remaining peaks were calculated from the FID on the basis of the effective carbon number method,[36] where the concentration of a compound was found as:

$$C_i = C_{ref} \cdot \frac{A_i}{A_{ref}} \frac{\nu_{eff,ref}}{\nu_{eff,i}} \quad (1)$$

Here C is the concentration, A the area of the peak in the FID spectrum, and ν_{eff} the effective carbon number. Index i refers to the compound with the unknown concentration and index ref refers to a reference compound where the concentration is known. In all calculations with this formula, heptane was used as reference. The effective carbon number was taken from the review by Schofield.[36]

The conversion, X, was calculated as:

$$X = \left(1 - \frac{C_{out,i} \cdot \nu_{out}}{C_{0,i} \cdot \nu_0}\right) \cdot 100\% \quad (2)$$

Here C_i is the concentration of compound i and ν is the volumetric flow. Index out refers to the conditions after the reactor, index 0 refers to the inlet conditions, and i refers to the compound of relevance. The conversions of both guaiacol and 1-octanol were evaluated.

The yields (Y_i) of relevant products were calculated as:

$$Y_i = \frac{C_{out,i} \cdot \nu_{out}}{C_{0,j} \cdot \nu_0} \cdot 100\% \quad (3)$$

Index i here refers to the compound of relevance and index j refers to the initial reactant, guaiacol or 1-octanol.

The selectivity (S_i) of a compound (i) was calculated as:

$$S_i = \frac{Y_i}{X} \cdot 100\% \quad (4)$$

The degree of deoxygenation (DOD) was calculated as:

$$DOD = \left(1 - \frac{F_{O,out}}{F_{O,in}}\right) \cdot 100\% \quad (5)$$

Here F_O is the molar flow of oxygen in oxygen-containing species except water either in or out of the reactor. To give further emphasis on the HDO of guaiacol, which only constituted 10% of the feed, the degree of deoxygenation for the guaiacol related compounds (DOD^{GUA}) was also calculated:

$$DOD^{GUA} = \left(1 - \frac{\sum_i F_{O\ of\ i,out}}{2 \cdot F_{Guaiacol,in}}\right) \cdot 100\% \quad (6)$$

Here index i refers to the oxygen-containing guaiacol related compounds, which were guaiacol, methanol, cyclohexanol, and 2-methoxy-cyclohexanol.

The carbon balance was evaluated on the basis of the GC-MS/FID and GC-TCD measurements:

$$\Delta C = \left(\frac{\sum_i \nu_i \cdot F_i - 7 \cdot F_{0,\text{Guaiacol}} - 8 \cdot F_{0,\text{1-Octanol}}}{7 \cdot F_{0,\text{Guaiacol}} + 8 \cdot F_{\mathbf{0},\text{1-Octanol}}} \right) \cdot 100\% \qquad (7)$$

Here ΔC is the carbon deviation in % and F_i is the molar flow of compound i. All compounds identified in the GC-MS/FID and GC-TCD analyses were included in the carbon balance. Generally the carbon balance was closed within 5%. This will be discussed in further detail later.

2.4 Catalyst characterization

The specific surface area was estimated by a seven-point BET measurement (Quantachrome iQ2).[37] Nitrogen adsorption at its boiling point was used in the p/p_0 range of 0.05–0.3. The produced Ni/ZrO_2 catalyst had a specific surface area of 130 $m^2\ g^{-1}$.

The local structure of the catalysts was characterized by XAS in terms of X-ray absorption near edge structure (XANES) and extended X-ray absorption fine structure (EXAFS) at the Ni-K edge at the XAS beamline at the synchrotron radiation source ANKA (Karlsruhe, Germany). The reduction of Ni/ZrO_2 was followed *in situ*, whereas the structures of the poisoned catalysts were analyzed *ex situ* after the corresponding reactions.

The catalyst reduction was followed by Quick-XAS in fluorescence detection mode.[38] For this purpose, a 63–125 μm sieved fraction of the calcined catalyst was filled into a quartz capillary microreactor (1 mm internal diameter) resulting in plug flow-like conditions.[39] The reaction mixture, 25% H_2 in He, in a flow rate of 50 mL min^{-1} was supplied by a gas delivery system. The microreactor was heated with a gas blower (FMB Oxford) from room temperature up to 500 °C using a heating rate of 5 °C min^{-1} similar to the setup in ref. 40. Spectra were recorded every 12.5 °C.

The *ex situ* studied catalysts were pressed to pellets using cellulose and then measured in transmission mode.

XAS data analysis was carried out using Athena and Artemis softwares of IFEFFIT.[41] The spectra were energy calibrated from a reference metal foil and the background was subtracted and then normalized. The structural parameters were obtained by adjusting theoretical backscattering phases and amplitudes (*ab initio* calculated with FEFFG).[42]

The relative proportions between the starting and the formed Ni species were estimated by linear combinations carried out using Athena IFEFFIT software.[41] Linear combination fitting was performed in the spectral range of −20 to 90 eV relative to the energy of the edge. This procedure allowed tracking the proportion of species consumed and formed during catalyst activation. The references for the linear combinations were the first spectrum at room temperature and the last spectrum at 500 °C.

Powder X-ray diffraction (XRD) measurements were carried out using a PANalytical X'Pert PRO diffractometer in a Bragg–Brentano Theta–Theta geometry. A 300–600 μm sieved fraction of the catalyst was analyzed at a $25° < 2\theta < 100°$ range using monochromatic Cu-Kα radiation (λ = 1.5418 Å). XRD data treatment was carried out using PANalytical HighScore Plus 3.0.5 and the average crystallite size was estimated using the Scherrer equation. The crystallite size analysis was carried out neglecting the lattice strain effects.

The elemental composition of the catalysts was analyzed by means of energy dispersive X-ray spectroscopy (EDX) with an FEI Quanta 200 ESEM FEG scanning electron microscope (SEM) operated at 10 kV and equipped with an Oxford Instruments 80 mm^2 X-Max silicon drift detector. A few particles of 300–600 μm sieved fractions of the catalyst were fixed to standard SEM aluminium stubs with Vishay Micro-Measurements M-Bond epoxy resin and mechanically polished in order to reach a flat geometry configuration.

EDX elemental maps were acquired using a FEI Osiris transmission electron microscope (TEM) operated at 200 kV in scanning mode (STEM). Catalysts were crushed in a mortar and dry dispersed on a copper TEM grid coated with lacey carbon. Maps were smoothed using a 7 × 7 pixels kernel smoothing algorithm implemented in the Bruker Esprit software.

Temperature programmed oxidation (TPO) was performed in a tubular furnace. Prior to the analysis the spent catalyst samples were washed in ethanol and dried. 50–100 mg of the catalyst was placed in a ceramic boat and placed in the center of the oven and heated at a ramp of 11 °C min^{-1} in a flow rate of 1100 Nml min^{-1} gas (10% oxygen in nitrogen). Online CO and CO_2 measurements were performed with an IR detector (ABB automation GmbH AO2020 Uras26) in order to quantify the amount of carbon on the catalyst. Carbon determination was done on the basis of the integration of the CO/CO_2 signal relative to flow and time.

Elemental analysis of nickel on the catalysts was performed using inductively coupled plasma atomic emission spectroscopy (ICP-OES). For the analysis, the samples were crushed and melted together with potassium pyrosulfate. This was dissolved in a solution of water and HCl and then analyzed by plasma emission spectroscopy. The instrument was calibrated with a certified nickel standard.

3. Kinetic model

For a more quantitative description of the catalyst activity a kinetic model was developed for the HDO of guaiacol and 1-octanol.

On the basis of the product distributions (see ESI†), guaiacol was indicated to react by the sequential reaction scheme shown in Fig. 2. Guaiacol was initially hydrogenated to 2-methoxy-cyclohexanol, followed by hydrogenolysis of the ether bond to form cyclohexanol and methanol. Both alcohols can subsequently undergo hydrodeoxygenation to produce, respectively, cyclohexane and methane. The same reaction scheme has been observed for the HDO of guaiacol over noble metal catalysts,[43–45] indicating that this is a general reaction path over transition metal catalysts.

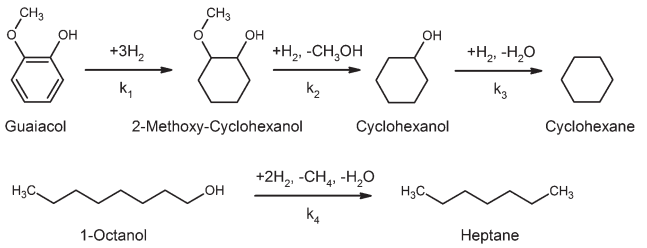

Fig. 2 Observed reaction path of guaiacol and 1-octanol.

Heptane was the primary product from 1-octanol (as shown in Fig. 2), and therefore a cracking type reaction appeared to be the primary path for this compound. Previous work on Pt catalysts with C_3 alcohols[46,47] has shown that these undergo an initial dehydrogenation to form an aldehyde, which can then undergo decarbonylation producing ethane and CO. Probably, the same reaction pathway occurs for 1-octanol over nickel catalysts. However, under the conditions used in our experiments, the CO produced can be hydrogenated into CH_4. Note that the Gibbs free energy of the reaction $CO + 3H_2 \leftrightarrow H_2O + CH_4$ is −96.4 kJ mol^{-1} at 500 K (calculated with the data from ref. 48), and the equilibrium is completely displaced toward CH_4 formation. This could explain why only CH_4 was detected in the gas phase.

Based on the experimental observations summarized in Fig. 2, the reaction rates of the four identified main reactions were assumed to be:

$$r_1 = k_1 \cdot C_{\text{Guaiacol}} \cdot P_{H_2}{}^{n} \quad (8)$$

$$r_2 = k_2 \cdot C_{\text{2-Methoxy-cyclohexanol}} \cdot P_{H_2}{}^{m} \quad (9)$$

$$r_3 = k_3 \cdot C_{\text{Cyclohexanol}} \cdot P_{H_2}{}^{l} \quad (10)$$

$$r_4 = k_4 \cdot C_{\text{1-Octanol}} \cdot P_{H_2}{}^{k} \quad (11)$$

Here r_i is the rate of reaction i, k_i is the rate constant for reaction i, C_i is the concentration of compound i in the liquid phase, P_{H_2} is the partial pressure of H_2, and n–k are the unknown reaction orders of hydrogen. All hydrocarbon reaction orders were assumed 1st order. Previous work has shown that 1st order reactions of guaiacol, anisole, and phenol HDO sufficiently describe these systems for simple interpretations.[19,21,49]

As a significant excess of hydrogen was used in all experiments the partial pressure of hydrogen was assumed constant and therefore the kinetic expressions were reduced to:

$$r_1 = k_1' \cdot C_{\text{Guaiacol}} \quad (12)$$

$$r_2 = k_2' \cdot C_{\text{2-Methoxy-cyclohexanol}} \quad (13)$$

$$r_3 = k_3' \cdot C_{\text{Cyclohexanol}} \quad (14)$$

$$r_4 = k_4' \cdot C_{\text{1-Octanol}} \quad (15)$$

Based on these rate terms a kinetic model was derived for a plug flow reactor system. The derivation of this model can be found in the ESI.†

4. Results and discussion

4.1 Long term stability

Two batches of 5 wt% Ni/ZrO_2 were prepared: one where the batch was calcined at 400 °C for 4 h and one where the batch was not calcined. Both samples were reduced at 500 °C as found from the analysis in the ESI.† In this way two different nickel particle sizes could be obtained, as described by Louis *et al.*[50] In the following, Ni/ZrO_2-CR will refer to the calcined and reduced sample and Ni/ZrO_2-DR will refer to the directly reduced sample.

Representative STEM-EDX elemental maps for both Ni/ZrO_2-CR and Ni/ZrO_2-DR are shown in Fig. 3(a) and (b), respectively. From these and other acquired maps it was possible to estimate the Ni particle size being on average 9 nm for Ni/ZrO_2-DR and 18 nm for Ni/ZrO_2-CR based on size measurements of more than 80 particles for each catalyst (size distributions are shown in Fig. 4). Although the number of analyzed particles cannot be considered fully statistically representative, the size distribution for Ni/ZrO_2-DR was noticed to be more homogenous than that for Ni/ZrO_2-CR. For the calcined sample, a tail toward larger particle sizes and the presence of very big ones (>100 nm) were observed (*cf.* Fig. 4(a)), indicating agglomeration of some nickel during the preparation procedure. It is worth mentioning that using the Ni signal to estimate the average particle size does not take into account any oxidation effect that could occur by exposure of the sample to air. However, XRD measurements did not reveal any evident oxidation of the Ni nanoparticles.

The two catalysts were tested at 250 °C and 100 bar with a feed of 0.2 ml min^{-1} and 10 vol% guaiacol in 1-octanol corresponding to a WHSV of 4.0 h^{-1}. In Fig. 5(a) and (b) the development in the conversion of guaiacol and 1-octanol and the degree of deoxygenation (DOD) is shown as a function of time on stream (TOS) for both catalysts.

For Ni/ZrO_2-CR (*cf.* Fig. 5(a)) a maximum DOD of 40% was achieved after 3.5 h of TOS and hereafter the activity decreased throughout the 80 h of TOS, ending at 23% DOD. The relative decrease of DOD^{GUA} was more pronounced, from a value of 17% to only 4% after 80 h TOS. Thus, little deoxygenation of the guaiacol was found at the end of the experiment.

For Ni/ZrO_2-DR (*cf.* Fig. 5(b)) the DOD was significantly higher, in the order of 90%. Also the stability of this catalyst was better, as the DOD^{GUA} only decreased from a value of 71% to 61% after 104 h TOS.

Both catalysts converted all guaiacol into 2-methoxy-cyclohexanol as a first step. However, the selectivities toward subsequently formed cyclohexanol and cyclohexane were only *ca.* 30% and *ca.* 1% on Ni/ZrO_2-CR, respectively, but *ca.* 50% and *ca.* 25% on Ni/ZrO_2-DR, respectively (detailed development in the yield of 2-methoxy-cyclohexanol, cyclohexanol,

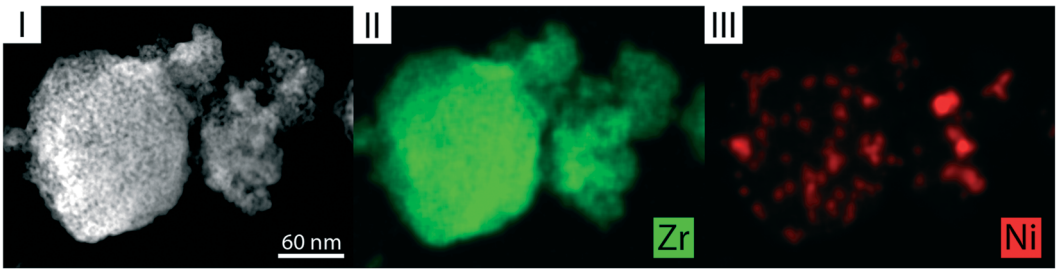

(a) STEM-HAADF micrograph of Ni/ZrO_2-CR

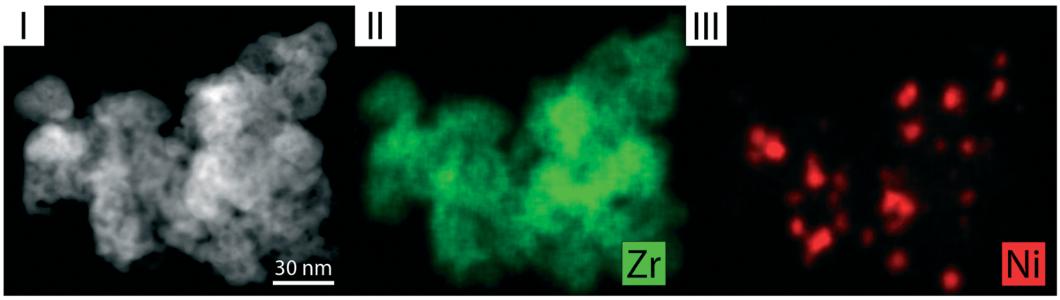

(b) STEM-HAADF micrograph of Ni/ZrO_2-DR

Fig. 3 STEM-HAADF micrographs of Ni/ZrO_2-CR (a) and Ni/ZrO_2-DR (b). Sub-image I: STEM-HAADF micrograph. Sub-image II: zirconium EDX elemental distributions. Sub-image III: nickel EDX elemental distributions.

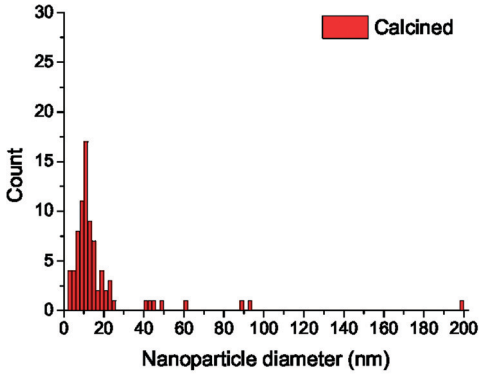

(a) Ni/ZrO_2-CR size distribution

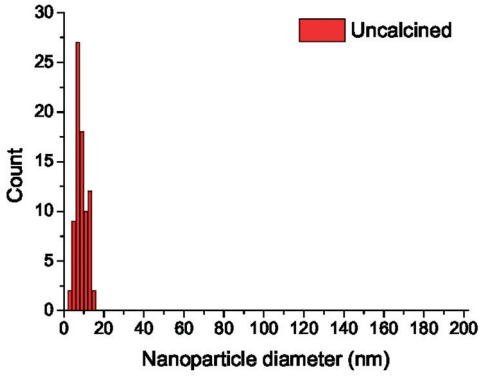

(b) Ni/ZrO_2-DR size distribution

Fig. 4 Size distributions of Ni/ZrO_2-CR (a) and Ni/ZrO_2-DR (b) based on the STEM-HAADF images.

cyclohexane, and heptane can be found in the ESI†). Similarly, the conversion of 1-octanol was around 30% on Ni/ZrO_2-CR but 100% on Ni/ZrO_2-DR. In both cases >90% selectivity toward heptane was observed.

Using the simple kinetic model in section 3, the catalytic activity of the catalysts was quantified, as summarized in Table 1. The rate of hydrogenation (k_1') could not be distinguished on the two catalysts, as both had 100% conversion. However, the rate of the three deoxygenation reactions (k_2', k_3', and k_4') were a factor of 2.4, 6.9, and approximately 10 times higher for Ni/ZrO_2-DR compared to Ni/ZrO_2-CR, respectively.

The large difference in activity can be linked to the difference in nickel particle size on the catalysts. In our previous study,[51] we have shown that the deoxygenation activity of nickel based catalysts can be increased by decreasing the nickel crystallite size due to an increasing fraction of step/corner sites on the nickel nanoparticles, which are more active for the C–O bond breaking reaction. Thus, Ni/ZrO_2-DR would also be expected to have the highest activity. Comparing the individual rate constants, the decarbonylation reaction and the deoxygenation reaction were most dependent on the type of nickel sites available, as k_3' and k_4' had the largest relative increase. In contrast, the hydrogenolysis reaction (k_2') was less structure sensitive, which may be linked to a lower bond dissociation energy of the methoxy group (343 kJ mol^{-1} (ref. 52)) compared to that of the alcohol group (385 kJ mol^{-1} (ref. 52)).

Detailed analysis of the GC-MS/FID data revealed that the side products included methanol, cyclopentane, cyclopentanol, octane, methoxy-cyclohexane, cyclohexanone, dicyclohexyl ether, and dioctyl ether. A complete carbon analysis from the experiment with Ni/ZrO_2-DR (*cf.* Fig. 5(b)) showed that 91% of the carbon fed to the reactor was recovered in the oil phase,

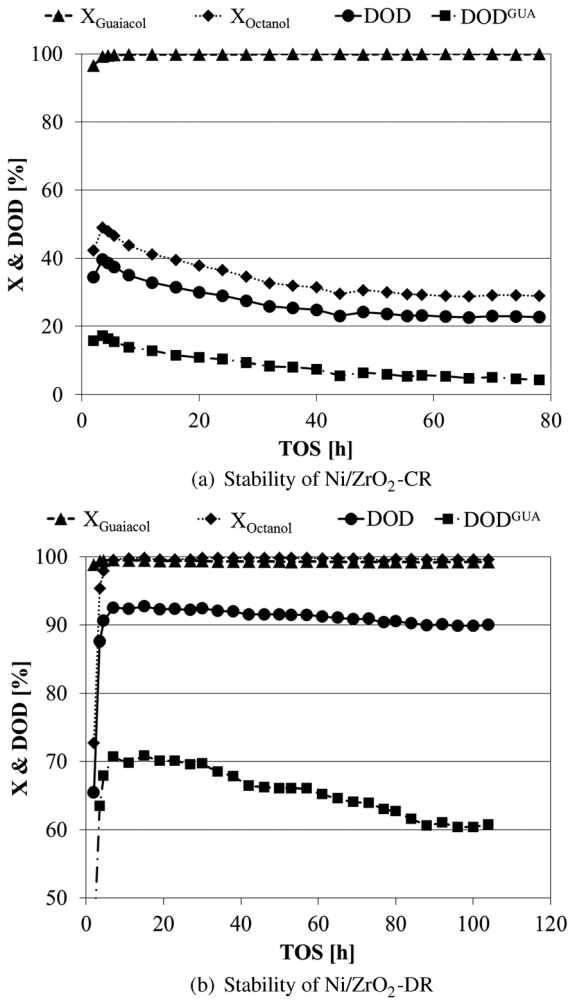

Fig. 5 Development of the conversions of guaiacol and 1-octanol and DOD for Ni/ZrO_2-CR (a) and Ni/ZrO_2-DR (b) as a function of TOS. DOD^{GUA} is the degree of deoxygenation of the guaiacol feed. Ni/ZrO_2-CR was calcined and then reduced while Ni/ZrO_2-DR was not calcined but reduced directly from nickel nitrate. T = 250 °C, P = 100 bar, F_{oil} = 0.2 ml min^{-1}, WHSV = 4.0 h^{-1}.

Table 1 Comparison between Ni/ZrO_2-CR and Ni/ZrO_2-DR, summarizing kinetic parameters, nickel particle size, and carbon build-up on the spent catalysts. Ni/ZrO_2-CR was calcined and then reduced while Ni/ZrO_2-DR was not calcined but reduced directly from nickel nitrate. Kinetic parameters evaluated at TOS = 4.5 h for Ni/ZrO_2-CR and TOS = 10 h for Ni/ZrO_2-DR. Carbon content measured on the basis of temperature programmed oxidation (TPO)

Catalyst	Ni/ZrO_2-CR	Ni/ZrO_2-DR
Total TOS [h]	79	106
Crystallite size [nm]	18	9
Carbon content [wt%]	3.7	1.5
Carbon content [mol C mol^{-1} Ni]	3.6	1.5
Carbon deposition rate [μg_C g_{cat}^{-1} h^{-1}]	463	144
k_1' [ml kg_{cat}^{-1} min^{-1}]	≥500	≥500
k_2' [ml kg_{cat}^{-1} min^{-1}]	51	126
k_3' [ml kg_{cat}^{-1} min^{-1}]	11	76
k_4' [ml kg_{cat}^{-1} min^{-1}]	52	≥500

1% in the aqueous phase, and 6% in the gas phase; the remaining 2% was unaccounted for. The aqueous phase contained methanol, cyclohexanol, and 2-methoxy-cyclohexanol as primary carbon-containing species. Loss of carbon to the gas phase was due to the formation of CH_4, which was linked to the reduction of methanol formed from guaiacol and the hydrogenation of CO from 1-octanol (see discussion in section 3).

In order to quantify the carbon on the spent catalyst, the used catalysts were subjected to TPO (*cf.* results in Table 1). For both catalysts the deposited carbon was oxidized in the temperature range of 200–500 °C with a peak in the CO/CO_2 evolution just below 400 °C. Comparing Ni/ZrO_2-DR to Ni/ZrO_2-CR, Ni/ZrO_2-CR had 3 times higher carbon deposition rate. This correlates with a more pronounced deactivation on Ni/ZrO_2-CR as a function of TOS (*cf.* Fig. 5(a)).

Borowiecki[53] showed that the carbon deposition rate during steam reforming of butane at 500 °C was highly dependent on the nickel crystallite size, increasing by more than an order of magnitude when increasing the nickel crystallite size from 6.5 nm to 35.7 nm. Bengaard *et al.*[54] later described that carbon nucleation takes place on the step sites on the nickel crystals and builds carbon layers from there. These layers are however only thermodynamically stable when the carbon layer is larger than ≈25 Å and therefore the associated nickel facet, on which the carbon layer is built, should be larger than this. Increasing the carbon layer size further decreases the total energy and therefore stabilizes carbon formation further. Thus, large nickel particles are in other contexts also found more prone to carbon formation.[53–55]

Another potential source of deactivation is the loss of active metal by leaching. Therefore, the nickel content was investigated in one case for Ni/ZrO_2-DR by ICP-OES. Prior to reduction, this catalyst had a nickel content of 4.5–4.9 wt%; the span is indicated because Ni/ZrO_2-DR contained some fraction of NO_3 which should be corrected for in the comparison. After 104 h of operation the nickel content was again measured to be 4.7 wt%. Hence, the extent of nickel leaching from the catalyst is negligible.

In conclusion, carbon deposition appears to be the most probable cause for the observed loss of activity in Fig. 5. This is supported by the observation that the rate of deactivation is faster on Ni/ZrO_2-CR compared to Ni/ZrO_2-DR, which correlates with the threefold higher carbon build-up rate on Ni/ZrO_2-CR compared to Ni/ZrO_2-DR.

4.2 Effect of impurities in the feed

To understand other potential deactivation mechanisms during the HDO of bio-oil, exposure to sulfur, chlorine, and potassium in the feed was simulated, as described in the following. Ni/ZrO_2-DR was used for all of these measurements due to the higher activity of this sample.

4.2.1 Effect of sulfur. In an experiment similar to those discussed in section 4.1, 0.3 vol% 1-octanethiol (corresponding to 0.05 wt% S in the feed) was added to the feed with 10% guaiacol in 1-octanol after 8 h of TOS. This impurity of sulfur is representative of what can be present in bio-oil.[25] Fig. 6(a)

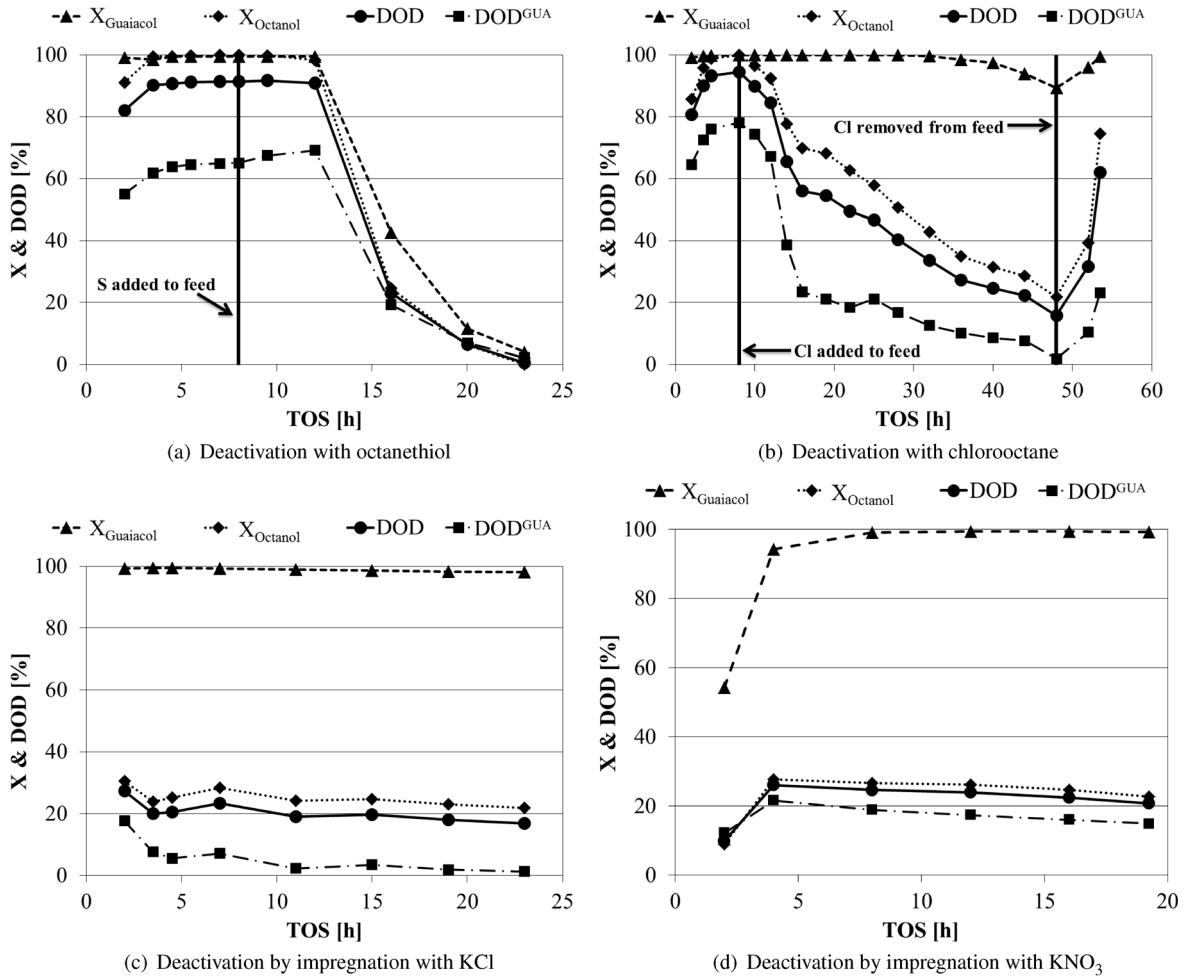

Fig. 6 Development of the conversions of guaiacol and 1-octanol and DOD over the Ni/ZrO_2-DR catalyst as a function of time when deactivated with 1-octanethiol (a), 1-chlorooctane (b), KCl (c), and KNO_3 (d). 1-Octanethiol and 1-chlorooctane were added to the feed in concentrations of 0.05 wt% S and 0.05 wt% Cl, respectively, after 8 h of TOS as indicated in the respective figures. 1-Chlorooctane was removed from the feed again after 48 h of TOS, as shown in Fig. 6(b). KCl or KNO_3 were impregnated in stoichiometric amounts relative to nickel on a fresh batch of catalyst prior to testing. DOD^{GUA} is the degree of deoxygenation isolated for the guaiacol feed. T = 250 °C, P = 100 bar, F_{oil} = 0.2 ml min^{-1}, WHSV = 4.0 h^{-1}.

shows the development in the conversion of guaiacol and 1-octanol and the DOD as a function of TOS. Initially, when sulfur was not present, the conversions of both 1-octanol and guaiacol were 100% and the DOD was in the order of 90–92%, similar to the experiment with no impurities present (*cf.* Fig. 5(b)). After the introduction of sulfur, the activity rapidly decreased. After only 12 h exposure to sulfur the conversions of both guaiacol and 1-octanol were almost 0%. The conversion of both compounds and the DOD decreased in a similar way, indicating that deactivation was taking place as a progressive front in the catalyst bed, inhibiting all types of reactions as the sulfur front progressed. The relative exposure to sulfur over the entire experiment was 1.1 mol S : mol Ni, showing an effective deactivation by sulfur.

1-Octanethiol was quantitatively converted to heptane or octane and H_2S throughout the experiment. Only in the final two liquid samples, where the activity had severely decreased, traces of 1-octanethiol could be found.

4.2.2 Effect of chlorine. In a similar experiment to the one described above, a new batch of catalyst was loaded and started with a standard feed of 10 vol% guaiacol in 1-octanol. After 8 hours of operation the feed was changed to 10 vol% guaiacol and 0.3 vol% 1-chlorooctane (corresponding to 0.05 wt% Cl in the feed) in 1-octanol. This corresponds to the quantity of organic bound chlorine, which can be found in bio-oil.[25] In Fig. 6(a) the development in the conversion of guaiacol and 1-octanol and the DOD is seen as a function of TOS. Initially, the activity was similar to the reference case (*cf.* Fig. 1) with no impurities in the feed, but after the introduction of chlorine to the feed the activity of deoxygenation steadily decreased; the DOD decreased from a level of 90–95% to 16% after 40 h exposure to the chlorine-containing feed. However, the DOD^{GUA} decreased even faster and dropped to below 25% after only 8 h of exposure.

The conversion of 1-octanol followed the development in the DOD. In contrast, the conversion of guaiacol was only

slightly affected, dropping a few percentage points only after 30 h of exposure. With respect to the product composition, the yield of cyclohexane decreased from 40% prior to deactivation to only a few percent after *ca.* 10 h exposure to chlorine. The cyclohexanol yield was not affected to the same extent and only decreased from a yield of 32% to 17% after 40 h of exposure. 2-Methoxy-cyclohexanol ended up being the primary product with a yield of more than 70% (see ESI†). Thus, chlorine deactivation is primarily associated with the deoxygenation activity of the catalyst.

Throughout the chlorine exposure period there was a complete conversion of 1-chlorooctane to heptane and HCl. Nickel has also previously been reported as effective in the hydrodechlorination (HDCl) reaction.[56–59] The exposure to chlorine atoms has therefore been high throughout the exposure period.

After 48 h of TOS the feed was changed back to the chlorine-free feed (10 vol% guaiacol in 1-octanol). At this point the activity increased (*cf.* Fig. 6(b)) toward the initial activity level before terminating the experiment. Thus, the deactivation by chlorine appears to be at least partly reversible, indicating that the Cl species blocking the surface sites required for HDO can desorb. The desorption of chlorine from the catalyst was further proven by verification of Cl^- in the liquid product collected at a TOS of 51–52 h by precipitation with $AgNO_3$.

In the 40 h where chlorine was fed to the reactor the relative exposure was 3.2 mol Cl : 1 mol Ni. All of this shows that the deactivation by chlorine was not as persistent as that by sulfur, which is probably linked to reversible adsorption.

4.2.3 Effect of potassium. In the third type of deactivation experiment, KCl was impregnated on a batch of Ni/ZrO_2-DR in stoichiometric amounts relative to nickel on the catalyst. Fig. 6(c) shows the conversions of guaiacol and 1-octanol and the DOD as a function of TOS for this catalyst. In this experiment the DOD was in the order of 20%, the conversion of guaiacol was 100% throughout 24 h of TOS, while the conversion of 1-octanol was in the order of 25%. The primary part of deoxygenation was from 1-octanol, as the DOD^{GUA} was only around 5% with the 2-methoxy-cyclohexanol yield being 76% (see ESI†). Thus, similar to the Cl deactivated catalyst, KCl deactivated mainly the deoxygenation reactions. However, in contrast to the Cl deactivated case this catalyst was persistently deactivated as the DOD was constantly low throughout the 24 h experiment.

The isolated effect of potassium was tested by impregnation of a batch of Ni/ZrO_2-DR with stoichiometric amounts of KNO_3 relative to nickel. In Fig. 6(d) the conversions of guaiacol and 1-octanol and the DOD are shown as a function of TOS in a 20 h experiment. Comparing to Fig. 6(c) with KCl deactivation, similar trends are seen: the conversion of guaiacol was high (100%) throughout the test, 2-methoxy-cyclohexanol was the primary product (56% selectivity) from guaiacol, and deactivation was persistent as the activity was stable throughout 20 h of TOS. However, the DOD^{GUA} was around 10–15% for the KNO_3 deactivated sample compared to 5% in the KCl case, and therefore the interaction with the guaiacol molecule was more hampered in the latter case.

4.3 XRD and TEM characterization of poisoned catalysts

4.3.1 Sulfur poisoning. The presence of sulfur in the spent catalyst was confirmed by STEM-EDX elemental maps, showing a very similar spatial distribution of sulfur and nickel signals (*cf.* Fig. 7). Thus, it appears that sulfur preferentially adsorbed on the nickel.

XRD measurements (*cf.* Fig. 8(a)) revealed the presence of zirconia and a reflection at $2\theta \approx 45.2°$ could be identified as NiS, confirming the permanent deactivation of the catalyst by the formation of a non-active nickel sulfide phase. XRD analysis was carried out on the same specimen used for XAS measurements, and therefore the presence of cellulose is due to the XAS sample preparation procedure. Three reflections at $2\theta \approx 41°$, 37.9° and 36.8° belong to the sample stage. Cellulose peak labelling was carried out according to Park *et al.*[60]

4.3.2 Chlorine poisoning. XRD analysis of the chlorine poisoned catalyst after reaction showed reflections belonging exclusively to zirconia and nickel (*cf.* Fig. 8(b)). The absence of chlorine species was further confirmed by EDX measurements carried out by SEM. This supports the non-persistent nature of chlorine indicated in the catalytic experiment described in section 4.2.2.

The nickel crystallite size was estimated from XRD patterns by applying the Scherrer equation on the $2\theta \approx 44.5°$ reflection. The nickel particle was estimated to be approximately 39 nm for the chlorine exposed sample, indicating a growth of nickel particles during exposure to chlorine. The growth of nickel nanoparticles could be explained by the formation of mobile Ni–Cl species upon reaction of HCl with surface oxides.[61]

In order to investigate in more detail the extent of chlorine poisoning, the deactivation experiment was repeated with a new batch of catalyst and without restoring the chlorine-free feed. XRD and SEM-EDX analyses of the sample after 48 h of TOS did not reveal the presence of chlorine species. Thus, it appears that chlorine species readily will leave nickel when exposed to air and/or hydrogen (during cooling down of the experiment).

4.3.3 Potassium poisoning. Impregnation of KCl on the catalyst resulted in the deposition of KCl crystals on the catalyst surface, as visualized by both STEM-EDX (Fig. 9) and XRD (Fig. 8(c)) measurements on the spent sample. The XRD measurements indicate an average crystallite size of >100 nm, approximately the size limit after which the

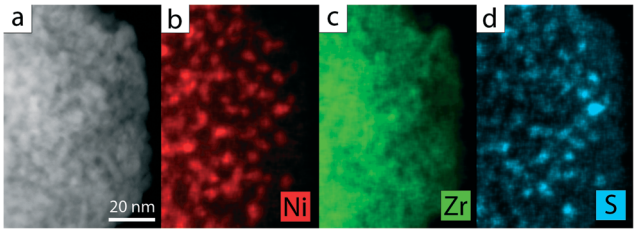

Fig. 7 (a) STEM-HAADF micrograph of the sulfur poisoned catalyst with (b) nickel, (c) zirconium and (d) sulfur EDX elemental distributions.

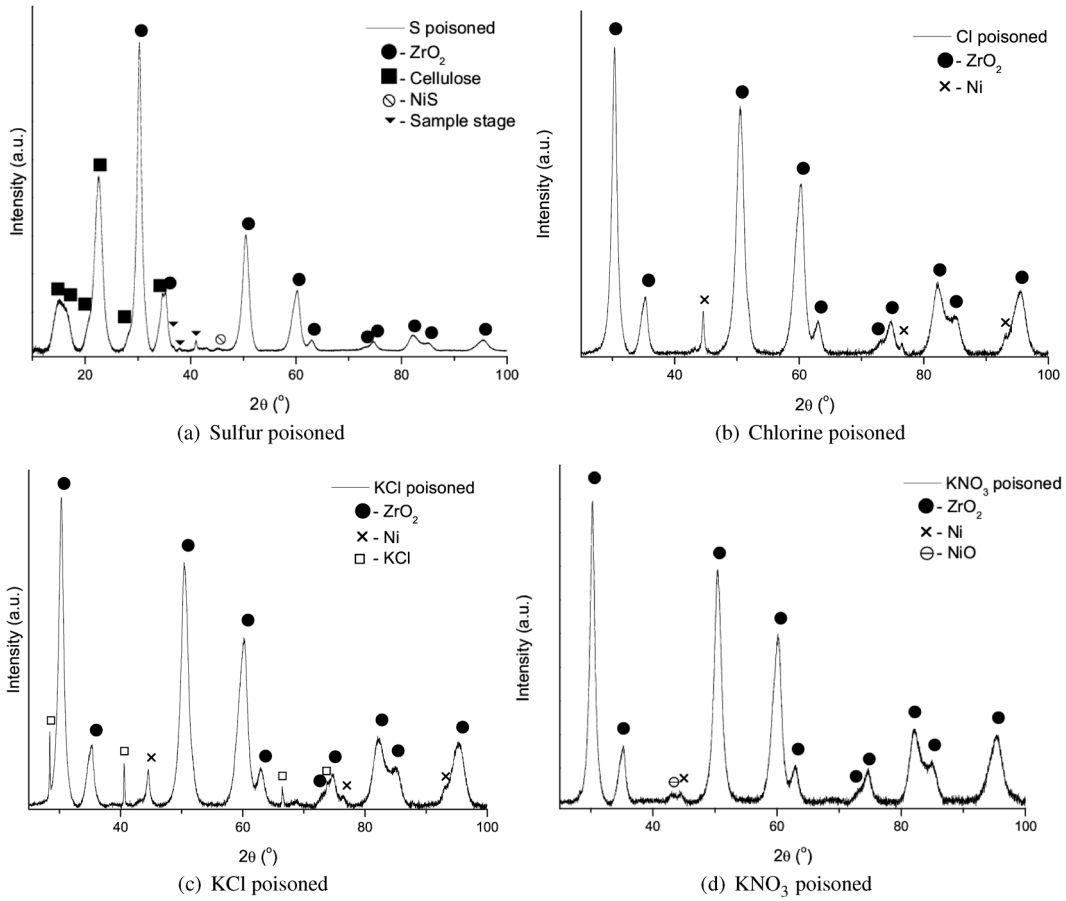

Fig. 8 X-ray diffraction patterns of the poisoned catalysts. (a) Sulfur poisoned catalyst, (b) chlorine poisoned catalyst, (c) KCl poisoned catalyst, (d) KNO_3 poisoned catalyst.

reflection peak width is dominated by instrumental broadening. KCl particle sizes of up to 600 nm were reported as shown by STEM-EDX maps in Fig. 9.

The nickel crystallite size was estimated to be approximately 24 nm for the KCl impregnated catalyst after 25 h TOS, indicating growth of the nickel particle size. However, this was less pronounced when compared to the chlorine poisoned samples but could be explained once more by the presence of HCl during reaction.

Analyzing the spent KNO_3 impregnated catalyst by SEM-EDX confirmed the presence of potassium. However, XRD analysis did not reveal any potassium-containing crystalline phase (*cf.* Fig. 8(d)). This indicates a more homogeneous deposition of potassium compared to that in the KCl impregnated catalyst.

In an attempt to visualize the potassium deposition, STEM-EDX mapping of this catalyst resulted in the redistribution of potassium all over the scanned area. This is due to the high mobility of potassium ions under the effect of the electron beam.[62,63]

4.4 XAS analysis of poisoned catalysts

To further understand the deactivation mechanism of the Ni/ZrO_2 catalyst caused by the impurities in the feed, the local structure of the poisoned samples was analyzed by XAS.

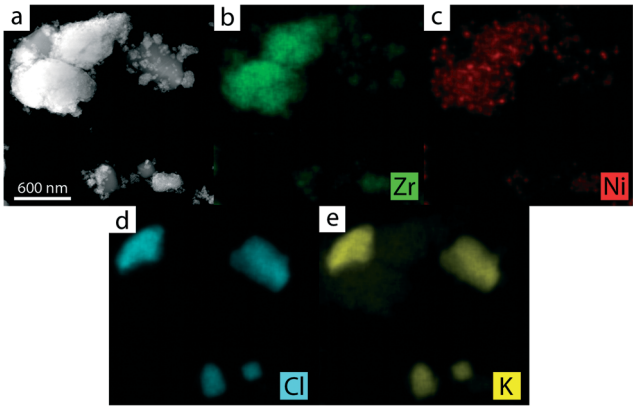

Fig. 9 (a) STEM-HAADF micrograph of the potassium chloride poisoned catalyst with (b) zirconium, (c) nickel, (d) chlorine and (e) potassium EDX elemental distributions.

Table 2 presents the respective refined structural parameters of the investigated samples. Additional information can be found in the ESI.†

Initially, the local structure of the unreduced Ni/ZrO_2-CR and the *in situ* reduction of this catalyst (as discussed in the ESI†) was studied by refining the extended X-ray absorption fine structure (EXAFS) spectra. Table 2 presents the respective

Table 2 Structural parameters around the Ni absorber atom refined from the EXAFS spectra of the Ni/ZrO_2 catalysts, comparing calcined, freshly reduced, and poisoned samples. Calcined is the fresh catalyst prior to reduction and reduced is the same catalyst after *in situ* reduction. *N* is the number of neighboring atoms, *r* the distance, σ^2 the mean-square disorder in the atomic distances, and ρ the misfit between experimental data and theory. $S_0^2 = 0.78$, calcined: $\Delta E_0 = -3.5 \pm 0.5$, reduced: $\Delta E_0 = 6.5 \pm 0.6$, carbon: $\Delta E_0 = 5.8 \pm 0.9$, chlorine: $\Delta E_0 = 6.6 \pm 1.4$, KCl: $\Delta E_0 = 7.1 \pm 0.7$, KNO_3: $\Delta E_0 = 6.6 \pm 1.0$ and $C_3 = 4.9 \times 10^{-4}$ Å^3, sulfur: $\Delta E_0 = 8.4 \pm 0.5$

Sample	Shell	Atom	*N*	*r* [Å]	$\sigma^2 \times 10^{-3}$ [Å^2]	ρ [%]
Calcined	1st	O	6.0[c]	2.06[a,e]	6.2 ± 0.5[e]	0.7
	2nd	Ni	8.6 ± 0.9[e]	2.96[a,e]	9.6 ± 1.0[e]	
Reduced	1st	Ni	9.2 ± 1.0[e]	2.48 ± 0.01[e]	5.5 ± 0.8[e]	3.2
	2nd	Ni	6.9 ± 3.4[e]	3.46 ± 0.02[e]	14.0 ± 0.5[e]	
	3rd	Ni	21.6 ± 7.8[e]	4.33± 0.01[e]	10.2± 3.3[e]	
Carbon poisoned[b]	1st	O	0.8 ± 0.3[e]	1.98 ± 0.05[e]	7.1 ± 0.1[d,e]	0.5
	2nd	Ni	8.7 ± 0.9[e]	2.48 ± 0.01[e]	6.3 ± 1.0[e]	
Chlorine poisoned	1st	O	0.8 ± 0.2[e]	2.00± 0.04[e]	7.2 ± 0.1[a,e]	0.9
	2nd	Ni	8.5 ± 0.6[e]	2.48[a,e]		
KCl poisoned	1st	O	0.6 ± 0.1[e]	2.00 ± 0.04[e]	7.2 ± 0.1[a,e]	0.9
	2nd	Ni	9.9 ± 0.4[e]	2.48[a,e]	6.8 ± 0.5[e]	
KNO_3 poisoned	1st	O	1.1 ± 0.3[e]	1.96 ± 0.01[e]	7.9 ± 4.5[a,e]	1.3
	2nd	Ni	8.3 ± 0.9[e]	2.48 ± 0.01[e]	9.2 ± 1.0[e]	
Sulfur poisoned	1st	S	5.0[c]	2.22 ± 0.01[e]	7.6 ± 0.4[e]	2.5

[a] Fitted uncertainty less than 1%. [b] Ni/ZrO_2-DR used in the long term testing in section 1 analyzed after 106 h TOS. [c] Constrained. [d] Ni–O σ^2 was constrained and fitted together with a $NiCO_3$ reference. [e] Fitted.

refined structural parameters. For the calcined catalyst, nickel was coordinated by 6 oxygen atoms at 2.06 Å, and the second coordination shell was composed of 8.6 ± 0.9 nickel atoms at 2.96 Å. This local order was similar to NiO as expected; however, the number of nickel atoms at the second coordination shell was lower than that for NiO (12 nickel atoms[64]), which indicates a small particle size of the NiO-like structure after calcination.

The local chemical environment of the reduced catalyst was similar to a metallic nickel phase; nevertheless, the refined 9.2 ± 1.0 coordination number of the first shell showed that the reduced phase of the catalyst was structured as small particles.

Analyzing the poisoned catalyst samples, the local nickel surroundings in the KNO_3, KCl, chlorine, and carbon (catalyst exposed to feed for 106 h TOS) poisoned catalysts remained similar to the reduced catalyst as seen from the refined structural parameters in Table 2 with the exception of a slight oxidation after reaction. This was evidenced by a peak shoulder around 2 Å at the Fourier transformed EXAFS spectra (see the ESI†). These oxygen atoms were most likely at the surface of the nickel metallic particles since the refined bond distances, varying between 1.96–2.00 Å, were shorter than the expected Ni–O distance in the NiO reference (2.08 Å).[64] The oxidation was probably a consequence of exposure to air in between the experiment and XAS measurements, as confirmed in the XRD pattern of potassium and chlorine poisoned catalysts (*cf.* Fig. 8) by the presence of a weak peak at $2\theta \approx 43°$, corresponding to a NiO phase.

The Fourier transformed EXAFS spectra of the carbon and KCl poisoned catalysts presented a significant amplitude reduction (see the ESI†). The structural refinements showed that this amplitude reduction was mainly caused by the increase of the structural disorder expressed by the mean-square disorder in the atomic distances.

The KNO_3 poisoned catalyst showed the strongest amplitude reduction as a result of high structural disorder. The refinement of its EXAFS spectrum required an additional structural parameter (the third cumulant of disorder, C_3), which measures the asymmetry of atomic vibrations. A reduction in the magnitude of the Ni signal was also observed in the XRD pattern of this catalyst (*cf.* Fig. 8). Note that in both the Fourier transformed EXAFS spectra (see the ESI†) and the EXAFS fit (*cf.* Table 2) there was a stronger contribution for backscattering at low *R* values. This provides evidence of stronger oxidation.

Overall, these XAS measurements support the observations in section 4.3 that chlorine and alkali metals did not induce a phase change of nickel crystals. Thus, the deactivation caused by these species was probably related to deposition on the nickel surface.

The Ni-K-edge XANES of the sulfur poisoned catalyst sample showed the presence of a completely different Ni species, as shown in Fig. 10. The refinements suggested the conversion of the metallic Ni phase to a NiS-like phase, which explains the total loss of the catalytic activity in this case. This is supported by the STEM-EDX map in Fig. 7, also showing that sulfur is distributed similar to Ni, confirming the tight interaction and the reflection of NiS in the XRD pattern (*cf.* Fig. 8(a)).

4.5 Comparison of deactivation mechanisms

For a quantitative comparison of the different deactivation phenomena, the kinetic constants (*cf.* section 3) for the four reactions were calculated, as summarized in Table 3. Sulfur was the worst poison as this catalyst was completely inactive with respect to both hydrogenation and deoxygenation after a relatively short exposure time.

XRD, STEM-EDX, and EXAFS analyses revealed that the sulfur deactivated catalyst was a bulk deactivation (*cf.* Fig. 10),

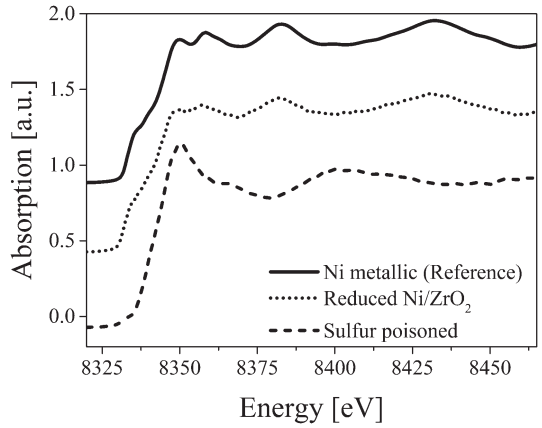

Fig. 10 Ni-K edge X-ray absorption spectra of the sulfur poisoned catalyst compared to fresh Ni/ZrO_2 and Ni reference.

Table 3 Rate constants for the HDO of guaiacol and 1-octanol deactivated with different poisons relative to the case shown in Fig. 5(b) with Ni/ZrO_2-DR and no poison. The effectiveness factor was in the order of 89–97% for the fastest reactions. TOS refers to when the kinetic parameters are evaluated in comparison to Fig. 5 and 6. T = 250 °C, P = 100 bar, F_{oil} = 0.2 ml min^{-1}, WHSV = 4.0 h^{-1}

	TOS	Exposure	k_1'	k_2'	k_3'	k_4'
Poison	[h]	[mol_{poison} mol_{Ni}^{-1}]	[ml kg_{cat}^{-1} min^{-1}]			
None[a]	—	—	607	124	80	602
Carbon[b]	104	3×10^4	>500	108	52	>500
Sulfur	23	1.1	0	0	0	0
Chlorine	48	3.2	181	25	6.1	20
KCl	11	1	>500	26	0.6	22
KNO_3	12	1	>500	53	0	24

[a] Determined from an intrinsic activity measurement with 1.5 g of 5 wt% Ni/ZrO_2 in a sieve fraction of 125–180 μm but otherwise similar experimental conditions with an effectiveness factor of ≥99% for the fastest reactions. [b] Ni/ZrO_2-DR used in long term testing in section 4.1.

which explains the distinct deactivation profile (*cf.* Fig. 6(a)). It has previously been shown that sulfur forms a saturated surface layer on nickel at p_{H_2S}/p_{H_2} ratios above 5×10^{-6}.[65] The p_{H_2S}/p_{H_2} threshold for the formation of bulk sulfides decreases with decreasing temperatures and is in the order of 10^{-4} at 400 °C[66] but even lower at 250 °C. In the current experiment the p_{H_2S}/p_{H_2} ratio was 2×10^{-4}, assuming all 1-octanethiol decomposed to H_2S, which is at the range where bulk nickel sulfides can be expected to form.

Sulfur deactivation of nickel catalysts has previously been established to be severely persistent and hardly reversible in hydrogen alone.[67,68] Removal of sulfur can be achieved to some extent by steaming of the catalyst, but this requires temperatures above 600–650 °C.[69,70] Thus, the catalyst appears to have little chance to avoid deactivation or to regain activity in the presence of sulfur species during HDO. Our results therefore do not confirm the observations by Song *et al.*[26,27] that a high hydrogen pressure can retain Ni in an active state in HDO. The reason for this difference is not clear but may be related to the fact that Song *et al.* made experiments in a batch reactor where deactivation phenomena are generally difficult to observe, especially if the reactor is overloaded with catalyst.

In steam reforming, where nickel catalysts have been extensively used, alkali metals are known to readily deactivate the catalyst.[28,29,55,71] Bengaard *et al.*[54] showed that the deactivation of nickel catalysts for steam reforming by alkali metals was due to adsorption at the step sites on the nickel crystallites.

In this study, doping with potassium hindered the deoxygenation reactions (k_2', k_3', and k_4' in Table 3), while the hydrogenation reaction was less affected. This correlates with the Ni/ZrO_2 catalyst having two different types of active sites: vacancy sites in the oxide support where phenolic compounds can adsorb prior to hydrogenation and exposed low coordinated metal sites facilitating the deoxygenation reactions.[51] Thus, it appears that potassium (and maybe also chlorine) preferentially interacts with low coordinated nickel sites, as primarily the deoxygenation reactions were affected.

The most striking difference in the deactivation by chlorine and potassium was the reversibility of chlorine poisoning. This reversibility of chlorine adsorption has also been observed previously.[72–75] During methane steam reforming over Ni/Al_2O_3, Ortego *et al.*[74] observed that the reforming activity decreased when co-feeding CH_3Cl. However, the activity was regained when removing the chlorine source from the feed. Richardson *et al.*[73] also found that the presence of chlorocarbons in the feed led to a decrease in the methane steam reforming activity of the Ni/Al_2O_3 catalyst. They concluded that chlorine formed an equilibrium surface layer on the nickel, which at high coverage could deplete the availability of hydrogen. Similarly, Kiskinova and Goodman[72] found that the poisoning effect on CO and H_2 adsorption on a Ni (100) surface increased in the order of P < S < Cl. However, despite Cl being the worst poison, it easily reacted with H_2 to form HCl. Thus, if the chlorine surface layer was not maintained, chlorine was found to not affect the catalytic activity for methanation.

In summary, the current and previous studies show that chlorine primarily affects the catalytic activity when fed to the reactor as the coverage appears to be determined by a fast adapting equilibrium with hydrogen and HCl. This is supported by the identification of Cl^- in the liquid product after ending the exposure to chlorooctane. However, investigation on the particle size by XRD did indicate that chlorine also causes the sintering of nickel particles on the catalyst.

Impregnation with KCl and KNO_3 shows similar trends. Deactivation by KCl, however, was slightly worse, especially considering the hydrogenolysis reaction (k_2). This may be linked to the sintering induced by the presence of chlorine.

5. Conclusion

In this study, the stability and resistance of Ni/ZrO_2 have been investigated during long term operation in a continuous

flow setup for the HDO of a mixture of 10% guaiacol in 1-octanol as a model system for bio-oil.

The stability and activity of the catalyst were dependent on the nickel particle size. Small nickel particles (9 nm) gave higher activity for HDO and produced less coke on the catalyst compared to larger particles (18 nm). Over a period of more than 100 h of operation a carbon build-up of only 1.5 wt% relative to the catalyst mass occurred for the 9 nm Ni/ZrO_2 catalyst and therefore the activity only decreased slightly from a DOD of 92% on the fresh catalyst to a DOD of 90% after 104 h TOS. The higher activity of the small crystallites was linked to their higher fraction of low coordinated sites which are efficient in the deoxygenation reaction. The smaller particle size was also responsible for lower carbon deposition since it is more difficult for carbon to form on these.

The catalyst stability was very sensitive to sulfur, chlorine, and potassium exposure. Addition of sulfur to the feed resulted in a fast deactivation of the catalyst, leading to the complete loss of activity over a period of only 12 h, which was roughly the time required to feed the stoichiometric amount of sulfur relative to the available nickel. In line with this, STEM-EDX, XRD, and XAS measurements unraveled the formation of a NiS-like phase, which was the reason for the complete loss of activity for this catalyst.

Chlorine did not deactivate the catalyst to the same extent as sulfur, as primarily the deoxygenation activity decreased after exposure to chlorine over a 40 h period, corresponding to the addition of 3.2 mol Cl : 1 mol Ni. Furthermore, the deactivation by chlorine was reversible as the activity could be partly regained when removing chlorine from the feed. XRD, XAS, or EDX could not identify chlorine on the spent catalyst, supporting the reversibility of the deactivation mechanism. It is suggested that chlorine binds to the nickel surface sites (preferentially low coordinated sites) and forms an equilibrium surface layer, but when not co-feeding Cl this layer is easily removed. However, chlorine also appeared to cause sintering of nickel particles on the catalyst, providing a more persistent deactivation/activity loss.

KCl and KNO_3 were impregnated on two different batches of catalyst to test the effect of potassium. The hydrogenation activity was not affected in any significant degree in the two cases, but the deoxygenation activity was markedly decreased and was persistent over more than 20 h of operation. Probably, potassium blocked low coordinated sites leading to the loss of deoxygenation activity, as these are considered crucial for this reaction.

Comparing the different poisons, sulfur was the most severe, while potassium and chlorine were in the same order of magnitude when looking at the activity. However, as potassium is a persistent poison this must be considered more severe than chlorine.

An overall conclusion is that it is difficult to obtain long term stability for nickel based catalysts for bio-oil HDO as any of the three types of poisons tested will lead to deactivation. From an application point of view it would be crucial to remove specifically sulfur from the feed beforehand and to minimize potassium and chlorine impurities. The present work shows the importance of studying the stability of catalysts for HDO of bio-oil under more realistic conditions.

Acknowledgements

This work is part of the Combustion and Harmful Emission Control (CHEC) research center at The Department of Chemical and Biochemical Engineering at the Technical University of Denmark (DTU). The present work is financed by DTU and The Catalysis for Sustainable Energy initiative (CASE), funded by the Danish Ministry of Science, Technology and Innovation.

The A. P. Møller and Chastine Mc-Kinney Møller Foundation is gratefully acknowledged for its contribution towards the establishment of the Center for Electron Nanoscopy at the Technical University of Denmark.

The Interdisciplinary Centre for Electron Microscopy (CIME) at EPFL is gratefully acknowledged for the use of the FEI Tecnai Osiris TEM.

We thank ANKA for providing beamtime and Stefan Mangold, Henning Lichtenberg, and Alexey Boubnov for help during or around beamtime.

BMBF is acknowledged for the support of the *in situ* infrastructure at ANKA (KIT, Karlsruhe) within the MatAkt project (05K10VKB).

References

1 P. M. Mortensen, J.-D. Grunwaldt, P. A. Jensen, K. G. Knudsen and A. D. Jensen, *Appl. Catal., A*, 2011, **407**, 1–19.
2 A. V. Bridgwater, S. Czernik, J. Diebold, D. Meier, A. Oasmaa, C. Peakocke, J. Piskorz and D. Radlein, *Fast Pyrolysis of Biomass: A Handbook*, CPL Press, Newbury, 1999.
3 J. Holmgren, R. Marinageli, P. Nair, D. C. Elliott and R. Bain, *Hydrocarbon Process.*, 2008, 95–103.
4 K. Raffelt, E. Henrich, A. Koegel, R. Stahl, J. Steinhardt and F. Weirich, *Appl. Biochem. Biotechnol.*, 2006, **129**, 153–164.
5 Q. Zhang, J. Chang, T. Wang and Y. Xu, *Energy Convers. Manage.*, 2007, **48**, 87–92.
6 T. V. Choudhary and C. B. Phillips, *Appl. Catal., A*, 2011, **397**, 1–12.
7 Q. Bu, H. Lei, A. H. Zacher, L. Wang, S. Ren, J. Liang, Y. Wei, Y. Liu, J. Tang, Q. Zhang and R. Ruan, *Bioresour. Technol.*, 2012, **124**, 470–477.
8 Z. He and X. Wang, *Catal. Sustainable Energy Prod.*, 2012, **1**, 28–52.
9 E. Furimsky, *Catal. Today*, 2013, **217**, 13–56.
10 H. Wang, J. Male and Y. Wang, *ACS Catal.*, 2013, **3**, 1047–1070.
11 D. C. Elliott, *Energy Fuels*, 2007, **21**, 1792–1815.
12 I. Graca, J. M. Lopes, H. S. Cerqueira and M. F. Ribeiro, *Ind. Eng. Chem. Res.*, 2012, **52**, 275–287.
13 D. C. Elliott, T. R. Hart, G. G. Neuenschwander, L. J. Rotness and A. H. Zacher, *Environ. Prog. Sustainable Energy*, 2009, **28**, 441–449.
14 D. C. Elliott and T. R. Hart, *Energy Fuels*, 2009, **23**, 631–637.

15 J. Wildschut, F. H. Mahfud, R. H. Venderbosch and H. J. Heeres, *Ind. Eng. Chem. Res.*, 2009, **48**, 10324–10334.
16 J. Wildschut, J. Arentz, C. B. Rasrendra, R. H. Venderbosch and H. J. Heeres, *Environ. Prog. Sustainable Energy*, 2009, **28**, 450–460.
17 V. A. Yakovlev, S. A. Khromova, O. V. Sherstyuk, V. O. Dundich, D. Y. Ermakov, V. M. Novopashina, M. Y. Lebedev, O. Bulavchenko and V. N. Parmon, *Catal. Today*, 2009, **144**, 362–366.
18 M. V. Bykova, D. Y. Ermakov, V. V. Kaichev, O. Bulavchenko, A. A. Saraev, M. Y. Lebedev and V. A. Yakovlev, *Appl. Catal., B*, 2012, **113–114**, 296–307.
19 M. V. Bykova, S. G. Zavarukhin, L. I. Trusov and V. A. Yakovlev, *Kinet. Catal.*, 2013, **54**, 40–48.
20 V. O. Dundich, S. A. Khromova, D. Y. Ermakov, M. Y. Lebedev, V. M. Novopashina, V. G. Sister, A. I. Yakimchuk and V. A. Yakovlev, *Kinet. Catal.*, 2010, **51**, 728–734.
21 P. M. Mortensen, J.-D. Grunwaldt, P. A. Jensen and A. D. Jensen, *ACS Catal.*, 2013, **3**, 1774–1785.
22 A. V. Bridgwater, *Catal. Today*, 1996, **29**, 285–295.
23 E. Furimsky and F. E. Massoth, *Catal. Today*, 1999, **52**, 381–495.
24 G. W. Huber, S. Iborra and A. Corma, *Chem. Rev.*, 2006, **106**, 4044–4098.
25 T. N. Trinh, P. A. Jensen, H. R. Sørensen, K. Dam-Johansen and S. Hvilsted, *Energy Fuels*, 2013, **27**, 1399–1409.
26 Q. Song, C. Wang and J. Xu, *Chem. Commun.*, 2012, **48**, 7019–7021.
27 Q. Song, F. Wang, J. Cai, Y. Wang, J. Zhang, W. Yu and J. Xu, *Energy Environ. Sci.*, 2013, **6**, 994–1007.
28 K. Aasberg-Petersen, T. S. Christensen, I. Dybkjær, J. Sehested, M. Østberg, R. M. Coertzen, M. J. Keyser and A. P. Steynberg, in *Fischer-Tropsch Technology*, Elsevier, Amsterdam, 2004, ch. 4: Synthesis Gas Production for FT Synthesis, pp. 258–405.
29 J. R. Rostrup-Nielsen, in *Handbook of Heterogeneous Catalysis*, John Wiley & Sons, Inc., New York, 2008, ch. 13.11: Steam Reforming, pp. 2882–2905.
30 P. R. Patwardhan, R. C. Brown and B. H. Shanks, *ChemSusChem*, 2011, **4**, 1629–1636.
31 M. S. A. Moraes, M. V. Migliorini, F. C. Damasceno, F. Georges, S. Almeida, C. A. Zini, R. A. Jacques and E. B. Caramão, *J. Anal. Appl. Pyrolysis*, 2012, **98**, 51–64.
32 E. Furimsky, *Appl. Catal., A*, 2000, **199**, 144–190.
33 E. Laurent, A. Centeno and B. Delmon, *Stud. Surf. Sci. Catal.*, 1994, **88**, 573–578.
34 H. S. Fogler, *Elements of Chemical Reaction Engineering*, Prentice Hall, New Jersey, 2006.
35 *CRC Handbook of Chemistry and Physics 92th Edition (Internet Version 2012)*, ed. W. M. Haynes, CRC Press, April 2010.
36 K. Schofield, *Prog. Energy Combust. Sci.*, 2008, **34**, 330–350.
37 P. L. Llewellyn, E. Bloch and S. Bourelly, in Surface Area/Porosity, Adsorption, Diffusion, *Characterization of Solid Material and Heterogenous Catalysts*, Wiley-VCH, Weinheim, 2012, ch. 19: Surface Area/Porosity, Adsorption, Diffusion, pp. 853–880.
38 J.-D. Grunwaldt, S. Hannemann, J. Göttlicher, S. Mangold, M. Denecke and A. Baiker, *Phys. Scr., T*, 2005, **115**, 769–772.
39 J.-D. Grunwaldt, M. Caravati, S. Hannemann and A. Baiker, *Phys. Chem. Chem. Phys.*, 2004, **6**, 3037–3047.
40 J.-D. Grunwaldt, N. van Vegten and A. Baiker, *Chem. Commun.*, 2007, 4635–4637.
41 B. Ravel and M. Newville, *J. Synchrotron Radiat.*, 2005, **12**, 537–541.
42 J. J. Rehr, J. J. Kas, M. P. Prange, A. P. Sorini, Y. Takimoto and F. D. Vila, *C. R. Phys.*, 2009, **10**, 548–559.
43 C. Zhao, J. He, A. A. Lemonidou, X. Li and J. A. Lercher, *J. Catal.*, 2011, **280**, 8–16.
44 Y.-C. Lin, C.-L. Li, H.-P. Wan, H. Lee and C.-F. Liu, *Energy Fuels*, 2011, **25**, 890–896.
45 C. R. Lee, J. S. Yoon, Y.-W. Suh, J.-W. Choi, J.-M. Ha, D. J. Suh and Y.-K. Park, *Catal. Commun.*, 2012, **17**, 54–58.
46 B. Peng, C. Zhao, I. Mejía-Centeno, G. A. Fuentes, A. Jentys and J. A. Lercher, *Catal. Today*, 2012, **183**, 3–9.
47 J. Ryu, S. M. Kim, J.-W. Choi, J.-M. Ha, D. J. Ahn, D. J. Suh and Y.-W. Suh, *Catal. Commun.*, 2012, **29**, 40–47.
48 I. Barin, *Thermochemical Data of Pure Substances*, VCH, Weinheim, 1989.
49 S. J. Hurff and M. T. Klein, *Ind. Eng. Chem. Fundam.*, 1983, **22**, 426–430.
50 C. Louis, Z. X. Cheng and M. Che, *J. Phys. Chem.*, 1993, **97**, 5703–5712.
51 P. M. Mortensen, *Ph.D. thesis*, Technical University of Denmark, 2013.
52 S. W. Benson, *Thermochemical Kinetics: Methods for estimation of thermochemical data and rate parameters*, John Wiley & Sons, Inc., New York, 1968.
53 T. Borowiecki, *Appl. Catal.*, 1982, **4**, 223–231.
54 H. S. Bengaard, J. K. Nørskov, J. Sehested, B. S. Clausen, L. P. Nielsen, A. M. Molenbroek and J. R. Rostrup-Nielsen, *J. Catal.*, 2002, **209**, 365–384.
55 J. R. Rostrup-Nielsen, J. Sehested and J. K. Nørskov, *Adv. Catal.*, 2002, **47**, 65–139.
56 G. Tavoularis and M. A. Kean, *J. Mol. Catal. A: Chem.*, 1999, **142**, 187–199.
57 C. Menini, C. Park, E.-J. Shin, G. Tavoularis and M. A. Keane, *Catal. Today*, 2000, **62**, 355–366.
58 B. Schrick, J. L. Blough, A. D. Jones and T. E. Mallouk, *Chem. Mater.*, 2002, **14**, 5140–5147.
59 M. A. Keane, *ChemCatChem*, 2011, **3**, 800–821.
60 S. Park, J. O. Baker, M. E. Himmel, P. A. Parilla and D. K. Johnson, *Biotechnol. Biofuels*, 2010, **3**.
61 Y. Ohtsuka, *J. Mol. Catal.*, 1989, **54**, 225–235.
62 K. Jurek and O. Gedeon, *Microchim. Acta*, 2008, **161**, 377–380.
63 S. Hodson and J. Marshall, *J. Microsc.*, 1971, **93**, 49–53.
64 S. Sasaki, K. Fujino and Y. Takeuchi, *Proc. Jpn. Acad., Ser. B*, 1979, **55**, 43–48.
65 J. R. Rostrup-Nielsen, *J. Catal.*, 1968, **11**, 220–227.
66 T. Rosenqvist, *J. Iron Steel Inst., London*, 1954, **176**, 37–57.
67 J. L. Oliphant, R. W. Fowler, R. B. Pannell and C. H. Bartholomew, *J. Catal.*, 1978, **51**, 229–242.
68 C. H. Bartholomew, G. D. Weatherbee and G. A. Jarvi, *J. Catal.*, 1979, **60**, 257–269.

69 J. R. Rostrup-Nielsen, *J. Catal.*, 1971, **21**, 171–178.
70 H. Oudghiri-Hassani, N. Abatzoglou, S. Rakass and P. Rowntree, *J. Power Sources*, 2007, **171**, 811–817.
71 T. S. Christensen, *Appl. Catal., A*, 1996, **138**, 285–309.
72 M. Kiskinova and D. W. Goodman, *Surf. Sci.*, 1981, **108**, 64–76.
73 J. T. Richardson, J. D. Ortego, N. Coute and M. V. Twigg, *Catal. Lett.*, 1996, **41**, 17–20.
74 J. D. Ortego, J. T. Richardson and M. V. Twigg, *Appl. Catal., B*, 1997, **12**, 339–355.
75 J. P. Trembly, R. S. Gemmen and D. J. Bayless, *J. Power Sources*, 2007, **169**, 347–354.

Inhibition and Deactivation of Ni-MoS_2 by Bio-oil Impurities during Hydrodeoxygenation of Phenol and Octanol

*Peter M. Mortensen[a,b], Diego Gardini[c], Christian D. Damsgaard,[c,d], Jan-Dierk Grunwaldt[e], Peter A. Jensen[a], Jakob B. Wagner[c], & Anker D. Jensen[a]**

[a]*Department of Chemical and Biochemical Engineering, Technical University of Denmark, Søltofts Plads, Building 229, DK-2800 Lyngby, Denmark*

[b]*Haldor Topsoe A/S, Haldor Topsøes Allé 1, DK-2800 Lyngby, Denmark*

[c]*Center for Electron Nanoscopy, Technical University of Denmark, Fysikvej,Building 307, DK-2800 Lyngby, Denmark*

[d]*CINF, Department of Physics, Technical University of Denmark, Fysikvej,Building 312, DK-2800 Lyngby, Denmark*

[e]*Institute for Chemical Technology and Polymer Chemistry, Karlsruhe Institute of Technology (KIT), Engesserstrasse 20, D-79131 Karlsruhe, Germany*

**Corresponding author. Tel.: +45 4525 2841 fax: +45 4588 2258. E-mail address: aj@kt.dtu.dk (A.D. Jensen).*

Abstract

The stability of Ni-MoS_2/ZrO_2 toward water, potassium, and chlorine during hydrodeoxygenation (HDO) of a mixture of phenol and 1-octanol has been investigated in a high pressure gas and liquid continuous flow fixed bed setup at 280°C and 100 bar. To maintain stability of the catalyst, sufficient co-feeding of a sulfur source is necessary. Feeding insufficient sulfur resulted in oxidation of the sulfide phase by oxygen replacement of the edge sulfur atoms in the MoS_2 structure. The addition of sulfur in the feed gas resulted in formation of sulfur containing compounds, mainly thiols, in the oil product if the residence time was insufficient. At the given conditions a WHSV of <4.9 h^{-1} was needed to maintain the liquid product sulfur content below 30 ppm_w. A higher co-feed of sulfur was needed when water was present in the feed and the H_2O/H_2S molar ratio should be below ca. 10 to maintain a decent stability of the catalyst. Potassium was a severe poison and deactivated the catalyst completely (<5% degree of deoxygenation) when impregnated on the catalyst in a stoichiometric ratio relative to the active metal. This deactivation was linked to saturation of the edge vacancy sites on the MoS_2 slabs by potassium. Chlorine caused an inhibition of the catalyst when co-fed to the reactor, but the activity could be completely regained when removing it from the feed. Commonly, HCl, H_2O, and H_2S all inhibited the activity of the catalyst by competing for the active sites, with HCl being by far the strongest inhibitor and H_2S and H_2O of roughly the same strength.

Keywords: Bio-oil, Hydrodeoxygenation, HDO, Stability, Inhibition

1. Introduction

It has become generally accepted that the oil reserves are depleting due to increased use of fossil fuels throughout the last 100 years [1]. In addition, this has led to a rising concentration of CO_2 in the atmosphere, which is correlated to a greenhouse effect on the Earth [2]. These aspects raise concerns and gives incitement for investigation of alternative ways for production of fuels, as well as bulk chemicals. A prospective path to these could be biomass based, as this constitutes a carbon containing resource which can be reproduced within a relatively short time [3,4].

A challenge with biomass is that it has a relatively low energy- and mass-density. This makes transport expensive and constrains its utilization [5]. Thus, it has been proposed to convert biomass into bio-oil by flash pyrolysis and subsequently upgrade this to fuel by hydrodeoxygenation, which is applicable with practically any type of biomass [6] [+Mortensen2011]. Hydrodeoxygenation (HDO) constitutes a prospective upgrading route for bio-oil. This is a high pressure catalytic upgrading process where hydrogen is used for exclusion of oxygen [Mortensen2011].

One of the major challenges in the HDO process is to develop an active catalyst which also is sufficiently stable. The latter aspect is challenged by the bio-oil's tendency to form coke and its content of alkali metals, sulfur, chlorine, phosphorus, and other impurities in the bio-oil [6,7].

Traditional hydrotreating catalysts, such as Co-MoS_2 and Ni-MoS_2, have been among the most tested catalysts for HDO of bio-oil [6,8–10]. This group of catalysts is already industrially established for hydrodesulfurization (HDS) of crude oil [11–14]. On these catalysts, HDO takes place by a Max-Van-Krevelen type reaction mechanism. The reaction is initiated by removal of a sulfur atom from the edge of the MoS_2 structure to generate a vacancy site. This site facilitates the adsorption of the oxy-compound and its deoxygenation [6,15]. In HDS, the activity of the catalyst has been linked to the availability of edge sites on the MoS_2 slabs [12,16–19]. As the mechanisms for HDS and HDO are similar, this type of sites are believed to be the active sites for HDO as well [20,21]. Promotion with either Co or Ni increases the availability of vacancy sites by lowering the Mo-S bond energy [12,14,17,22,23].

Long term stability of MoS_2 based catalysts during HDO has not been thoroughly investigated. One of the concerns raised, is the requirement for co-feeding sulfur in order to retain the active sulfide form of the catalyst, but this could potentially contaminate the otherwise sulfur scant bio-oil [22,24,25]. Furthermore, little is known about the influence of bio-oil impurities on the catalyst stability.

In the current work, the stability of Ni-MoS_2/ZrO_2 is investigated in a series of prolonged continuous flow reactor experiments. The stability was evaluated in the presence of H_2S, H_2O, potassium and organic bound chlorine. For this purpose a bio-oil model system of phenol in 1-octanol was used to simulate some of the more complex and refractory molecules in the bio-oil and the more accessible simple alcohols. Ni-MoS_2/ZrO_2 was chosen as catalyst, as promotion by nickel previously has been shown to be slightly superior to cobalt promotion [8,22] and ZrO_2 has been found to be a suitable support for HDO [26–30] and does apparently not suffer from the instability in high concentration of water, as reported for the conventionally used γ-Al_2O_3 support for hydrotreating catalysts [8,31,32].

2. Experimental

2.1. Catalyst Synthesis

Ni-MoO_3/ZrO_2 (3 wt% Ni, 15 wt% Mo) was prepared by sequential incipient wetness impregnation. The zirconia was supplied by Saint-Gobain NorPro, type SZ6*152 having an impurity of 3.3% SiO_2, a specific surface area of 140 m^2/g, and a pore volume of 0.32 ml/g. In the synthesis,

the precursor was dissolved in water equivalent to the pore volume of the support and subsequently mixed with the support. 15 wt% Mo was initially impregnated from a solution of $(NH_4)_6Mo_7O_{24}\cdot 4H_2O$ (Sigma-Aldrich, ≥ 97.0%) in water on ZrO_2 (sieve fraction 300-600 µm) and then dried overnight at 70°C. $Ni(NO_3)\cdot 3H_2O$ (Sigma-Aldrich, ≥ 96.0%) was dissolved in water and impregnated on the dry Mo-loaded catalyst to a level of 3 wt% Ni and then dried at 70°C overnight. Finally the catalyst was calcined by heating to 400°C at a rate of 10°C/min in air and held there for 4 h.

The catalysts was sulfided in the continuous flow reactor setup prior to testing by initially heating a portion of the catalyst to 200°C in N_2 and then heating at a rate of 5°C/min to 350°C in a flow of 800 Nml/min H_2 and 0.2 ml/min dimethyl disulfid (DMDS, Sigma-Aldrich, ≥ 99%) at atmospheric pressure. Sulfidation was done for 2.5 h at 350°C. Assuming complete decomposition of DMDS to H_2S the feed concentration of the gas would be: 12% H_2S, 12% CH_4, and 76% H_2.

2.2. Catalyst Testing

The experiments were performed in a high pressure gas and liquid continuous flow packed bed setup. The setup has been thoroughly described in previously published work from our group [7].

2.5 g of catalyst sieved to 300-600 µm was mixed with 7.5 g glass beads of sieve fraction 212-245 µm to dilute the catalyst bed and thereby obtain better control of the exothermic reactions. The glass bead/catalyst mixture rested on a quartz wool plug in the reactor, which was supported on a crossbar in the reactor.

Evaluation of transport limitations by Mears criterion [33] for the given sieve fraction of catalyst particles revealed that the system was not limited by boundary layer diffusion. On the contrary some internal diffusion limitation was present, at least for the most active catalysts. However, as the present work deals with stability it was concluded that this limitation did not influence the interpretation of the results. Detailed information of the evaluation of the transport limitations can be found in the electronic supporting information (ESI).

A feed mixture of 50 g/l phenol (Sigma-Aldrich, ≥ 99%) and 2-5 vol% DMDS in 1-octanol (Sigma-Aldrich, ≥ 99%) was used as bio-oil model compound system and generally fed at a flow of 0.2 ml/min. 1-octanol was chosen as co-reactant (despite it not is a usual bio-oil component) due to its relative high boiling point (195°C at ambient pressure [34]) and ability to mix with phenol in a single homogenous phase. Hydrogen (AGA, 99.9%) and nitrogen (AGA, 99.9%) were fed to the reactor at a flow of respectively 200 Nml/min and 50 Nml/ml, corresponding to 5 times the stoichiometric hydrogen requirement of the feed oil. Nitrogen was used as internal standard. During the reactions, the reactor was maintained at a constant pressure of 100 bar and the set point of the reactor furnace was 280°C.

In the experiments with varying WHSV, the H_2/oil feed ratio was kept constant at 1000 Nml/ml, and N_2 was not co-fed in these experiments. Each feed rate was kept for at least 8 h to ensure representative product samples.

2.3. *Product Analysis*

Analysis of the liquid product was done on a Shimadzu gas chromatograph GC-MS/FID-QP2010 UltraEi fitted with a Supelco Equity-5 column. Identification was made on mass spectrometer (MS) and quantification was done using a flame ionization detector (FID). External standards were prepared for phenol, cyclohexanol, cyclohexane, methanol, 1-octanol, and octane. The concentration of the remaining peaks were calculated from the FID on the basis of the effective carbon number method [35], where the concentration of a compound was found as:

$$\boldsymbol{C_i = C_{ref} \cdot \frac{A_i \cdot \nu_{eff,ref}}{A_{ref} \cdot \nu_{eff,i}}} \quad (1)$$

Here C is the concentration, A the area of the peak in the FID spectrum, and ν_{eff} the effective carbon number. Index i refers to the compound with the unknown concentration and index ref refers to a reference compound where the concentration is known. In all calculations using Eq. 1, octane was used as reference. The effective carbon number was taken from the review by Schofield [35].

The weight hourly space velocity (WHSV) was calculated as:

$$\boldsymbol{WHSV = v_0 \cdot \frac{\rho_{feed}}{m_{cat}}} \quad (2)$$

Here v_0 is the volumetric feed flow, ρ_{feed} the density of the liquid feed, and m_{cat} the mass of catalyst used. The residence is roughly the inverse of the WHSV.

The conversion (X) was calculated for both phenol and 1-octanol as:

$$\boldsymbol{X = \left(1 - \frac{C_{out,i} \cdot \nu_{out}}{C_{0,i} \cdot \nu_0}\right) \cdot 100\%} \quad (3)$$

Here C_i is the concentration of compound i and ν is the volumetric flow. Index out refers to the conditions after the reactor, index 0 refers to the inlet conditions, and i refers to the compound of relevance.

The yields (Y_i) of relevant products were calculated as:

$$\boldsymbol{Y_i = \frac{C_{out,i} \cdot \nu_{out}}{C_{0,j} \cdot \nu_0} \cdot 100\%} \quad (4)$$

Index i is here referring to the compound of relevance and index j is referring to the initial reactant, phenol or 1-octanol.

The selectivity (S_i) of a compound (i) was calculated as:

$$\boldsymbol{S_i = \frac{Y_i}{X} \cdot 100\%} \quad (5)$$

The degree of deoxygenation (DOD) was calculated as:

$$\boldsymbol{DOD = \left(1 - \frac{F_{O,out}}{F_{O,in}}\right) \cdot 100\%} \quad (6)$$

Here F_O is the molar flow of oxygen (excluding water) either in or out of the reactor.

To make an additional quantification of the activity of the catalyst, the first order rate constants from both the phenol and 1-octanol conversion was calculated assuming plug flow in the reactor:

$$\boldsymbol{X_i = 1 - \exp\left(-k_i \cdot \frac{W}{v}\right)} \quad (7)$$

Here k_i is the rate constant of reaction i and W the mass of catalyst. Previous work has shown that HDO of guaiacol, anisole, and phenol with sufficient accuracy follows 1st order kinetics [30,36–38].

2.4. Catalyst characterization

Elemental analysis of the catalysts was performed using inductively coupled plasma atomic emission spectroscopy (ICP-OES). In the analysis, the samples were crushed and melted together with potassium pyrosulfate. This was dissolved in a solution of water and HCl and then analyzed by plasma emission spectroscopy. The instrument was calibrated with certified standards for the elements analyzed for.

Powder X-Ray Diffraction (XRD) measurements were carried out using a PANalytical X`Pert PRO diffractometer in a Bragg-Brentano Theta-Theta geometry. The catalysts were analyzed in a $10° < \theta < 70°$ range using a monochromatic Cu-Kα radiation ($\lambda \approx 1.5418$ Å). XRD data treatment was carried out using PANalytical HighScore Plus 3.0.5 software.

Bright Field (BF) micrographs were acquired using a FEI Titan 80-300 transmission electron microscope (TEM) operated at 300 kV and EDX elemental maps were acquired using a cubed FEI Titan operated at 120 kV. Catalyst powders were crushed in a mortar and dry dispersed on a non-coated gold TEM grid. Fitting of EDX spectra was carried out using OriginPro 2015 software.

3. Results and Discussion

3.1. Characterization of the as-sulfided catalyst by electron microscopy and X-ray diffraction

In order to verify the correct synthesis of Ni-MoS_2/ZrO_2 and study the distribution of the active phase on the zirconia support, a characterization approach involving the combination of electron microscopy and X-ray diffraction was used.

XRD of the as-sulfided catalyst showed strong reflections belonging to the crystalline ZrO_2 support and minor reflections that were indexed as MoS_2, NiS and Ni (cf. Figure 1(a)). The presence of crystalline Ni species probably represents leftovers from the synthesis procedure. The effective sulfidation of Mo oxide precursor species was furthermore confirmed by the identification of lamellar structures in BF-TEM imaging (cf. Figure 1(b)). The measured interlayer distance was 0.62 nm, matching MoS_2 *c* stacking distance [39].

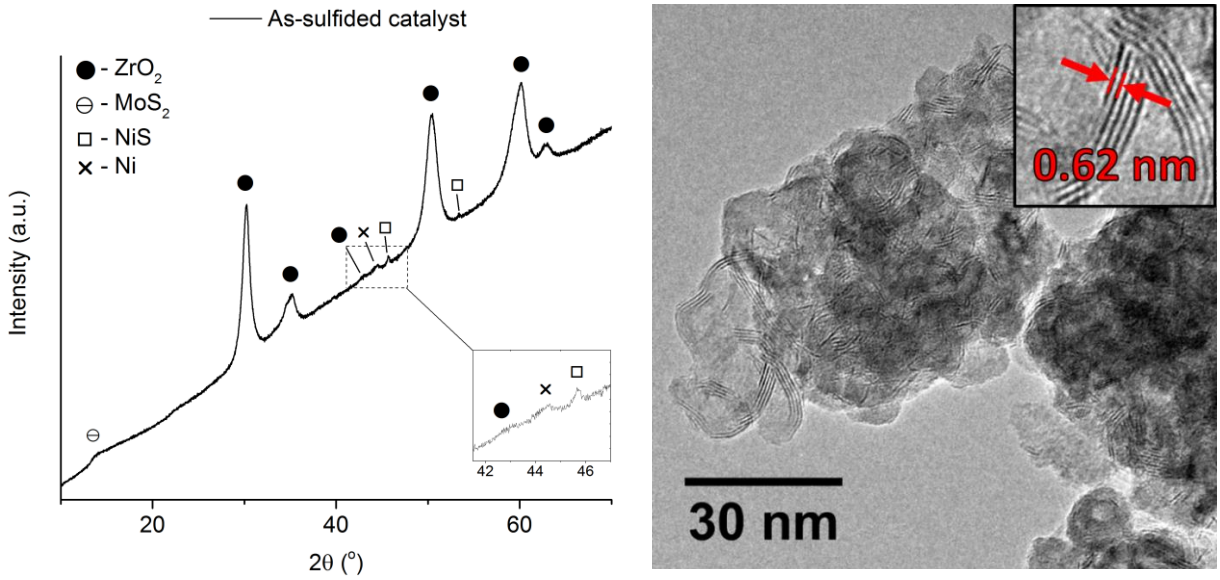

(a) XRD diffraction pattern **(b) BF-TEM micrograph**

Figure 1: Characterization of Ni-MoS_2/ZrO_2 catalysts by (a) X-ray diffraction and (b) TEM imaging. Inset in (b) shows MoS_2 structures with characteristic interlayer distance of 0.62 nm.

In order to univocally identify the active phase of the catalyst, STEM-EDX elemental maps were acquired, as mass-thickness contrast in bright-field imaging was found to be insufficient. Figure 2 shows two characteristic areas of an as-sulfided catalyst. In both cases, elemental maps II, III and IV can be compared in order to evaluate the spatial distribution of S, Zr and Mo elements, respectively. Overall, MoS_2 structures were found to effectively cover the ZrO_2 support (Figure 2(a)) forming in some cases areas of higher density (Figure 2(b)).

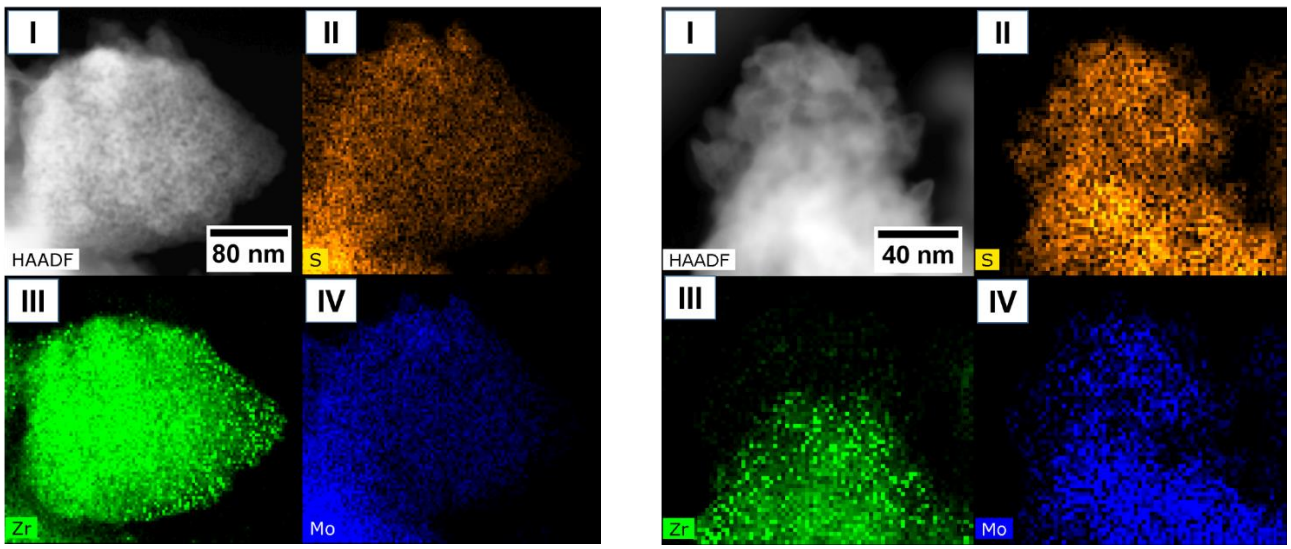

(a) General sulfide coverage **(b) Areas richer in sulfide phase**

Figure 2: HAADF-STEM imaging and EDX mapping of Ni-MoS_2/ZrO_2 as-sulfided catalysts presenting (a) general MoS_2 coverage and (b) areas richer in sulfide phase. Sub-image (I): Overview of the site in analysis. Sub-images (II) sulfur, (III) zirconium and (IV) molybdenum EDX elemental distributions.

Further elemental maps were acquired in order to study the distribution of nickel species in the as-sulfided catalyst. As Figure 3 shows, Ni X-rays were detected when analyzing a portion of the sample containing MoS_2 structures, showing the effective incorporation of the promoter in the layered sulfide and the formation of the desired Ni-MoS_2 active phase. Furthermore, Ni-based nanoparticles were identified (Figure 3(II)), in accordance with the results of the XRD analysis (cf. Figure 1(a)).

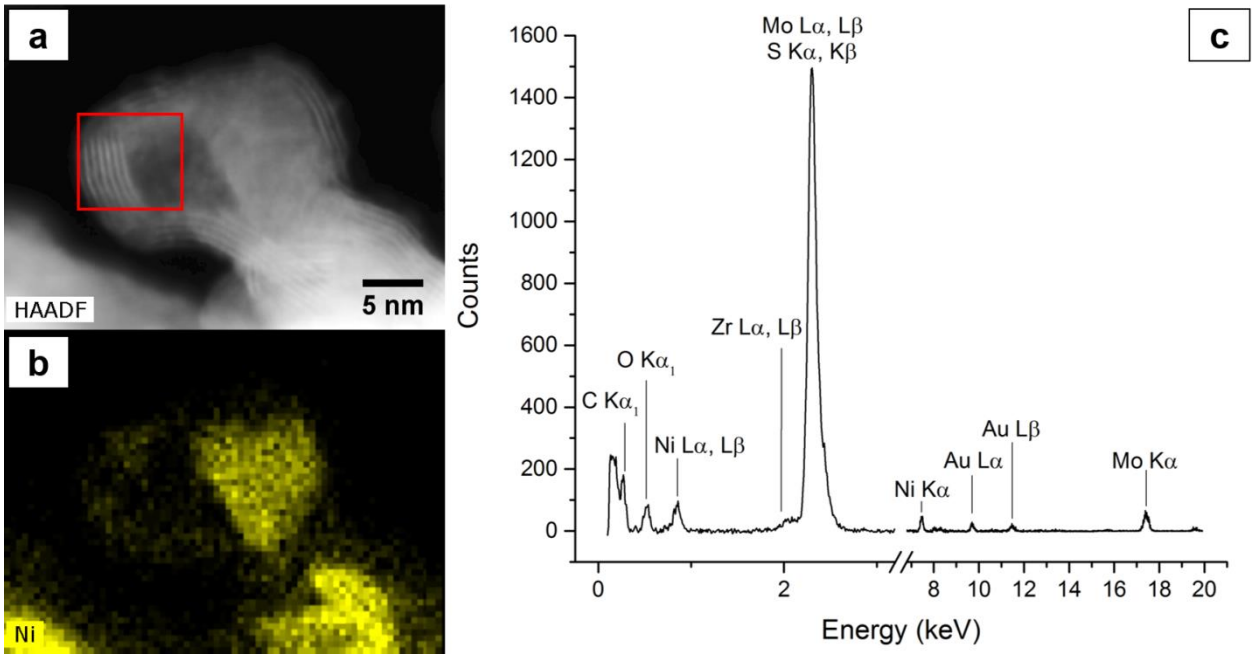

Figure 3: Nickel distribution in the as-sulfided catalyst. Sub-image (a): HAADF-STEM micrograph of the portion of the sample analyzed. In red, an area containing MoS_2 structures is highlighted. Sub-image (b): Nickel EDX elemental distribution. Sub-image (c): EDX spectrum of the area highlighted in Sub-image (a).

3.2. The Effect of Residence Time

Initially the effect of residence time was investigated for HDO of phenol in 1-octanol, with a co-feed of 2 vol% DMDS (corresponding to 8170 ppm H_2S in the gas feed). The DMDS was added to ensure that the catalyst remained in the sulfide form. The conversion of 1-octanol and phenol and yields of cyclohexane, cyclohexene, octane, and octene are shown together with the sulfur content calculated from organic sulfur compounds in the product as a function of the WHSV in Figure 4. For 1-octanol, decreasing the WHSV increased the conversion, with octane as the primary product. 1-octene was an important intermediate with a selectivity of 12% at a WHSV of 1.4 h^{-1}, but decreasing to 0% at a WHSV of 4.9 h^{-1}. Thus, HDO of 1-octanol over this catalyst proceeds by a dehydration reaction scheme, producing 1-octene, which subsequently reacts with hydrogen to form octane as the final product, as shown in Figure 5.

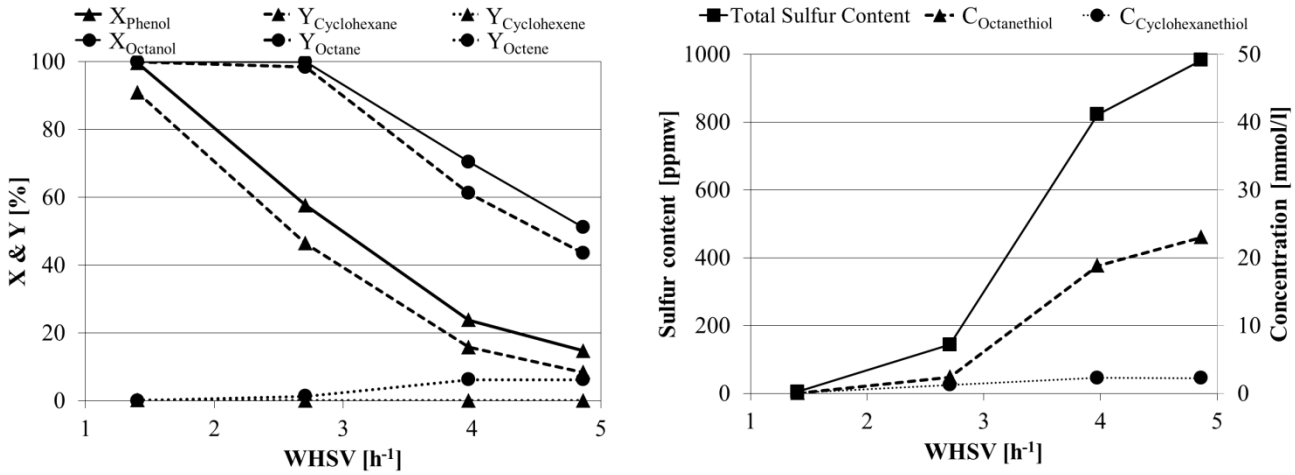

(a) Oil product distribution. **(b) Sulfur content in oil.**

Figure 4: Effect of the residence for HDO of 50 g/l phenol and 2 vol% DMDS in 1-octanol over Ni-MoS_2/ZrO_2. (a) conversions of 1-octanol and phenol and yields of octane, octene, cyclohexane, and cyclohexene and (b) sulfur content in the liquid product. T = 280°C, P = 100 bar.

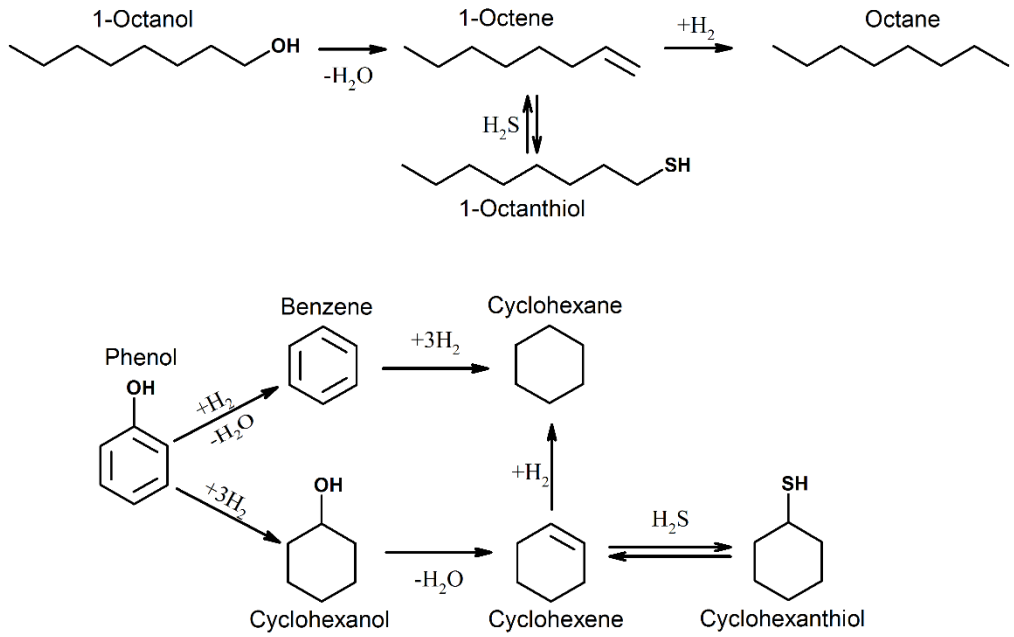

Figure 5: Reaction scheme of 1-octanol and phenol over Ni-MoS_2/ZrO_2.

For phenol, cyclohexane was observed as the primary product at all WHSV's, but also benzene (up to 5% selectivity), cyclohexanol (up to 18% selectivity), and cyclohexene (up to 41% selectivity) were detected. HDO of phenol can take place by two paths as summarized in Figure 5: a direct deoxygenation of phenol to benzene, followed by hydrogenation to cyclohexane, or an initial hydrogenation of phenol to cyclohexanol followed by dehydration to cylohexene and then hydrogenation to cyclohexane. The preferred reaction path will be dependent on catalyst and reaction conditions [40–46]. Apparently, the hydrogenation path is preferred under the given

conditions in this work, as evidenced by the high fraction of cyclohexanol and cyclohexene at especially the high WHSV. Notice that thermodynamic equilibrium between cyclohexane and benzene is completely displaced towards cyclohexane at the given conditions, and this will of course also influence the reaction path.

Besides the hydrocarbon products, also 1-octanethiol and cyclohexanethiol were formed. The selectivity toward 1-octanethiol and cyclohexanethiol dropped from 3.1% and 0.8%, respectively, at 1.4 h^{-1} to < 0.1% at 4.9 h^{-1}, as shown in Figure 4(b). These compounds are most likely formed in side reactions by saturation of the double bonds in 1-octene and cyclohexene with H_2S (cf. Figure 5), as both are present in high concentrations at the higher WHSV's. However, as the Ni-Mo catalyst is widely used as HDS catalyst [11–14], it also possess desulphurization capabilities and therefore the thiols are removed again. Thus, the sulfur content of the product oil ended below 5 ppm_w at the lowest WHSV tested in Figure 4(b). In conclusion, the tendency of Ni-MoS_2 to form sulfur containing compounds can be circumvented by increasing the residence time.

3.3. The Effect of H_2S

The stability of the Ni-MoS_2/ZrO_2 catalyst and the influence of the sulfur source were investigated in two experiments: one with 0.3 vol% 1-octanethiol in the feed and one with 2 vol% DMDS in the feed, corresponding to respectively 280 ppm and 8170 ppm H_2S in the gas feed, assuming complete decomposition of the feed sulfur compounds. The first case is representative of the type of sulfur containing components and concentration that could be expected in bio-oil [47]. The second case was an attempt to improve the catalyst stability. The conversion of phenol and 1-octanol in these experiments are summarized in Figure 6.

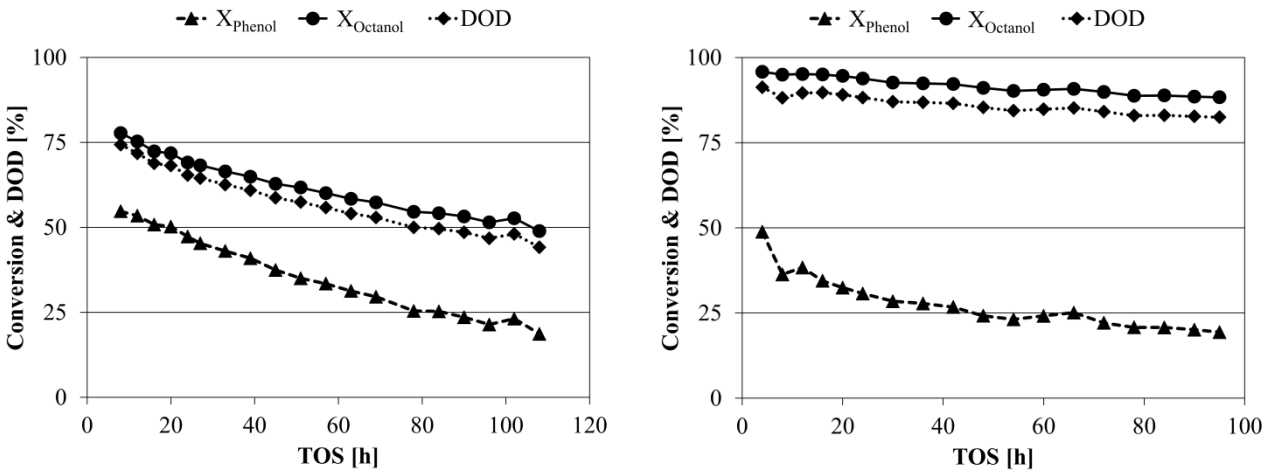

(a) 0.3% 1-octanethiol in the feed.

(b) 2% DMDS in the feed.

Figure 6: Stability of Ni-MoS_2/ZrO_2 during HDO of phenol and 1-octanol. (a) Conversions of 1-octanol and phenol in a case with 0.3 vol% 1-octanethiol in the feed and (b) Conversions of 1-octanol and phenol in a case with 2 vol% DMDS in the feed. T = 280°C, P = 100 bar, F_{oil} = 0.2 ml/min, WHSV = 4.0 h^{-1}. Detailed product distributions can be found in the ESI.

In the case with 0.3 vol% 1-octanethiol in the feed, the activity steadily decreased throughout the 110 h of testing. The 1-octanol conversion decreased from 78% to 49% and the phenol conversion decreased from 56% to 21% (cf. Figure 6(a)). In comparison, adding 2 vol% DMDS to

the feed resulted in a significantly better stability, as the 1-octanol conversion only dropped from 95% to 88% over 96 h of testing and the phenol conversion dropped from 36% to 19% in the same time frame (cf. Figure 6(b)).

The concentration of thiols in the liquid product increased from 13 ppm_w sulfur in the case co-feeding 0.3 vol% 1-octanethiol to 381 ppm_w in the case co-feeding 2 vol% DMDS. Thus, the concentration will be dependent on the residence time (as discussed in Section 3.2) and also the concentration of sulfur in the feed.

Analysis of sulfur on the spent catalyst with ICP-OES revealed that the sulfur content in the case co-fed with 0.3 vol% 1-octanethiol had decreased to 7.5 wt%, compared to 10.9 wt% on the as-sulfided catalyst (cf. Table 1). In comparison, the catalyst co-fed with 2 vol% DMDS had a content of 8.4 wt% sulfur on the spent catalyst. Thus, both catalysts lost sulfur during operation, but the case co-feeding 1-octanethiol lost significantly more. The theoretical sulfur content as MoS_2 on the fresh catalyst should be 9.1 wt%, compared to 10.9 wt% in Table 1. This indicates that some of the initial sulfur content could be present as non-chemical bond sulfur on the as-sulfided catalyst, which probably is easy to desorb.

Table 1: Elemental content of sulfur and carbon on spent catalyst tested with different sources of sulfur in the feed and varying H_2O/H_2S feed ratios. Fresh catalyst is a catalyst analyzed directly after sulfidation.

Sulfur in feed	TOS_{Total} [h]	H_2O/H_2S ratio	S [wt%]	C [wt%]
As-sulfided	-	-	10.9	1.9
0.3 vol% 1-octanethiol	110	0	7.5	3.7
2 vol% DMDS	95	0	8.4	2.0
2 vol% DMDS	96	46	8.9	2.1
5 vol% DMDS	100	16	8.2	1.7
5 vol% DMDS	92	9.7	8.3	3.1

In addition to ICP-OES, more local and qualitative investigations were carried out by means of STEM-EDX mapping of as-sulfided and spent Ni-MoS_2/ZrO_2 catalysts tested with different sources of sulfur in the feed and varying H_2O/H_2S feed ratios. For each catalyst the ratio between Mo $K\alpha_{1,2}$ and S $K\alpha_{1,2}$ X-ray emission peaks from Ni-MoS_2 rich areas was calculated by multiple Gaussian fit of portions of the EDX spectrum and is representative of the relative concentration of the two elements in the sample. A more detailed explanation of the quantification is given in the ESI.

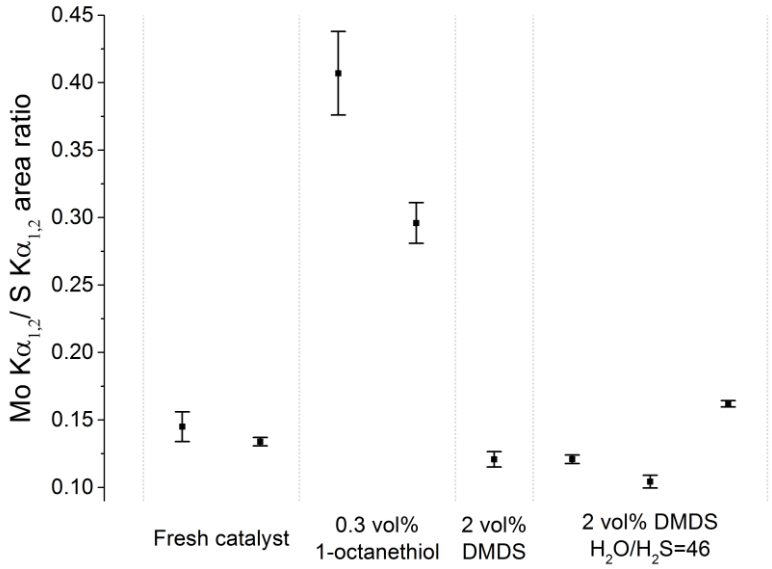

Figure 7: Mo $K\alpha_{1,2}$ / S $K\alpha_{1,2}$ X-ray emission peaks ratios for freshly sulfided Ni-MoS_2/ZrO_2 catalysts and catalyst tested with different sources of sulfur in the feed and varying H_2O/H_2S feed ratios. Multiple data points per catalyst represent measurements carried out in different areas of the same sample.

As Figure 7 shows, active phase rich areas of the catalyst co-fed with 0.3 vol% 1-octanethiol presented the highest Mo/S X-ray emission ratio, indicating a more severe loss of sulfur during catalytic testing. On the other hand, in the case of co-feeding 2 vol% DMDS the ratio was found to be similar to the fresh catalyst, meaning that consistently less sulfur is lost from the sample. It is important to point out that these ratios are representative of the sole active phase composition and hence cannot be directly compared to the elemental analysis measurements shown in Table 1, accounting for the whole catalyst composition. However, the result of this EDX quantification follows in a qualitative way the trend of the ICP-OES analysis and is complementary to it, confirming that the variation of sulfur level in the spent catalysts is connected to a loss of sulfur from the active phase.

Additionally, the ICP-OES analysis revealed that the tendency for carbon formation was low on both catalysts with less than 4 wt% carbon at end of run. Roughly half of this could be deposited already during sulfidation, as 2 wt% carbon was found on a freshly sulfided catalyst (cf. Table 1). Carbon structures were identified by means of electron microscopy in multiple areas of the catalyst co-fed with 0.3 vol% 1-octanethiol. STEM-EDX mapping revealed the presence of carbon containing flakes characterized by a lamellar structure with an interlayer distance of 1.96 nm (cf. Figure 8). The origin and the nature of these structures remain at present unknown, however their presence could be the main reason for the higher carbon content measured for this catalyst by ICP-OES(cf. Table 1).

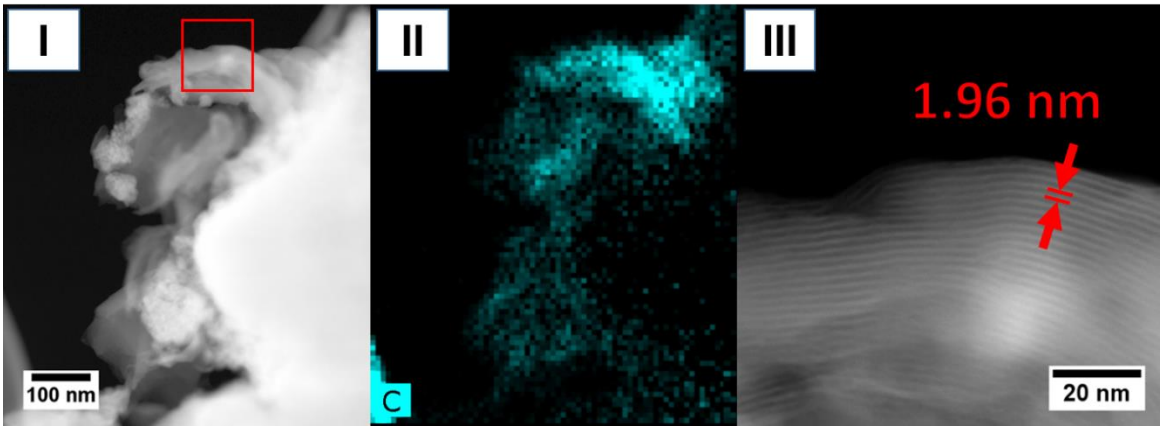

Figure 8: Carbon structures identified in Ni-MoS_2/ZrO_2 co-fed with 0.3 vol% 1-octanethiol. Sub-image (I): HAADF-STEM micrograph of the area analyzed. Sub-image (II): carbon EDX elemental distribution. Sub-image (III): magnified view of the layered structure highlighted in sub-image (I).

The combination of ICP-OES elemental analysis (cf. Table 1), and more local EDX peak area analysis (cf. Figure 7), indicates that feeding insufficient sulfur will result in a depletion of sulfur of the sulfide phase. Previous work has also shown that oxygen atoms from the HDO reaction can replace framework S-atoms in the MoS_2 with insufficient sulfur in the feed [42,48–51]. The natural content of sulfur in bio-oil does not appear sufficient for sustaining the catalyst in the active form during operation and addition of DMDS/H_2S is recommended during HDO of a real bio-oil feed.

Comparing the initial activity in the two cases in Figure 6, increasing the H_2S concentration resulted in an increase in the 1-octanol conversion from 77% to 95%, but a decrease in the initial phenol conversion from 55% to 36%. It has previously been described that co-feeding H_2S during HDO on MoS_2 type catalysts results in a competitive adsorption between H_2S and the oxy-compound [21,41,48,52]. Based on DFT calculations, Badawi et al. [20] found that the adsorption of H_2S and H_2O was stronger on CoMoS sites compared to phenol and these species therefore have an inhibiting effect on the catalyst. This explains why the phenol conversion decreased when increasing the H_2S concentration. Maybe, 1-octanol and H_2S adsorb at a similar strength and the conversion of 1-octanol therefore increases as this readily adsorbs on the catalytic surface while phenol does not, leaving more active sites for 1-octanol.

3.4. The Effect of H_2O

To test the stability of the Ni-MoS_2/ZrO_2 catalyst in the presence of water, a series of experiments were carried out co-feeding water with a separate feed line. Three experiments were made with H_2O/H_2S ratios of 9.7, 16, and 46, with the ratios calculated in the gas phase assuming complete conversion of DMDS to H_2S. The highest H_2O/H_2S ratio of 46 was with 33 vol% H_2O in the feed, which corresponds to a bio-oil with a high content of water (the typical water content is ca. 25 wt% [53,54]). 2 vol% DMDS was added to the feed oil, as this was found sufficient to maintain a decent activity of the catalyst in the stability experiments in Section 3.2. In the experiment, the DOD started at 58%, but during the 96 h of TOS, the catalyst lost most of its activity, ending at a DOD of 16%, *i.e.* a relative decrease of 74% in the DOD.

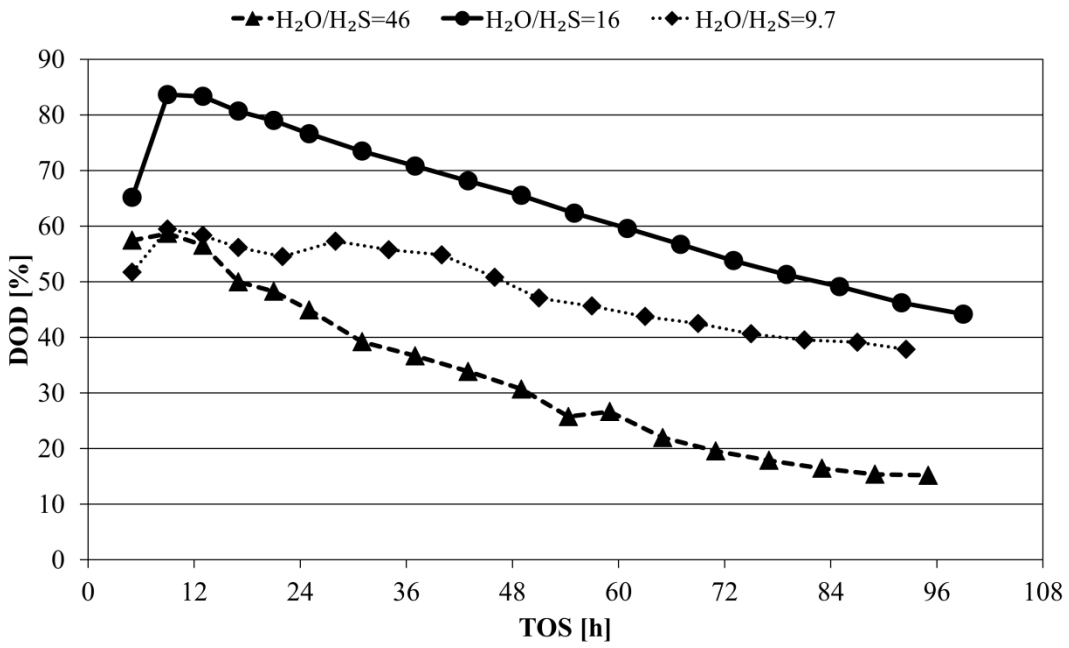

Figure 9: DOD of a phenol/1-octanol feed over a Ni-MoS_2/ZrO_2 catalyst when co-feeding water. H_2O/H_2S ratio of 46: 2 vol% DMDS in feed oil, F_{oil} = 0.2 ml/min, F_{H_2O} = 0.07 ml/min, WHSV = 5.8 h^{-1}. H_2O/H_2S ratio of 16: 5 vol% DMDS in feed oil, F_{oil} = 0.2 ml/min, F_{H_2O} = 0.07 ml/min, WHSV = 3.5 h^{-1}. H_2O/H_2S ratio of 9.7: 5 vol% DMDS in feed oil, F_{oil} = 0.33 ml/min, F_{H_2O} = 0.07 ml/min, WHSV = 5.1 h^{-1}. T = 280°C, P = 100 bar. Detailed product distributions can be found in the ESI.

In an attempt to improve the stability of the catalyst, the content of DMDS in the feed oil was increased to 5 vol% and the catalyst loading was increased, but the feed water concentration was maintained at 33 vol%, giving a H_2O/H_2S ratio of 16. This increased the stability of the catalyst somewhat, with the relative drop in the DOD now being 48% (cf. Figure 9). The general higher DOD in this case was due to the lower WHSV in this experiment.

Trying to increase the stability even further, the oil/water feed ratio was increased by increasing the oil feed rate, giving an effective water concentration of 20 vol% and a H_2O/H_2S ratio of 9.7. In this case, the DOD decreased from 58% to 38% (a relative decrease of 36%) throughout the 92 h of testing. This experiment displayed the best stability of the investigated cases.

Comparing the activity in the case of co-feeding water in Figure 9 to the case not co-feeding water in Figure 6(b), the activity decreased significantly when introducing water. This is consistent with previous work, where it has been shown that H_2O competes for the active sites on the MoS_2 [20]. This inhibiting effect is elaborated on in Section 3.7.

Calculating the Gibbs free energy for reactions between bulk MoS_2 and water at the given conditions (see ESI for elaboration), showed that ΔG is positive for all relevant reactions, indicating that oxidation of the molybdenum by water should not readily take place. This was supported by quantification of the sulfur on the used catalysts, as this was similar comparing cases with H_2O/H_2S ratios varying from 0 to 46 (cf. Table 1). Mo $K\alpha_{1,2}$ / S $K\alpha_{1,2}$ X-ray emission peaks ratio for catalysts exposed to 2 vol% DMDS without co-feeding water and in the case of H_2O/H_2S=46 was also found to be similar (cf. Figure 7).

Badawi et al. [21] showed by DFT calculations that it is the stability of the sulfur atoms located along the edges of the MoS_2 slabs which is important in this system. In their calculations, they

found that a H_2O/H_2S ratio above 40 resulted in exchange of sulfur with oxygen (S-O exchange) along the slab edges. However, the results of Figure 9 indicate that this threshold is even lower.

3.5. The Effect of Potassium

To test the effect of potassium, Ni-MoS_2/ZrO_2 was impregnated with KNO_3 to a molar a ratio of K/(Ni+Mo) of 1. This catalyst was tested with a feed of 50 g/l phenol and 2 vol% DMDS in 1-octanol, i.e. similar to the experiment presented in Figure 6(b). The development in the DOD and the conversion of phenol and 1-octanol in this experiment is shown in Figure 10. The DOD rapidly stabilized at ca. 5% and remained there for the duration of the 46 h experiment. The deoxygenation only took place by converting some of the 1-octanol, with a conversion in the order of 5%. There was practically no activity for phenol deoxygenation and the conversion was <1.5%, with the primary product being octyl phenol. This reaction was probably facilitated by the ZrO_2, as the acid sites on this previously has been found to catalyze this [46].

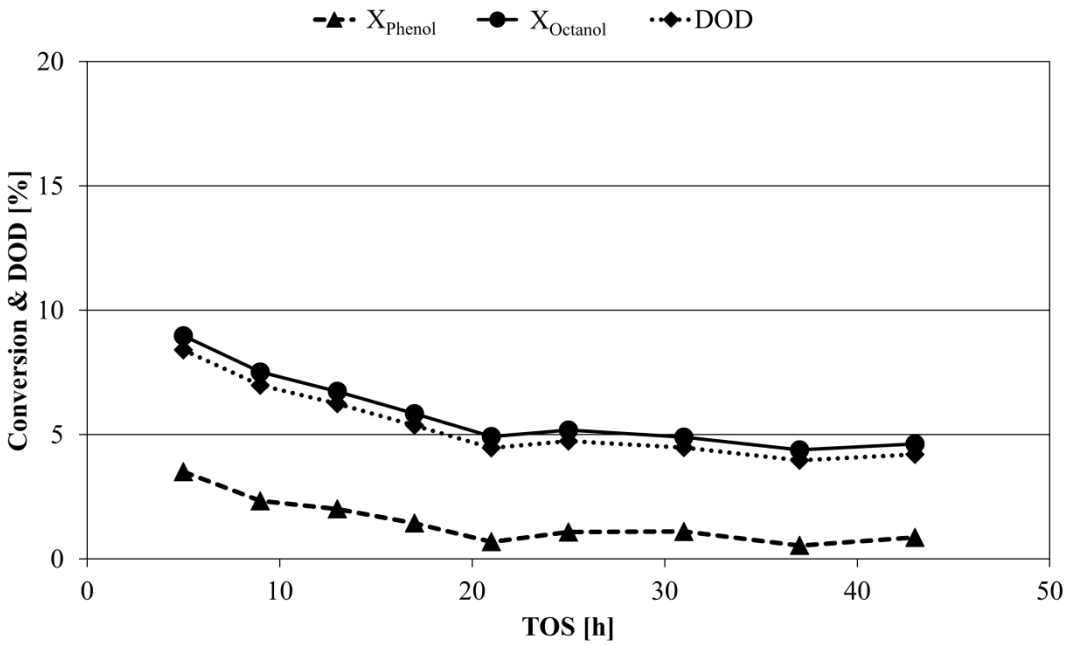

Figure 10: DOD and conversions of phenol and 1-octanol during HDO over a potassium doped Ni-MoS_2/ZrO_2 catalyst. T = 280°C, P = 100 bar, F_{oil} = 0.2 ml/min, WHSV = 4.0 h^{-1}, feed: 50 g/l phenol and 2 vol% DMDS in 1-octanol. Detailed product distributions are found in the ESI.

Comparing these results to the reference case in Figure 6(b), the DOD was on the order of 80% lower, showing severe loss of activity of the catalyst when poisoned by potassium.

Similar, Kubicka and Horacek [51] found that the primary source of deactivation of Co-MoS_2/γ-Al_2O_3 for HDO of waste rapeseed oil was deposition of alkali metals on the active sites. Andersen et al. [55] made first principle DFT calculations of potassium doped MoS_2 for CO hydrogenation. Their results showed that potassium readily binds to the edges of the MoS_2 slabs, blocking both Mo and S sites. This means that CO dissociation could not take place on the catalyst and H_2 dissociation was limited at the edges as well. Comparing this to the mechanism for HDO on MoS_2 type catalysts, the vacancy sites on the slab edges are readily blocked by potassium. Based on the

DFT calculations by Andersen et al. [55], it would therefore also be expected that the HDO activity will be suppressed by addition of potassium.

3.6. The Effect of Chlorine

To test the effect of chlorine on the stability of the catalyst, 0.3 vol% 1-chlorooctane (corresponding to 0.05 wt% Cl) was added to a feed of 50 g/l and 2 vol% DMDS in 1-octanol, simulating a typical chlorine concentration in bio-oil [47]. Figure 11 shows the development in the conversion of phenol and 1-octanol and the yields of the primary products as a function of TOS. Comparing the activity in the current case to the similar case without chlorine in the feed (cf. Figure 6(b)), the conversion of 1-octanol dropped from ca. 91% in the chlorine free case to ca. 74% with 1-chlorooctane in the feed. However, this conversion was stable throughout the 52 h of exposure to chlorine. This indicates that chlorine is not deactivating the catalyst, but rather competitively inhibit the active sites. Probably, HCl competes with the oxy-compounds for the active sites, similar to H_2O and H_2S.

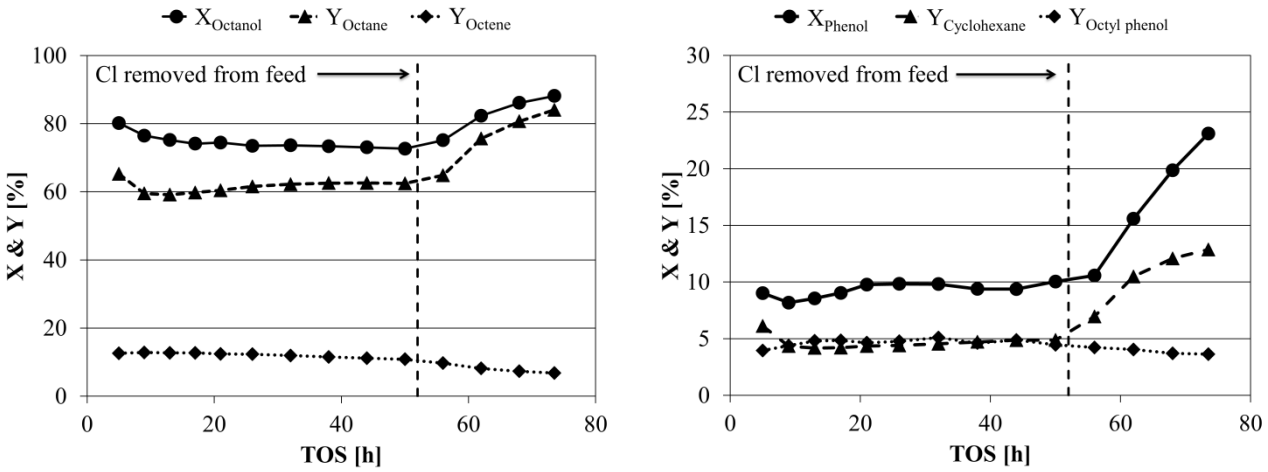

(a) Conversion and yields of 1-octanol related compounds.

(b) Conversion and yields of phenol related compounds.

Figure 11: Stability of $NiMoS_2/ZrO_2$ during HDO of phenol and 1-octanol when co-feeding 1-chlorooctane, (a) shows conversion and yields of 1-octanol related compounds and (b) shows conversion and yields of phenol related compounds. The concentration of 1-chlorooctane in the feed was 0.3 vol%, corresponding to 0.05 wt% Cl. At 52 h TOS the 1-chlorooctane was removed from the feed. T = 280°C, P = 100 bar, F_{oil} = 0.2 ml/min, WHSV = 4.0 h^{-1}, feed: 50 g/l phenol, 2 vol% DMDS, and 0.3 vol% 1-chlorooctane in 1-octanol.

The octene/octane ratio in the oil product increased from ca. 0.06 in the chlorine free case to 0.2 when co-feeding chlorine. Thus, it appears that the chlorine inhibits hydrogenation sites more pronounced than the dehydration sites. This is maybe because the dehydration partly can take place on the support [46]. Similar to 1-octanol, also the phenol conversion dropped when exposed to chlorine. Comparing to the chlorine free case, the conversion of phenol dropped from ca. 25% to ca. 10 % when feeding 1-chlorooctane. The drop in the phenol conversion is therefore more pronounced than that of 1-octanol. The conversion of phenol was, however, stable throughout the exposed time frame. The higher drop in the phenol conversion compared to 1-octanol is related to the inhibiting effect on the hydrogenation sites, as the HDO of phenol partly is dependent on the hydrogenation of the aromatic ring before deoxygenation (cf. Figure 5).

In the experiment, the conversion of 1-chlorooctane to octene/octane and HCl was ca. 40%. Cl- was verified in the aqueous phase product by precipitation of AgCl with $AgNO_3$. 40% conversion of 1-chlorooctane in the feed containing 0.3 vol% 1-chlorooctane corresponds to a release of Cl atoms relative to Mo atoms on the catalyst in a ratio of 1.1 mol Cl per mol Mo over the 52 h TOS. Thus, a constant exposure of Cl/HCl was present on the catalyst and sufficient to cause a potential deactivation.

After 52 h of TOS the 1-chlorooctane was removed from the feed. At this point the activity immediately started to increase (cf. Figure 11), slowly rising toward the activity level of the unpoisoned catalyst (cf. Figure 6(b)). This proves that the chlorine is only inhibiting and not deactivating the HDO reaction on Ni-MoS_2. In the start of the experiment the chlorine inhibition was established within the first 9 h of TOS, however re-establishing the activity after removing the chlorine from the feed was a slow process in comparison, taking more than 20 h.

3.7. Inhibition Strength of H_2S, H_2O, and HCl

From Section 3.3, 3.4, and 3.6, it follows that the presence of H_2S, H_2O, and/or HCl will inhibit the activity of the catalyst and especially the activity for HDO of phenol. To further quantify this, the experimental data was fitted to a kinetic model. HDO of model compounds as phenol has previously been indicated to follow 1st order kinetics [30,36–38], indicating that the adsorption of the reactant is rate determining. Thus, it would also be a fair assumption that the surface of the catalyst has a low coverage of the reactant while predominantly being saturated by other compounds in the feed. Considering the different species as inhibitors competing for the active sites on the catalyst, the 1st order rate constants can be expressed by the availability of free sites, in a Langmuir-Hinshelwood kinetic model [56,57]:

$$\boldsymbol{k_{eff,i} = k_{0,i} \cdot \Theta_*} \quad (8)$$

Here, k_{eff} is the effective rate constant for reaction i measured in the experiment, k_0 is the rate constant for reaction i of a catalyst with no inhibiting/deactivating species, and Θ_* is the fraction of free sites. If it is assumed that Θ_* only varies with the concentration of the impurity (i.e. nearly empty surface with respect to oxygenates), but otherwise is similar across the experiments, this is given by:

$$\boldsymbol{\Theta_* = 1 - \Theta_H - \Theta_{SH} - \Theta_{OH} - \Theta_{Cl}} \quad (9)$$

Here, Θ_H, Θ_{OH}, Θ_{SH}, and Θ_{Cl} are the fractional coverage of respectively H, OH, SH and Cl on the catalyst. These coverages are determined from the reactions:

$H_2S + 2^* \leftrightharpoons H^* + SH^*$ (10)

$H_2O + 2^* \leftrightharpoons H^* + OH^*$ (11)

$HCl + 2^* \leftrightharpoons H^* + Cl^*$ (12)

$H_2 + 2^* \leftrightharpoons 2H^*$ (13)

Assuming these reactions are in quasi equilibrium, the coverages of the species can be found as:

$$\boldsymbol{\Theta_i = \frac{K_i \cdot P_i}{\sqrt{K_{H_2} \cdot P_{H_2}}}} \quad (14)$$

Here, K_i is the equilibrium constant for the coverage of species i and P_i the partial pressure of species i. Index i represent either H_2O, H_2S, or HCl. Thus, Θ_* becomes:

$$\boldsymbol{\Theta_*} = \frac{\mathbf{1}}{\mathbf{1}+\sqrt{\boldsymbol{K_{H_2}\cdot P_{H_2}}}+\frac{\boldsymbol{K_{H_2S}\cdot P_{H_2S}}}{\sqrt{\boldsymbol{K_{H_2}\cdot P_{H_2}}}}+\frac{\boldsymbol{K_{H_2O}\cdot P_{H_2O}}}{\sqrt{\boldsymbol{K_{H_2}\cdot P_{H_2}}}}+\frac{\boldsymbol{K_{HCl}\cdot P_{HCl}}}{\sqrt{\boldsymbol{K_{H_2}\cdot P_{H_2}}}}} \quad (15)$$

$\sqrt{K_{H_2}\cdot P_{H_2}}$ was assumed constant and equal in all experiments in these calculations.

Using the two experiments with different concentrations of feed sulfur presented in Section 3.1 (see also Figure 6), k_0 and $K_{H_2S}/\sqrt{K_{H_2}}$ were calculated. Notice that k_0 was calculated from the overall conversion of phenol or 1-octanol (cf. Eq. 7). Assuming the found values of k_0 and $K_{H_2S}/\sqrt{K_{H_2}}$ constant for the experiment with water and chlorine, also $K_{H_2O}/\sqrt{K_{H_2}}$ and $K_{HCl}/\sqrt{K_{H_2}}$ were calculated, as summarized in Table 2. K_{H_2S} and K_{H_2O} were almost identical, differing by less than a factor of 1.5. Contrary, K_{HCl} was two orders of magnitude higher than both K_{H_2S} and K_{H_2O}. Thus, HCl was by far the worst inhibitor of the investigated species. From the analysis of Cl inhibition in Section 3.6 this strong effect of chlorine was not immediately apparent, but this was because only a limited release of chlorine took place due to the low conversion of 1-chlorooctane, resulting in a low partial pressure of HCl in this experiment (cf. Table 2).

Table 2: Kinetic data and inhibition constants for H_2S, H_2O, and/or HCl on a Ni-MoS_2/ZrO_2 catalyst. TOS refers to the point of evaluation in the respective experiment. k_{Ph} is the rate constant for phenol conversion k_{Oc} is the rate constant for 1-octanol conversion.

i	TOS [h]	p_{H_2S} [bar]	p_{H_2O} [bar]	p_{HCl} [bar]	k_{Ph} [ml/kg/min]	k_{Oc} [ml/kg/min]	k_0 [ml/kg/min]	$\frac{K_{H_2S}}{\sqrt{K_{H_2}}}$ [bar$^{-1/2}$]	$\frac{K_{H_2O}}{\sqrt{K_{H_2}}}$ [bar$^{-1/2}$]	$\frac{K_{HCl}}{\sqrt{K_{H_2}}}$ [bar$^{-1/2}$]
H_2S	8	0.02	0	0	65	123	67	14	-	-
H_2S	8	0.5	0	0	36	239	67	14	-	-
H_2O	9	1.9	18	0	12	91	67	14	19	-
HCl	26	0.5	0	0.009	8	109	67	14	-	6508

A similar analysis was not possible for the 1-octanol HDO reaction, because H_2S did not inhibit this reaction but rather promoted it, as already discussed in Section 3.3. However, comparing the rate constants in Table 2 for k_{Oc} shows that water and HCl both caused a significant decrease in the activity for 1-octanol HDO, as both were of roughly the same order of magnitude. However, considering that the partial pressure of H_2O was 3-4 orders of magnitude higher than the HCl partial pressure, it is clear that HCl is also the strongest inhibitor for this reaction.

As ZrO_2 previously has been shown to have a low activity at the current conditions [46], the results in Table 2 reflect that the changes in activity of Ni-MoS_2/ZrO_2 when exposed to different impurities must be due to changes in the catalytic active phase and that this very likely could be a symptom of available active sites, as initially assumed.

In conclusion, the results show that the strength of inhibition of the investigated species qualitatively is given as:

$$HCl >> H_2O \approx H_2S \quad (16)$$

In a broader context, H_2S, H_2O, CO, and NH_3 are all inhibitors of sulfide catalysts as they compete for the active sites [20,41,52,58]. Badawi et al. [20] found the following order of inhibition for HDO of guaiacol on MoS_2 based on DFT calculations:

$$CO > H_2S \approx H_2O \quad (17)$$

Their results also indicate that H_2S and H_2O are roughly equally strong inhibitors. Laurent and Delmon [41] evaluated first order rate constants for a Ni-MoS_2/γ-Al_2O_3 catalyst and found the following order of inhibition of the hydrotreating reaction:

$$NH_3 > H_2S > H_2O \quad (18)$$

To put the current work into perspective, it seems apparent that performing HDO of a real bio-oil with a Ni-MoS_2 based catalyst will be challenged by the many impurities found in bio-oil. Potassium should be removed prior to the HDO reactor as this is a source of severe and persistent deactivation (cf. Figure 10). A guard bed prior to the hydrotreating reactor has been proposed to prevent metal deposition [58]. Here metals would be trapped in a porous material like alumina, bauxite, magnesium silicate, clays, or similar. This will however not trap organic bound metals. Alternatively, Bridgwater [53] suggested that nearly all alkali metals can be captured in the ash fraction in the flash pyrolysis plant, and so it is not a question of removing potassium from the bio-oil, but avoiding that it comes there in the first place.

It may not be necessary to remove H_2S, H_2O, and Cl (as organic chlorine or HCl) prior to the HDO reactor, but they will inhibit the activity of the catalyst as they compete for the active sites. If the content of chlorine is low this can probably be tolerated if the residence time is chosen accordingly. On the other hand, the presence of water needs to be balanced by a sulfur source which could be done by either addition of sufficient sulfur (as DMDS, H_2S, etc.) or recirculation of part of the hydrocarbon product to decrease the water concentration in the feed. Recirculation is probably needed for bio-oils with high water contents, as 5 vol% DMDS was insufficient to maintain stability of an oil with 33 vol% water. Addition of such high levels of DMDS seems questionable. The requirement of a sulfur feed will additionally require an increased residence time, both to circumvent the inhibiting effect of H_2S, but also to ensure that any sulfur containing byproducts which have been formed in the process efficiently are desulfurized again to ensure a sulfur lean product.

4. Conclusion

The stability of Ni-MoS_2/ZrO_2 has been investigated during HDO of phenol in 1-octanol, as a bio-oil model compound system. Constant addition of sulfur is essential to obtain prolonged stable operation of the catalyst and it was found that adding thiols to the feed in a concentration comparable to what can be found in bio-oil is insufficient to ensure stable operation. Instead, DMDS was found as a good sulfur source during the process, which should be added to the feed in a concentration of >1 vol%. This requirement was furthermore confirmed by STEM-EDX investigations, revealing a loss of sulfur from the active phase of the catalyst when co-feeding insufficient amounts of sulfur during HDO.

The downside of adding sulfur is that this leads to incorporation of sulfur in the product. Especially unsaturated double bonds (formed from dehydration reactions) were found to willingly react with H_2S to form thiols. However, operating at sufficiently high residence time (WHSV<4.9 h^{-1}) reduced the presence of thiols in the oil product as the catalyst also is active in HDS.

Water was found to be an inhibitor and the H_2O/H_2S ratio is essential in determining the catalyst stability. This ratio should be kept lower than at least 10 to obtain reasonable stability. Even lower ratios may be needed to obtain sufficient stability during prolonged operation (>100 h). While bulk MoS_2 is thermodynamically stable towards oxidation by H_2O, it is replacement of the edge sulfur atoms with oxygen which is critical in the presence of water.

Impregnation of Ni-MoS_2/ZrO_2 with KNO_3 to a molar a ratio of K/(Ni + Mo) of 1 was found to severely decrease the activity of the catalyst. Without potassium a DOD of ca. 90% could be achieved, but adding potassium the DOD was only ca. 5%. The deactivation was caused by occupation of vacancy sites along the MoS_2 edges by potassium, blocking the active sites for HDO.

Simulating the presence of organically bound chlorine in bio-oil by adding 1-chlorooctane, it was found that Ni-MoS_2/ZrO_2 was inhibited by this species. This effect was explained by competitive adsorption of the formed HCl on the active sites. However, removing 1-chlorooctane from the feed restored the activity of the catalyst to a level similar to the un-poisoned case, showing that chlorine poisoning was completely reversible.

Commonly, H_2S, H_2O, and HCl inhibits HDO of especially phenol. Competitive adsorption was described by a Langmuir-Hinshelwood approach and applied to quantify the inhibition of these species. This analysis showed that HCl was by far the strongest inhibitor followed by H_2O and H_2S of roughly equal strength. However, potassium was the strongest poison of all the investigated impurities, leading to complete and persistent loss of activity.

Overall, Ni-MoS_2/ZrO_2 is a prospective catalyst for HDO of phenol with promising stability, as long as a sufficient co-feed of sulfur is supplied. Of the investigated bio-oil impurities, potassium was the worst while H_2S, H_2O, and HCl primarily inhibited the catalyst. When using this catalyst it is recommended to use a high residence time to manage the inhibitors and furthermore to remove potentially formed thiols.

Acknowledgement

This work is part of the Combustion and Harmful Emission Control (CHEC) research center at The Department of Chemical and Biochemical Engineering at the Technical University of Denmark (DTU). The present work is financed by DTU and The Catalysis for Sustainable Energy initiative (CASE), funded by the Danish Ministry of Science, Technology and Innovation. The A. P. Møller and Chastine Mc-Kinney Møller Foundation is gratefully acknowledged for its contribution towards the establishment of the Center for Electron Nanoscopy at the Technical University of Denmark. The research leading to these results has received funding from the European Union Seventh Framework Programme under Grant Agreement 312483 - ESTEEM2 (Integrated Infrastructure Initiative–I3).

References

[1] S. Sorrell, J. Speirs, R. Bentley, A. Brandt, R. Miller, Energ Policy 38 (2010) 5290–5295.
[2] S. Joussaume, J. Penner, F. Tangang, Working Group Contribution to the IPCC Fifth Assessment Report Climate Change 2013: The Physical Science Basis, Intergovernmental Panel on Climate Change, 2013.
[3] M. Balat, Energ Convers Manage 52 (2011) 858–875.

[4] A. Roedl, Int J Life Cycle Assess 15 (2010) 567–578.
[5] K. Raffelt, E. Henrich, A. Koegel, R. Stahl, J. Steinhardt, F. Weirich, Appl Biochem Biotech 129 (2006) 153–164.
[6] P.M. Mortensen, J.-D. Grunwaldt, P.A. Jensen, K.G. Knudsen, A.D. Jensen, Appl Catal Gen 407 (2011) 1–19.
[7] P.M. Mortensen, D. Gardini, H.W.P. de Carvalho, C.D. Damsgaard, J.-D. Grunwaldt, P.A. Jensen, J.B. Wagner, A.D. Jensen, Catal Sci Technol 4 (2014) 3672–3686.
[8] D.C. Elliott, Energy Fuels 21 (2007) 1792–1815.
[9] E. Furimsky, Catal Today 217 (2013) 13–56.
[10] R.V. Chaudhari, A. Torres, X. Jin, Subramaniam, Ind Eng Chem Res 52 (2013) 15226–15243.
[11] H. Topsøe, B.S. Clausen, F.E. Massoth, Hydrotreating Catalysis, Springer-Verlag, 1996.
[12] H. Topsøe, K.G. Knudsen, L.S. Byskov, J.K. Nørskov, B.S. Clausen, in:, Sci. Technol. Catal., Elsevier, 1999, pp. 13–22.
[13] R. Prins, in:, John Wiley & Sons, Inc.: New York, 2008, pp. 2695–2718.
[14] P. Raybaud, Appl Catal Gen 322 (2007) 76–91.
[15] Y. Romero, F. Richard, S. Brunet, Appl Catal B Env. 98 (2010) 213–223.
[16] S. Helveg, J.V. Lauritsen, E. Lægsgaard, I. Stensgaard, J.K. Nørskov, B.S. Clausen, H. Topsøe, F. Besenbacher, Phys Rev Lett 84 (2000) 951–954.
[17] R. Prins, Adv Catal 46 (2001) 399–464.
[18] J.V. Lauritsen, J. Kibsgaard, S. Helveg, H. Topsøe, B.S. Clausen, E. Laegsgaard, F. Besenbacher, Nat Nanotechnol 2 (2007) 53–58.
[19] F. Besenbacher, M. Brorson, B.S. Clausen, S. Helveg, B. Hinnemann, J. Kibsgaard, J.V. Lauritsen, P.G. Moses, J.K. Nørskov, H. Topsøe, Catal Today 130 (2008) 86–96.
[20] M. Badawi, J.-F. Paul, S. Cristol, E. Payen, Catal Commun 12 (2011) 901–905.
[21] M. Badawi, J.-F. Paul, S. Cristol, E. Payen, Y. Romero, F. Richard, S. Brunet, D. Lambert, X. Portier, A. Popov, E. Kondratieva, J.M. Goupil, J.E. Fallah, J.-P. Gilson, L. Mariey, A. Travert, F. Mauge, J Catal 282 (2011) 155–164.
[22] W. Mu, H. Ben, A. Ragauskas, Y. Deng, Bioenerg Res 6 (2013) 1183–1204.
[23] J.K. Nørskov, B.S. Clausen, H. Topsøe, Catal Lett 13 (1992) 1–8.
[24] O.I. Senol, E.-M. Ryymin, T.-R. Viljava, A.O.I. Krause, J. Mol. Catal. Chem. 277 (2007) 107 – 112.
[25] O.I. Senol, T.-R. Viljava, A.O.I. Krause, Appl. Catal. Gen. 326 (2007) 236 – 244.
[26] K.C. Pratt, J.V. Sanders, V. Christov, J Catal 124 (1990) 416–432.
[27] M. Breysse, J.L. Portefaix, M. Vrinat, Catal Today 10 (1991) 489–505.
[28] V.A. Yakovlev, S.A. Khromova, O.V. Sherstyuk, V.O. Dundich, D.Y. Ermakov, V.M. Novopashina, M.Y. Lebedev, O. Bulavchenko, V.N. Parmon, Catal Today 144 (2009) 362–366.
[29] V.N. Bui, D. Laurenti, P. Delichére, C. Geantet, Appl Catal B Env. 111 (2011) 246–255.
[30] P.M. Mortensen, J.-D. Grunwaldt, P.A. Jensen, A.D. Jensen, ACS Catal 3 (2013) 1774–1785.
[31] E. Laurent, B. Delmon, J Catal 146 (1994) 281–291.
[32] A.L. Jongerius, J.R. Copeland, G.S. Foo, J.P. Hofmann, P.C.A. Bruijnincx, C. Sievers, B.M. Weckhuysen, ACS Catal 3 (2013) 464–473.
[33] H.S. Fogler, Elements of Chemical Reaction Engineering, Prentice Hall: New Jersey, 2006.
[34] W.M. Haynes, ed., CRC Handbook of Chemistry and Physics 92th Edition (Internet Version 2012), CRC Press, 2010.
[35] K. Schofield, Prog Energ Combust 34 (2008) 330–350.
[36] S.J. Hurff, M.T. Klein, Ind Eng Chem Fundam 22 (1983) 426–430.
[37] P.M. Mortensen, J.-D. Grunwaldt, P.A. Jensen, A.D. Jensen, Submitt. Catal Today (2015).
[38] M.V. Bykova, S.G. Zavarukhin, L.I. Trusov, V.A. Yakovlev, Kinet Catal 54 (2013) 40–48.
[39] R.G. Dickinson, L. Pauling, Am Chem S 45 (1923) 1466–1471.
[40] B.S. Gevert, J.-E. Otterstedt, F.E. Massoth, Appl Catal 31 (1987) 119–131.
[41] E. Laurent, B. Delmon, Ind Eng Chem Res 32 (1993) 2516–2524.

[42] T.-R. Viljava, S. Komulainen, T. Selvam, A.O.I. Krause, in:, G.F.F. B. Delmon, P. Grange (Eds.), Hydrotreatment Hydrocracking Oil Fractions, Elsevier: Amsterdam, 1999, pp. 145 – 152.
[43] F.E. Massoth, P. Politzer, M.C. Concha, J.S. Murray, J. Jakowski, J. Simons, J Phys Chem B 110 (2006) 14283–14291.
[44] E.-M. Ryymin, M.L. Honkela, T.-R. Viljava, A.O.I. Krause, Appl Catal Gen 389 (2010) 114–121.
[45] Q. Bu, H. Lei, A.H. Zacher, L. Wang, S. Ren, J. Liang, Y. Wei, Y. Liu, J. Tang, Q. Zhang, R. Ruan, Bioresour. Technol 124 (2012) 470–477.
[46] P.M. Mortensen, H.W.P. and de Carvalho, J.-D. and Grunwaldt, P.A. Jensen, A.D. and Jensen, J Catal 328 (2015) 208–215.
[47] T.N. Trinh, P.A. Jensen, H.R. Sørensen, K. Dam-Johansen, S. Hvilsted, Energy Fuels 27 (2013) 1399–1409.
[48] T.-R. Viljava, R.S. Komulainen, A.O.I. Krause, Catal Today 60 (2000) 83–92.
[49] E.-M. Ryymin, M.L. Honkela, T.-R. Viljava, A.O.I. Krause, Appl Catal Gen 358 (2009) 42–48.
[50] M. Badawi, S. Cristol, J.-F. Paul, E. Payen, C R Chim. 12 (2009) 754–761.
[51] D. Kubicka, J. Koracek, Appl Catal Gen 394 (2011) 9–17.
[52] A.Y. Bunch, X. Wang, U.S. Ozkan, J Mol Cat Chem 270 (2007) 264–272.
[53] A.V. Bridgwater, Biomass Bioeng 38 (2012) 68–94.
[54] D. Meier, B. van de Beld, A.V. Bridgwater, D.C. Elliott, A. Oasmaa, F. Preto, Renew Sust Energ Rev 20 (2013) 619 – 641.
[55] A. Andersen, S.M. Kathmann, M.A. Lilga, K.O. Albrecht, R.T. Hallen, D. Mei, J Phys Chem C 115 (2011) 9025–9040.
[56] I. Chorkendorff, J.W. Niemantsverdriet, Concepts of Modern Catalysis and Kinetics, John Wiley & Sons, Inc.: New York, 2007.
[57] P. Stoltze, J.K. Nørskov, in:, John Wiley & Sons, Inc.: New York, 2008, pp. 1479–1492.
[58] E. Furimsky, F.E. Massoth, Catal Today 52 (1999) 381–495.

Title: Visualizing the Mobility of Silver During Catalytic Soot Oxidation

Author: Diego Gardini Jakob M. Christensen Christian D. Damsgaarda Anker D. Jensen Jakob B. Wagner

PII: S0926-3373(15)30209-5
DOI: http://dx.doi.org/doi:10.1016/j.apcatb.2015.10.029
Reference: APCATB 14336

To appear in: *Applied Catalysis B: Environmental*

Received date: 12-8-2015
Revised date: 9-10-2015
Accepted date: 12-10-2015

Please cite this article as: Diego Gardini, Jakob M.Christensen, Christian D.Damsgaarda, Anker D.Jensen, Jakob B.Wagner, Visualizing the Mobility of Silver During Catalytic Soot Oxidation, Applied Catalysis B, Environmental http://dx.doi.org/10.1016/j.apcatb.2015.10.029

Visualizing the Mobility of Silver During Catalytic Soot Oxidation

Diego Gardini[1], Jakob M. Christensen[2], Christian D. Damsgaard[1,3], Anker D. Jensen[2], Jakob B. Wagner[1*]

[1]Center for Electron Nanoscopy, Technical University of Denmark, Fysikvej, Building 307, DK-2800 Kgs. Lyngby, Denmark.

[2]Department of Chemical and Biochemical Engineering, Technical University of Denmark, Søltofts Plads, Building 229, DK-2800 Kgs. Lyngby, Denmark

[3]Center for Individual Nanoparticle Functionality, Department of Physics, Technical University of Denmark, Fysikvej, Building 307, DK-2800 Kgs. Lyngby, Denmark

Corresponding author. Tel: +4545256471. E-mail: jakob.wagner@cen.dtu.dk

GRAPHICAL ABSTRACT

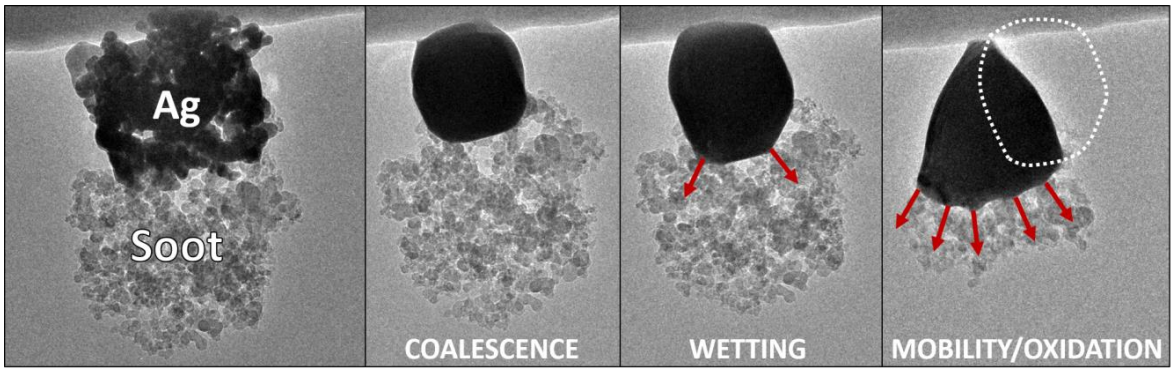

Highlights

- Silver particles exhibit significant mobility during catalytic soot oxidation due to attractive forces between the metal and the moving carbon oxidation front.
- Mobility ensures the constant presence of a reactive carbon-silver-oxygen interface during oxidation.
- Smaller silver particles show mobility at lower temperatures due to their lower internal cohesive energy and are hence able to catalyze more efficiently soot oxidation at lower temperatures.

Abstract

The catalytic activity and mobility of silver nanoparticles used as catalysts in temperature programmed oxidation of soot:silver (1:5 wt:wt) mixtures have been investigated by means of flow reactor experiments and *in situ* environmental transmission electron microscopy (ETEM). The carbon oxidation temperature was significantly lower compared to uncatalyzed soot oxidation with soot and silver loosely stirred together (loose contact) and lowered further with the two components crushed together (tight contact). The *in situ* TEM investigations revealed that the silver particles exhibited significant mobility during the soot oxidation, and this mobility, which increases the soot/catalyst contact, is expected to be an important factor for the lower oxidation temperature. In the intimate tight contact mixture the initial dispersion of the silver particles is greater, and the onset of mobility occurs at a lower temperature which is consistent with the lower oxidation temperature of the tight contact mixture.

Keywords: silver mobility; environmental TEM; soot oxidation

1. Introduction

Soot particles in the exhaust from diesel vehicles are likely to cause lung cancer and to affect the local climate and air quality [1-6]. For that reason the soot particles are typically removed from the exhaust gas by filtration through a ceramic filter [7, 8]. The filter needs periodic regeneration, in which the filter temperature is increased, and the soot is burned away. The growing back pressure due to the soot deposits and the increased temperature required for filter regeneration increase the fuel consumption [9, 10]. To limit this extra fuel consumption it is desirable to develop low temperature soot oxidation catalysts to lower the regeneration temperature. The heterogeneously catalyzed soot oxidation is a gas/solid/solid interaction, and the contact between soot and catalyst is very important for the catalytic activity [11]. In tests where soot and catalyst are crushed together (so-called tight contact), the oxidation occurs at a significantly lower temperature, compared to when soot and catalyst are stirred together with a spatula (so-called loose contact) [11]. Several experiments with diesel soot filters [10, 12-15] have indicated the presence of both contact types. An explanation of this may come from the environmental scanning electron microscopy experiments by Kameya and Lee [16], who observed that the catalytic oxidation at the interface between the bottom of the soot cake and the catalyst containing filter caused the soot cake to crack, leading to a delamination and subsequent diminishment or even loss of soot/catalyst contact [16]. It is thus likely that the development of catalysts for real filter applications will benefit from an understanding of both types of contact.

In terms of what constitutes a good catalyst both the surface area [17-19] and the strength of the oxygen-catalyst bond are very important for the catalytic activity [20]. Silver is able to activate oxygen by dissociative adsorption already at low temperature [21, 22], and in a number of cases silver-based catalysts have been reported to exhibit high activity for catalytic soot oxidation [18, 23-33]. It is particularly interesting that soot oxidation at relatively low temperatures has been achieved in loose contact with silver [24, 33]. It is therefore relevant to investigate the behavior of silver at the conditions of catalytic soot oxidation. In this work we employ catalytic oxidation tests and environmental transmission electron microscopy (ETEM) during *in situ* soot oxidation to evaluate the behavior of silver at the conditions relevant for catalytic soot oxidation. ETEM is a unique tool for visualizing and characterizing the dynamic evolution of soot oxidation catalysts in action as illustrated by earlier works [34,35].

2. Experimental

2.1 Materials

A commercial Ag nanopowder sample from Sigma-Aldrich (2.1 m^2/g, <932 ppm metal impurities, ~2 wt% PVP) was used as catalyst in the experiments. The identity of the silver sample was verified by X-Ray diffraction (Figure S1 in the Supplementary Information). The soot used in the experiments was a reference material from NIST: "SRM 2975 Diesel Particulate Matter" (91 m^2/g, 86-87 wt% C, 1-2 wt% H, ~1 wt% S, 2.7 wt% extractable organics [19, 34-36]).

2.2 Catalyst characterization

Morphology, chemical composition and crystallinity of silver and soot were investigated with a FEI Titan 80-300 Analytical transmission electron microscope (TEM) operated at 300 kV in bright-field (BF) and high-angle annular dark field (HAADF) scanning TEM (STEM) mode. The soot:silver mixtures were dry dispersed onto lacey carbon supported copper grids and loaded on a standard single tilt TEM holder.

2.3 Catalytic soot oxidation in flow reactor

The catalytic activity of Ag in soot oxidation was measured using temperature programmed oxidation (TPO) in a flow reactor setup described elsewhere [20]. For the activity tests soot (~2 mg) and catalyst in a ratio of 1:5 (wt:wt) were stirred together with a spatula (loose contact) or crushed together for 6 minutes in an agate mortar (tight contact). The soot/catalyst mixture was transferred to a 7 cm long, 1 cm wide alumina sample holder, which was placed in the center of a quartz tube (length: 65 cm, inner diameter: 24 mm) within a horizontal, tubular furnace. The sample was then subjected to a 1 NL/min flow of 10.2 vol% O_2 in N_2. The feed gases (N_2 and O_2 from AGA A/S) were dosed by means of Bronkhorst EL-FLOW mass flow controllers. When the sample had been installed in the oven, and once any remnants of air had been purged from the reactor (when the CO_2 signal from ambient air had dropped below the detection limit) the reactor was heated at a rate of 11 °C/min to a final temperature of 750 °C. The temperature was monitored by a type K thermoelement at the external surface of the quartz tube wall. The concentrations of CO and CO_2 in the reactor effluent were monitored continuously using an ABB AO2020 IR gas analyzer calibrated using a certified $CO/CO_2/N_2$ gas mixture from AGA A/S. During the experiments the levels of CO and CO_2 in the effluent stream were in the 0-500 ppmv range, and the oxygen conversion was thus negligible in the present experiments. In one experiment the supply of pure oxygen was replaced with a 1 vol% O_2 in

N_2 gas mixture (AGA A/S) to obtain an oxygen partial pressure (296 Pa) almost identical to the one employed in the ETEM experiments.

2.4 In situ soot oxidation in the environmental transmission electron microscope

In situ soot oxidation was investigated in a FEI Titan 80-300 transmission electron microscope equipped with a differentially pumped environmental cell [37]. The soot:silver mixtures (1:5 wt:wt) in loose and tight contact mode were dry dispersed on the surface of MEMS thermal EMheaterchips (DENSsolutions) with no carbon support film and then mounted in an SH30 heating holder (DENSsolutions). In the electron microscope, the samples were exposed to 300 Pa O_2 and heated in the temperature range 150 – 854 °C at a rate of 11 °C/min.

3. Results and Discussion

3.1 Soot/catalyst contact

The bright field TEM (BF-TEM) micrographs of soot:silver mixtures (1:5 wt:wt) in Figure 1 illustrate the contact between the solids in the two contact conditions. In loose contact silver was observed to form big agglomerates sharing a limited number of contact points with the soot agglomerates. In tight contact silver particles were instead observed to be more dispersed, and most of the surface of the catalyst appears to interface the soot.

Scanning Transmission Electron Microscopy (STEM) analysis of the two samples revealed the presence of a distribution of small nanoparticles of approximately 2-5 nm diameter in both contact modes (cf. Figure 2). These were mostly identified in the near vicinity of big silver clusters, but were found as well mixed with the soot cake far from the main Ag agglomerates. STEM Energy Dispersive X-Ray Spectroscopy (STEM-EDX) measurements carried out on a single small nanoparticle (cf. Figure 3-a) and on areas containing few particles (cf. Figure 3-b) revealed in both cases the presence of the elements silver, carbon and sulfur. The presence of carbon and sulfur were ascribed to the soot fraction [34]. The small nanoparticles identified by STEM might represent a finely divided fraction of the silver catalyst. The copper signal in the spectrum originated from the sample holder, and the observed sodium might be a part of the ash in the soot.

3.2 Activity in catalytic oxidation

Figure 4 shows the oxidation rate as a function of temperature for pure soot, and for soot mixed with Ag in tight or loose contact in the flow reactor tests. The silver catalyst generally shows a high activity for soot oxidation. The significant activity in loose contact, where the temperature of maximal oxidation rate is shifted downwards by 123 °C compared to pure soot, is especially noteworthy, since it is very challenging to achieve a significant activity in this situation [11, 20]. The reason for the high activity in loose contact will be discussed further in section 3.4 below. The sharp peak in the oxidation rate at a temperature of 325 °C is due to oxidation of polyvinylpyrrolidone (PVP), which is present as as a stabilizer/dispersant in the commercial silver nanoparticle sample. Figure S2 in the Supplementary information shows how the oxidation of this polymer in the absence of soot occurs in a sharp peak just above 300 °C (see also Shen et al. [38]). In a rerun experiment, where the spent silver sample is again mixed with soot in loose contact, the activity is decreased, however despite having been exposed to high temperature the silver catalyst retains significant activity for loose contact soot oxidation ("Loose contact rerun" in Figure 4).

3.3 In situ soot oxidation in the environmental transmission electron microscope

It is known [11, 20] to be a great challenge to achieve a significant lowering of the oxidation temperature with loose contact between catalyst and soot, and the significant effect of metallic silver in loose contact with soot is thus a particularly striking feature in Figure 4. Assuming an intermediate oxygen coverage the heat of oxygen chemisorption on metallic silver should be in the order of 130 kJ/mol [39-41], which should make silver well suited for oxygen activation [20, 42]. However there might also be behavioral traits that contribute towards enabling silver to achieve soot oxidation at relatively low temperatures. In order to improve the understanding of the catalytic behavior of metallic silver, soot:silver mixitures in both tight and loose contact conditions were investigated using environmental transmission electron microscopy (ETEM). *In situ* oxidation was carried out in an oxygen partial pressure p_{O_2} = 300 Pa by heating the mixtures from 150 to 854 °C using the same temperature ramp as in the flow reactor experiments (11 °C/min). Micrographs of the oxidation reaction are acquired every 25 seconds and finally combined together to form playable time-lapses of 8 FPS (Movie 1 and 2) and 10 FPS (Movie 3).

In situ oxidation in loose contact

Figure 5 shows four key frames representing soot oxidation in the ETEM in the loose contact condition. As Movie 1 shows, in the temperature range 25-280 °C no evident changes in soot or Ag

morphology were observed (Figure 5-a). As the temperature increased from 280 to 472 °C, silver particles began to coalesce, forming larger rounded agglomerates (Figure 5-b). At 500 °C coalesced silver agglomerates were observed to be mobile, moving on the soot cake and actively oxidizing the soot particles. Soot oxidation at the Ag/C interface was visually confirmed by the disappearance of soot particles in contact with silver. The mobility was estimated visually to be maximal around 700 °C (Figure 5-c) and oxidation was reported to end at about 760 °C, when all the soot was consumed and the silver had coalesced to a single particle (Figure 5-d).

In situ oxidation in tight contact

Similarly to what has been presented in the previous paragraph for loose contact, the four steps of *in situ* soot oxidation in the tight contact condition are summarized in Figure 6. As Movie 2 shows, in the temperature range 25-250 °C no obvious changes in soot or Ag morphology were observed except for the collapse of part of the soot structure on the right hand side of the specimen area (Figure 6-a). Between 250 and 338 °C silver particles coalesced forming round agglomerates (Figure 6-b). Silver coalescence was observed to occur approximately 30 °C earlier compared to the loose contact condition due to the presence of smaller silver particles in the sample– naturally requiring lower temperatures for initiating the coalescence process. Starting from T=342 °C the small silver particle groups exhibited high mobility over the soot cake. Oxidation activity by silver particles could again be identified by disappearance of soot. Silver mobility was estimated to have its peak around 526 °C (Figure 6-c). Around 700 °C soot oxidation was observed to be complete (Figure 6-d).

3.4 Origin of silver mobility and its implications on catalytic activity

Previous studies in literature have shown that the oxidation of graphite single crystals can be effectively catalyzed by a two-step mechanism involving the mobility of metallic nanoparticles [43, 44]. At 500 °C in a 670 Pa O_2 atmosphere, platinum nanoparticles were reported to initially penetrate the graphite basal plane to produce pits. Upon temperature increase to 735 °C the particles were found to move parallel to the graphite surface, digging relatively straight channels with sudden change of direction by 60 and 120° [43]. In a similar experiment, between 327 – 577 °C and in an atmosphere of 4.5 – 13 Pa O_2, silver nanoparticles deposited on graphene were reported to catalytically remove carbon atoms producing channels aligned parallel to the <100> graphene directions [45]. This channeling effect could be explained by taking the adhesion energy between the metal particle and the carbon edge atoms in contact with it into consideration. This adhesion has

been ascribed to van der Waal forces at the metal/carbon interface [44], although chemical bonding cannot be completely excluded. In DFT calculations Pizzocchero et al. [46] did observe a bonding between the edge of graphene and silver. During oxidation, the temperature is high enough to enhance the mobility of silver atoms and cause wetting of the graphite surface. As carbon atoms are removed by catalytic oxidation these attractive forces at the interface pull the silver particle along with the reaction front causing the particle to move. The straightness and preferential orientation of the channels would then arise from the anisotropic reactivity of the oxidation reaction along different lattice directions, as seen in both graphite and graphene oxidation where channels were found to be oriented parallel to the <100> directions. Silver particle motion on an amorphous and tridimensional structure like soot is not expected to follow any preferential direction, but rather to reflect the local variations of the Ag-C interface due to soot morphology. As shown in Section 3.3 and summarized in Table 1 the onset of silver mobility and the mobility peak temperatures remain very dependent on the initial contact, although silver was found to start coalescing at approximately the same temperature for both loose and tight contact. The presence of PVP might have an influence on the initial silver coalescence. Oxidation of the PVP stabilizer layer is most likely needed before Ag nanoparticles start to coalesce. This may justify the similar temperature needed to trigger this sintering process for both contact modes.

Overall, mobility of silver in the tight contact condition was found to occur at consistently lower temperature than in the loose contact condition. As Movie 3 shows, in loose contact, silver particles in larger clusters are kept together by the Ag-Ag cohesive energy from large agglomerates in contact with the soot cake (cf. Figure 7-a). Upon temperature increase, silver particles start to coalesce forming round agglomerates (cf. Figure 7-b). Silver was observed to maintain its crystalline state after coalescence phase and throughout the rest of the *in situ* oxidation experiment for both contact modes. This was confirmed by the report of typical BF-TEM diffraction halos from silver particles and the acquisition of time lapsed electron diffraction patterns during additional *in situ* oxidation experiments (cf. Figure S3 in Supplementary Information). As the temperature rises, silver layers situated at the edge of the coalesced agglomerates have sufficient energy to overcome the internal Ag-Ag cohesive energy and start wetting the soot surface causing a local deformation of the agglomerate (cf. Figure 7-c). When the temperature is high enough, catalytic carbon oxidation occurs and the attractive forces between silver and soot will maintain the contact between silver and the progressing oxidation front, causing a net movement of the Ag agglomerate (cf. Figure 7-d). The local geometry of the silver/soot interface can greatly influence the magnitude of the attractive forces. In extreme cases, wetting can

cause portions of silver agglomerates to deform to the point where separation occurs and smaller silver particles released from the main Ag agglomerate start to move on the soot cake (cf. Figure 8). It thus seems reasonable that silver exhibits a relatively high loose contact activity, as the relatively high mobility of the silver helps to overcome the initially poor dispersion of the catalyst particles in loose contact.

In the case of tight contact, where the oxidation occurs at a lower temperature, the silver is present as smaller agglomerates (or isolated silver particles), and not only is the carbon/silver interface greater than in the loose contact case, but the mobility of an isolated silver particle is also not restricted by the same Ag-Ag cohesive energy as a silver particle within a larger cluster. It is hence reasonable that the tight contact mixture exhibits mobility at lower temperatures compared to loose contact in complete consistency with the lower oxidation temperature. A clear example of this mobility behavior is further shown in Movie 3, where small (< 10 nm) silver nanoparticles dispersed on the soot fraction were observed to be mobile at lower temperatures than the large silver agglomerate (c.f. Figure 9).

Ag mobility thus plays a key role in the catalyzed oxidation of soot by constantly ensuring the presence of a silver-carbon-oxygen reactive interface. This reciprocal relationship between oxidation and mobility was verified in an *in situ* control experiment, wherein a soot:silver mixture in tight contact mode did not show any mobility effect when heated in absence of oxygen (vacuum), thus confirming that soot oxidation is necessary for mobility to take place (cf. Figure S4 in Supplementary Information).

3.5 Effects of oxygen pressure

The oxidation temperature differences observed in the flow reactor experiments for soot:silver mixtures in loose and tight contact conditions (cf. Section 3.3, Table 2), could then be ascribed to the different temperatures required to trigger the mobility of silver for the two different contact conditions. In tight contact, small silver particles requires lower temperatures to start moving and actively oxidize the soot cake while being moved by attractive forces, possibly van der Waal forces. Vice-versa, in loose contact, higher temperatures are needed in order for van der Waal forces to overcome the silver agglomerate's internal Ag-Ag cohesive energy and initiate oxidative mobility.
In this case the ETEM experiments at a comparatively low oxygen pressure are used to explain the behavior in the flow reactor tests with a partial pressure representative for real diesel vehicle exhaust, and the pressure gap should thus be taken into account. For both loose and tight contact conditions the temperature offset between overall silver mobility as observed in ETEM experiments and carbon

oxidation rate from TPO experiments could be related to the different oxygen pressures used in the two setups. If it is assumed that the soot oxidation is first order in the oxygen pressure and other kinetic parameters are fitted to the measured data one obtains the following rate expression:

$$\frac{dX}{dt} = 3268\,\mathrm{min}^{-1}\cdot Pa^{-1}\cdot \exp\left(\frac{-125^{kJ/mol}}{RT}\right)(1-X)^{3/2}\, p_{O_2}$$

Where X is the degree of carbon conversion, R is the gas constant, T is the temperature and p_{O_2} is the partial pressure of oxygen. The reaction order in the carbon conversion is usually interpreted in terms of the development in reactant surface area with carbon consumption (⅔ for shrinking spheres, 1 for a fully porous solid). A reaction order above one implies that the surface area increases with increasing consumption, which is usually not realistic. However, in the present case, where the degree of conversion is increased through increasing temperature, the *in situ* TEM studies illustrate that the very important Ag-soot interfacial area can increase at higher temperature as a result of silver's mobility, so the high reaction order in the carbon conversion is to some extent consistent with the observed behavior of the catalyst. Figure 10 shows the measured carbon oxidation rates in TPO experiments at two different partial pressures of oxygen, namely 10335 Pa (as used in the other TPO experiments) and 296 Pa (representing the pressure used in the in situ TEM experiments) as well as the predicted rate profiles using the fitted rate expression. The figure shows that the same rate expression can be used to provide a reasonable description of the behavior at both the two oxygen pressures, and since the occurrence of the oxidation in the *in situ* TEM experiments agrees well with TPO experiments in 296 Pa oxygen it seems that the temperature differences between TEM and TPO experiments (compare Table 1 and Table 2) can be attributed mainly to the pressure difference between the two methods.

4. Conclusion

In this study the catalytic behavior of metallic silver nanoparticles during soot oxidation was studied by means of TPO experiments carried out in a flow reactor and in an environmental transmission electron microscope. Soot:silver mixtures in a ratio 5:1 wt:wt showed different catalytic activity depending on the contact condition between soot and catalyst, which was determined by the preparation method. Crushing soot and silver together in a mortar (tight contact condition) resulted in a much finer dispersion of silver particles within the soot cake as compared to soot:silver mixtures prepared by simply stirring the two powders with a spatula (loose contact condition). Flow reactor TPO experiments showed that silver in both contact types is able to achieve a relatively low carbon

oxidation temperature. In a flow of 10 vol% O_2 in N_2 the maximal carbon oxidation rate of non-catalytic oxidation occurred at a temperature of 654 °C, whereas the maximal oxidation rate occurred at significantly lower temperatures in loose contact (520 °C) or particularly in tight contact (450 °C) with Ag nanoparticles. The considerable activity of silver in both contact conditions should at least in part be ascribed to the behavioral characteristics of the silver particles, particularly their significant mobility, responsible for ensuring the constant presence of a reactive carbon-silver-oxygen interface during oxidation. Mobility of silver was observed by *in situ* oxidation experiments in the ETEM. Attractive forces, possibly van der Waal forces, exist between the metal and carbon, and in an oxidizing atmosphere, where the carbon is oxidized at the catalyst/carbon interface and the reaction front thus moves, these attractive forces pull the silver particles along with the progressing reaction front and cause significant mobility of the catalyst particles. The relatively good loose contact activity of silver could be related to the fact that the high mobility of the silver helps to overcome the poor initial dispersion of the catalyst particles. Concerning the difference between loose and tight contact, the mobility was observed in ETEM experiments to be triggered at lower temperatures for mixtures in tight contact (342-700 °C), compared to loose contact (500-760 °C). The mobility is a process highly influenced by the balance between attractive forces connecting silver agglomerates to the porous soot matrix and the size of the silver agglomerates themselves, which dictates their internal cohesive energy. As an example an isolated silver particle is not restricted by an internal cohesive energy in the same way as a silver particle within a larger silver cluster, and the isolated particle can therefore be set in motion by the progressing reaction front at a lower temperature as observed in the ETEM experiments.

The high mobility of silver shown here is of importance for the understanding of silver catalysts used for soot oxidation and should also be of importance for other soot oxidation catalysts that could derive mobility from e.g. a low melting point, for example vanadium oxide.

Acknowledgements

Financial support from The Danish Council for Strategic Research (DSF) is gratefully acknowledged (Grant No. 2106-08-0039). The A. P. Møller and Chastine Mc-Kinney Møller Foundation is gratefully acknowledged for its contribution towards the establishment of the Center for Electron Nanoscopy at the Technical University of Denmark.

References

[1] Ris, C. US EPA health assessment for diesel engine exhaust: A review. Inhal. Toxicol. 2007; 19:229-239.

[2] Chameides, WL, Bergin, M. Soot takes center stage. Science 2002; 297:2214-2215.

[3] Kerr, RA. Soot is warming the world even more than thought. Science 2013; 339:382-382.

[4] Frank, B, Schuster, M, Schlögl, R, Su, DS. Emission of highly activated soot Particulate—The other side of the coin with modern diesel engines. Angew. Chem. Int. Ed. 2013; 52:2673-2677.

[5] Kittelson, DB. Engines and nanoparticles: A review. J. Aerosol Sci. 1998; 29:575-588.

[6] Andreae, MO, Ramanathan, V. Climate's dark forcings. Science 2013; 340:280-281.

[7] Van Setten, BAAL, Makkee, M, Moulijn, JA. Science and technology of catalytic diesel particulate filters. Catal. Rev. Sci. Eng. 2001; 43:489-564.

[8] Adler, J. Ceramic diesel particulate filters. Int. J. Appl. Ceram. Technol. 2005; 2:429-439.

[9] Stamatelos, AM. A review of the effect of particulate traps on the efficiency of vehicle diesel engines. Energy Convs. Mgmt. 1997; 38:83-99.

[10] Southward, BWL, Basso, S. An investigation into the NO_2-decoupling of catalyst to soot contact and its implications for catalysed DPF performance. SAE paper 2008-01-0481, 2008.

[11] Neeft, J, Makkee, M, Moulijn, JA. Metal oxides as catalysts for the oxidation of soot. Chem. Eng. J. 1996; 64:295-302.

[12] Konstandopoulos, AG, Lorentzou, S, Pagkoura, C, Ohno, K, Ogyu, K, Oya, T. Sustained soot oxidation in catalytically coated filters. SAE paper 2007-01-1950, 2007.

[13] Konstandopoulos, AG, Papaioannou, E. Update on the science and technology of diesel particulate filters. Kona 2008; 26:36-65.

[14] Konstandopolous, A, Papaioannou, E, Zarvalis, D, Skopa, S, Baltzopoulou, P, Kladopoulou, E, et al. Catalytic filter systems with direct and indirect soot oxidation activity. SAE paper 2005-01-0670, 2005.

[15] Kumar, PA, Tanwar, MD, Bensaid, S, Russo, N, Fino, D. Soot combustion improvement in diesel particulate filters catalyzed with ceria nanofibers. Chem. Eng. J. 2012; 207-208:258-266.

[16] Kameya, Y, Lee, KO. Soot cake oxidation on a diesel particulate filter: Environmental scanning electron microscopy observation and thermogravimetric analysis. Energy Technol. 2013; 1:695-701.

[17] Liang, Q, Wu, X, Wu, X, Weng, D. Role of surface area in oxygen storage capacity of ceria–zirconia as soot combustion catalyst. Catal. Lett. 2007; 119:265-270.
[18] Shimizu, K, Kawachi, H, Satsuma, A. Study of active sites and mechanism for soot oxidation by silver-loaded ceria catalyst. Appl. Catal. B 2010; 96:169-175.
[19] Christensen, JM, Deiana, D, Grunwaldt, J-D, Jensen, AD. Ceria prepared by flame spray pyrolysis as an efficient catalyst for oxidation of diesel soot. Catal. Lett 2014; 144:1661-1666.
[20] Christensen, JM, Grunwaldt, J-D, Jensen, AD. Importance of the oxygen bond strength for catalytic activity in soot oxidation, submitted.
[21] Böcklein, S, Günther, S, Wintterlin, J. High-Pressure scanning tunneling microscopy of a silver surface during catalytic formation of ethylene oxide. Angew. Chem. Int. Ed. 2013; 52:5518-5521.
[22] Campbell, CT. Atomic and molecular oxygen adsorption on Ag (111). Surf. Sci. 1985; 157:43-60.
[23] Kayama, T, Yamazaki, K, Shinjoh, H. Nanostructured ceria− silver synthesized in a one-pot redox reaction catalyzes carbon oxidation. J. Am. Chem. Soc. 2010; 132:13154-13155.
[24] Yamazaki, K, Kayama, T, Dong, F, Shinjoh, H. A mechanistic study on soot oxidation over CeO_2-Ag catalyst with 'rice-ball' morphology. J. Catal. 2011; 282:289-298.
[25] Corro, G, Pal, U, Ayala, E, Vidal, E. Diesel soot oxidation over silver-loaded SiO_2 catalysts. Catal. Today 2013; 212:63-69.
[26] Ikeue, K, Kobayashi, S, Machida, M. Catalytic soot oxidation by $Ag/BaCeO_3$ having tolerance to SO_2 poisoning. J. Ceram. Soc. Jap. 2009; 117:1153-1157.
[27] Machida, M, Murata, Y, Kishikawa, K, Zhang, D, Ikeue, K. On the reasons for high activity of CeO_2 catalyst for soot oxidation. Chem. Mater. 2008; 20:4489-4494.
[28] Aneggi, E, Llorca, J, de Leitenburg, C, Dolcetti, G, Trovarelli, A. Soot combustion over silver-supported catalysts. Appl. Catal. B 2009; 91:489-498.
[29] Shigapov, A, Dubkov, A, Ukropec, R, Carberry, B, Graham, G, Chun, W, McCabe, R. Development of PGM-free catalysts for automotive applications. Kin. Catal. 2008; 49:756-764.
[30] Shimizu, K, Katagiri, M, Satokawa, S, Satsuma, A. Sintering-resistant and self-regenerative properties of Ag/SnO_2 catalyst for soot oxidation. Appl. Catal. B 2011; 108:39-46.
[31] Lim, C-B, Kusaba, H, Einaga, H, Teraoka, Y. Catalytic performance of supported precious metal catalysts for the combustion of diesel particulate matter. Catal. Today. 2011; 175:106-111.
[32] Yamazaki, K, Sakakibara, Y, Dong, F, Shinjoh, H. The remote oxidation of soot separated by ash deposits via silver–ceria composite catalysts. Appl. Catal. A 2014; 476:113-120.

[33] Haneda, M, Towata, A. Catalytic performance of supported Ag nano-particles prepared by liquid phase chemical reduction for soot oxidation. Catal. Today. 2015; 242:351-356.
[34] Im, J, Lee, CM, Coates, JT. Comparison of two reference black carbons using a planar PCB as a model sorbate. Chemosphere 2008; 71:621-628.
[35] Braun, A, Mun, BS, Huggins, FE, Huffman, GP. Carbon speciation of diesel exhaust and urban particulate matter NIST standard reference materials with C (1s) NEXAFS spectroscopy. Environ. Sci. Technol. 2007; 41:173-178.
[36] Gustafsson, Ö, Bucheli, TD, Kukulska, Z, Andersson, M, Largeau, C, Rouzaud, J-N, Reddy, CM, Eglinton, TI. Evaluation of a protocol for the quantification of black carbon in sediments. Global Biogeochem. Cycles 2001; 15:881-890.
[37] Hansen, TW, Wagner, JB, Dunin-Borkowski, RE. Aberration corrected and monochromated environmental transmission electron microscopy: Challenges and prospects for materials science. Mater Sci. Technol. 2010; 26:1338-1344.
[38] Shen, J, Ziaei-Azad, H, Semagina, N. Is it always necessary to remove a metal nanoparticle stabilizer before catalysis?. J. Mol. Catal. A 2014; 391:36-40.
[39] Czanderna, AW. Isosteric heat of adsorption of oxygen on silver. J. Vac. Sci. Technol. 1977; 14:408-411.
[40] Ostrovskii, VE. The chemisorption of oxygen on group IB metals and their surface oxidation. Russ. Chem. Rev. 1974; 43:921-932.
[41] Engelhardt, HA, Menzel, D. Adsorption of oxygen on silver single crystal surfaces. Surf. Sci. 1976; 57:591-618.
[42] Nørskov, JK, Bligaard, T, Logadottir, A, Bahn, S, Hansen, LB, Bollinger, M, et al. Universality in heterogeneous catalysis. J. Catal. 2002; 209:275-278.
[43] Baker, RTK, France, JA, Rouse, L, Waite, RJ. Catalytic oxidation of graphite by platinum and palladium. J. Catal. 1976; 41:22-29.
[44] Hennig, GR. Catalytic oxidation of graphite. J. Inorg. Nucl. Chem. 1962; 24:1129-1137.
[45] Booth, TJ, Pizzocchero, F, Andersen, H, Hansen, TW, Wagner, JB, Jinschek, JR, et al. Discrete dynamics of nanoparticle channelling in suspended graphene. Nanolett. 2011; 11:2689-2692.
[46] Pizzocchero, F, Vanin, M, Kling, J, Hansen, TW, Jacobsen, KW, Bøggild, P, et al. Graphene edges dictate the morphology of nanoparticles during catalytic channeling. J. Phys. Chem. C 2014; 118:4296-4302.

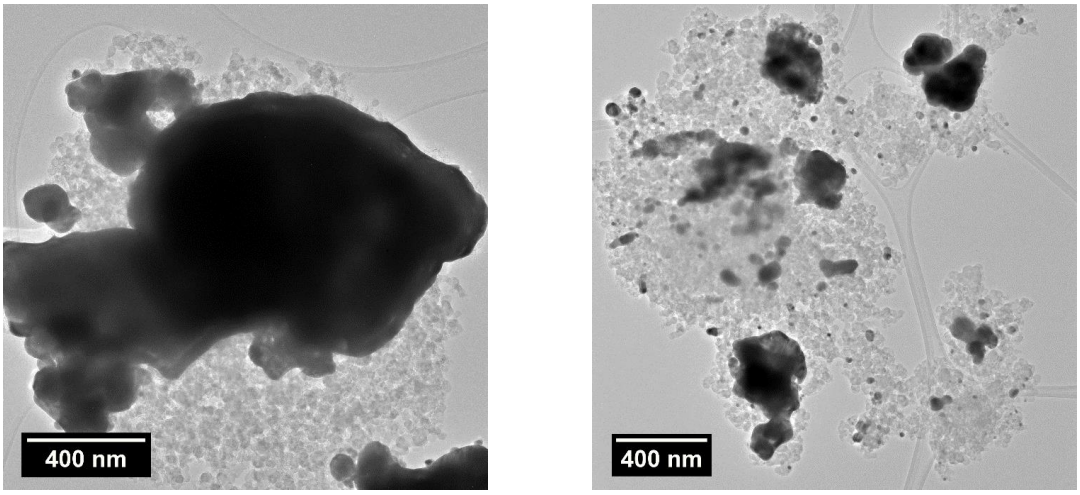

Figure 1 Bright Field TEM micrograph of a soot:silver (1:5 wt:wt) mixture in **(left)** loose contact and **(right)** tight contact condition. Darker agglomerates represent the silver fraction of the specimen while the lighter porous structure is the soot. In both micrographs a portion of the lacey carbon support holding the specimen is visible.

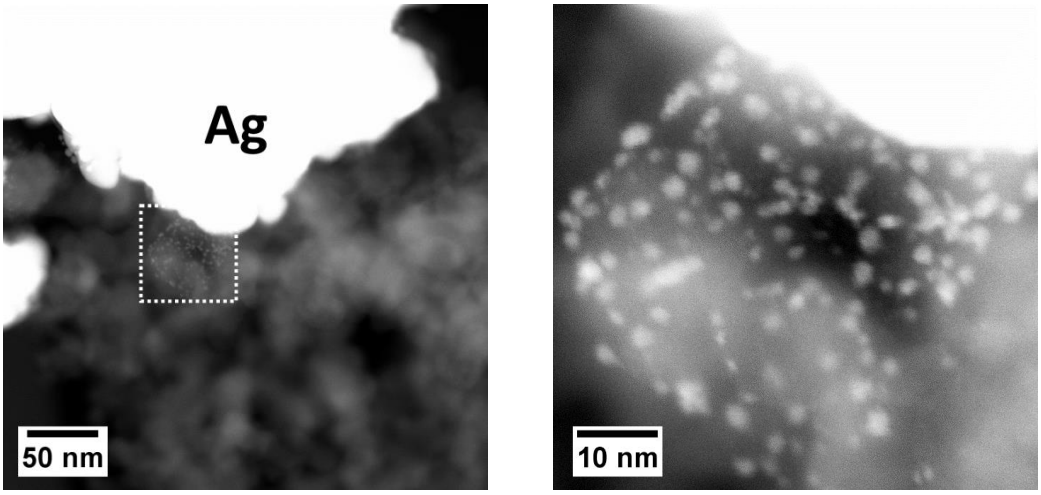

Figure 2 (Left) STEM micrograph of a soot:silver (1:5 wt:wt) mixture in loose contact mode. A group of small nanoparticles (bright spots in the white box) close to a silver agglomerate is highlighted. **(Right)** Close-up on the particle area. Contrast has been enhanced in order to better visualize the soot underlying the catalyst.

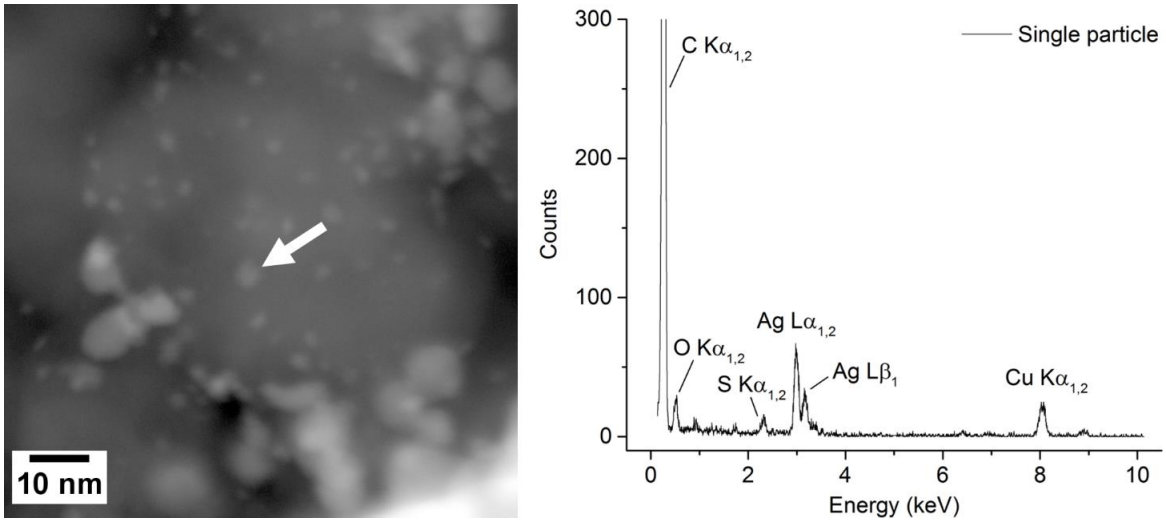

(a) Single particle analysis

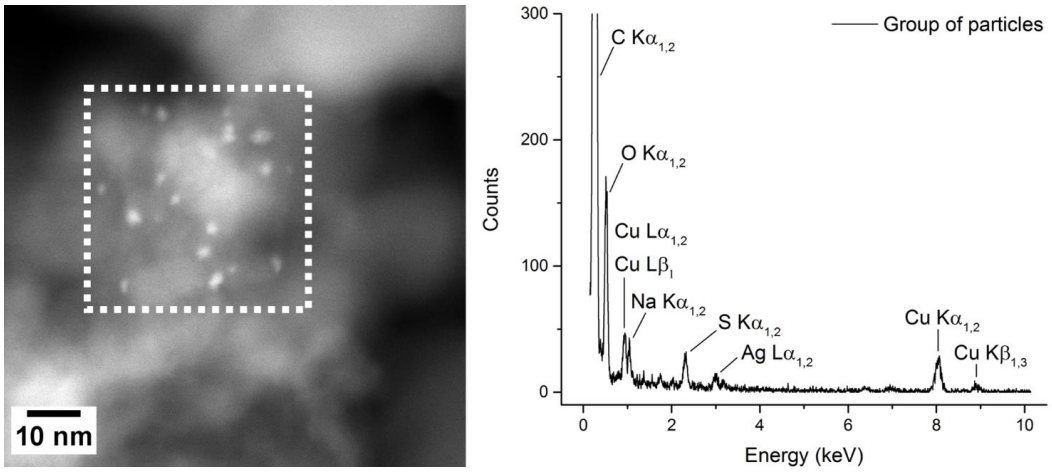

(b) Group particles analysis

Figure 3 STEM micrograph (left) and STEM-EDX spectrum (right) of **(a)** a silver single particle and **(b)** a group of silver particles. Graphical elements in white indicate the origin of the EDX signal on the sample.

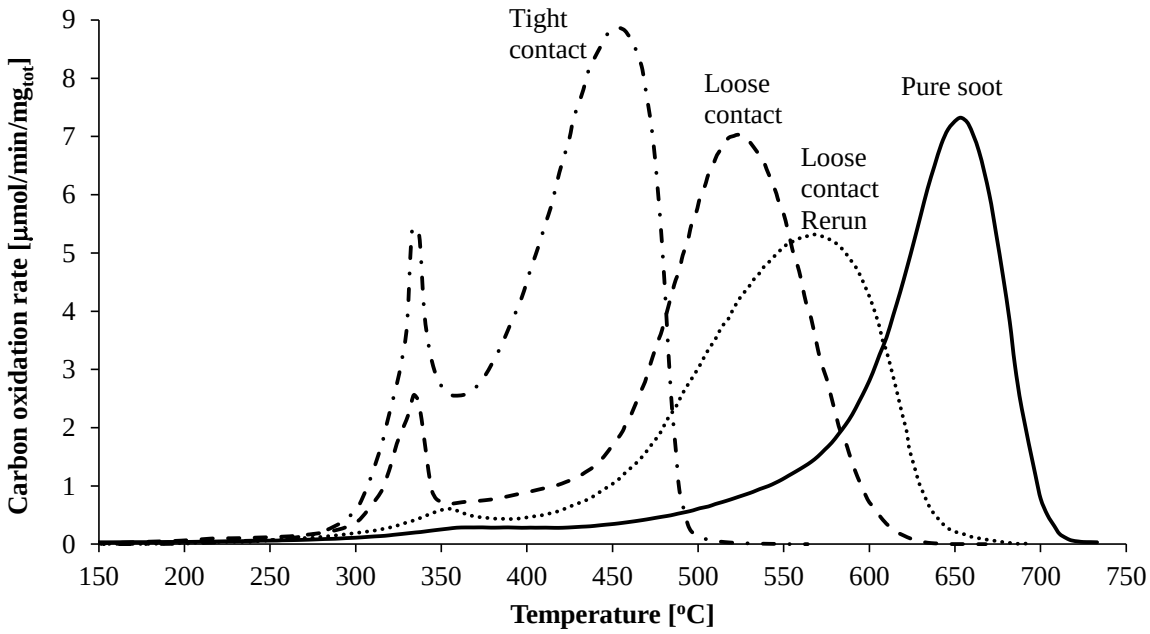

Figure 4 The rate of carbon oxidation (normalized by the total, initial mass of carbon) during TPO experiments with silver catalyzed soot oxidation. Experimental conditions: soot:silver = 1:5 wt:wt, ramp = 11 °C/min, 1 NL/min, 10.2 vol% O_2 in N_2.

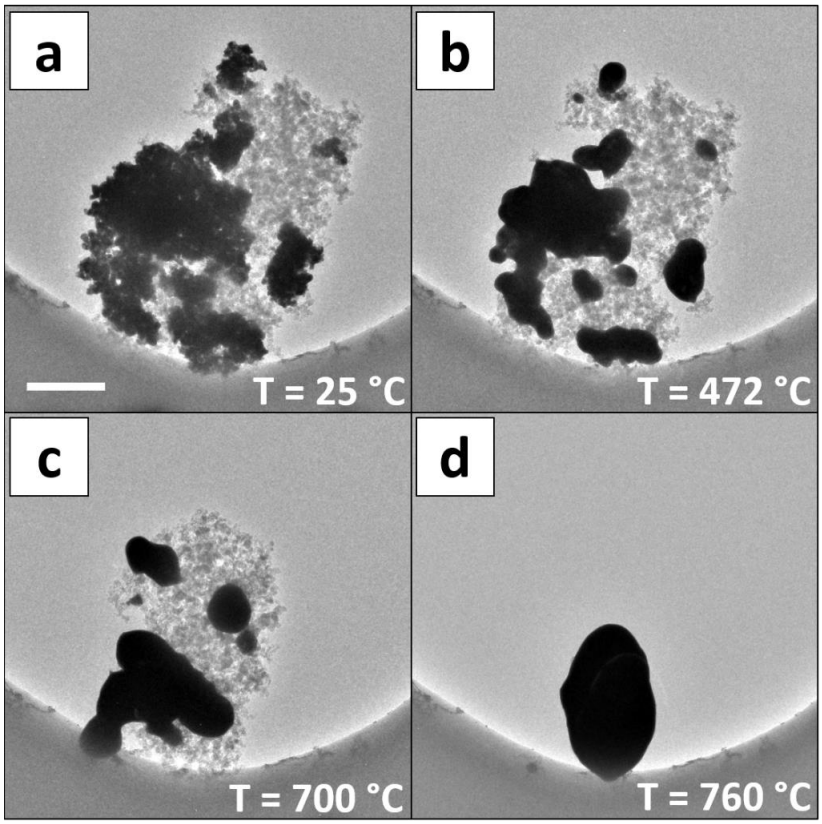

Figure 5 BF-TEM micrographs of *in situ* soot oxidation in the ETEM in loose contact condition showing (a) initial distribution and morphology of silver and soot, (b) coalescence of silver particles, (c) mobility of coalesced silver agglomerates over the soot cake and (d) final silver agglomeration. Scalebar is 500 nm.

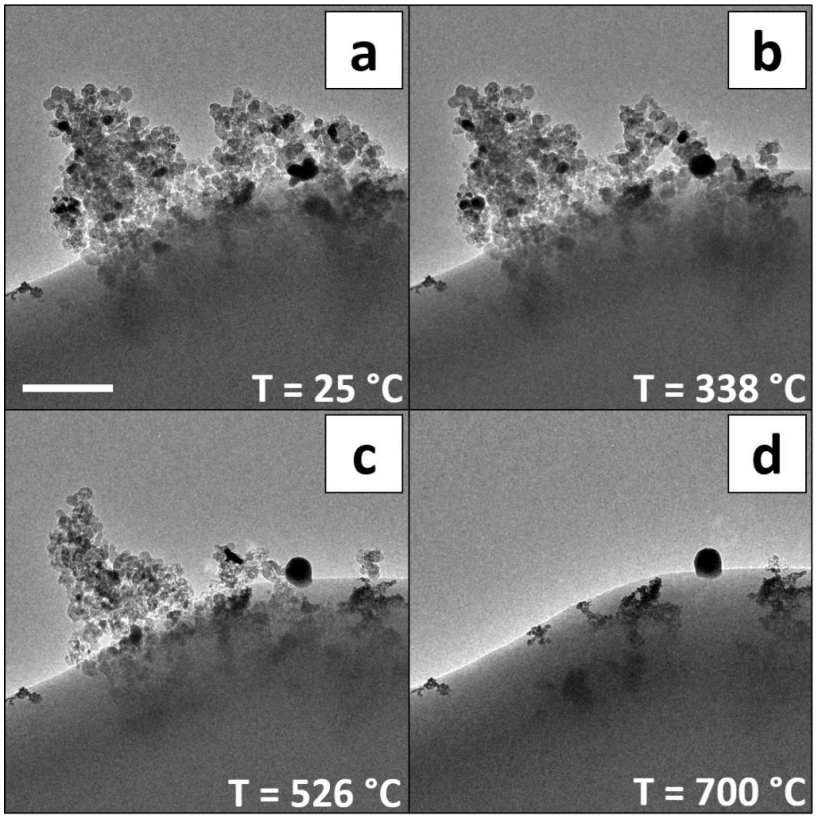

Figure 6 BF-TEM micrographs of *in situ* soot oxidation in the ETEM in tight contact condition showing (a) initial distribution and morphology of silver and soot, (b) coalescence of silver particles, (c) mobility of coalesced silver agglomerates over the soot cake and (d) final silver agglomeration. Scalebar is 300 nm.

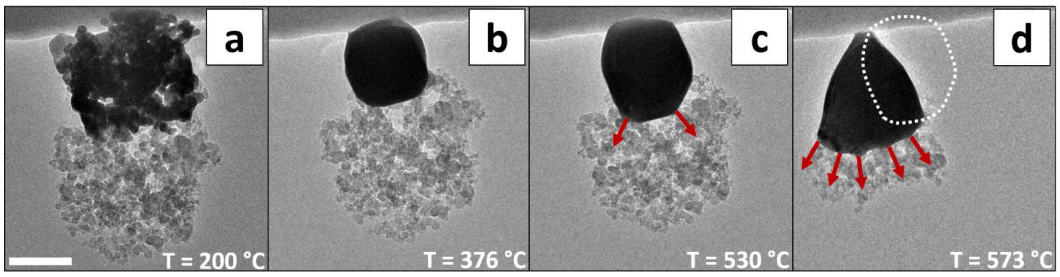

Figure 7 Wetting and movement of a silver agglomerate during *in situ* oxidation of soot:silver mixture in loose contact condition. BF-TEM micrographs shows (a) initial agglomeration and morphology of silver and soot, (b) coalescence of silver particles, (c) initial deformation of coalesced silver agglomerate due to capillary forces and (d) movement of silver agglomerate. Arrows in red indicate the direction of deformation of the silver agglomerate. The previous position of the silver agglomerate as observed in (c) is highlighted in subfigure (d) with a dashed white line. Scalebar is 200 nm.

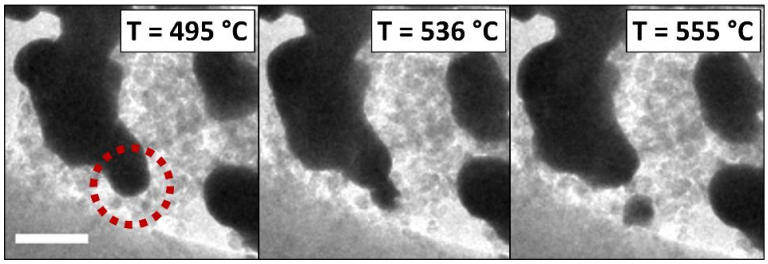

Figure 8 BF-TEM micrographs showing the detachment of a small portion of silver from a bigger agglomerate during *in situ* oxidation of soot:silver mixture in loose contact condition. The red dashed ring indicates the region where detachment occurs. Scalebar is 200 nm.

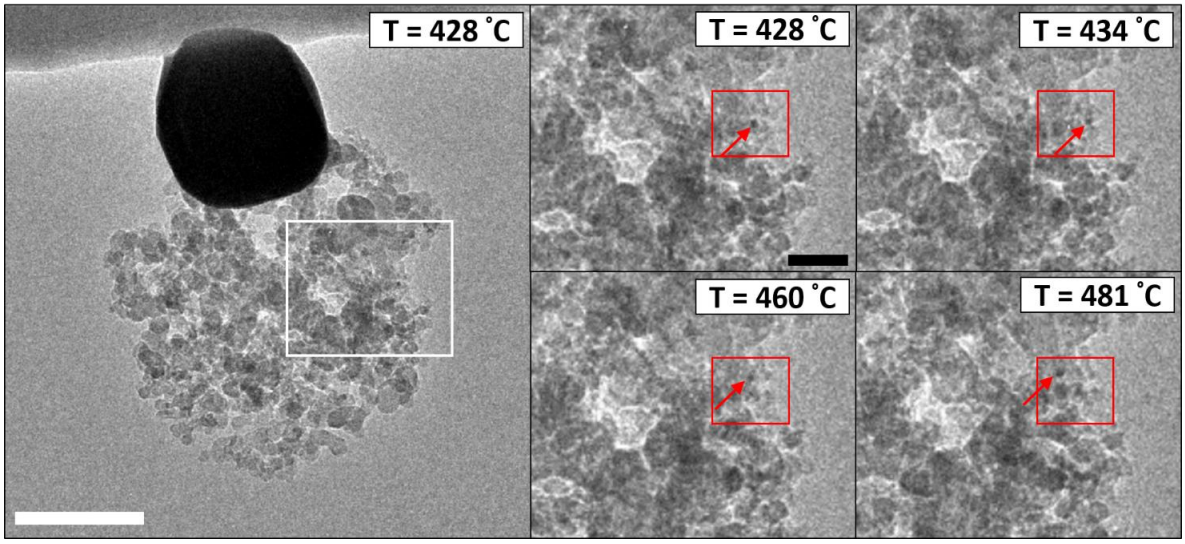

Figure 9 Mobility of small (< 10 nm) silver particles during *in situ* oxidation of a soot:silver mixture in loose contact condition. The area highlighted in the white rectangle is magnified in the subfigures on the right. Scalebar in the main figure is 200 nm. Scalebar in the subfigures is 50 nm. The position of the red rectangle is fixed and can be used as a reference for the eye in order to track the movement of the silver particle.

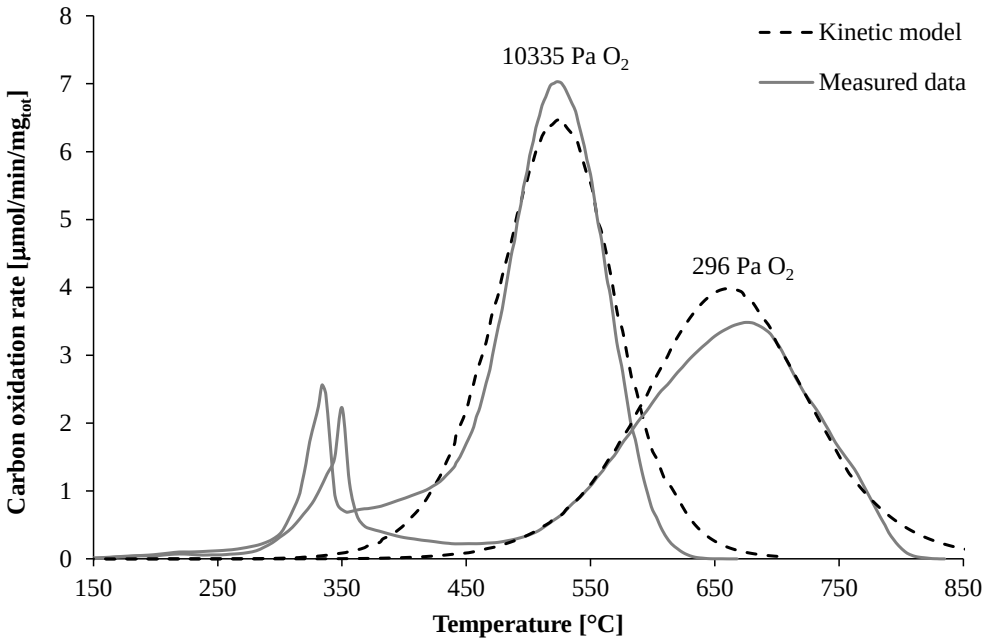

Figure 10 The rate of carbon oxidation (normalized by the total, initial mass of carbon) during TPO in loose contact with silver at two different oxygen partial pressures. Solid lines represent the experimental data and dashed lines the theoretical profiles calculated according to the presented kinetic model. Experimental conditions: Soot:silver = 1:5 wt:wt, T ramp = 11 °C/min, 10335 Pa O_2 = 1 NL/min, 10.2 vol% O_2 in N_2, 296 Pa O_2 = 1NL/min 2960 ppmv O_2 in N_2.

Table 1 Temperature (in °C) onsets and ranges for coalescence, mobility onset, maximal mobility and end of oxidation as observed from ETEM experiments.

	Loose contact	**Tight contact**
Coalescence	280-472	250-338
Mobility onset	500	342
Maximal mobility	700	526
End of oxidation	760	700

Table 2 Peak and ending temperatures (in °C) of soot oxidation as observed from activity measurements (Section 3.3).

	Loose contact	**Tight contact**
Carbon oxidation rate peak	520	440
End of oxidation	625	500

Supplementary information for

"Visualizing the Mobility of Silver During Catalytic Soot Oxidation"

Diego Gardini[1], Jakob M. Christensen[2], Christian D. Damsgaard[1,3], Anker D. Jensen[2], Jakob B. Wagner[1]*

[1]Center for Electron Nanoscopy, Technical University of Denmark, Fysikvej, Building 307, DK-2800 Kgs. Lyngby, Denmark.

[2]Department of Chemical and Biochemical Engineering, Technical University of Denmark, Søltofts Plads, Building 229, DK-2800 Kgs. Lyngby, Denmark

[3]Center for Individual Nanoparticle Functionality, Department of Physics, Technical University of Denmark, Fysikvej, Building 307, DK-2800 Kgs. Lyngby, Denmark

The crystallinity of the various metal or metal oxide catalysts samples were investigated by X-ray diffraction (XRD). XRD patterns were acquired with a PANalytical X'Pert PRO diffractometer with a Cu-Kα X-ray source operated at 45 kV and 40 mA and with a Ni-filter, automatic anti-scatter and divergence slits and a monochromator on the diffracted beam. Patterns were recorded between $2\theta = 10°$ and $2\theta = 80°$ with a step width of $2\theta = 0.0130°$. The total duration of an XRD measurement was 100 minutes.

Corresponding author. Tel: +4545256471. E-mail: jakob.wagner@cen.dtu.dk

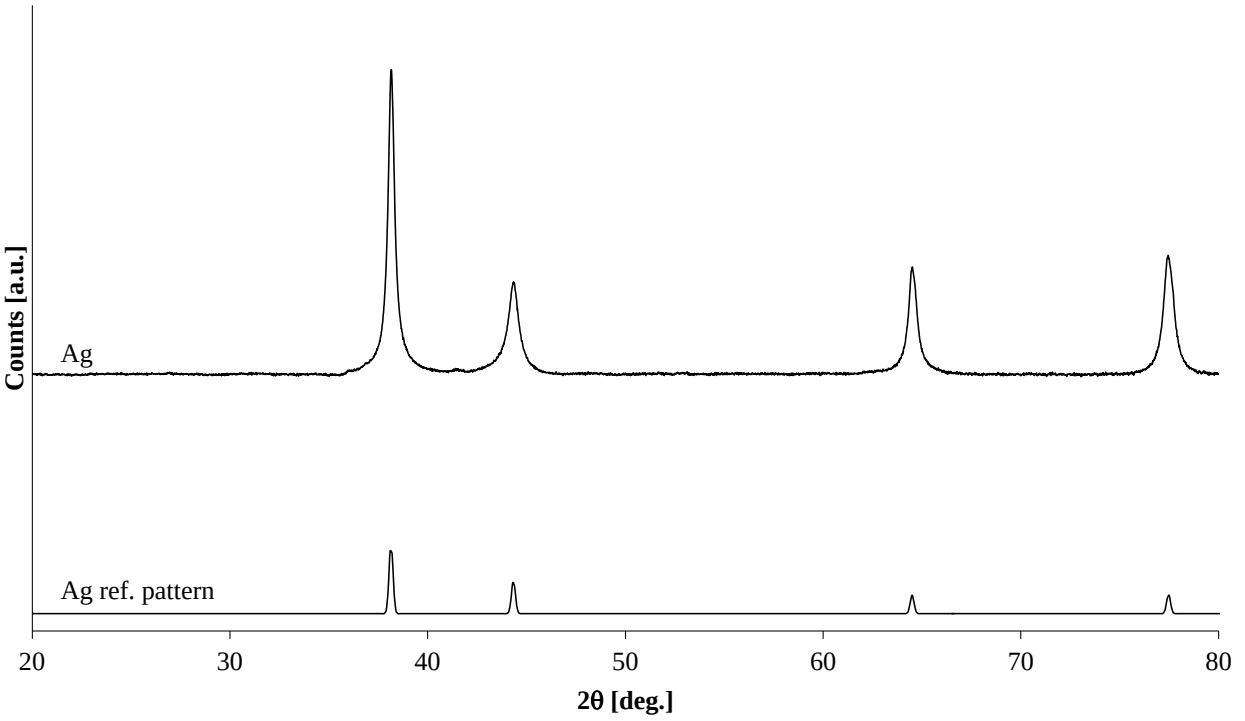

Figure S1 X-ray diffraction patterns of the employed silver samples.

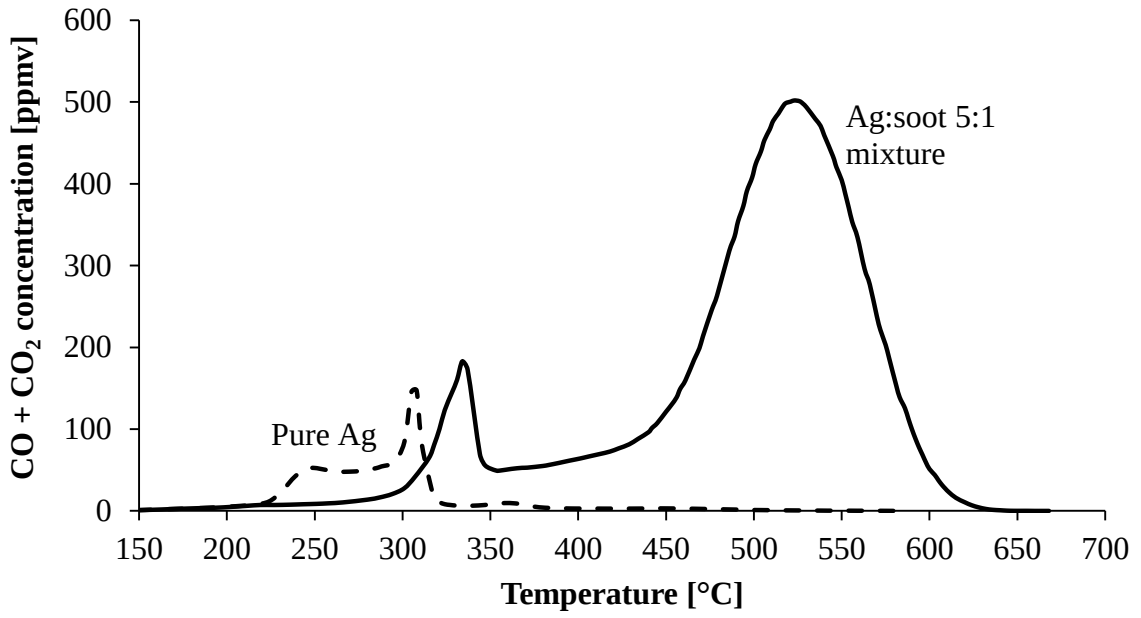

Figure S2 The total CO_x concentration in the effluent stream as a function of temperature during oxidation of an Ag:soot mixture (10 mg:2 mg) in loose contact and by oxidation of 15.2 mg of the pure Ag sample.

The figure illustrates that the oxidation of the PVP stabilizer/dispersant occurs slightly above 300 °C giving an early peak in the oxidation profile. It also seems that the presence of soot delays the early peak slightly. Experimental conditions: Soot:Catalyst = 1:5 wt:wt, ramp = 11 °C/min, 1 NL/min, 10.2 vol% O_2 in N_2.

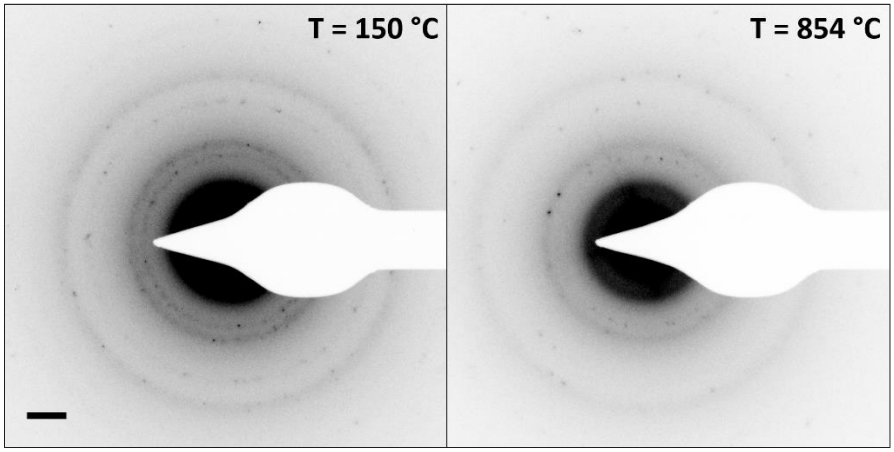

(a) Loose contact condition

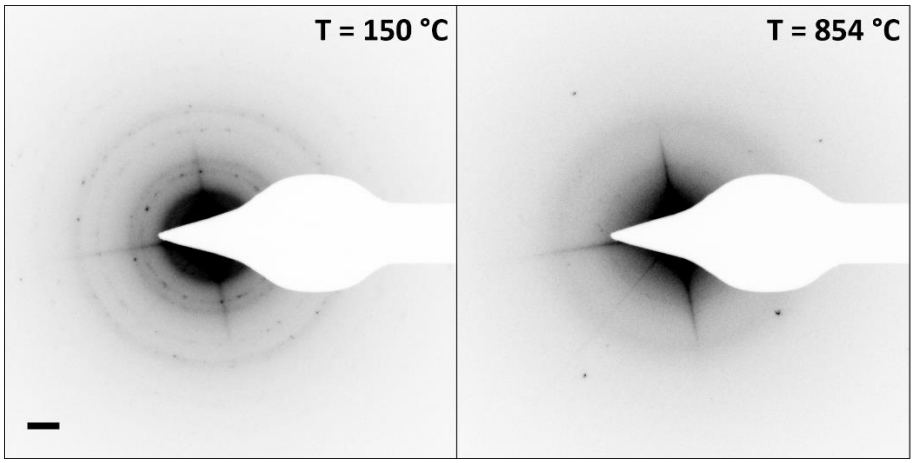

(b) Tight contact condition

Figure S3 Electron diffraction patterns acquired at the beginning and at the end of *in situ* oxidation of a silver:soot mixture in (a) loose and (b) tight contact conditions. Scalebar is 2 nm^{-1}.

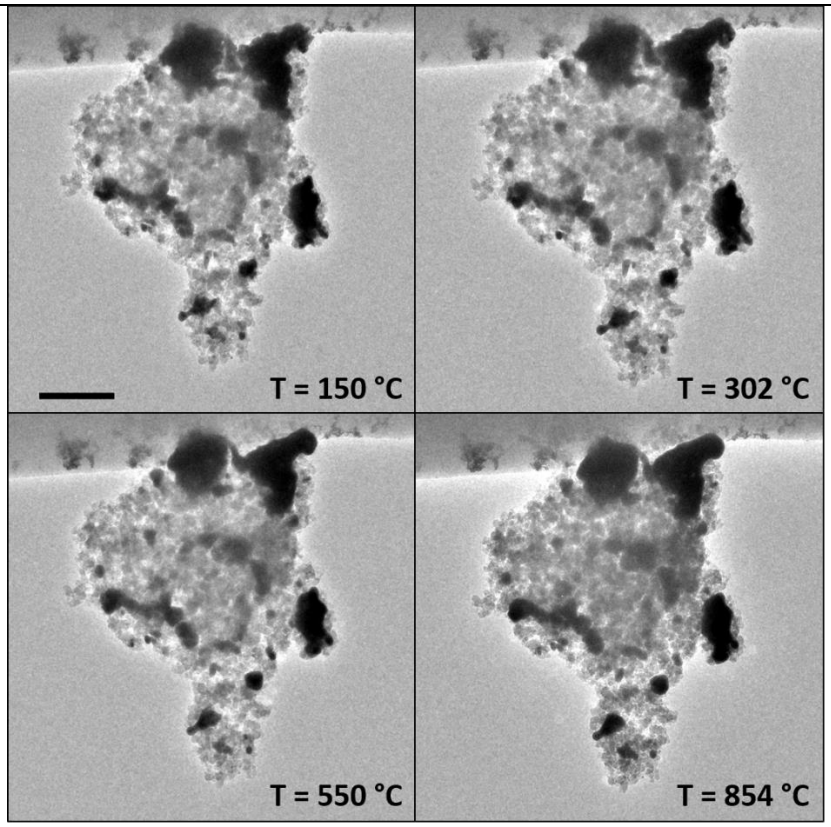

Figure S4 BF-TEM micrographs of *in situ* heating in vacuum of a silver:soot mixture in tight contact condition. Scale bar is 400 nm.